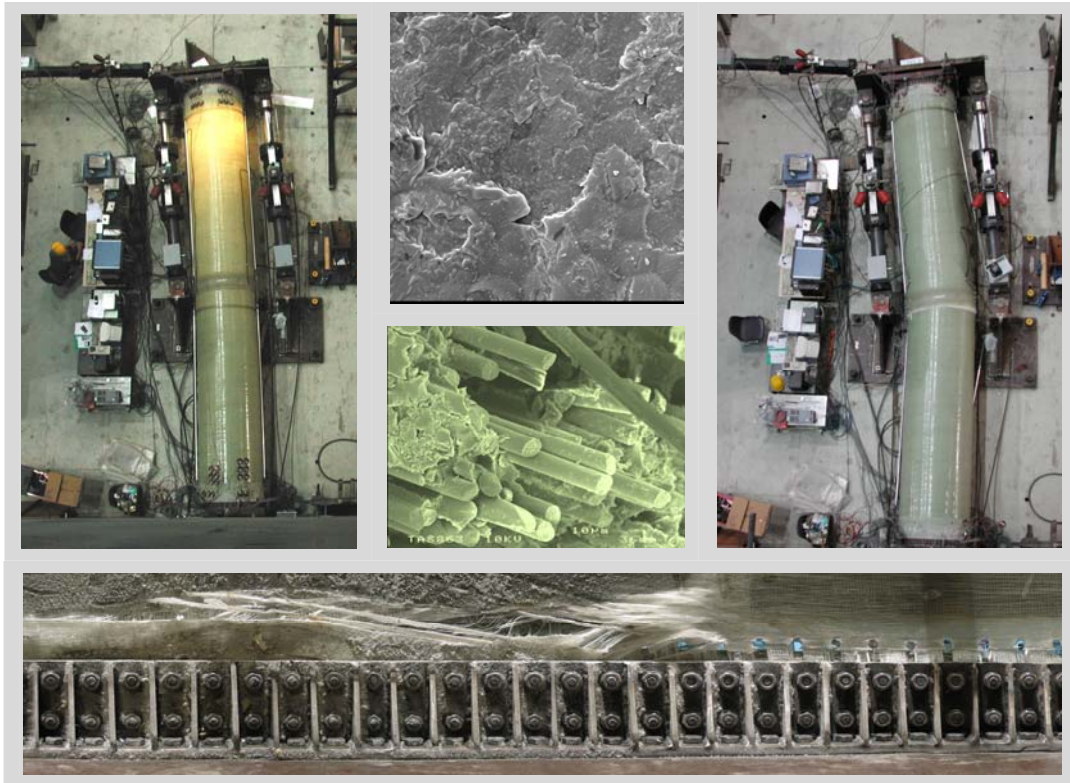**EUROPEAN COMMISSION**
JOINT RESEARCH CENTRE

Institute for the Protection and Security of the Citizen
European Laboratory for Structural Assessment (ELSA)
I-21020 Ispra (VA), Italy

A wind turbine tower design based on the use of fibre-reinforced composites.

E. Gutiérrez, S. Primi, F. Taucer, P. Caperan, D. Tirelli (ELSA-JRC),
J. Mieres, I. Calvo J. Rodriguez, F. Vallano (NECSO),
C. Galiotis, D. Mouzakis (FORTH),

2003   **EUR 20786 EN**

LEGAL NOTICE

A great deal of additional information on the
European Union is available on the Internet.
It can be accessed through the Europa server
(http://europa.eu.int)

FP5 PROJECT ENK5-CT-2000-00328
MEGAWIND

Deliverable D2 Work Package 2

Document Control Sheet

Abstract:

This report summarises the key features of the MEGAWIND FRP composite tower design and the experimental campaign conducted on 1/3 scale prototype specimens. The report highlights the problems and lessons learnt from the manufacturing process and how these affect the overall design. The results of Finite Element models are compared to experimental data and are then used to predict the behaviour of the proposed full-scale prototype. The effects of environmental factors on the constituent materials are studied with an accelerated ageing campaign and recommendations are made on the basis of the observed degradation.

PROJECT FUNDED BY THE EUROPEAN COMMUNITY UNDER THE FP5
PROGRAMME

Contents

1 Introduction

MEGAWIND PROJECT, ENK5-CT-2000-00328

The following report describes the contribution of the various partners involved in Work Package 2 (WP2) of the MEGAWIND project. The aim of the work package was to conduct research in order to develop new design concepts for wind turbine towers based on the use of fibre-reinforced-composite (FRP) materials.

At the outset of the project, the main objective of WP2 and the closely related WP4 (Tower manufacture and implementation) was defined as :

Design and development of an alternative tower allowing for on-site manufacturing of the tower including wind turbine self-erection. The design implementation involves research on materials and large-scale structural tests on representative subassemblies of the tower. The part of the tower structure that is to be manufactured from composite materials will be transported in low weight, low volume, pre-forms or pultrusions

1.1 Aspects of innovation

In terms of innovation it was expected that a tower designed on the basis of using FRP technology would offer new possibilities for on-site logistics and assembly and specifically contribute to the development of a compact easily transportable MW-sized wind turbine system for erection in sites of difficult access such as mountainous terrain or offshore.

Whereas standard concrete and steel towers offer competitive prices in standard erection sites this is not generally the case in isolated locations or in water depths of over 10 metres. New structural solutions are possible by using advanced composite materials technology that may offer cheaper whole-life solutions by increasing the net area of commercially viable wind sites and prolong the life, or reduce the maintenance cost, of the wind generator superstructure. The research was motivated by the expectation that a tower made from composite materials would have a number of advantages over a standard steel tower that would offset the higher material costs such as: lower maintenance costs, improved dynamic damping characteristics, extended fatigue life, reduced logistic costs for installation and, potentially, the capacity to improve on some aspects of environmental (landscape) pollution.

The aim was to provide an alternative to the existing steel or standard concrete designs particularly where the site and accessibility conditions are difficult. Implicit in the use of FRP materials is the scope of selecting the appropriate construction and manufacturing methodology in order to reduce the logistic burden (heavy cranes and ancillary equipment), usually incurred when erecting towers made up of large monolithic elements. The original concept was based on using lightweight composite formwork segments that could be assembled on site. The initial plan for the tower construction was that it be erected as a series of hollow-section concentric rings generating a 50-60m tall cylindrical component. On the basis of the local force demands (i.e. depending on the height of the tower module) each ring section was to be filled with either high-strength concrete (both for the purposes of structural stability and ballast) or other core material in order to generate an optimum sandwich panel having the required structural, static, and dynamic characteristics. Given the technical challenge of the project, the design work plan included a backup design that could still exploit the manufacturing versatility of composites; this design is based on the use of pultruded composite sections that were to be joined to produce a mast-like structure.

In addition to its primary use as a load carrying structure, the tower was, ideally, to be designed as the principal crane to erect the nacelle and the rotor. This last aspect would make large wind-tower erection in isolated locations more attractive (this is a key issue in Europe where due to the high roughness factors of the terrain, many locations that offer high wind power potential incur prohibitive installation costs).

The innovative use of composite materials is also of interest for offshore applications. In this case the advantages are those qualities that are afforded by the low chemical inertness of fibre-reinforced composites in saline environments, as well as the reduced logistic and transportation costs. Although the tower design will revolve around a land-based tower, the advantages will show that such constructions may offer new structural solutions for offshore platforms in waters over 10 metres in depth.

1.2   Work Package content and deliverable

The main scope of WP2 is to conduct research on designs and perform tests of representative elements of the wind turbine tower. In the original work two main tasks were defined:

Task 2.1. Design options survey, component design and testing

The work regards the research on alternative tower designs focusing on transportation easiness, on site manufacturing and nacelle/rotor self-erection capabilities. Extensive research on composite materials suitable for composite structures. Testing of specific components such as joints and foundation parts will be performed.

Task 2.2. Tower design and subassemblies testing

The work regards the design of the tower with exterior composite shells and concrete or foam-core interior. The materials will be chosen according to the results of Task 2.1. The key aspects are the on site manufacturing capability, the light structure design and the wind turbine nacelle and rotor self-erection capability. Large-scale structural tests will be carried out on representative subassemblies of the tower design before a final construction is approved.

Deliverables

D.2 Composite tower design and testing report.

Outline of document

The following chapters will outline the tasks and sub-tasks described above that represent the deliverable D2, which is contained by this report. The content is organised as follows:

Chapters 2 to 4 deal with Task 2.1 starting with the preliminary design types, manufacturing and joining details for tower sections and foundation components. Chapters 5 to 8 describe the main aspects identified with Task 2.2 related to the subassembly tests on the various tower modules studied. Further to this, in Chapters 10 to 11, analytical methods are presented to evaluate the structural performance of the tower, in particular the basic serviceability and limit load criteria. Chapter 10 provides a simplified structural analysis tool that may be used for hybrid (FRP-concrete) tower modules that may be used as input for the global analysis of the complete wind-turbine system whereas Chapter 11 presents more detailed FE analyses. Finally Chapter 12 deals with environmental aspects and the effects of accelerated ageing on structural performance.

2   Preliminary designs and calculations

The design approach is shown schematically in Figure 1. The approach was to consider a basic geometric design for the tower modules and then proceed to analyse the effects that the most pertinent parameters may have on the conceptual design. Various criteria were considered based on the general design guidelines, cost, environmental and manufacturing methods available. Other factors that are considered were related to logistic aspects of installation and inspection methods. These concepts were then traded against each other in order to assess if the initial concept was viable, in which case a decision would be made to either dispense the design or proceed to the next phase whereby a more detailed analysis would be carried out in conjunction with a targeted experimental campaign on representative structural elements.
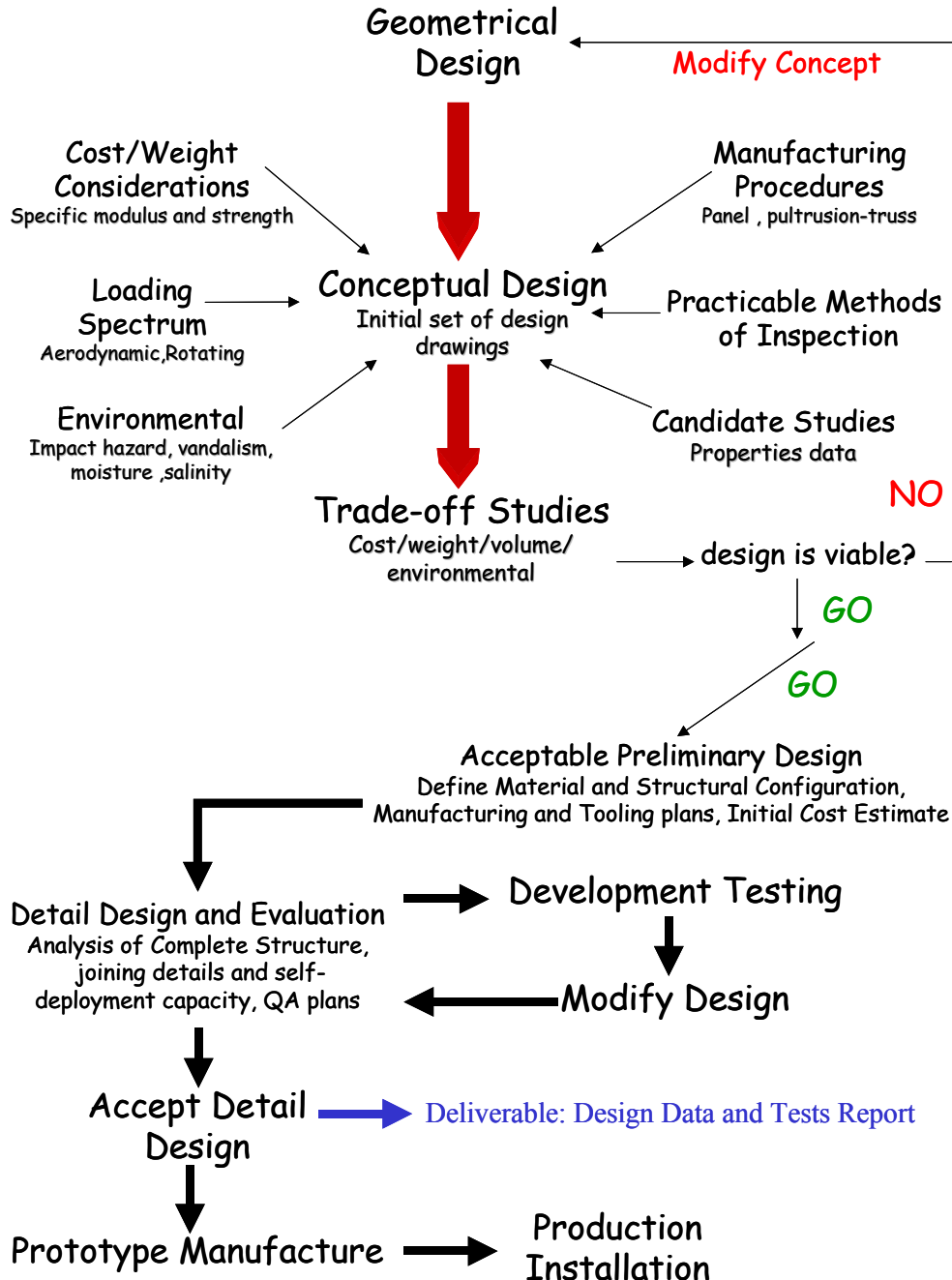
Figure 1 Design and analysis sequence for tower.

3

2.1   Conceptual design concepts

The initial design proposal made by the consortium was to design the tower structure from shells of revolution manufactured from a composite sandwich system, whose core would consist of either high strength concrete (for the lower sections) or a lighter polymer or metallic core (top sections) see Figure 2. Another back up solution was to design a lattice structure manufactured from FRP pultruded sections. Frame structures manufactured from pultruded sections are becoming more common; but typically they are used in relatively light engineering applications where the main loading condition is self-weight. The main reason for this is that the strength of the pultruded profile itself but rather from the joining methods Structures manufactured from joined pultruded sections (other than for carrying pure in-plane bending loads) are subject to delamination failure at the joint connections.
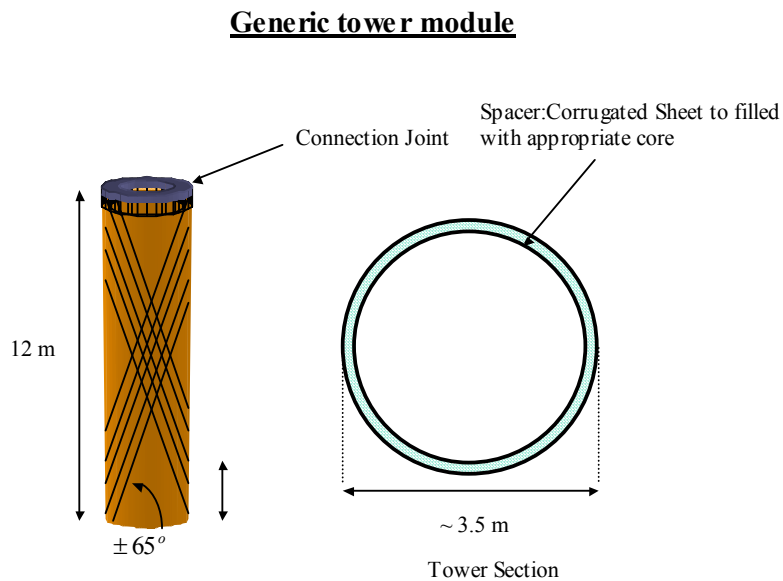
Generic tower module

Connection Joint

Spacer:Corrugated Sheet to filled with appropriate core

12 m

$\pm 65^{o}$

~ 3.5 m

Tower Section

Figure 2 Conceptual design of tower module.

The performance of such joints when subjected to high bending loads usually fail as a result of the out-of-plane stresses that generate through thickness stresses: the weak point for any composite laminate. Usually this results in pullout of the web from the flange or delamination of the pultruded connector pieces. To remedy this problem, fully 3-D isotropic materials such as steel or aluminium brackets are used as connectors, however this has the effect of increasing the weight of the structure as well as adding to the cost and piece count. Moreover, the problem of delamination of the web from the flange in the main pultruded component is not resolved. Another method studied was to manufacture the frame from tubular sections (pultruded or filament wound) with slotted axial steel connectors (a technique currently used in maritime applications for connecting spars to masts); this would relieve the out of plane stresses in the pultrusion by introducing, essentially, only axial load through each strut; however based on an initial cost estimate of the connectors, this project was also discarded.

With regards to the natural frequency of the structure another aspect that precludes the manufacture of the tower as a lattice structure from standard pultrusions is that these are usually

manufactured from glass-fibre, in such a manner that typical lay-up and stratification yield an equivalent modulus of the order of 20 GPa. Based on typical manufacturers data for dimensions of pultruded profiles, an approximate calculation of the dimensions required in order to avoid dynamic resonance resulted in a footing at the base of the tower of over 10 metres. The above reasons, in addition to the advantages for ease of access for serviceability for the nacelle components, precluded the design of a pultruded lattice structure.
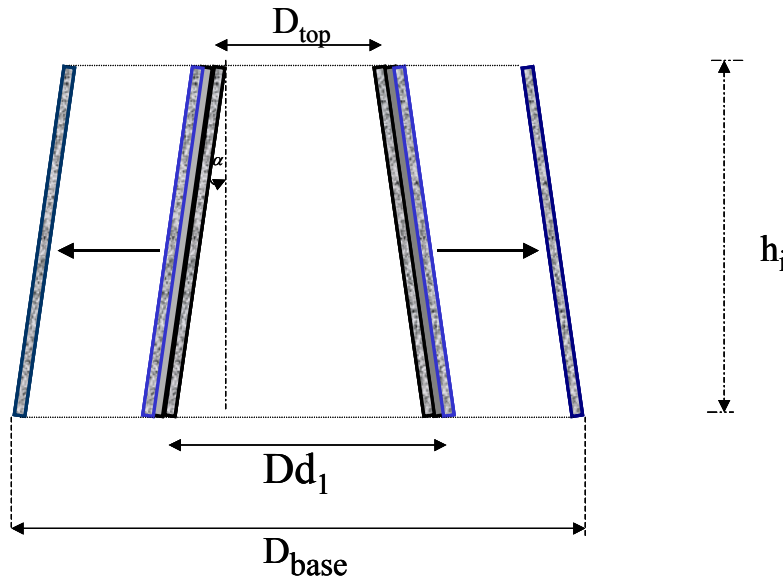

Figure 3 Conceptual design of conical module.

It was proposed that the tower be assembled from sequential sections of conic shell elements as shown in Figure 3. The dimensions of the segments was to be so that, for a given height of each conical section and the foreseen shell thickness, a considerable saving in volume could be achieved by inserting each cone paper-cup style. The advantage that these could be slotted into each other for ease of transport is fundamental to the potential for reducing installation and transportation costs as it is often the case that the volume of the transported goods and not necessarily their weight that affects transportation, which in this case would be relatively low. However, due to the prerequisites of the manufacturing costs this geometry could not be produced wit the filament winding technique as requested by NECSO. In conclusion, the geometry reverted to the original cylindrical section but maintaining the possibility of a hybrid FRP-concrete-core sandwich at the base and lighter cores, or even a purely monolithic FRP section at the top. A purely monolithic section was also considered as viable for the complete structure if it were proved to be seen to be sufficiently strong and stiff enough, in which case, the concrete core could be dispensed with. It was foreseen that the tower would be composed of four 12-metre modules that would be transported separately and installed and joined on site. In the case of the hybrid module the concrete would be poured on-site in low volume grouts using pre-packed and mixed concrete that would not require delivery from heavy dumper trucks.

A module of the working prototype for the hybrid FRP-concrete sandwich tower module is shown in Figure 4 for the 1/3 scale model in the size to be tested at the ELSA laboratory (we show the sandwich section although the monolithic version will have similar overall dimensions).
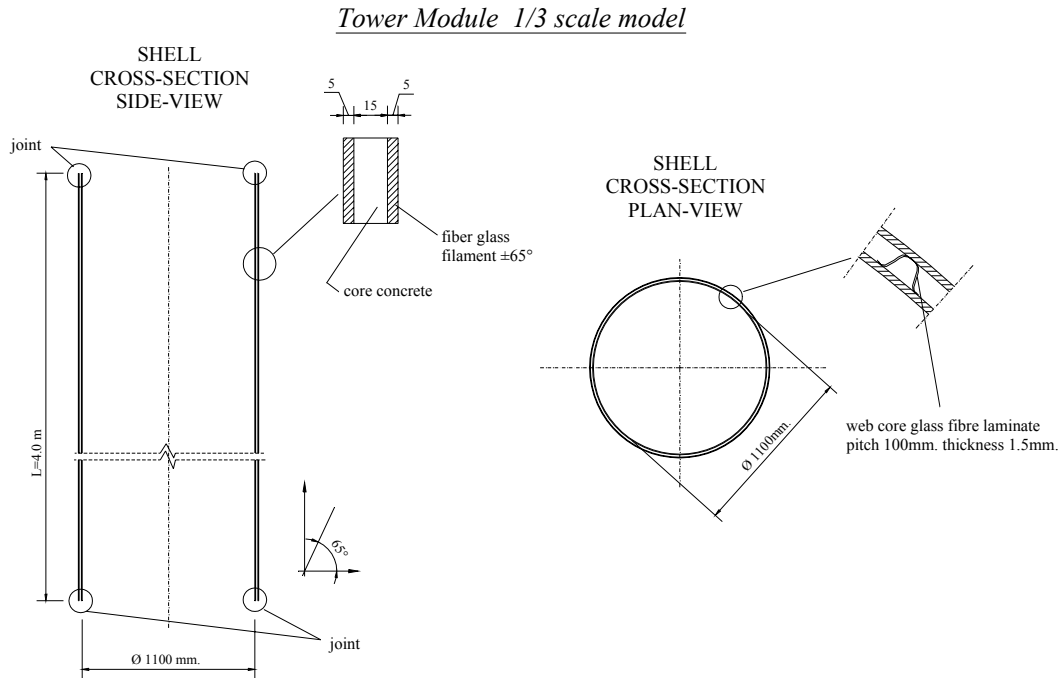
Tower Module 1/3 scale model

Figure 4: The cylindrical shell design for hybrid FRP-concrete section.

2.2   Loading and structural calculations

For all the design proposals described above, preliminary structural calculations were conducted in order to highlight any major design flaws. Both Finite Element (FE.) and simpler calculation methods were tried out. FE calculations were carried out by the various WP2 partners, as shown in Figure 5, the results were compared to those obtained from simplified methods in order to study the feasibility of providing simple design tools for general implementation in the wind turbine design package.

In the case of the tower manufactured from shells using concrete core, the structure was analysed in the linear (un-cracked concrete) and non-linear regimes. In the case of fully monolithic sections only linear models were implemented. In both cases the JRC identified the range of material thickness and material types that would meet the required criteria of:

- Natural frequency of complete tower.
- Strength and limit states in the event of extreme gust conditions.

In the case of the concrete core tower, simple models to predict the natural frequency of the tower, based on the variation of the secant stiffness and the condensed masses of the tower, nacelle and rotor were proposed. It will be described in Section 10 how the natural frequency of the system varies according to the effective thrust of the wind, but that in the usual working regime i.e. when the wind speeds are less than those for shutdown, the 1st mode of the tower would not enter into resonance with the driving frequency of 0.31Hz.
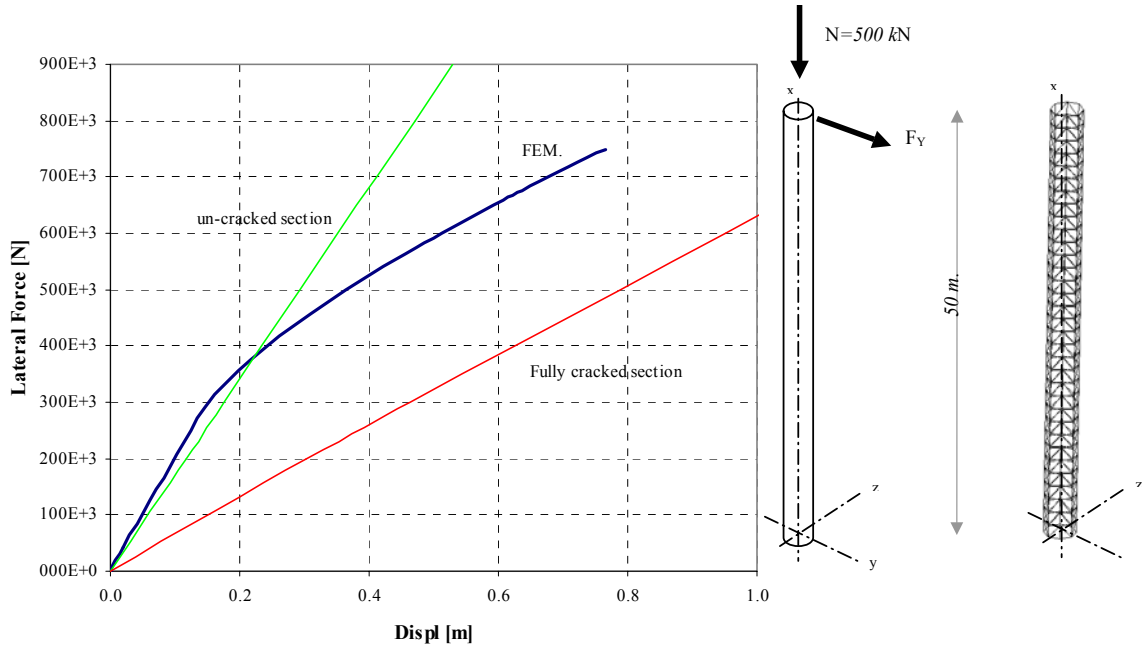
Figure 5: Non-linear orthotropic FE. calculation of the response of the full-scale prototype tower in the event of extreme loads. The stiffness degradation as a function of the imposed load is compared to the limit cases of un-cracked section (top green) and fully cracked (bottom red). Apart from tensile cracks all materials remain in the linear regime.

2.3 Design Trade off Studies

The trade off studies developed the process whereby, with due consideration of budget, environmental factors, structural performance and logistics of tower deployment, the feasibility of the materials and methods used for manufacture are selected. The selection of the most appropriate manufacturing system and the choice of materials was a difficult task, this is simply due to the fact that the best reinforcing fibre for the tower is carbon and the best resin system is epoxy, however, due to the design should be made at a competitive cost. The use of mixed carbon/glass reinforcing systems was considered in the first designs but was still too expensive to be used in the overall design, however, it will be considered in for use in critical areas such as openings and section transitions where stress concentrations are generated. The same arguments can be applied for aramid fibres; in fact the effective flexural cost (i.e. the fibre modulus divided by the typical manufactured cost) is typically not as competitive compared with low modulus carbon fibre. This constraint results in a material selection restriction to glass fibre systems that are not ideal in terms of structural and environmental properties, but, essentially, the only viable selection of materials is glass fibre and resins from the polyester family. In part this was addressed in 2.1 given that, as was stated, the final design was critically conditioned by the manufacturing and material costs. Thus although conical sections would be more optimal in terms of structural efficiency and ease of transport such sections are, at present, too uneconomic to be manufactured using wet lay-up, or pre-preg techniques. These sections could have been filament wound but the tooling costs would be prohibitive for a single prototype. The filament winding method had originally been considered but was discarded on the grounds that it could not produce a sufficiently low winding angle to meet the stiffness requirements; however, fibre wrapping has been suggested as an alternative means of obtaining a satisfactory fibre orientation.

2.4   Manufacturing procedures

For the reasons given in 2.3 above, the manufacturing suggestions based on moulding methods to generate the sandwich shell which were originally proposed, were abandoned in favour of the more economical, filament winding production method. Filament winding can produce large composites tubes of high quality, however, such quality assurance is aimed at the aerospace market. Good quality can also be achieved for specialist pressure equipment but this is usually carried out on small winding machines. For the case of the tower modules (considering size and low cost), the filament winding companies that could produce large cylinders in high volume are those whose market is in the low cost manufacture of large low-pressure vessels or piping. It is typical for these companies to work with low cost resins and glass fibres, however the quality assurance is not as high as for other filament wound products, and, crucially their machinery is geared to work with low winding (i.e. hoop direction) angles whereas for the tower the preferential direction, especially given the low modulus of GRP, is in the longitudinal direction. Quite often the nomenclature and related terms that are used to define the winding angle by staff from the filament winding companies is usually in the orthogonal direction to that used in by the design team when selecting the laminate lay-up, thus special care was given to establishing production specifications. Even so, as will be shown below the QA assurance of production runs is not always complied by the manufacturer.

In order to gain some insight into the capabilities of the proposed manufacturing methods, production and tooling, visits were arranged to filament winding companies in order to prepare bids and orders for the manufacture of both the 1/3-scale specimens and the full-scale prototype. This task is closely linked to the activities in Task 4, and involved close collaboration between the partners involved in both tasks. Eventually it was also decided to order the manufacture of a half-length lower section of the 1/3 scale sandwich shell which was to be filled with high strength concrete to be tested in the laboratory.

2.5   Development Testing

Having established an acceptable preliminary design the project entered a second phase dealing with practical testing and development. This included the preparation of both experimental and theoretical analysis of the tower. As will be shown in the proceeding chapters, experimental procedures and tests were devised in order to confirm the initial preliminary calculations, but, more importantly to reveal weaknesses in the design or manufacturing methods that could be ironed out in the full-scale prototype design. As was mentioned in 2.3 above, two 1/3-scale specimens were manufactured with a view to compare the two main viable, module types for the tower, however, whereas at the outset of the project it was not clear in what manner the tower subassemblies would be tested, it was decided that the tower modules should be subjected to a loading condition that could best simulate the real working conditions of the tower. Moreover, it was thought appropriate that the modules should be loaded up to failure. This ruled out the possibility of carrying out simple axial compression tests in order to induce shell buckling as the loads required to do so would be too high for available equipment. Thus it was proposed to design a test rig comprising three pistons that could induce a complex combination of shear forces and bending moments with which to recreate, on a substructured tower element, the performance of the full-length 1/3-scale tower (Figure 6).
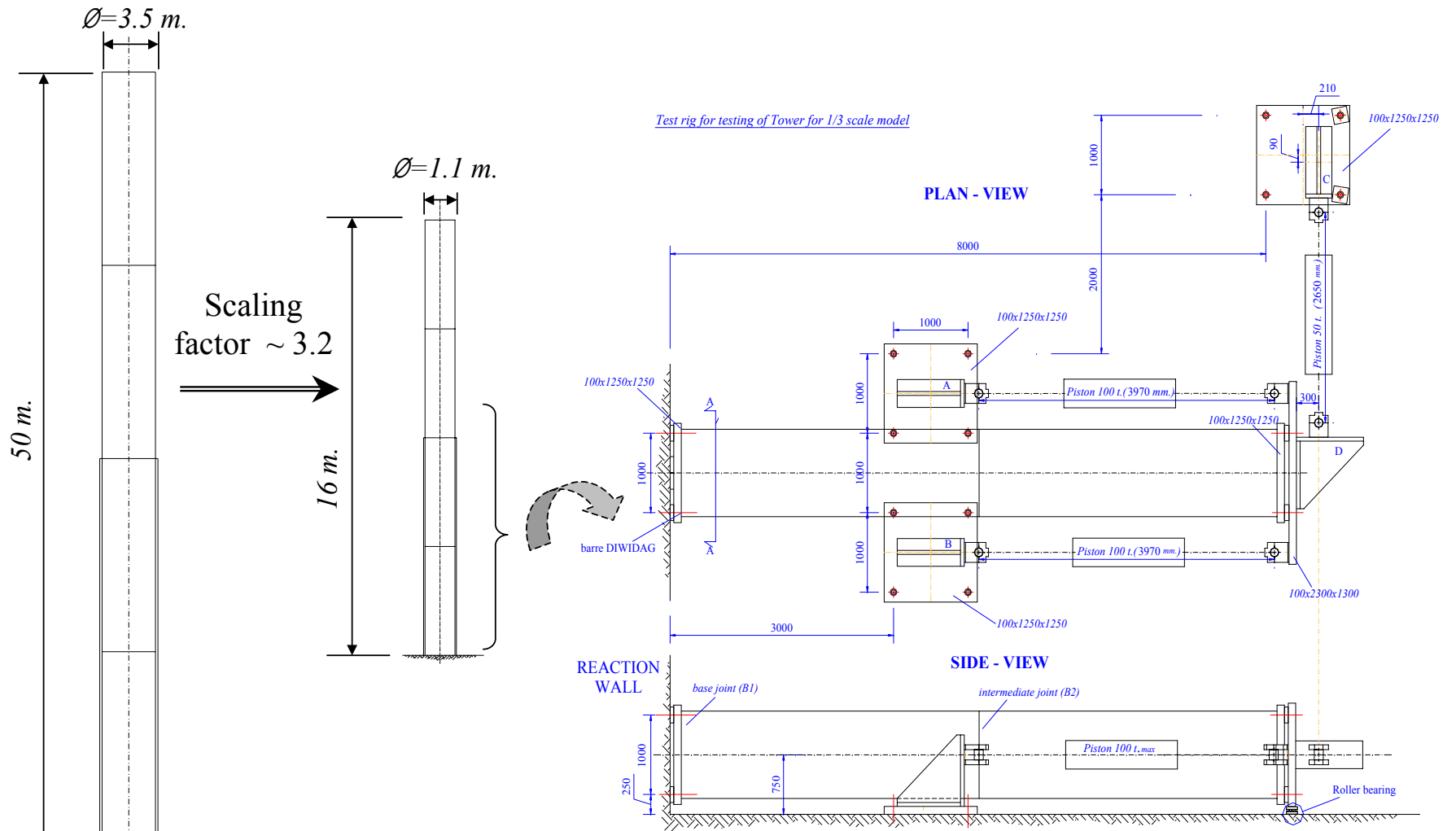
Ø=3.5 m.

Ø=1.1 m.

Scaling factor ~ 3.2

50 m.

16 m.

Test rig for testing of Tower for 1/3 scale model

PLAN - VIEW

1000

8000

2000

210

90

100x1250x1250

C

100x1250x1250

1000

100x1250x1250

A

Piston 100 t.(3970 mm.)

Piston 50 t. (2650 mm.)

300

100x1250x1250

100x1250x1250

1000

1000

D

A

A

barre DIWIDAG

1000

B

Piston 100 t.(3970 mm.)

1000

100x1250x1250

3000

100x2300x1300

REACTION WALL

SIDE - VIEW

base joint (B1)

intermediate joint (B2)

Piston 100 t.max

1000

250

750

Roller bearing

Figure 6 Experiment: 1/3 scale composite wind Tower.

3   Manufacturing

3.1   Manufacturing Design:

Although there are many methods available in composite manufacture, at present the only pultrusion or filament winding methods have enough production capacity to conceivably satisfy the potential volume demand that would result from the installation of a sizeable number of wind-turbine towers. Both methods have the advantage in that the production costs can be kept relatively low (costs of the order of 5-10 €/kg is typical) and that, in principle; the quality of the manufactured product can be of medium to high standard.

The use of pultruded elements to generate a truss-like structure as the main load-bearing FRP structural member was abandoned in favour of a manufactured shell of revolution; hence the pultrusion technique was not considered as the primary manufacturing method. However, as we shall discuss below, it may be considered appropriate for the manufacture of the mesh elements that make up the shear core separators between the concentric skins of a shell structure.

The filament winding method was therefore chosen to manufacture both the monolithic and hybrid tower modules and the first trials would be carried out on the 1/3 scale subassembly specimens to be tested at the ELSA laboratory. As was stated in the preceding section dealing with structural design, the ideal shape for the tower would be a standard truncated conical shell just as is normally done for steel towers. However, in order to generate such a shape with the filament winding technique a special conical mandrel tool would have to be manufactured solely for the purposes of manufacturing a single prototype and the two scaled laboratory specimens. As this would imply a severe cost for the project it was decided to generate the full length of the tower from a constant cylindrical section and adapt only the top-most sections to align with the dimensions of the turbine bearing mechanisms.
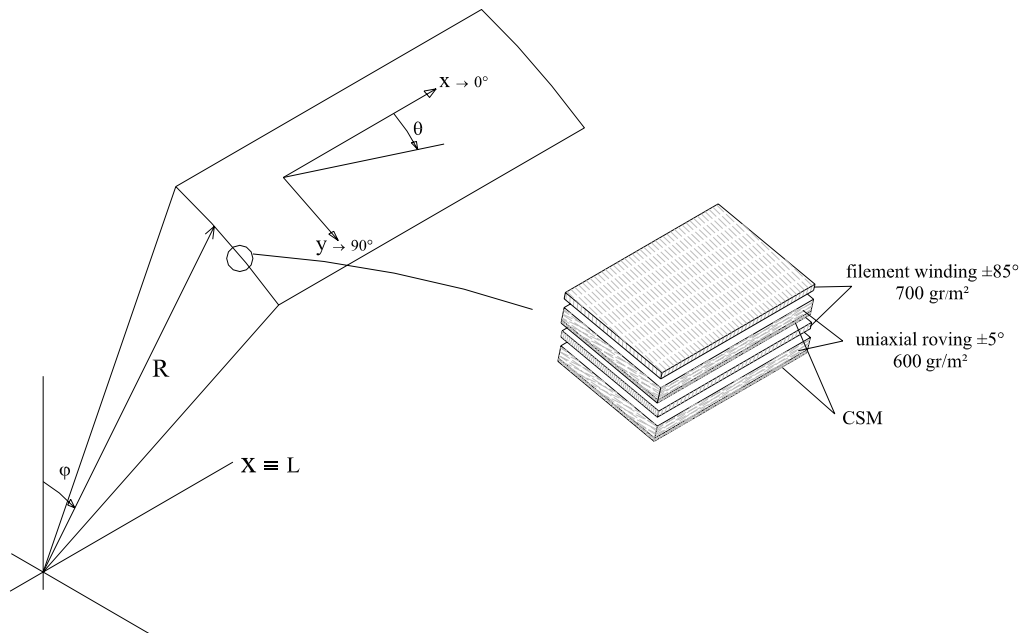

Figure 7 Schematic representation of winding surface and lay-up angles.

10

Another aspect to be considered for the manufacture was the correct positioning of the glass-fibre strands in order to generate the desired laminate properties that would result in a sufficiently stiff structure to meet the serviceability criterion (that the 1st natural mode of the tower when complete loaded with nacelle and rotor be substantially higher than 0.31 Hz). Essentially this required the generation of a cylindrical shell where the orientation of the fibres could be selected at a low angle, θ, with respect to the main tower axis. However, in the filament winding processing, such low angles are, in fact, not usually implemented unless in very short cylinders compared to the dimension of the winding machine. In view of the technical limitations in generating a shell with the very low winding angle –as requested by the design team to the filament winding companies– the lay up was adapted to include a stitched unidirectional fibre (UD) cloth as shown in Figure 7.

The laminate is made up of layers of UD cloth, stitch-bonded, onto a light chopped strand mat (CSM) backing that allows the fibre to be draped over the tool hub during the winding process. The material was to wound at an angle of 85° to the tower axis, L; hence, the UD fibre was to be effectively be wound on at ±5° to the axis of the tower in order to provide the required stiffness in the axial direction. Between each layer of fabric a layer of ±85° filament (i.e. nearly circumferential) is wound over the fabric in order to achieve the necessary compaction onto the hub. Assuming a fibre volume fraction of 60% and glass fibre reinforcement, and based on the material weight specifications provided by the manufacturer for the production stock they intended to use, the Q matrix for the system was evaluated to be:

$$Q_{[UD\pm5^{\circ},FW\pm85^{\circ}]_s} = \begin{bmatrix} 24.6 & 2.3 & 0 \\ 2.3 & 27.5 & 0 \\ 0 & 0 & 8.2 \end{bmatrix} GPa.$$

from where it is possible to evaluate the elastic constants as :

$$E_x = 24.5 GPa. , E_y = 27 GPa. , \nu_{xy} = 0.08 , \nu_{yx} = 0.09 , G_{xy} = 4.1 GPa.$$

These elastic properties would ensure a sufficiently high modulus to enable the monolithic shell tower to meet both the stiffness and strength requirements. The sandwich shell skins would, nominally, have the same elastic properties as the monolithic shell, however, the combined stiffness of the sandwich shell was expected be higher than that of the monolithic as a result of the concrete core.

The selection of the resin system was also driven by cost. Given the budget constraints an epoxy-based system was automatically discarded in favour of an isophtalic polyester resin, that provides acceptable mechanical properties combined with a low water absorption capacity.

3.1.1 Monolithic Specimen:

The manufacture of the monolithic 1/3 scale 8-metre tower section was commissioned by NECSO and was performed without any major problems and was delivered to the ELSA laboratory (see Figure 8) in time for preliminary experimental testing by the first quarter of 2002. From the production drawings, shown in Figure 10 and the cross-section through the tube is shown in the Figure 9 the details of intermediate join and the end flanges can be seen in more detail. The effective shell thickness was 16mm rather than the 15mm requested, this is simply due to the fact that the ply-lamina unit thickness may not necessarily fit an integer number of times into the full laminate thickness, clearly the percentage error becomes smaller for the full-scale laminate for which case the effective thickness is much larger than that of the unit lamina. In order to connect the ends to the steel ring plates, the shell thickness increases gradually over a length of 400 mm from 16mm to 25 mm at both ends.

Figure 8 The tower in the laboratory.
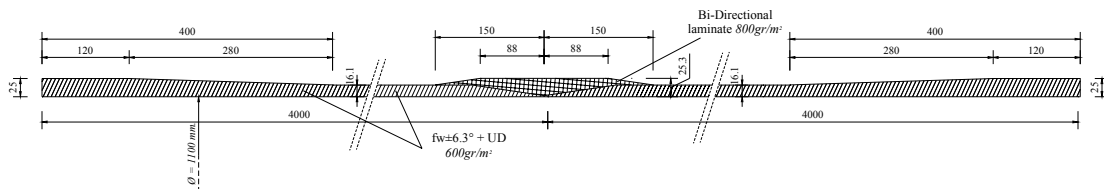
Figure 9 Cross-section of the monolithic tower and winding lay-up.
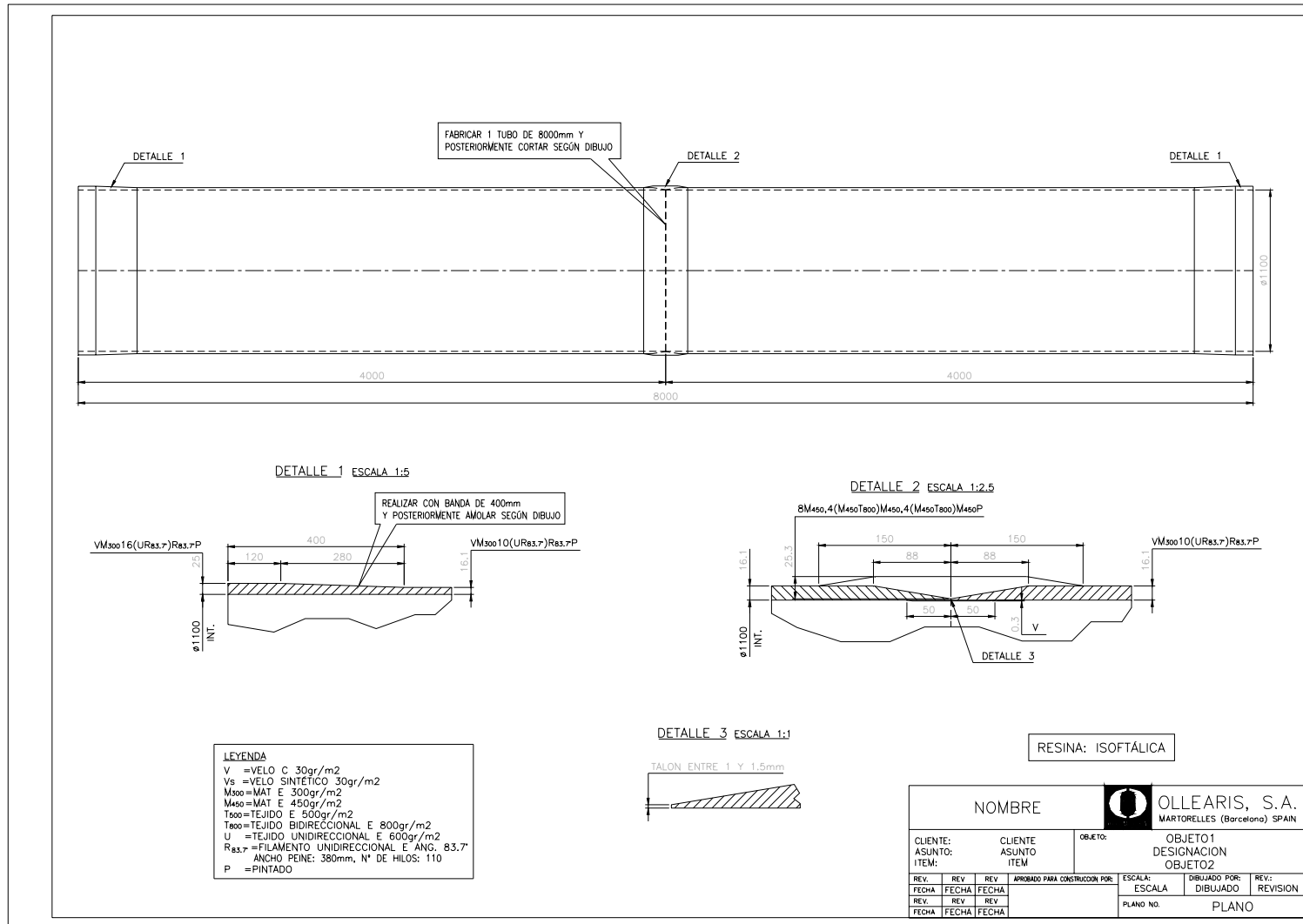
Figure 10 The executive drawings and details for the monolithic tower.

3.1.2 Hybrid Specimen

The second tower design, i.e. the hybrid section module, commissioned by ELSA, suffered delays, in part due to the fact that the manufacturer could not obtain a supply of the glass-fibre cloth for the winding angle requested for the design. In view of these difficulties the glass-fibre winding angle and lay-up were reviewed to accommodate the manufacturer whilst still, nominally, providing adequate material properties in the glass fibre skins. The manufacture of the 8-metre sandwich tower went ahead and was monitored by two JRC staff. A number of technical problems occurred during the lay-up of the outer sandwich skin so that the separation between the two skins was uneven and could jeopardize the subsequent concrete grouting process; consequently, the specimen was not accepted. Given the technical difficulties, a new order was placed with the same filament winding company that had produced the monolithic section.

Some stages of the manufacture of the tower are shown in Figure 11: in Figure 11a some details of the polycarbonate spacer can be seen (note that to hold it in place on the mandrel an adhesive film has been used); Figure 11b shows the glass fibre roving and mat used, finally in Figure 11c some stages of the manufacture during the filament winding (on left) and the application of the UD cloth and filament (on right). The production drawings and details for the hybrid tower are shown in Figure 12. The hybrid part of the tower was designed nominally to consist of 15 mm of concrete sandwiched between two 5 mm skins generating an overall thickness of 25 mm. i.e. the same nominal thickness as the connecting elements at either end. Essentially the tube was to be prismatic along the length. However, due to manufacturing constraints it was not possible to find a core spacer that would generate a 15 mm gap between the skins, thus considering the thickness of the shear core separator the actual thickness of the hybrid part of the tube is quoted in the production drawings as 28 mm, although from the structural point of view the extra 3mm thickness of the polycarbonate core separator is not considered to contribute to the structural behaviour.

Also, in addition to the 8-metre sandwich section, it was decided to order a ring section of the sandwich cylindrical shell using identical lay-up and materials in order to provide coupon tests for the forthcoming environmental campaign. However, upon inspection of the empty shell of the hybrid tower module a number of defects became apparent.

The FRP corrugated sheet that had been requested as a spacer –i.e. core- between the skins was not available in the dimensions required for the 1/3 scale specimen. Instead a fine-surface polycarbonate sheet was used that conferred practically no surface roughness and hence would not be expected to provide suitable shear transfer between it and the concrete. Moreover, the sheet was very poorly bonded to the skins. This meant that the sheet even if there were some shear locking between the sheets and the concrete it would not have been capable of transmitting the shear transfer from the concrete to the skins. The only mechanism left for shear transfer is where the concrete is in direct contact with the rough skin surfaces, which, given the geometry of the polymer sheet, would only be possible on alternate pitch faces of the corrugated sheet see Figure 13.

The other main function of the corrugated sheet is to increase the radial stiffness and resistance to localised radial buckling of the two concentric rings, thus enabling them to function as a pressure vessel for the concrete until it sets. Given the very poor bond-strength between the sheet and the skins it became clear that it would be difficult to gauge the pressure head of wet concrete that could be poured into the cavity without the inner skin buckling inwards (this phenomenon had already been observed on the tests carried out on a dummy shell: see WP2 progress report Nov.2001-Jan 2002). The buckling pressure which tends to separate the inner skin from the sandwich spacer depends, not so much on the effective radial stiffness of

the shell (calculations indicated that elastic stiffness of the shell would be more than sufficient to contain the pressure head required) but rather on the sandwich peel strength; i.e., the delamination is not stiffness dominated but, rather, strength dependent. It was therefore suggested that for the full scale prototype, a trial radial section should be manufactured and then tested for peel strength –climbing drum test or otherwise– in order to calculate the maximum head of wet concrete that can be poured in one go.

a)

b)

c)

d)

e)

f)
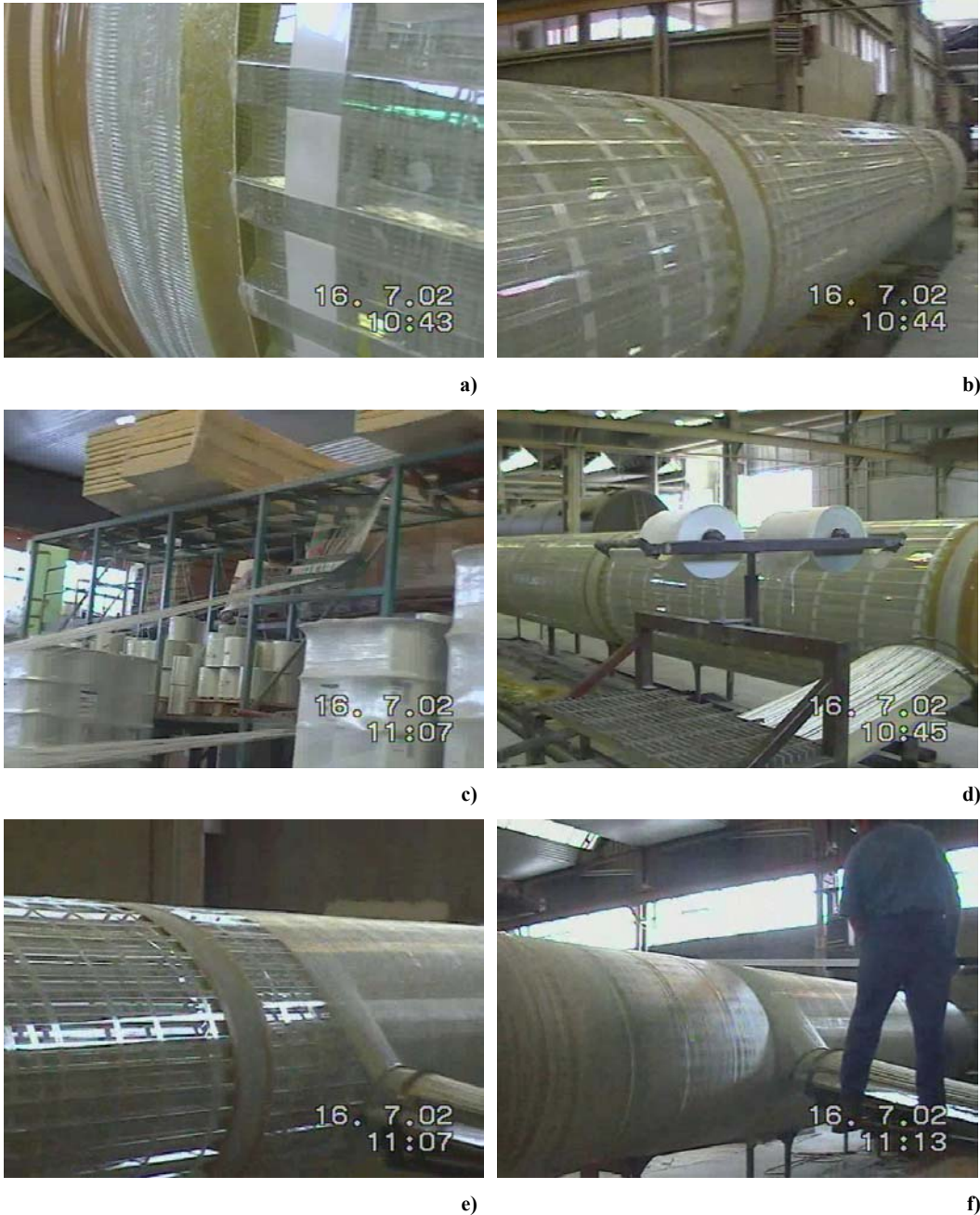
Figure 11 Manufacture hybrid tower.
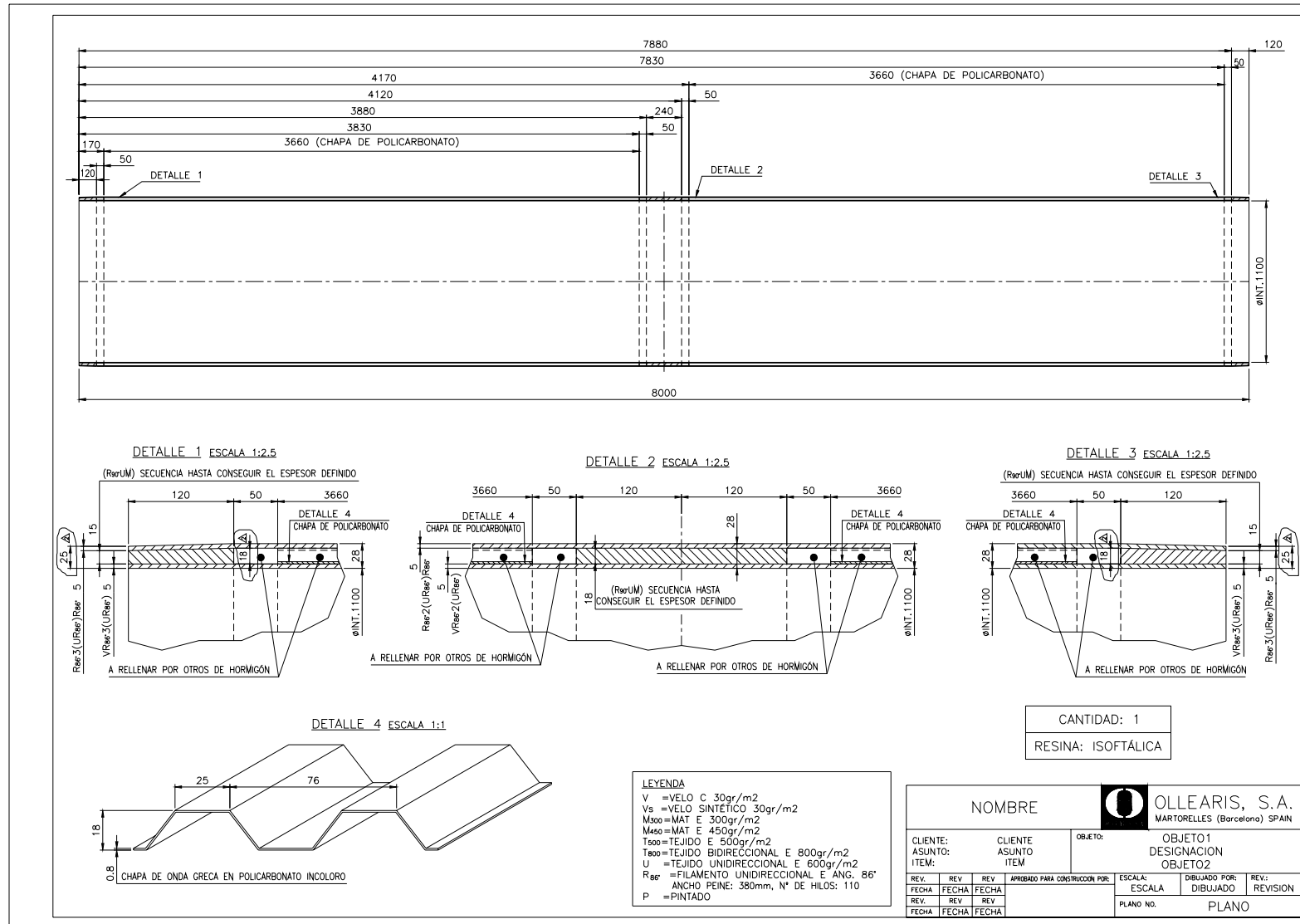
Figure 12 The executive drawings and details for the hybrid tower.

3.1.3   Environmental coupons:

In addition to the 1/3 scale tower specimens the manufacturer was commissioned to produce material and subassembly coupons that consisted of flat plates of the FRP skins as well as a reduced ring section of the 1/3 scale sandwich specimen. To complement these, concrete samples were also taken during the pouring of the sandwich tower.

The manufactured concrete-filled ring for environmental testing of the hybrid tower section is shown in Figure 13. Dimensions are 0.5 m height, 1.1m diameter, 16 mm spacer-core width and 5mm skins. The cross-section dimensions were identical to the complete scaled tower module. It can be seen that only the open side of the corrugated sheet (i.e. every other pitch) offers contact area between the concrete and the skins. Filling the ring section core was not problematic as the concrete was able to flow quite easily into the cavities making it accessible for direct pouring. The specimen was then shipped to FORTH where it was subsequently sectioned and prepared for ageing

Figure 13 Concrete-filled ring coupon section and detail of empty core. The gap size is 16 mm.

In the case of the 8-meter specimen, the constraints imposed by the reduced dimensions were more problematic. The 8-meter tower section consists of two 4-metre modules; each composed of multiple longitudinal cavities that are interconnected by the hoop ring cavities at either end as shown in section in Figure 14.
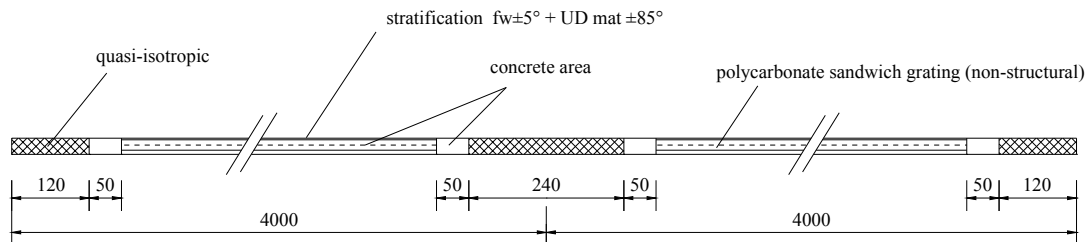
Figure 14 Cross-section of the sandwich shell showing longitudinal and hoop cavities for concrete grouting.

It was decided to fill the core with the tube laying on its side, thus keeping the pressure head of poured concrete to a minimum; however, this meant that the concrete was pumped into the cavity at a very low pressure as shown in Figure 15. It was noted that some concrete-void areas

remained along the topmost part of the specimen where the pressure was lowest. In the second tube section, a vacuum pump was placed at the head of one of the hoop cavity openings, thus drawing in the concrete from a container placed at the entry of the hoop cavity at the other end of the tower section. Although this helped to move the concrete along the length of the tube though the core, it left some empty patches as a result of irregularities in the flow caused by the vacuum pump: essentially concrete chokes at the inlet cavities to some areas that had not yet been completely filled.

Figure 15 Grouting of concrete mortar: detail of flow along channels.

The voids (Figure 16 before and after) were easily identified by visual inspection through the translucent formwork. Having identified these voids, the major ones were later pressure-grouted with a high strength mortar. Based on the cavity volume calculations and the measured weight of concrete poured, it is expected that the volume of voids is in the order of 1 to 2%. To reduce the effects of void defects on the measured structural properties, it was decided to mount the tower in such a manner that both the axis of bending and its base offered the surfaces with least voids.

Figure 16 Voids in hybrid-sandwich section (left) and after filling with fine high-strength mortar grout.

Clearly, pouring concrete into such a narrow cavity will be avoided in the full-scale tower so it is expected that filling the 50 mm spacing will not be as problematic, especially if the grouting is done vertically. After setting and once the concrete had matured, the ½ length tower section was mechanically connected to the loading attachment plates as shown in Figure 17.

Figure 17 Hybrid tower section with mounted end plates.

3.1.4   Joint areas

The manufacture of the joint areas was undertaken directly at the filament winding shop. The details of both monolithic joint areas are shown in Figure 9. The joint areas that were to be bolted were placed at the ends of the 8-metre tower section, essentially corresponding to the base and mid-height of the tower. The ends were to be slotted into the steel ring attachment plates and then bolted as shown in Section A-A (Figure 20). In order to relieve the stress concentrations around the bolt holes the thickness of the laminate was increased from 15 mm up to 25 mm using a quasi-isotropic lay-up which is specified in the production drawings. For the intermediate joint between the 1st and second modules (i.e. at the 4 metre length), a scarf joint was manufactured by splicing layers of filament winding and cross-ply cloth over the a previously lapped tube ends as shown in the detail of the production drawings in Figure 10.

The joint areas for the hybrid tower were manufactured as shown in Figure 12. At either end of the specimen: i.e. at the base and mid-height of the tower the two shell skins overlap a monolithic section. The thickness of the tube in this area is nominally 25-26 mm whereas the thickness of the hybrid section of the tube is 28 mm. Thus there is a gradual taper from the hybrid section to the joint area. This change of geometry results from the fact that the tube must fit at either end within the ring annulus of the top and bottom, attachment plates.

4   Testing of joints and attachment systems.

4.1   Background

The manufacturing aspects for the main body of the tower have been discussed in the preceding chapters. The original generic tower design concept was based on modular components that were to be spliced on site using either wet lay-up, or pre-preg materials. Having opted for a filament winding manufacturing process, it was decided that, for certain intermediate connections, a wet lay-up bond be implemented. The method is essentially an adaptation of filament winding that uses layers of cross-ply cloth in order to generate a half scarf joint; the advantage of this technique is that it is possible to perform the joining of the tower modules quickly, on-site, independently of the governing environmental conditions. However it is, in essence, a chemical bonding technique; thus should it be required to dismantle the tower, either for inspection or demolition, it would only be possible to do so by cutting the joined modules. It was thought appropriate however, to study the feasibility of other mechanical joining systems based on standard mechanical bolted fastenings. Another reason for studying the feasibility of bolted joints is that although they are not as mechanically efficient as the – usually stiffer- bonded joints, they are not as sensitive to quality control and environmental factors during their execution, especially if done outside laboratory conditions. Mechanical joining techniques were therefore studied for the base and mid-height connections of the tower.

Before proceeding to describe the tower joints that were designed and tested, it should be noted that other anchoring solutions were considered for the base of the tower. Given the manufacturing characteristics of the hybrid tower module, the most immediate solution for the anchorage at the base would be to extend the footing of the tower into the main structural foundation and embed it in concrete. This method is essentially a mechanical fastening, as the tower would be mechanically anchored to the foundation by shear key locks around the tower perimeter embedded in the concrete. This method, apart from transmitting the moments from the tower to the foundation in an efficient manner, is the most amenable to onsite construction as it is a natural follow up to the usual foundation works. However, as is the case for bonded joints, the tower base would have to be sectioned in the event of a controlled dismantling.

4.2   Mechanical Joints

For the tower base and mid-height joint the geometries of the various techniques proposed are shown in Figure 18 for the 1/3 scale case (here represented joining hybrid module sections). The scope was ascertaining the strength of the possible joining types irrespective of the module they were supposed to connect. Type A and B1 joints were considered for use at both the base and mid-height; whereas type B2 was considered only for the mid-height joint. The tests were carried out on a specially designed testing rig (Figure 19) in order to simulate the loading conditions imposed on a representative element of the tower. . The details of the calculations of the dimensions of the steel connector ring are given in (Appendix B). For the case of type A, the joint consists of an FRP component loaded in tension under differing boundary conditions in order to reproduce the constraints and bolt preloads that may be encountered in service. In the case of type A the test specimen consisted of the FRP component plus a representative element of the steel base attachment ring (Figure 20).These designs were not considered as final but rather models with which to conduct research on the particular behaviour of each type of joint. These findings would then be used as a base for potential designs: for this purpose the experimental data obtained were used to calibrate Finite Element models.

Both A and B1 are bolted joints, however, type A is simpler to mount and the bolts can be pre-stressed thus reducing the potential for slack. Conversely type B1 has a higher number of

parts and is inherently more complex to mount. However, based on preliminary quotes from potential manufacturers and filament winders, the production costs of the preparation work for type A joint at the full-scale 3.5-diameter would be considerably more expensive than type B1 even though the steel parts-cost for B1 would be higher.

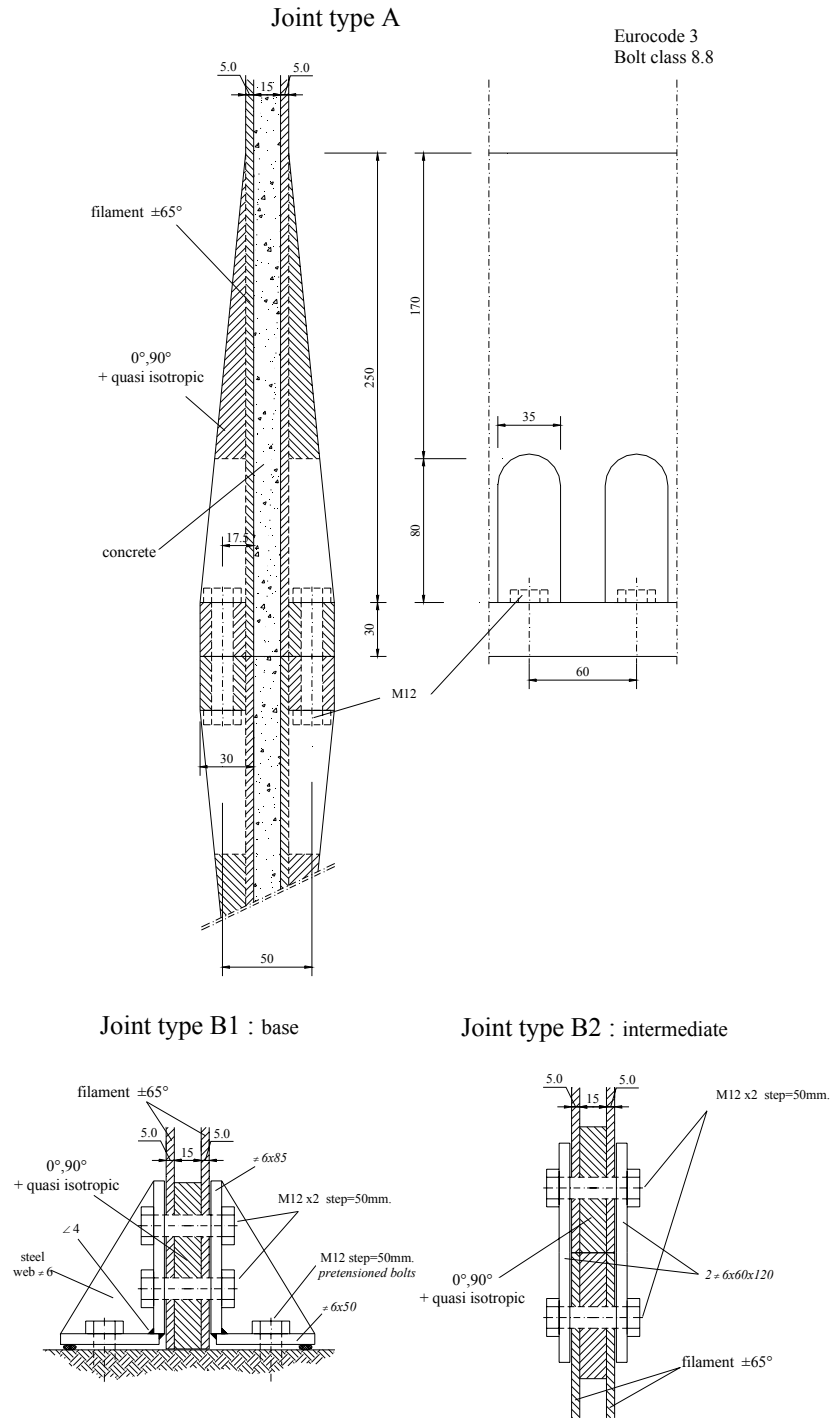*Tower Joints for 1/3 scale model [unit mm.]*

Joint type A

Joint type B1 : base   Joint type B2 : intermediate

Figure 18 Mechanical joints considered for tower assembly
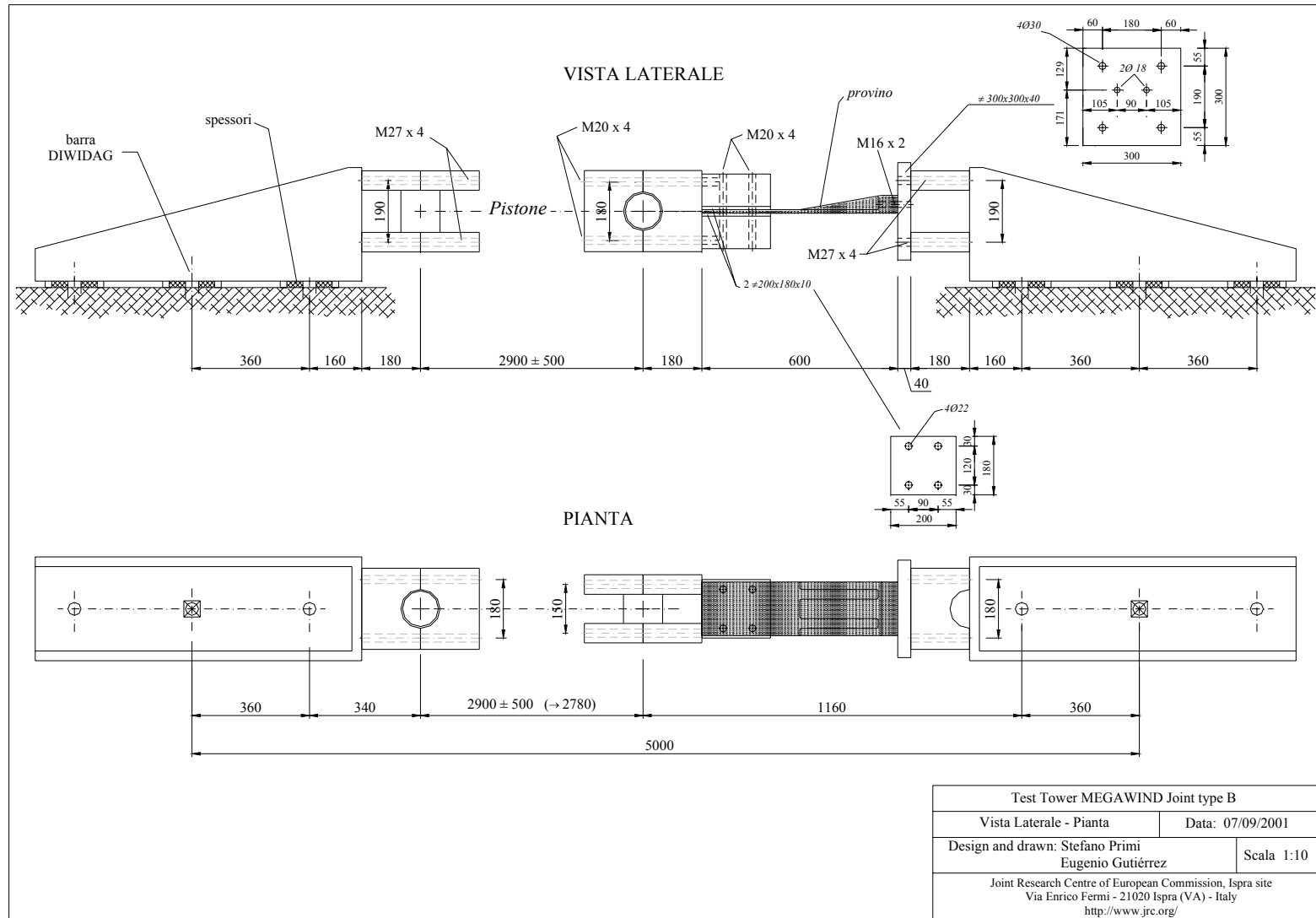
Figure 19 Test set-up for tensile loading of mechanical joints.
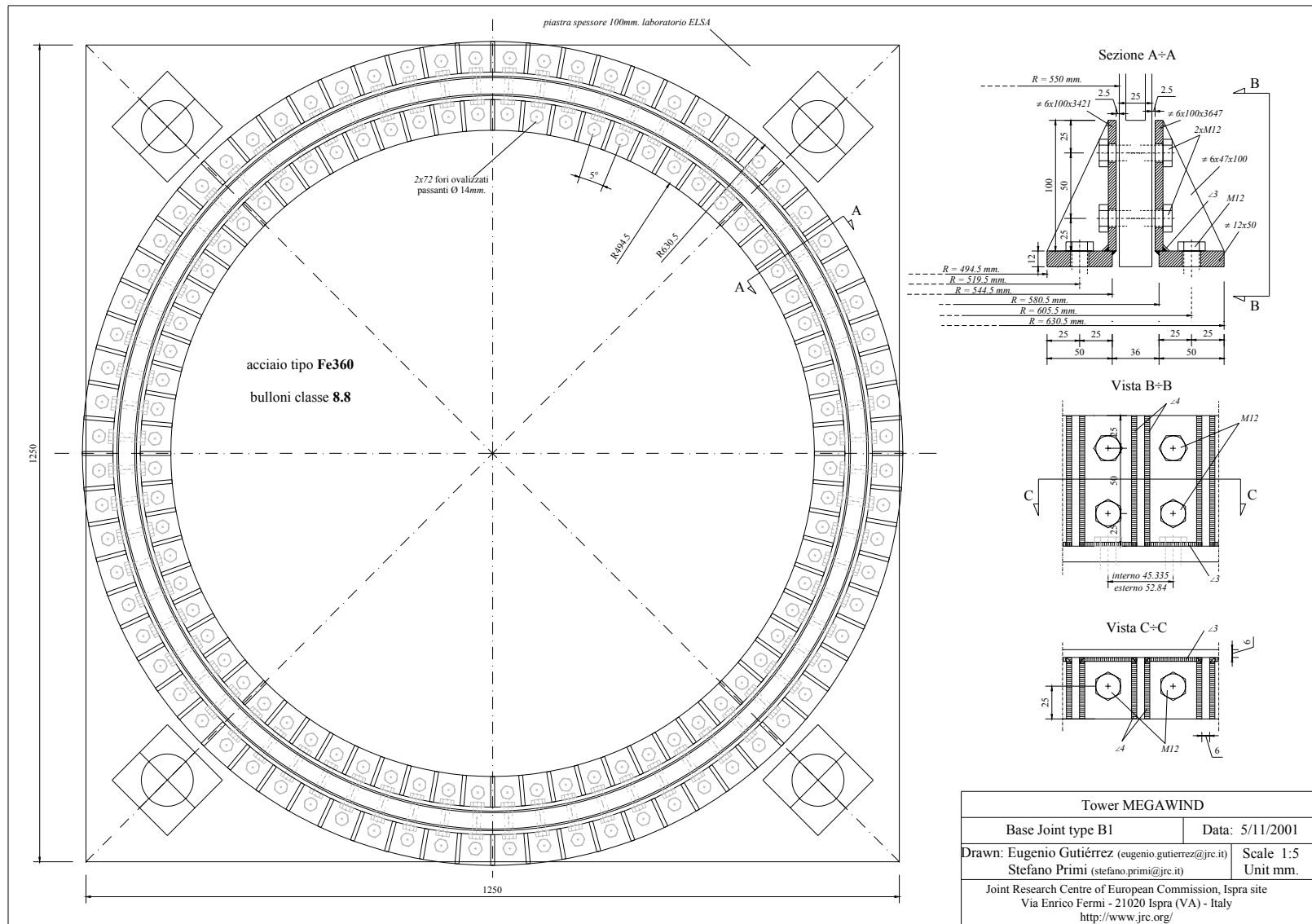
Figure 20 Base connecting joint.
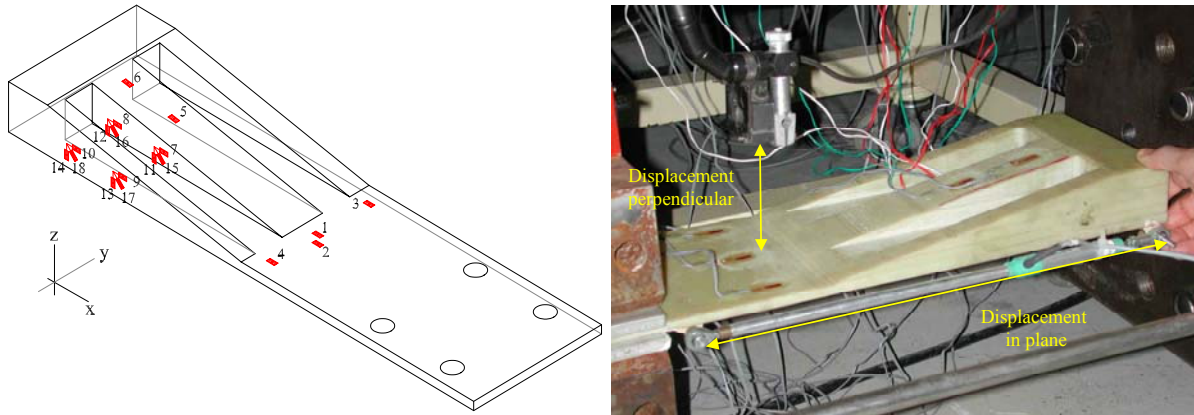
Figure 21 Detail of tensile test and instrumentation for joint type A.

4.2.1   Testing:

Type A specimens were manufactured from stacks of bonded 9 mm quasi-isotropic pre-preg GRP plates. The bonding system used was a rigid epoxy adhesive of low fracture toughness. The specimens were then machined in order to produce the final shape as shown in Figure 21: the slotted grooves allow the positioning of the bolts onto the reaction connecting plate. The instrumentation on the specimen consisted of resistance strain gauges mounted as shown in Figure 21 and lateral and vertical displacement transducers. The loading set-up was designed to study the effect of imposing eccentric loads on the joint: essentially the lines of action of the piston and the bolts are on different planes. Loading thus tends to generate high out-of plane shear stresses that produce de-bonding between layers: this, in turn, resulted in clean monolithic fractures between the stacks, i.e., no fibre or intra-laminar failure. The failure modes of two tests are shown in Figure 22.
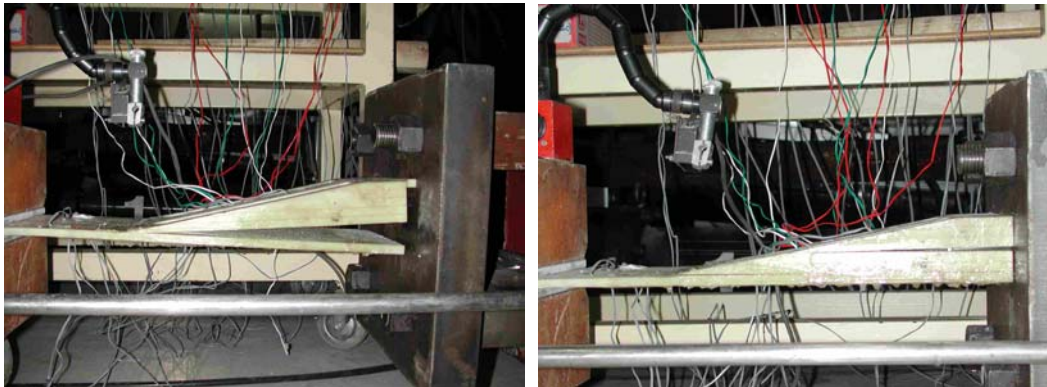
Figure 22: Failure of type A joint. Test T02: free to rotate at base (left). Test T07: constrained rotation (right).

Four tensile tests using different boundary conditions as shown in Table 1. Each condition generated differing levels of constraint or pre-load: the preload strain at three relevant strain gauge positions is given in the table. It can be seen that the constraint plays a significant role in the ultimate load capacity of the joint. When the rotation of the base of the joint is impeded, as in test T07 (i.e. blocking it tightly against the anchorage plate), the peak load reaches 8.34 tons as opposed to only 3.42 tons when left free to rotate (test T02). Clearly the boundary conditions do not represent the joint with the concrete core sandwich system given that the 3D geometric effects (as well as the constraining effects of the concrete core) are not included in these experiments; however, these tests provide qualitative information concerning the effect of the

constraint, or pre-load, in reducing the out-of-plane stresses through the thickness of the joint. The tests confirm the well-known sensitivity of FRPs to out of plane stresses.

The FE calculations predicted this type of behaviour quite well: a 3D orthotropic analysis simulating the type of loading conducted during the tests is shown in Figure 23, whereas in Figure 24 the FE plot shows the geometric rotation that generates the out-of-plane hear stresses that affect the transition zone between the flat and tapered parts of the joint.

Based on these findings, it is not recommended to use this kind of joint for any part of the tower due to its sensitivity to boundary conditions that are too difficult to monitor in real service conditions. An alternative to this type of joint is the so-called T-bolt slotted connecting joint to be used to connect the blade root to the hub rotor. In this case there are no out-of-plane stresses generated as the bolt runs through the middle thickness of the laminate in line with the load. However for the tower the costs of manufacturing for the full-scale prototype would be even higher than in the type A joint, principally due to the increased parts-cost and the precise radial and longitudinal boring that would be required.
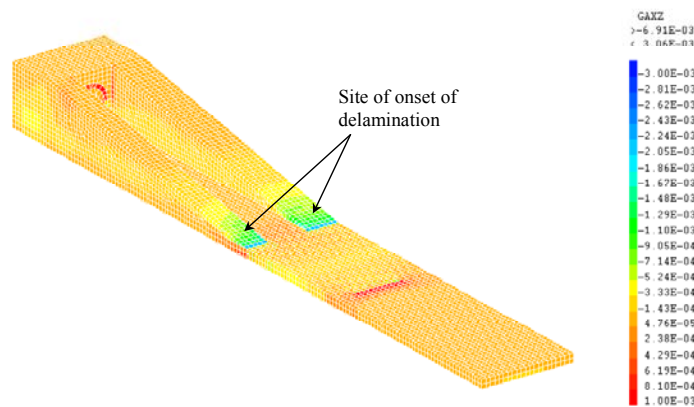
Figure 23 Delamination shear stresses caused by eccentric loading.
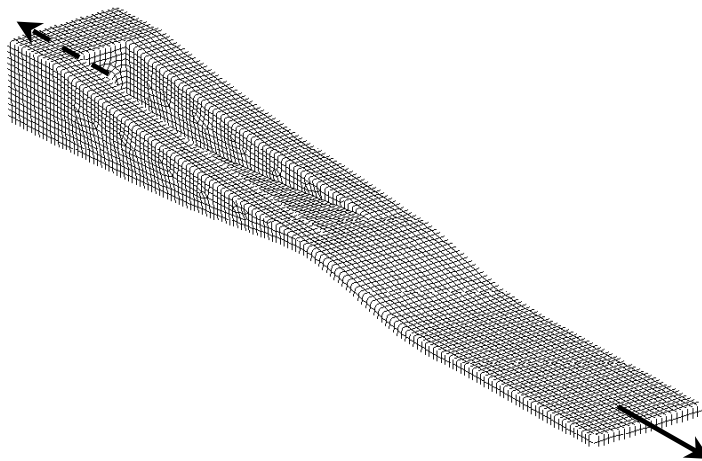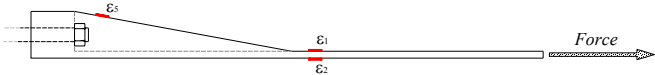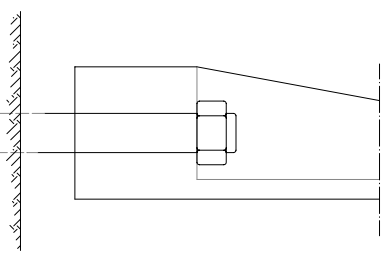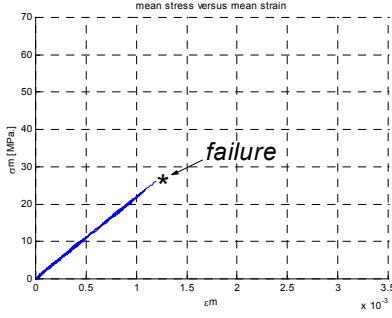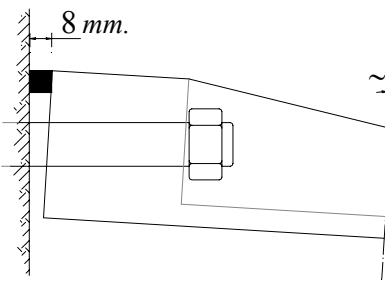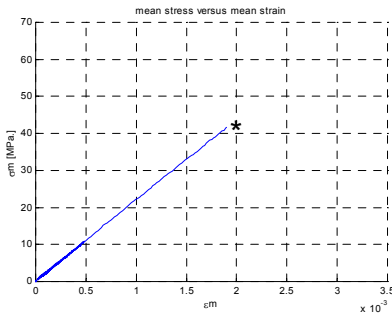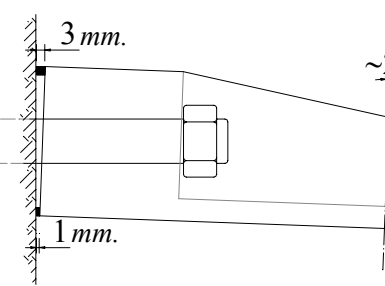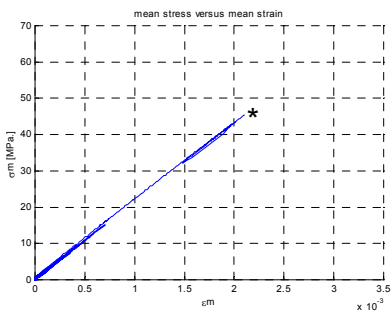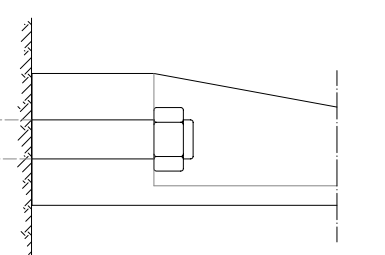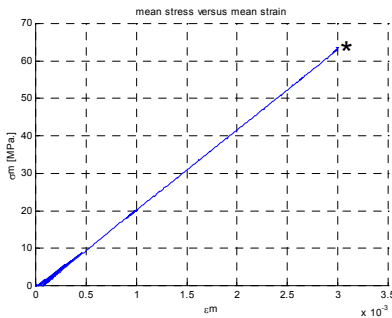
Figure 24 Out of plane rotation caused by eccentric loading.

Table 1 Summary of tests on type A joint (1/2 of symmetric sandwich shell) indicating boundary conditions, peak load and normalized stress-strain charts for the shell sections away from joint area

Boundary Conditions		Force [t.]	Strain	$\sigma_m = \dfrac{Force}{A_{specimen(164 \cdot 8)_{mm^2}}} \quad \varepsilon_m = \dfrac{\varepsilon_1 + \varepsilon_2}{2}$
Test 02		Pre-load — 0.0	$\varepsilon_1 = 0.0 \cdot 10^{-3}$ $\varepsilon_2 = 0.0 \cdot 10^{-3}$ $\varepsilon_5 = 0.0 \cdot 10^{-3}$	
		Failure-load — 3.42	$\varepsilon_1 = 2.06 \cdot 10^{-3}$ $\varepsilon_2 = 0.49 \cdot 10^{-3}$ $\varepsilon_5 = 0.33 \cdot 10^{-3}$	
Test 05	8 mm. ~3°	Pre-load — 0.0	$\varepsilon_1 = -0.43 \cdot 10^{-3}$ $\varepsilon_2 = 0.50 \cdot 10^{-3}$ $\varepsilon_5 = -1.3 \cdot 10^{-3}$	
		Failure-load — 5.47	$\varepsilon_1 = 1.86 \cdot 10^{-3}$ $\varepsilon_2 = 1.94 \cdot 10^{-3}$ $\varepsilon_5 = -0.07 \cdot 10^{-3}$	
Test 06	3 mm. ~2° 1 mm.	Pre-load — 0.0	$\varepsilon_1 = -0.13 \cdot 10^{-3}$ $\varepsilon_2 = 0.20 \cdot 10^{-3}$ $\varepsilon_5 = -0.22 \cdot 10^{-3}$	
		Failure-load — 5.95	$\varepsilon_1 = 2.57 \cdot 10^{-3}$ $\varepsilon_2 = 1.29 \cdot 10^{-3}$ $\varepsilon_5 = -0.07 \cdot 10^{-3}$	
Test 07		Pre-load — 0.0	$\varepsilon_1 = 0.98 \cdot 10^{-3}$ $\varepsilon_2 = -1.04 \cdot 10^{-3}$ $\varepsilon_5 = 0.46 \cdot 10^{-3}$	
		Failure-load — 8.34	$\varepsilon_1 = 4.1 \cdot 10^{-3}$ $\varepsilon_2 = 1.85 \cdot 10^{-3}$ $\varepsilon_5 = 0.88 \cdot 10^{-3}$	

For the type B1 joint the geometry and instrumentation of the test specimens are shown in Figure 25 and Figure 26 respectively). In this case two tests were performed on nominally identical specimens. To transfer the load from the piston to the FRP plate two 10 mm sand-blasted aluminium plates were bonded onto the faces of the FRP these were bolted to the piston loading grips via the four 22mm holes at one of the specimen, thus initially the load transfer was via the adhesive film between the FRP and aluminium plates.
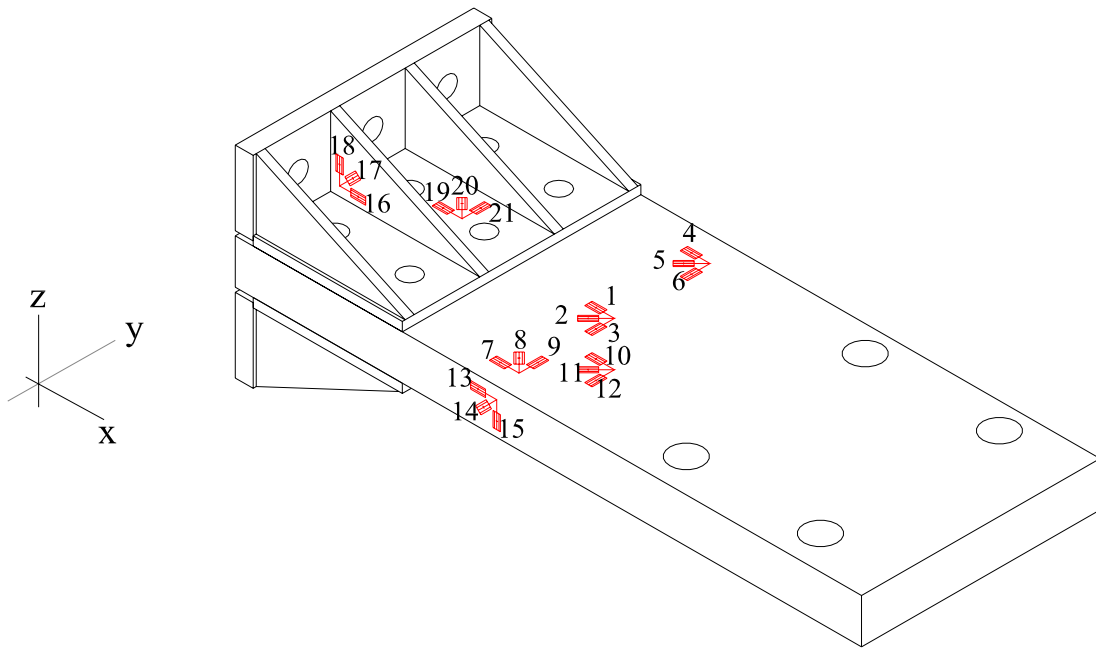
Figure 25 Joint type B1; Position of strain gauges.
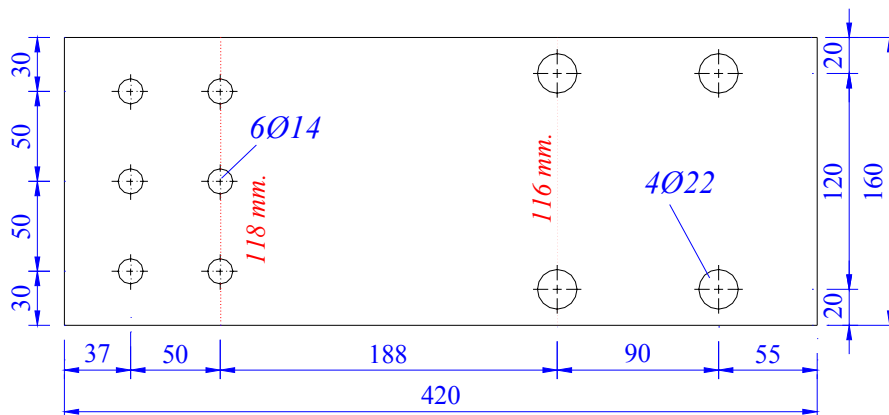
Figure 26 Joint type B1 detail of anchorage positions to steel base plate.

The performance of the specimens is shown in Figure 27 and Figure 28. The loading history, under displacement control, is shown as a function of the data points of acquisition: the loading was performed manually up to a load of 350KN was reached in both cases. In Figure 27 the stresses are shown at corresponding to strain gauges 16,17 and 18 as shown in Figure 25. The jump in stress towards the end is a result of the redistribution of stresses in the flange as a a result of local plasticity around the bolt area.
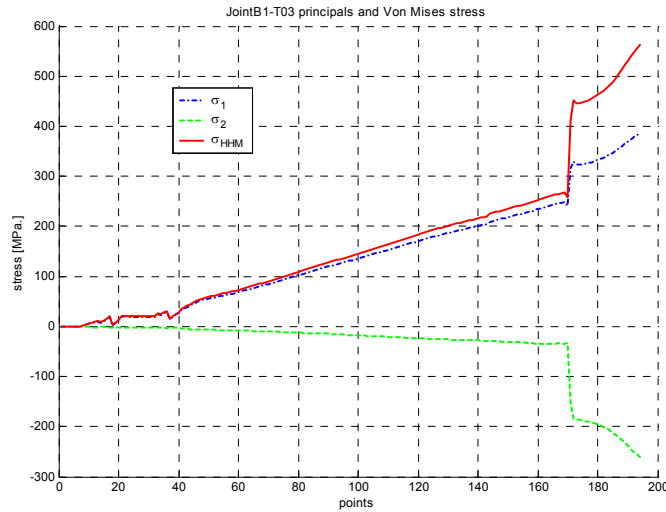
Figure 27 Test JointB1 T03 principal and Von Mises stresses in steel flange.
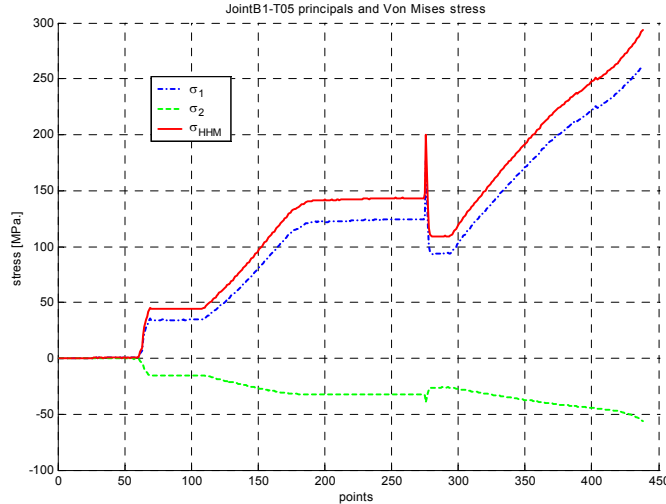
Figure 28 Test JointB1 T05 principal and Von Mises stresses on steel flange.

In Figure 28 the loading rate is somewhat irregular due to sudden glitches in hydraulic pressure, however the final Von Mises stress is lower than in the preceding case (for the same nominal load) as a result of the plasticity around the boltholes, which generates a more uniform loading across the entire flange. In both tests failure occurred at the end connecting the specimen to the piston i.e. that part of the specimen representing the connecting of the FRP tube to the steel joint performed batter than the joint from to the piston. This is not surprising as the thickness at either end was approximately the same; however the initial failure occurs as the interface between the aluminium plate and the FRP gives way, after which all the load is

28

transferred to the 4 22mm bolt holes where, it is conjectured, the stress concentration took the local stresses above the failure strain. In both cases the failure loads (*350KN* or *100Mpa GRP shell skin stresses)* were in excess of the design limit stresses (*260KN* or *55Mpa GRP shell skin stresses* computed from the equivalent loads in the full-scale tower supporting a maximum wind gust of 90 tons.

4.3   Conclusions

Two mechanical joining methods were studied experimentally in order to gain insight into the generic behaviour of bolted joints to be used to anchor the tower base to the foundation. In the case of the tapered FRP joint it was found that the pre-load generated by the axial slotted bolts affected considerably the ultimate load that could be carried by the specimen before delamination failure occurred. In the case of the FRP joint connected to the base with through thickness bolts connected to a steel anchorage plate it was found that the strength of the joint was sufficient to carry the limit loads required.

5   Modal Analysis

The purpose of the modal analysis campaign was to investigate the elastic mechanical properties of the FRP material from which the shell structure is to be manufactured. The procedure consisted in performing an experimental modal analysis campaign on the ½ length of the 1/3 scale tower module measuring the major mode shapes and eigenvalues. In order to do so, simply supported and built in boundary conditions were chosen as benchmarks. The experimental data was compared to the spectral properties predicted from the modal analysis using an FE model. By matching the FE predictions to those of the experiments it is possible to measure the hypothetic moduli of the FRP shell material in the principal directions and, in turn, compare these to the moduli calculated from laminate theory.

The test campaign was conducted on the monolithic shell specimen as shown in Figure 29. The tube has a ratio of length to diameter of 7.2. For this aspect ratio the beam-like frequencies that may be calculated using beam theory may still provide a reasonably valid comparison to the analogous modes arrived at from shell solutions. However, the fact that the material properties may be orthotropic, in addition to the fact that identifying the lower shell modes is easier than deriving the higher beam modes meant that only the full 3D FE analysis would be capable of providing sufficiently accurate answers.

Figure 29 Detail of monolithic tower with accelerometers mounted near the bolt area, for modal analysis in the radial direction.

The test set up for the simply supported case is shown in Figure 30. The boundary conditions are not quite those of a classically supported case: the edge supports at either end are provided by two steel C-section steel brackets of 220 mm width, that provide a stable support for the cord of the shell ring. These boundary conditions were duly considered in the F.E. model.

The experimental modal analysis was carried out using the impact transfer function technique. The modes of the beam were excited with an instrumented impact hammer (5Kg mass 3500N/Volt sensitivity) fitted with a soft rubber head. The impact transfer function at various positions on the structure is measured between the force signal from the impact hammer and the accelerometer. It is possible to, first, identify the modes in a qualitative manner by monitoring the sign of the phase component of the transfer function in correspondence with the position on the tube and then map them to those with the same phase correspondence from the

FE analysis identify the modes. Having identified the signature of the mode it is then possible to assign its corresponding eigenvalue.

The main mode shapes correspond to beam-like and radial modes. The initial FE analyses were obtained assuming mechanical properties calculated on the basis of the production specification supplied by the filament winding company, i.e.: 60% volume fraction of fibre to resin, and fabric weights of 720 gr/m^2 for the filament winding in the hoop direction and 600 gr/m^2 for the UD cloth in the meridional (tower main axis). Although the match in eigenvalues for the case of the first modes was acceptable, there was a mismatch between the hoop and axial values that may have been attributable to the differences in material properties caused by the effective fibre volume fractions used in manufacturing and those requested in the specifications requested. Upon inspection of the specimen the percentage of fibre volume fraction was revised to 40%. On this basis FE calculations were repeated using mechanical property data taken from laminate theory based on the presumed reduced fibre volume fractions of the reinforcing materials. This results in a noticeable drop in both hoop and axial moduli.

The results for the simply supported case are shown in Figure 30. The main modes were identified and compared: these are the first beam and radial modes. The agreement between FE and experimental data assuming orthotropic properties or the GFRP is acceptable given the difficulty of establishing the precise boundary conditions at the supports.

The results for the built in case are shown in Figure 31. It is possible to match the observed and calculated eigenvalues and so obtain an estimation of the effective moduli as shown in Table 2. From these data it is important to note that the effective weight of fibre in the hoop direction is higher than in the meridional: this is contrary to the requirements of the tower where it is more appropriate to increase the axial stiffness at the expense of the hoop modulus – particularly so when using a low stiffness fibre like glass.

Table 2 Frequency from modal analysis.

case	mode	Analytic	Experimental
Simply supported	first	9.0 Hz	10.0 Hz
	second	12.7 Hz	14.2 Hz
Cantilever	first	9.6 Hz	9.3 Hz
	second	25.0 Hz	24.2 Hz

As will be seen in Section 7 the revised elastic modulus in the principal direction agrees well with the results from the quasi-static tests conducted in the main experimental campaign. Even though the load levels used to excite the main frequencies in the modal analysis are far lower than those used in the quasi-static tests, this technique is a useful method to track the quality production. In the example above it was possible to determine that that the expected elastic moduli were considerably less than that requested. The problems associated with quality assurance in production will be discussed further in the case of the manufacture of the hybrid tower module.

Simply Supported Case

mode *1* frequency *9.0Hz* [experimental *10.0Hz*]

E_x=17.5 Gpa
E_y=21 Gpa
υ_{xy}=υ_{yx}=0.12
G_{xy}=2.2 GPa
Assumed properties F.E. analysis
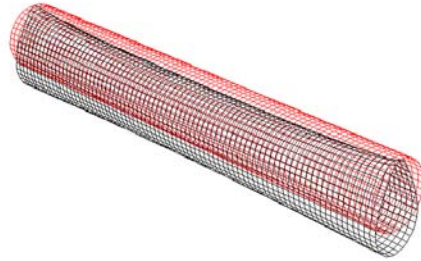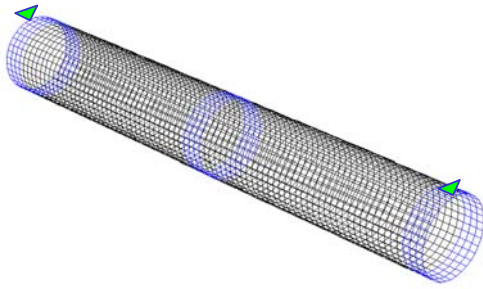
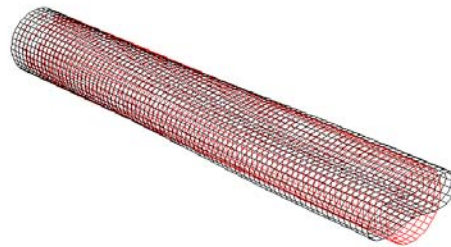mode *2* frequency *12.7Hz* [experimental *14.2Hz*]
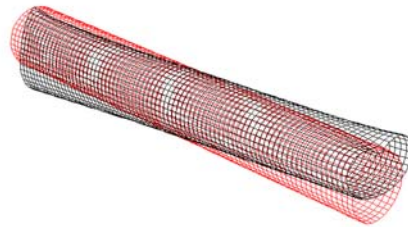
Figure 30 Simply supported case, comparison of experimental modal analysis with FE calculations.

Cantilever Case

mode *1* frequency *9.6Hz* [experimental *9.3Hz*]

E_x=17.5 Gpa
E_y=21 Gpa
υ_{xy}=υ_{yx}=0.12
G_{xy}=2.2 GPa
Assumed properties F.E. analysis
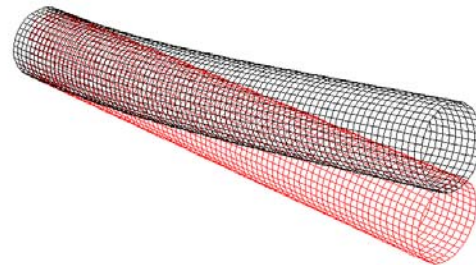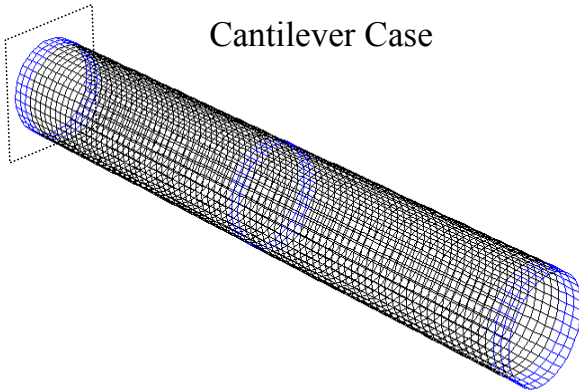
mode *2* frequency *25.0Hz* [experimental *24.2Hz*]

Figure 31 Example of comparison of experimental modal analysis with FE calculations.

6   Quasi-static test method: sub-structuring

6.1   Introduction:

Whereas the main scope of the modal analysis was to perform diagnostic tests on those material properties that affect serviceability of the structure (vibration modes etc), the main scope of the quasi-static tests was to measure the static strength capacity of the various structural configurations chosen.

In the case of standard steel tower components, the mechanical properties are well known or can be identified from modal analysis. From these data it is possible to calculate the limit loads for various types of failure; be it by elastic buckling or material failure itself. In the case of monolithic FRP shells or sandwich shells and panels manufactured with standard core materials, there exists considerable literature that can be consulted in order to optimise the design of shell structure. However, in the case of the hybrid tower there are no norms or standards that can be readily applied, as the nature of the design is innovative and little has been published by way of experimental data that can be used to aid in the design. There are numerous references to the application of FRPs bonded to concrete and other brittle materials used in construction; however in most applications the FRP is directly bonded onto the hardened and specially prepared RC structure. In those cases the shear transfer between FRP and adherent is usually of high quality and relies on the chemical bond between the materials. In the case of the proposed hybrid tower the shear transfer is left solely to the mechanical interference locking between the hardened concrete and the FRP Shell: in this sense the associated mechanical model is closer to a steel rebar, albeit extended along the complete adherence surface). Ultimately both the serviceability and structural capacity (particularly the local and global buckling load) are critically dependent on this type of interface of which few experiments have been conducted at this scale.

Given these considerations it is important to ascertain the structural performance in the typical service regime so as to calibrate simplified non-linear models to determine the effective tower stiffness (hence eigenvalues) and its variation as a function of the applied moment. The ultimate strength of the prototype designs has to be validated in order to assess the safety factor of the structure in the event of extreme wind events. Given the high cost of performing such controlled tests at full scale using the full structure it was decided to perform the tests at 1/3 scale, which permitted the use of the same constituent materials without having recourse to unrealistic scaling laws for the materials themselves. The scaling factors applied relate the stresses and strains within the structure proportionally to the scaling factor, whereas the effective natural frequency of the full-scale tower is evaluated from the calibrated constitutive properties of the material tests performed on the test coupons and the 1/3-scale tests.

In essence a structural validation requires a representative scale test with which to calibrate both FE and simplified models. In order to do so it is appropriate to subject the structure to a well defined loading condition such as a pure bending moment, shear load or combination of both. These conditions can then be reproduced in the analytical calculation in order to calibrate material properties and potential failure modes of interest. If possible the most convenient method is to load the structure in the same fashion, as it would be in service conditions. As stated above, due to excessive costs size limitations the laboratory specimen tests could not possibly be constructed at the full length of the tower, thus excluding the possibility of reproducing the maximum bending moment at the base by applying a simple shear load at the full height

In the project description for WP2, Task 2.2 it is stated that large-scale tests would be carried out on representative subassemblies of the tower. Performing two such tests on ½ length segments of the 1/3 scale tower assembly completed this part of the task. One specimen was

manufactured from a purely FRP (monolithic) material solution with no use of either concrete or other sandwich solution. A second specimen having identical external dimensions was manufactured as a sandwich structure using FRP skins with a high-strength concrete core.

6.2   Experimental Set-up:

Load Application:

The testing plan for the 1/3-scale prototypes is presented in Figure 32, which consists of a trio of servo-assisted hydraulic pistons. Each piston is controlled independently with a dedicated industrial computer fitted with a digital control hardware and software developed at the ELSA laboratory. Each computer receives displacement and force information from the pistons that it can use, on-line, to generate commands either in force or displacement control mode. With this set up it is possible to apply arbitrary, independent, combinations of shear and axial loads as well as moments. As regards the technical details in which the test is conducted we give a brief description below.

$$P_1 = F$$
$$P_2 = F \cdot \alpha + F_{sw}/2$$
$$P_3 = -F \cdot \alpha + F_{sw}/2$$
$$\alpha = \frac{16 - 8.56}{2}$$
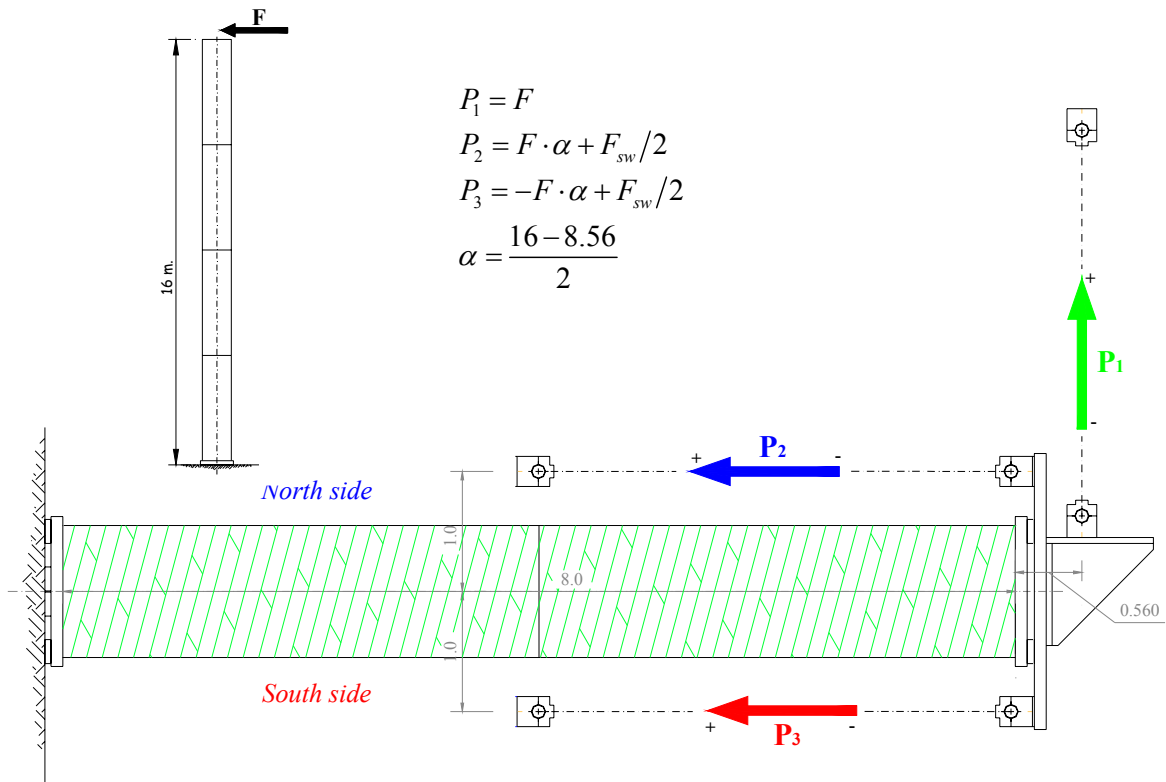
Figure 32 Conceptual representation of sub-structuring

The scope of the experimental set-up is to apply a large bending moment to the tower substructure through a combination of lateral and applied bending moments. This can be achieved by coupling the force measured by the lateral piston to drive the other two. The lateral load piston P1 applies a displacement-controlled path to the steel flange and plate at the top of the ½ length of the tower. The piston pair P2 and P3, both under load control, are slaves to P1 and apply a load proportional to ±F1, i.e.: the load measured in real-time by the load cell of P1. Although P1 can also be force controlled, the three-piston set-up system would be inherently unstable once the collapse load is reached; however, maintaining P1 under displacement control ensures that, at failure, and once the load in P1 drops, the moment applied by P2 and P3 will

also tend to decrease. Finally in addition to a dynamic load generated by the displacement of the structure, the two vertical pistons P2 and P3 may continuously apply a static axial load, in order to simulate the effect of self-weigh or added gravity loads. This reference signal is taken from the analogue output from the 500KN piston and is routed to the lateral pistons (prior change of polarity in the case of P3).

Under load control, a reference signal of 1volt represents, nominally, a load of 200KN for Pistons P2 and P3 whereas it is only 100KN for P1. Thus the total gain factor is includes a software multiplier that considers the effective geometric moment, as well as the ratio of the force/voltage sensitivity of each piston (itself based on the hardware calibration from the load cell).

Figure 33 Tree-point piston set-up.

6.2.1 Mechanical Connections:

The tower is mounted horizontally onto the Reaction Wall. The ends of the tower are connected to two ring collars fitted with radial, concentric bolt holes (144 M12 bolts) as shown in Figure 20. The two rings are then bolted to a solid 1.25x1.25x 0.1 steel plates that can in turn be either anchored to the reaction wall at the base of the tower or a second steel plate fitted with the piston attachment cleaves.

The ends of the FRP tube were inserted into the ring gaps of the joining flanges and when then bored in situ passing the drill through the bolt holes of the ring flange. The high number of bolts resulted in a mechanical interference fit, which as will be shown later proved to be relatively slack free.

6.2.2 Instrumentation set-up:

The primary instrumentation is that which assists in controlling or monitors the performance of the pistons. For this purpose each actuator is fitted with a load cell consistent with the range

of its loading capacity: 50 and 100 tonnes respectively for the lateral shear load piston and the two vertically acting ones on either side of the tower. Both on-board and external displacement transducers monitor the displacement of each piston. This part of the instrumentation is shown schematically in Figure 70 and Figure 73 in plan view. The arrows point to the positive direction of the physical unit being measured; hence as the piston pulls and draws in, displacements tend to become positive. Likewise traction on the piston arm is associated with a positive force.

The secondary instrumentation consists of displacement and strain gauge channels mounted on the structure in order to monitor its structural performance. Figure 71 and Figure 72 (see Appendix 0)the show the disposition of the displacement channels and are shown in plan view in the plane where the actuator force acts. For convenience we refer to the North side of the tower when the lateral piston would pull with a positive force and positive displacement. The strain gauge channels are shown in Figure 74 and Figure 75 and represent side views of the North and South faces of the tower, thus the North face of the tower moves towards the reader when the lateral piston executes a positive displacement.

Concerning the displacement transducer devices: these consisted of Gefran resistance transducer the ranges of which are given in Table 12 and Table 14. These are generally small range devices suitable to measure the relatively small displacements associated with the axial deformations of the tube; however they were also used at the tube mid-height (corresponding to ¼ length on tower) to measure the bending deflection. In addition to these a ± 150 mm LVDT was mounted at the top of the end tower module (corresponding to ½ length on tower) on the steel ring plate anchorage plate. For measurements in excess of 150 mm a digital encoder with a range of ± 250 mm was mounted to the second steel connecting plate anchored to the lateral piston. In the description of the experimental data the channels will be identified in the graphs and plots in accordance with this numbering procedure.

Concerning the strain gauge channels the numbering system does not follow on from the displacement transducers but rather is reset from #1. Both simple and rosette strain gauges were used. The rosettes are identified on the diagrams by the fact that three channel numbers are given for each position. The ordering is such that the lowest number in the triad represents the gauge aligned in the axial (0°direction), followed by the gauge at 45° and 90° in the hoop direction. Strain gauges and their positions from fixed points on the structure are shown in mm noting that in figures reference is made to both internal and external sides of the tower. The physical characteristics and strain gauge factors for the various gauges used are given in Table 12 and Table 15. All rosette channels consisted of 120Ω resistance gauges whereas 350Ω were chosen for the single unidirectional gauges.

All the gauges were mounted on a full-bridge circuit using a constant voltage source. Given the relatively low thermal conductivity of the FRP material, and in order to reduce errors in strain measurement due to the local heating effects, a 1.5V excitation voltage was applied for all channels. In the description of the experimental data the channels will be identified in the graphs and plots in accordance with this numbering procedure; however the channel number will be preceded by the Greek lower case letter ε or γ respectively for simple and shear strains and the letter Latin letters x, xz or z indicating respectively the measured strain in the 0° 45° or 90° directions, for example $\varepsilon_{xz}37$ is the strain measured on gauge 37 on a rosette in the 45º direction.

There are some minor differences in the instrumentation between the monolithic and sandwich towers and these are pointed out in the diagrams and tables below. These changes concern the position of the strain gauges (positions 1-4) on the inside surface of the intermediate joint area that, in the sandwich module, have been moved to the lower end of the tower in order to monitor incipient buckling of the skins from the concrete core.

6.2.3   Optical measurements

The overall displacement of the specimen was also monitored with two CCTV cameras. A computer sampled frames from the cameras at the same frequency as the other data channels allowing the synchronisation CCTV frames and the transducer data. Using such a system it is possible to associate an image of any particular point in the experiment to the measured physical data. One camera was mounted looking inside along the length of the tower module from the top attachment plate down to the base of the tower. In order to monitor the possible local duckling of the shell walls, markers were bonded onto the inner sides of the tower stretching one metre from the tower base. In the case of the monolithic tower, the external camera was mounted at a height of 3 metres looking down along the tower length to the base. In the case of the hybrid tower it was placed at a height of 16m above the specimen and looked up from the base towards the mid-section attachment plate.

6.3   Substructuring:

Substructuring as commonly used in FE analysis or as is done here in an experimental context, is a method that may be applied in order to study that part of the structure that is if most interest and, where, it is presumed, the most complex behaviour may occur. The remaining part of the structure, i.e. those parts that are well understood analytically or experimentally, are not represented to their full extent but rather appended in a simplified, but still representative manner.

In the context of FE models this technique makes it possible to generate savings in calculation time or computational power. In the context of experimental mechanics it can represent a large saving in specimen manufacture and instrumentation. In the case of very large specimens as is the case herein; it is possible to reproduce only a part of the structure at a feasible scale and still claim that it is representative of the overall behaviour, clearly in this case it is to be expected that failure due either to in-plane stresses or buckling of the shell would occur at the tower base. When the constituent material properties are available, one can perform an FE pre-calculation to identify the critical section to be tested experimentally, however in the case of the hybrid tower insufficient literature and experimental reporting is available about the macroscopic behaviour of the sandwich elements -especially in the out-of-plane direction- in order to provide guidelines that may be used to design a sub-element test specimen with which to study a critical zone. Another aspect is that if the effective physical length of the sub-element is too short it tends to behave less like a beam element and more ring-like, thus it becomes ever more difficult to apply consistent beam-like boundary conditions. Although in order to calibrate the structural performance of the specimen against FE models it is not necessary to load the structure exactly as it would be in service, simulating such conditions would offer more insights into the order of failure mechanisms rather than imposing a failure mode a priori, hence the preference to perform a ½ length sub-structuring bending test.

For this reason it was decided to test the ½ length of the tower given that for this geometry it is still possible to model the local effects at the truncated length as a sub-structured beam element: essentially applying the same shear force as for the full length with an added bending moment proportional to the missing ½ length. For comparison consider that at full scale even testing the half length of the tower would require the application of a bending moment of the order of 20 MNm: this would require the use of jacks capable of applying 450 tons and the design of massive anchorage plates, which, although within the capabilities of the laboratory would exceed the initial project proposal, both in terms of cost and the initial experimental design.

The set-up for the scaled 1/3 scale 16-meter tower is thus sub-structured using only the first 8-meter base section, seen schematically in Figure 32.

A moment is to be applied at the tip of the tower simulating the thrust of the rotor for various loading conditions. With this set up it is possible to apply any combination of loads on the structure such with a maximum lateral shear load of 500KN and a bending moment of 4MNm resulting in a maximum moment at the base of the tower of the order of 6MNm.

The control signal for the moment pair is read directly from the load cell of P1 and multiplied by a factor corresponding to the geometric scale of the ratio of moment arm between the piston attachment plates and the effective missing length of the top half of the tower.

6.4   Calculation of curvature

The calculation of the curvature is obtained from the line of strain gauges mounted around the perimeter at the base of the tower as shown in Figure 34. The channels used in the actual computation are denoted by the index in the equation below. The validity of the weights assigned to each strain position is demonstrated in Figure 35 showing the linear regression fit of strain distribution across the tower diameter at near full-load demonstration that the linear fit for Equation 1 is a valid assumption. The stiffness of the tower may be obtained from the moment curvature ($M - \chi$) diagram at the base section. The curvature is obtained from the ring of strain gauges at the base of the tower (essentially channels 24, 27,30,36,39,42) By expressing the structural performance in terms of ($M - \chi$) it is possible to obtain the effective modulus from:

$$E = \frac{M}{I \cdot \chi}.$$

Where I is the second moment of area of the tower section. We note that this presumes that the structure is deforming primarily in beam mode.
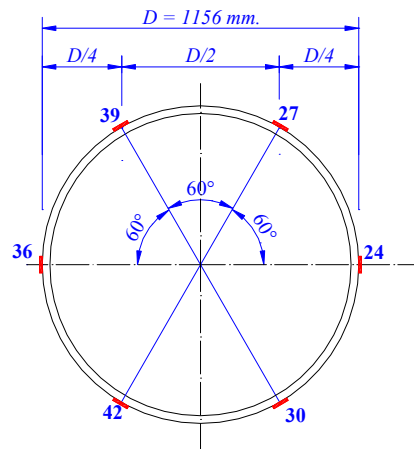
Figure 34 Position of Strain gauges at base of tower across diameter.

Equation 1

$$\chi = \frac{\varepsilon_{36} - \varepsilon_{24}}{D} \cdot \frac{1}{2} + \frac{\varepsilon_{39} - \varepsilon_{27}}{D/2} \cdot \frac{1}{4} + \frac{\varepsilon_{42} - \varepsilon_{30}}{D/2} \cdot \frac{1}{4}$$
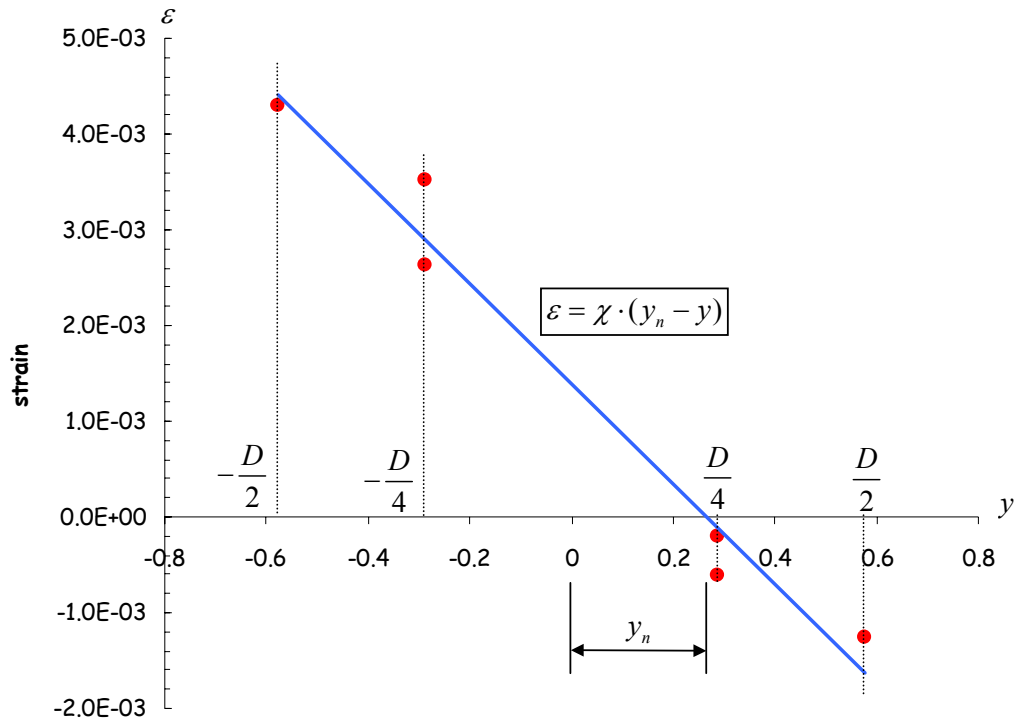
Figure 35 Curve fitting of linear regression of strains across tower diameter at near full load.

7 Monolithic Glass

7.1 Background

Synopsis: The scope of these tests was to observe if there was any significant structural degradation as a result of repeated loading at high load values. In this range the tower is not designed to be functioning in the working regime but it is expected to survive the effects of repeated high wind load cycles. A number of tests were conducted and the results indicate that the structure is sufficiently resilient to survive repeated excursions in this range.

The main aim of the quasi-static test campaign on the monolithic tower was to verify the overall structural capacity as well as the behaviour of the joining elements at the base and mid-height. In addition to this it was required to verify the serviceability of the tower itself by crosschecking the modal analysis measurements concerning the effective elastic modulus.

Initial experiments using the piston set-up at low loads indicated that the modulus might have been considerably less than that obtained from the modal analysis data, and it was presumed that if this were true it could have been due to a low fibre volume fraction. Moreover, it would have implied that the modal analysis was substantially in error. However, upon analysis of the strain gauge data the indications were that the structure was being loaded asymmetrically with high local strains arising from the side of P2, even though the nominal control voltage rates were correct to within a few percent of experimental error. In essence, the structure was being loaded under a near pure bending moment plus an added axial load.

It was later discovered that an electronic hardware calibration setting on the load cell amplifier circuit of P1 was incorrectly set, with the result that the applied force was, in fact, 6.18 times more than had nominally been presumed. The electronic control circuit had, in fact, functioned correctly. In voltage terms there was no error, rather the actual applied load was not consistent with our expectations, being in fact higher than presumed. This calibration error was present and constant for all the tests and loading protocols conducted on the monolithic tower specimen. The implications for the test campaign is that the boundary conditions imposed were not those selected at the outset, however, the new boundary conditions still define a valid structural test, and the simulation with FE analysis was conducted using the effective loading applied during each test.

7.2 Example of medium level test: tm22

The medium level tests on the monolithic tower were conducted to monitor the overall performance of the tower at significant load levels. The problems encountered with the electronic hardware in the piston controller have already been explained in 7.1; other than that it can be claimed that the instrumentation and the data recorded reveals that the performance of the tower module is consistent with the mechanical properties as obtained from the modal analysis tests described above.

We reproduce an example for a low load test, tm22. The imposed displacement history load measurements and moments are shown in Figure 76. It can be seen that P2 is providing most of the force with P1 and P3 being much lower. As a consequence nearly 80% of the total moment and static compressive axial load is generated by P2. In fact the static axial load applied by P2, is also 6.18 times higher than the nominal required; the overall static axial load was therefore just over three times the nominal (P3 having applied the load as planned), moreover by virtue of the imbalance between the levels of P2 and P3, the axial load varies considerably and essentially

follows the general trend of P2. However whereas the boundary conditions can be reproduced arbitrarily on the FE calculations, the real failure modes associated with the structure are dependent on the boundary conditions and ideally these should highlight the weakest point of the structure in the event of the such loading occurring to the structure. Given that the scope of the tests was also to reproduce the likely failure modes under extreme wind loading, the idealised boundary conditions should attempt to reproduce these conditions. In the case of the tower, the base and lower joints are subjected to high bending moments.

For this test he peak moment of just under 0.6MNm is significantly close to the maximum moment 0.75 MNm associated with the maximum design thrust for the 'hurricane event'. The comparison between the modulus obtained from the modal analysis (17.5 GPa) and that obtained from the moment curvature diagram (18.5GPa average secant modulus) are acceptably comparable given the size of the structure and the very different manner in which the data are obtained. However we note than in both cases the modulus is lower than the expected modulus presumed based on the lay-up and volume fibre specifications provided to the manufacturer.

Concerning the nature of the hysteretic cycles (Figure 77) we note that there is no noticeable difference between repetitions indicating that no structural degradation is taking place. It is therefore conjectured that the hysteresis –as seen in the moment curvature diagrams– is caused by the friction force in the swivel connectors of the two parallel moment-pistons P2 and P3. As the head of the tower moves sideways, the swivels accommodate a rotation proportional to that of the tower head connecting plate, and given that the P2 and P3 exert noticeably high loads, even a low friction coefficient may generate a lagging friction force capable of generating the hysteresis loops seen in Figure 77. Another factor consistent with this conjecture is the repeatability of the cycle and its actual shape: reminiscent of generic dry friction hysteretic behaviour.

It is to be noted also that upon changing the direction of movement a sudden drop in the magnitude is observed, as is the phenomenological nature in friction systems. The magnitude of the hysteresis force corresponds the vertical height separating the two nearly parallel branches of the loop: the effective friction coefficient in the pistons may be obtained by equating this force to the sum of P2 and P3. The deformations and strains along the tower are consistent with the type of loading imposed –essentially a pure eccentrically applied moment.

We note that the performance of the end connecting joints was satisfactory in that the slack between the tower ends and the steel connecting plates was of the order of 1.5 mm. This is consistent with fact that the interference generated by the 74 bolt heads mitigated the individual gaps generated by the tolerances of each bolthole. An example is seen in Figure 84, where –as measured by the displacement transducers 1,8 and 15 and 7,9 and 16– we show the evolution of the displacement between the base steel ring and base of the tower. As the load is increased the displacement between the tower base and the steel anchorage ring increases sharply (as is usually associated with slack) and then only grows proportionately to the application of load. However, even such a small spurious displacement will be magnified by the rotation of the tower at the tip by a factor of approximately eight. Hence a measurement of the tower stiffness only in terms of force displacement at the tip would result in a lower stiffness reading than that obtained from the ($M - \chi$) diagram.

The general distribution is consistent with a loading that is consistent with a large, nearly constant bending moment along the length of the module; thus in Figure 78 the longitudinal strains at the base of the structure (21,24,27 30 North 33,36,39,42 South) are comparable in magnitude to those at the top (9,12, 24 North and 15,18, 36 South).

The strains around the intermediate joint are shown in Figure 79 in both the internal and external tube positions. It would be expected that those strain gauges positioned in the centre of the joint (2,6,4 and 7) would measure less absolute strains as they correspond to positions where

the section of the joint is thickest. However the proportions between of the strain ratios of opposing -internal and external- gauges are not equal so that the differential strain along the joint in the axial direction is more pronounced in the external gauges. Another possibility is that due to the combination of eccentric axial load and bending moment the load paths from the top of the tower to the base may not be symmetrical in the North and South faces, thus the effect of the axial load applied by P2 is localised around the top rim of the tower and at the joint height and only attains the nominal value at the base.

For the remaining strain distributions we note that the hoop and shear strains (Figure 80 and Figure 81 respectively), are nearly an order of magnitude lower than the corresponding axial strains, testifying to local Poisson ratio of the order of 0.18. This value is slightly higher than expected and is thought to reflect the relatively high volume fraction of resin that would tend to increase the Poisson ratio, which for a normal cross-ply would be of the order of 0.1.

The strains in the steel flange at the base of the tower can be seen in Figure 82 all of which were well below the plasticity limits for the medium carbon steel used for their manufacture. Finally, from the ring of strain gauges on the base of the tower it was possible to calculate the position of the neutral axis as shown in Figure 83. Allowing for numerical singularities it would seem that, on average the neutral axis is slightly offset by 50-100 mm from the centre of the circular section. The plot is only indicative as it is taken from the weighed mean of the ring of strain gauges, which may be affected by strain readings resulting from the orthotropic nature of the FRP substrate and geometric distortions of the strain field.

The transversal and longitudinal displacements along the length of the tower are shown in Figure 84. In general the sum of the axial displacements on both sides of the tower (9 to 13 North and 2 to 6 South) generates an average strain along the length of the tube of the order of 0.2% strain that matches the typical strain gauge readings shown in Figure 78. The slack between the steel base ring and the tower in the axial direction (8,1) has already been discussed above in the context of the spurious displacements that affect the overall stiffness measurements. It is to be noted that the slack in the top attachment plate are approximately equal. We also note there is some slack in the transverse direction at both connection areas of the order of 0.3 mm.

7.3   Final destructive test: tm28

Synopsis: The tower was loaded monotonically up to failure according to the loading protocol shown in Figure 85. A plan view of the tower during and after testing can be seen in Figure 133 (see 15.1). The base moment at failure exceeded the ultimate design load by a factor of 2.3; and given that the ultimate design load includes a safety factor of 1.5 on the maximum expected thrust at the tower hub height, this implies an overall safety factor of 2.3 on the material properties. However, in view of the fact that the modulus of the material was of the order of 19GPa rather than the 25GPa expected, it may be considered that the overall safety factor would have been of the order of 3.4.

Also from Figure 85 we show the evolution of the piston forces and associated moments. We note that the effect of applying the nominal axial load produced an effective moment as a result of the eccentricity of the couple applied by pistons P2 and P3. As expected the load in P2 is much higher than P3 thus the effective axial load was not constant but rose more or less in proportion to P2. Thus it can be claimed that the load at failure was generated by a bending moment associated with a high axial load and a relatively low transverse shear load. The axial load is given as the sum of P2 and P3, and given the high gain in the controlling voltage of P2, the axial load at the end stages was more than an order of magnitude higher than the static

design dead load. Towards the end of the final test the load in P2 is seen to become stationary at about 93 tons, this is because the servo-valve is not capable of sending any more oil to the piston chamber, at which stage the load required by the other two pistons to move the tower by the same amount increases. At this point P2 cannot provide any extra moment and hence the incremental load is taken up by P1 and P3, whose rate of loading is seen to increase considerably coinciding with the onset of the constant load regime at P2. This effectively reduces the total axial load somewhat in such a manner that, at failure, the total axial load has decreased to approximately 70 tonnes, having been reduced from a peak of about 90 tonnes (we should note that the nominal axial load should have been 5 tonnes). Considering the arguments above, it can be said that the monolithic tower was loaded under very unfavourable conditions as the effect of the high compressive axial load is not well tolerated by composites and is aggravated near the joint area.

From the strain-gauge data at the base of the tower, it is possible to plot the total base moment versus curvature as shown in Figure 86, from where it can be seen that the tower behaves elastically up to failure. The effective modulus obtained from the moment-curvature plot is 19.7 GPa. The influence of the high compressive load, although more critical for materials weak in tension, may also have played a role in so much as it introduces second order transverse loading which at high displacements may add a significant component to the effective base moment; however, this would imply that the tower is stiffer as this spurious component was not added to the total base moment computation.

The strain levels in the tower are of the order of 0.5% at the top and bottom flange areas as shown in Figure 87. Some strain channels (5, 15 and 18) were not available during this test, however the general load level at the top flange area is given by channel 12 which can be directly compared to channel 24 at the base of the tower. The longitudinal strains at the base along the main axis of bending are given by channels 21,24 North and 33,36 South: as expected, gauges 21 and 33 are respectively lower than 24 and 36 as they are mounted nearer to the rim of the tower footing where the thickness is highest. However, the remaining ring gauges on the North side (27,30) are not symmetric to their images on the South side (39,42), which, on average, are half as low.

In Figure 134 and Figure 135 it is possible to observe the failure area around the intermediate joint on the tensile side of the tower: it can be seen how the connected faces are sheared away along the bond line of the joint. However, it is thought that the failure of the tower was associated with the compressive failure at the inner surface of the intermediate joint as shown in Figure 136, this is observed in the strain-gauge data: in Figure 88 (channels 5 and 7 were not available) we plot the strain gauges on the inner surface of the tube where it can be seen that as the applied moment is increased the strain on the compressive side shows clear signs of growing at a faster rate than that on the tensile face. This phenomenon is replicated in the data obtained from the local transducers that measure the displacement across the joint area, and here, as is the case for the strain gauges, the lateral tower displacements are, in general, asymmetric due to the initial offset displacements resulting from the spurious moment generated by P2. It can be seen that from point 300 till 400, the rate of increase in compressive displacement (using piston nomenclature, an inward movement is a positive signal) is much higher than in the corresponding tensile side of the tube. Subsequently the rate of growth in compression is slowed down, but only to be followed by discontinuities (point 500) after which the rate of extension in tension is faster than in compression. Thus at the joint area we observe a complex redistribution of forces arising from a the variation of contact stresses around the joint area as a result of failure across the joint. The final rupture of the tube was accompanied by a sudden liberation of strain energy and a loud, explosive, noise.

The remaining strains in the hoop Figure 89 and shear directions Figure 90 are approximately one order of magnitude lower than the longitudinal. The hoop strain mirrors the

axial strains at a lower strain level and indicate to a partial redistribution at the higher strains associated with the non-linearity at the time when the mid-joint area begins to fail. For the shear strains, this phenomenon is accentuated and seems to appear at a lower strain level: during the final stages of the we note that the strain does not grow monotonically up to failure and, in fact, may change sign.

The strain levels in the steel flange area are below typical plasticity limits, however, some pseudo-plasticity was noted around the bolt area as shown in Figure 137 as a result of the stress concentrations. The bolts themselves were plastically deformed as expected for these load levels.

7.4   Conclusions

The monolithic tower design meets all the serviceability and safety criteria required. Regarding serviceability issues: on the basis of a 50 m tall 3.5 m diameter tower having a constant cylindrical section with an added mass at full height of 50 tones, the natural frequency would be expected to be in the range of 0.38 Hz compared to the 0.31 1p rotating frequency.

Regarding safety aspects: on the basis that the full-scale tower must survive a peak thrust of 45 tones (including a 1.5 safety factor on wind gust) at hub height, which is equivalent to peak bending moment at the base of 0.72MNm at the 1/3 scale, and considering that the final failure of the test specimen occurred at a bending moment of 1.8MNm it can be deduced that the overall material safety factor is of the order of 2.3. If however the quality assurance on the filament winding lay-up affecting the elastic modulus had been improved upon, then the safety factor would have been of the order of 3.2.

8   Hybrid Glass/Concrete

8.1   Background

The main aim of the quasi-static test campaign on the hybrid tower was to establish if the configuration of a reinforcing FRP formwork system could provide the sufficient stiffness and strength to meet both the serviceability and strength criteria required of the wind turbine. In the preceding sections we have outlined the research aspects linked to the manufacture of the tower and how they have affected the design of the 1/3 scale prototype specimen presented in this report. The design and dimensioning of the tower depended on certain assumptions concerning the nature of the crack formation in the concrete along the height of the tower as it exceeds the tensile strength limit: this affects the stiffness profile of the tower which is a non-linear function of the effective applied moment. For a given set of FRP and concrete properties the stiffness distribution is dominated by the shear transfer capacity between the tensile reinforcing elements (FRP) and the concrete in tension. Essentially the FRP should act to limit the depth and reduce the distance between the incipient cracks in the concrete. This mechanism relies (Figure 37 and) either on a good adhesive bond between the concrete and the FRP or can be performed by the interaction of mechanical keys much as is done for standard reinforced concrete steel re-bars. In the case of the FRP formwork designed for the tower, no adhesive bond was foreseen, however it was expected that the design of the cylindrical formwork would produce shear transfer via two mechanisms, on the one hand by the contact surfaces of the concrete with the inner and outer cylinder surfaces, and the other by the shear locking of concrete to the web separator which, in turn, would transmit the shear load directly to the skins via the top and bottom flanges bonded onto the formwork skins.
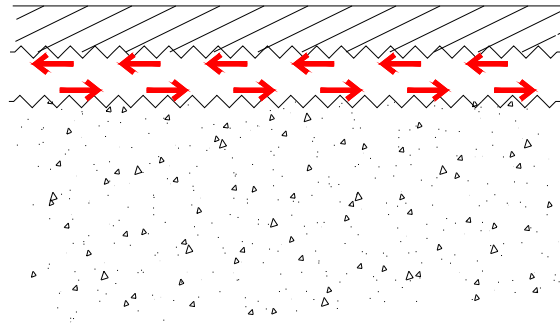
Figure 36 Schematic representation of interface shear transfer between FRP skin and concrete.

For the examples shown below the substructuring loading method was implemented in accordance with the principles outlined in Chapter 6.3 thus the loading on the mid-section of the tower at 8 metre height is equivalent to a 16 metre tower loaded with the same shear thrust load. The scaling factor is such that the shear load ratio between the 50 m tower and the 16 m model is the scale squared (~10), whereas the for the equivalent moment is the scale cubed ~30. Thus the ratio of measured stresses and strains for equivalent (scaled) tower heights is 1 to 1. The data graphs (apart from minor changes that will be highlighted) are presented in the same manner as was done for the monolithic tower. The loading protocol for these tests is shown in Figure 38; each test consisting of a scaled version of the load path given. The exception to this scheme is the last destructive test which consisted of two small amplitude cycles and a monotonic ramp up to failure.
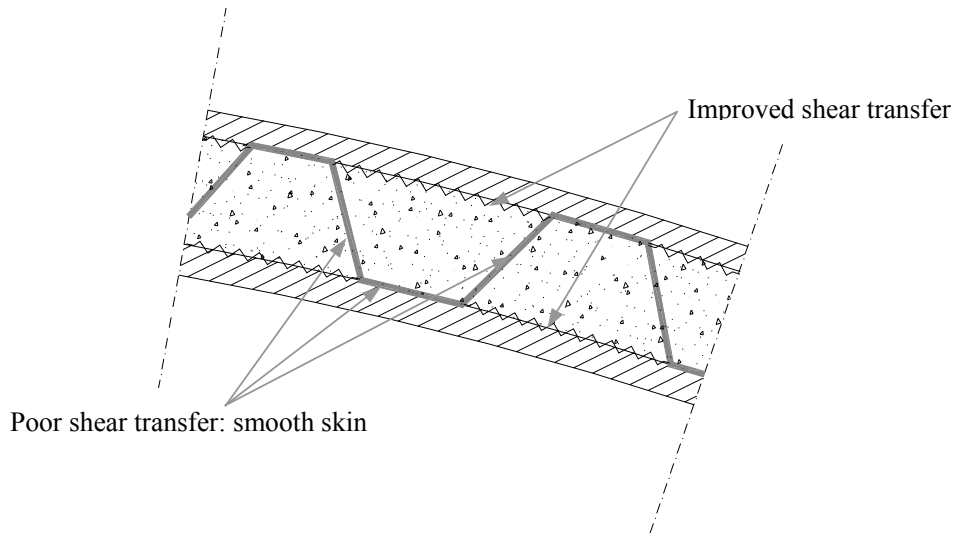
Figure 37 Schematic of adherence of concrete to FRP skins in FRP formwork.

All the main tests up to failure are reported in this section. These can be divided into three main sets: t04 is a low-level test in order to gauge the initial onset of cracking. This is followed by test t05 where a higher displacement is imposed sufficient to cause extensive cracking: the equivalent load in this case approaches the limit design case for maximum thrust at hub height. Finally tests t06 and t07 induce damage in excess of the design limit loads up to failure.
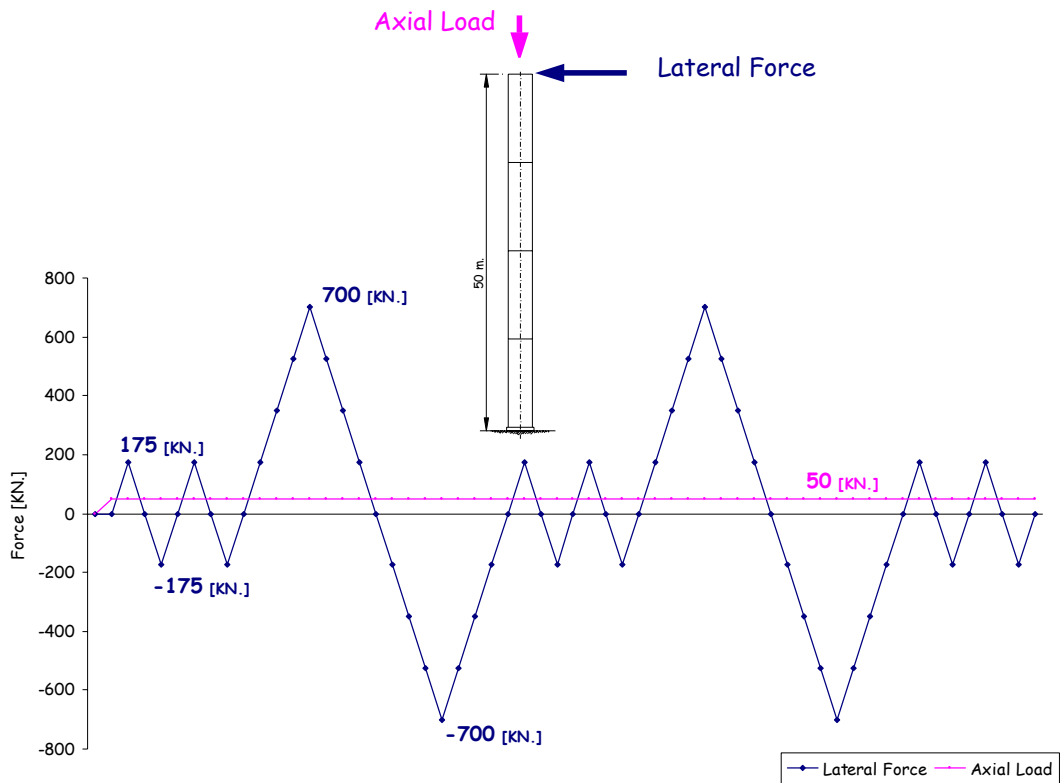
Figure 38 Generic loading protocol for hybrid tower.

8.2   Low level tests:t04

These tests were intended to study the behaviour of the tower in order to monitor the first onset of cracking and hence to gain insight into the manner of shear transfer between the concrete and the FRP walls.

In Figure 94 we show the loading protocol using a very small lateral displacement chosen in order to monitor the onset of cracking in the tower. The repetition of the two smaller cycles following the large cycle is intended to monitor the degradation, or path dependency, of the mechanical properties. The loads and moments provided by each piston are given in the two lower graphs of Figure 94. It can be seen that the control on the axial load (given by the sum of P2 and P3) is quite constant. For this range of lateral displacements the level of axial load is higher than the cyclic variation of the individual loads from each P2 or P3, which, in turn are higher than the load on P1. Seen in terms of applied moment though it should be noted also that the moment provided by the sum of P2 and P3 is approximately equal to that provided by P1, corresponding to the nominal loading condition where the substructured moment (from P2+P3) should be equal to that from P1. The small difference are due to the static offsets on P2 and P3 are higher than their cyclic components and thus small differences are appreciable at such a load level.

Whereas in the presentation of the monolithic tower data only the moment curvature ($M - \chi$) diagram was given, here we include a force-displacement diagram in such a manner that assuming the substructuring method permits the interpretation of the test as equivalent to one on a 16 metre tower. Hence for the force-displacement diagram shown, the load refers to the shear load applied at the nominal 16m height which is nominally identical to that applied at the tower mid-height (at the top attachment plate), whereas the displacement corresponds to that measured at the mid-height scaled by a factor of 3 −consistent with the deformation ratios of an elastic beam at full and half length heights.

The force displacement and moment curvature diagrams are given in Figure 95. The peak load level corresponds to approximately 1/10 of the design limit level (4.5KN or 0.72MNm). The difference between the two small cycles is minimal indicating that the effect of the larger cycle on hysteretic behaviour is smaller than experimental error and moreover, that the effect of the axial load cancels the structural non-linearity caused by the concrete cracking, i.e. the axial load is sufficient to keep the cracks closed, at least in this range. Examining the larger cycle we notice what appears to be the onset of first cracking of concrete coinciding with the change of slope in both the hysteresis diagrams. Applying Mohr's law to the moment-curvature loops of the large cycle it is possible to calculate the equivalent modulus for the tower, this gives a value of the order of 56 GPa for the steep slope before cracking (this is calculated by assuming an equivalent un-cracked concrete section and the second moment area corresponds to the full annular area of the concrete section). This value, although lower than the 73 GPa provided by the manufacturer is within the expected range considering it is assumed that at this level of load the concrete section has no voids and is un-cracked, a scenario that is precluded by the indications of the slope change at the cycle peaks. Applying this same concept to the slopes of the smaller cycles a value of 65GPa is obtained which agrees satisfactorily with the theoretical values. We note that, as was the case for the monolithic tower, part of the observed hysteresis is due to the friction in the swivel of the P2 and P3 pistons. The degradation of the mechanical properties can be monitored with the secant stiffness (the evolution of the secant stiffness with increasing cycle amplitude will be described in the following sections for tests t05, t06 and t07). The order of the secant stiffness for the 1st set of two cycles is 305KN/m whereas for the large cycle it is 210KN/m. The secant stiffness for the second set of repeated cycles is only marginally lower than the first and can be explained by the fact that at this low amplitude the axial load is sufficient to close any previously opened cracks.

From the strain gauge data along the North and South sides of the tower, as shown Figure 96, it is possible to appreciate the strain asymmetry caused by having the concrete filler between the FRP skins. In general the strain level is in compression as the axial force component is dominant and so all the strain signals are offset. The cyclic excursions in the tensile and compressive directions are of the same magnitude indicating that due to the level of the axial force and the general low moments applied: the concrete is providing most of the load carrying capacity both in tension and compression.

The distribution of the strain at on the inside of the tower and at the intermediate joints is shown in Figure 97. We note that the internal gauge positions (1,2,3 and 4) have been shifted nearer the base of the tower with the scope of monitoring any eventual local buckling or delamination between skins and core. It is noted that at this load level, (noting the small axial offset) the cycles are reasonably symmetric in the compression and tension cycles: this implies that the overall tower section is not noticeably cracked, however it is noted that gauge 5, which is on the border of the intermediate zone, is higher than gauge 6 (placed in the solid FRP area) and the cycles are not symmetric, indicating a cracked or damage section on the other side of the tower when in tension. Conversely on the other side of the tower (South) the peak in the monolithic area is higher than at the transition stage which is more consistent with the strain distribution from a high modulus core to the, softer, FRP area. These irregularities may show up at such low loads as they heighten imperfections in the concrete section perhaps as a result of pouring that show up as anomalous strain distribution ain the skin material.

The hoop, shear and steel flange strains (Figure 98, Figure 99 and Figure 100 respectively), are as expected nearly one order of magnitude smaller than in the main principal direction. Finally from the strain gauge ring at the base it the variation of the neutral axis is shown in Figure 101.

The displacements along the tower are given in Figure 102 following the same nomenclature and arrangement of the figures as given in the section dealing with the monolithic tower. The overall displacement field −given as the sum of the displacement transducers on the North and South faces indicate to a general symmetric behaviour and that the average strain field over the length of the tower is in agreement with the typical axial strain measurements given above.

The overall longitudinal displacements measured from the concatenated transducers on the North and South faces, as shown in Figure 102, agrees with the typical strain measurements described above, the effect of the axial load accounts for the offset between compressive and expansion cycles.

The displacement channels between the tower base and the steel anchorage plates and the base (1,8,15) and top (7 14 and 18) are of the order of 0.1 mm with no indication of slack (presumably as a result of the tight interference between the tower base and the steel ring connector).

8.3   Intermediate level tests:t05

Following on from the low level tests the tower was subjected to a displacement path as shown in Figure 103. Whereas in to4 the peak cyclic loads had not exceeded the compressive axial load, for this case the combined moment applied is sufficient to cause considerable cracking. From the hysteresis cycles shown in Figure 104 it is noted that the repetition of the two small cycles following the larger results in some degradation (secant stiffness for 1st cycles 180KN/m compared to 135KN/m for the second batch). Essentially the two green cycles are stiffer than the two black. However the repetition of a cycle at given amplitude does not result in an increase of damage. It is expected that the normal working regime of the tower would be in

the range of the small cycles, thus the tests indicate that having performed a large cycle in the near limit case, the tower will have incurred further cracking but will not continue to incur further damage when it returns to the lower load levels associated with the typical working regime.

The stiffness of the first two cycles at an equivalent amplitude of ~0.07 m (i.e. at 16 m height) is somewhat lower that that large cycle of t04, whose secant stiffness was given before as 210KNm. This is consistent with the fact that the amplitude for that cycle was only 0. 025m and hence it is expected to have a moderately higher secant stiffness.

The manner of the longitudinal strain distribution (Figure 105) in this load range has also changed considerably. It is clear now that the structure is behaving much like a standard reinforced concrete element, in such a manner that the strain in the compressive cycles being much lower than the tensile: this is simply a result of the much higher modulus of the concrete core compared to the FRP. The effect of the new cracking induced by the large cycle can be seen in the manner of the strain distribution: the first two small cycles having a strain distribution different from the last two, indicating that new cracked surfaces have been generated by the previous large cycle. The tensile strains at the gauge stations nearest the base of the tower (21 and 33) are of the order of 2%, however during the tensile loading on the North face gauge 21 suffers a discontinuity although the strain gauge itself still seems to be active. It was later discovered that the projection of the outer skin into the joint area nearest this gauge might have delaminated from the main body of the monolithic part of the joint around the bolt area. This might then have resulted in the slippage of the spliced skin material from the from the monolithic joint area with the consequent discontinuity in strain measured at gauge 21.

The strains at the inner surfaces and intermediate joints -as shown in Figure 106- follows from the remaining longitudinal gauges. The transition from the hybrid area to the monolithic FRP intermediate joint is well defined: essentially the tensile stresses on the FRP in the concrete filled area must be higher than in the monolithic joint area that follows it. Thus on the North side the tensile strains are higher just before the skin ends (5) than at the monolithic section of the joint (6), likewise on the South side the tensile strain on the skin (7) just before the monolithic section is also higher than the thicker monolithic section (8).

The hoop strains, as shown Figure 107, are markedly different in nature to the corresponding ones in the previous low-level test. This may be due to the fact that as the concrete fails in tension some of the transverse load normally taken up by the concrete is transferred to the skins (see for example channels 23 and 26. This phenomenon is repeated in the shear strain measurements, Figure 108, such as in $\gamma xz22$ shear where an apparent high shear strain is measured as a result of the second peak in the large cycle. Finally from the strain gauge ring at the base it the variation of the neutral axis is shown in indicatively in Figure 110.

The displacement channels along the tower length Figure 111 reflect the hybrid nature of the tower, and so, in accordance with the corresponding strain data the compressive displacements (as before positive displacement implies a shortening or compression) are considerably smaller than the tensile. The slack in the attachment joints was quite modest as seen from channels 8 1 and 15 (tower base) and 14,7 and 18 at the tower mid-section, in only one case barely exceeding 1 mm.

8.4 High level tests:t06

This test along with t05 preceding and t07 afterwards can be considered as a single event in the sense that there was no resetting of the boundary conditions between tests; thus after the completion of series of cycles in t05 (Figure 103), the loading protocol file for t06 and t07

(Figure 112 and Figure 121 respectively) were applied without resetting the position of the pistons nor unloading any of the offset loads (including axial) resulting from t05. Thus the data treatment for the start of t07 matches the last data points of t06, which, in turn, starts off from the last point of t05.

The hysteresis loops for t06 and are shown in Figure 113. The equivalent secant stiffness of the first batch for the small amplitude (~0.14 m) cycles is 129KNm, which matches the value from the last batch of small-amplitude cycles from t05 which were performed at a approximately half the amplitude (~0.07 m). The application of the large cycle in a base-moment of 0.9MNm which is considerably above the 0.72MNm that would result from the extreme gust event. Upon repetition of the smaller amplitude cycles (black dots) it would seem that even at this level of loading, the structural properties (i.e. the secant stiffness defining the natural frequency of the tower) for normal working conditions have not been severely affected.

The apparent width of the hysteresis loops is less that in test t05, this is due to the fact that the effect of the friction force on the swivels is reduced in proportion to the overall load. The degradation in the secant stiffness due to the repetition of the two small-amplitude cycles is more apparent in the force-displacement plane than in that of the moment-curvature plane, in both cases it is not possible to claim a noticeable degradation even at these high load levels.

The strain gauge records in the longitudinal direction (see Figure 114) reveal that at peak load the strains are of the order of 0.55% indicating that near stress concentrations at anchorage points, the failure strain may not be far off. The general strain levels were higher than expected indicating that the material properties of the FRP were much lower than expected based on the material lay-up and configuration requested from the manufacturer. In fact by performing an equivalent static analysis based on the weighted average of the longitudinal strain gauge ring around the tower base (24, 27, 30, 3, 39 and 42) the modulus of the FRP in the longitudinal direction was calculated to be of the order of 12GPa, whereas the expected value should have been 25GPa. It will be shown below that this was due to an inappropriate lay-up and manufacture that resulted in FRP skins having a low volume fraction of fibre (of the order of 40% rather than 60% requested) and a reduction in the number of longitudinally oriented glass-fibre mat whereby only two out of the three layers were effectively in place.

Likewise the internal and intermediate joint strains as shown in Figure 115 reveal the effect the concrete has on the strain distribution on the tensile and compressive faces, thus the strain gauges placed over the monolithic FRP part of the joint have lower tensile stresses than those nearer or on the hybrid part whereas on the compressive side the strains in the monolithic FRP section are higher. The hoop and shear strains (Figure 116 and Figure 117 respectively) show increasing levels of complexity as the extension of crack opening generates local skin stresses. From the strain date at the ring section the position of the neutral axis is shown in Figure 119.

The displacement transducers Figure 120 confirm the overall aspect of the strains along the tower axis. The average strain field obtained by the concatenated displacement signals on the North and South side of the tower is of the order of 0.3% which is in agreement with that obtained from the strain gauges, confirming the reliability of the data obtained from both cases.

8.5 Final tests:t07

The loading protocol was modified to include two preliminary cycles at low amplitude followed by a monotonic ramp up to failure as shown in Figure 121. The axial control on the forces functioned adequately although as was the case for t06 when the load demand on P2 and P3 increases there are some oscillations in the control of constant axial load. This was most

probably due to the high latent oscillations in the fluid-flow across the servo-valve demand on the two large pistons.

The hysteresis cycles for the loading curves are shown in Figure 122, the monotonic loading up to failure, shown in red, follows the two initial cycles, in green. Failure occurred at a moment of 1.15MNm i.e. with a safety factor of 1.6 on the maximum expected wind gust event.

From the longitudinal strain gauge data (Figure 123) it can be seen that the maximum strain at the base immediately before failure was of the order of 0.7% (gauge 33 was destroyed just before the failure of the specimen). The strain gauge on the corresponding compression side (gauge 21) was not operational and hence as a surrogate we can observe the compression in at station 24 just above from it along the tower axis, where the compressive strain is of the order of 0.125% just before failure: this would imply that the stress on the concrete would be of the order of 92 MPa. These levels contrast with the predicted strain levels obtained with FE calculations using material constitutive property models developed from laminate theory for the FRP and material data provided by the manufacturer for the concrete. It was stated in 8.4 that the FRP skin strains measured were not consistent with the expected modulus of 24GPa and that based on static equilibrium the modulus would have to be of the order of 12GPa. Thus even though the FRP modulus was only half the design value, the failure load was still in excess of that for ultimate design.

The longitudinal strains in the tower near mid-height gauge 18 at 0.3% is still of considerable magnitude however the strain drops considerably on gauge 15 because it is placed further along just at the border of the monolithic joint area at the mid-section joint. The strains on the inside and intermediate joint, as shown in Figure 124, reflect the general trend for the remaining longitudinal strains; however some interesting effects can be seen in the hoop strains, Figure 125, most notably gauges 35 and 41 whereby a sudden drop in absolute strain occurs near point 700 although complete failure did not happen until near data point 750. Hoop and shear strains are shown respectively in Figure 126 and Figure 127. The position of the neutral axis is shown in Figure 128.

From the displacement data graphs, Figure 129, it is possible to monitor the overall displacements along each side of the tower, noting that on the south side the total elongation was in the range of 35 mm equivalent to an average strain of 0.43% whereas the compression displacements were barely a quarter as much. From the photographs shown in Figure 138 to Figure 144 it is possible to gain some insight into the manner and causes of the failure. In all cases it can be seen that the effective volume fraction of the unidirectional fibres in the main tower axis was low, hence it is to be expected that the measured axial modulus was much lower than expected, and, in consequence, the ultimate strength. It can be seen how the skins were pulled out from the boltholes and it is presumed that most of the load would have been taken directly by the skins as a result of slippage caused by the delamination between these and the main FRP monolithic core; this is shown clearly in Figure 143 for example.

8.6 Conclusions

The hybrid tower design would meet both the serviceability and limit load design criteria, however the experiments indicate that the quality assurance during the production stages did not meet the production order.

The lay-up and fibre volume fraction of the skins was not sufficient to guarantee the generation of the required material properties. Upon inspection of the failure surfaces it was concluded that the number of unidirectional mat layers that were supposed to provide the required longitudinal reinforcement were only two in number whereas three layers per skin were specified. The volume fraction of the unidirectional material itself was less than the 60%

volume fraction requested; it was thought that this was due to the separation of the fibre tows as it was wound onto the cylindrical form.

The shear transfer between the concrete and the inner and outer skins was very poor. In fact there was little if any possibility for shear key locking between concrete, because either the concrete was sealed off from the skin surface by the corrugated polycarbonate shell separator or the surface roughness of the skin itself was insufficient to provide shear lock.

These defects affect not only the ultimate strength of the tower but also the natural frequency, thus it is expected that if the tower, in spite of the deficiencies encountered in material quality and production, can meet the structural requirements then there is scope for optimisation of by reducing the effective tower wall thickness.

The base moment at failure was 1.17 MNm which provides a further material safety factor of over 1.6 given that the peak wind gust including safety factor would generate a moment of 0.72MNm. However had the FRP material modulus been at best only equal to the monolithic tower then the safety factor would go up to 2.5. In the event of manufacturing FRP skins to the 24GPa prescribed the safety factor could be as high as 3.25.

Concerning the frequency it is possible to define the frequency in terms of the equivalent section modulus for a given amplitude range. The equivalent modulus is a hypothetical concept that assumes that all the tower section is un-cracked and that the total thickness of the section includes both concrete and FRP skins (i.e. 25 mm). If the tower oscillates within a certain amplitude range it is assigned an equivalent modulus; the frequency of oscillation of the tower is obtained from the equivalent modulus and the geometry and weight of the tower plus dead load (assuming 50 tones at top). Based on the experimental data the frequency of the tower in the high amplitude regime (extreme wind gusts) would be of the order of 0.41 Hz. Based on the simplified analysis described in Section 10 and assuming the modulus of the FRP were to be 24GPa, the natural frequency would be of the order of 0.48 Hz.

9 Photogrammetry displacement monitoring

This section describes a photogrametric monitoring method based on the use of a CCTV camera system linked to the general data acquisition set-up used in the experimental tests discussed in the preceding sections. The method is presented as a means of monitoring *a posteriori* the 2D displacement field of the tower module during the test. The method, at present, is not as accurate as the individual displacement sensors used at the local level, however, the versatility of target selection and the fact that it is a non contact, makes it of great interest for it has the potential to monitor displacement fields of large structures accurately, and hence, it may be used to measure the displacement of full-scale structures such as the proposed destructive test on the 50 metre tower. The example shown below concern the final test on the hybrid tower.

9.1 Camera positioning and pre-processing of the video images

The camera was positioned at the top of the reaction wall, approximately 17 m above the laboratory ground. The tube and all its actuators were completely in the field of vision. With this set-up, a pixel corresponds approximately to 1.5 cm, but due to the inclination of the optical axis with respect to the laboratory ground, this scale varies with the position in the image and the effective distance z of the physical points to the ground (see Figure 39).

The video camera used in this study is of a common type and has noise. Thus the video images were filtered along time through Haar wavelet analysis, which permitted to eliminate part of the small-scale noise polluting the sequence.

9.2 Determination of physical frame

The sequence of video images was taken from an oblique point of view. To convert pixel coordinates to laboratory coordinates, it was necessary on one hand to have the elevation of each point of the image in the laboratory frame, on the other hand to calibrate the camera position and internal characteristics. This was made possible by using reference points on the laboratory ground (yellow circles in Figure 39). These points have been used to calibrate the camera intrinsic and extrinsic parameters.

To illustrate the effectiveness of the calibration, the image points (in pixel coordinates) of vertical lines passing through specific points of the laboratory have been computed from the calibration data, and plotted on figure 1. One can see that the results are satisfying.

In the following, we will consider that the targets on the top generatrix of the cylinder are at a constant distance from the ground during all the experiment. In this way, their physical position in laboratory space could be computed.

The displacement of particular points (see Figure 39) on the images was evaluated through covariance between successive video images. The successive positions of these points on the images were used to compute the best transformations between the first image and the successive images along time. Thus, the temporal series of transformations T_n permits to pass from any point of the cylinder on the original image to its corresponding displaced point at a given time. To check the validity of this method, a comparison with the reference Heidenhain displacement sensor (a 2 micron resolution digital encoder placed at the top of the tower loading plate) was made.

9.3   Comparison of optical measurements with Heidenhain sensor

The attachment point A of the Heidenhain is shown in Figure 39 (cyan circle) in which the Heidenhain is indicated by a green dotted line. The elongation between a fixed point on the Heidenhain and the attachment A is measured at each time by computing the successive displacements of A, as obtained through the successive transformations T_n. The temporal plot of the Heidenhain sensor and of the optical measurement is shown in Figure 40. The curves are apparently superposing. However, the difference between each signal (see in Figure 41) reveals the summation of three different types of errors: a cyclic error synchronised with the basic phases of the Heidenhain signal, an error at shorter frequencies, with a cyclic pattern of which amplitude is approximately 1 to 1.5 mm peak to peak, and a random error. The first type of error could be related to inaccuracy of the calibration, or to the method used to model the Heidenhain (this has been shown sensitive). The second type of error could be related to the intrinsic error of the covariance method that would not have been completely smeared out by the evaluation process of the T_n. Improving some experimental set-up and refining models could probably reduce the effect of these two types of error. The third type corresponds to the intrinsic error of the optical method, and to the noise of the video camera. The overall error is 2 mm at maximum, which is quite satisfying if one consider that the local scale on point A is 1.4 cm per pixel.

9.4   Comparison of optical measurements with Gefran sensors

Some supplementary comparisons have been done with sensors 16, 17 and 3, 10 (see yellow indications in Figure 39) and show a pretty good agreement (Figure 42, a, b, c & d). The displacement of the extremity nearest to the wall of bar 10 is approximately the sum of sensors 8 and 9. This has been used for comparison with optical method, on figure 4 e. The same has been made with respect to bar 3, and is shown in figure 4 f. In analysing these data one can see that some offsets appear on the sensor signal (Figure 42 b, d & e). If these offsets are not taken into account, the error varies from 1 mm (e.g. Figure 42 c) to 2 mm (e.g. Figure 42 e). Even in the case when the noise of the optical method is high, the general trend is followed (Figure 42 e & f). The variability of the noise could be linked to the various patterns that are followed to evaluate the covariance, as its quality varies with the optical properties of the patterns.

9.5   Deformation profiles

The temporal deformation profiles have been computed from points regularly spaced on the top generatrix of the cylinder. These profiles are plotted in Figure 43, for the sequence going from point 470 (A) to 534 (B, see Figure 40). Given any generatrix on the cylinder, it is possible to compute the displacement on this generatrix (with the hypothesis of constant coordinate z during all the experiment). This could be used for comparison with numerical results.

9.6   Conclusion

The object under study was viewed from a distance of 17 m, and the optical resolution obtained in this experiment is less than 2 mm for a pixel size of 14 mm. This is already a good result if one considers the low-grade video camera that has been used in this study (the wavelet filtering has already improved the results). This is a technical problem that could find a solution in the use of the Icam camera, now available for optical measurements.

The main advantages of the optical method which are illustrated here are, among others:

- The absolute calibration that can be done on the experiment. To improve it, one needs a set of accurate reference points, clearly visible on the image. A framework of reference points in the

laboratory should be set-up so that direct calibration of the cameras could be accomplished, with a sufficiently good accuracy.

- The possibility of measuring the displacement of any point appearing in the sequence of images (if its visibility and sharpness are sufficient). This opens the possibility to make a posteriori measurements in a place were no conventional sensor was positioned.
- The access to 3-D information, whether by using a set of cameras (stereo-vision), or by having an a-priori knowledge of one coordinate (as in this case).
- The possibility to deliver measurements on regular mesh, so that direct comparison with numerical models could be easily done.

The weakness of the covariance method has been compensated by a second processing stage that consists in a best fit of a transformation family T_n to the sequence of video images. The result will obviously depend on the characteristics of the transformations and a careful use of this second stage should be done.

One could envisage doing photogrammetry in open-air, but the trade-off would be a reduced accuracy of the method unless a good calibration could be done in place.
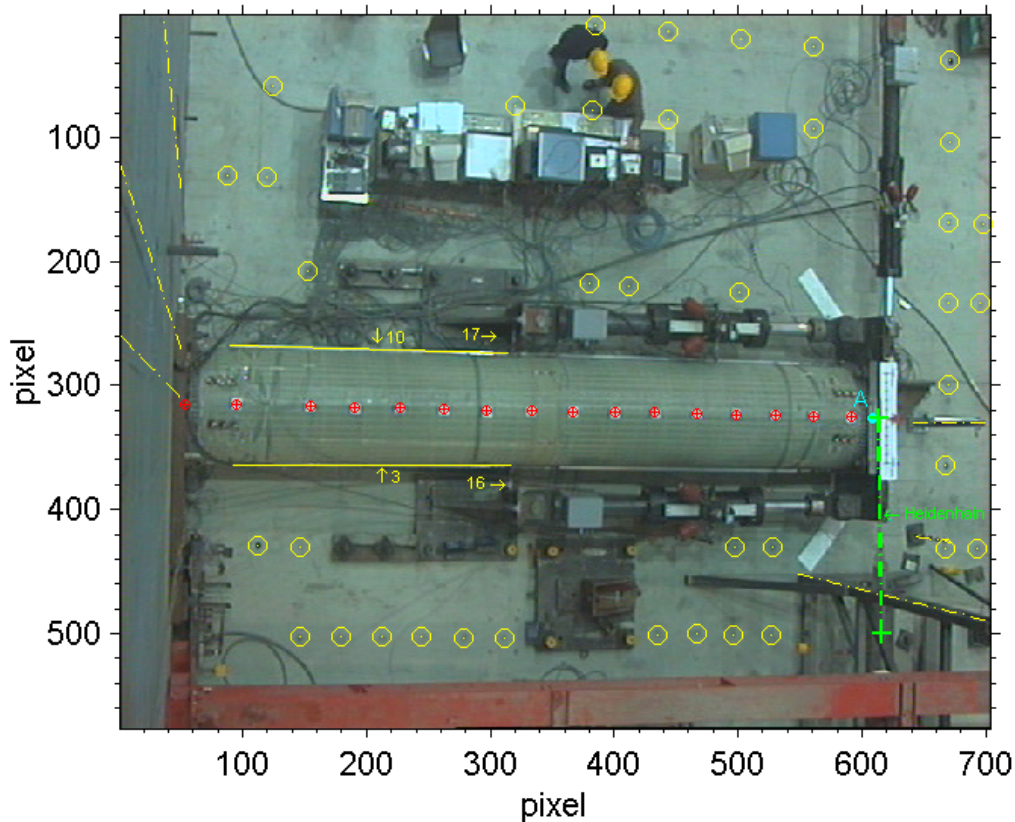
Figure 39: Top view of the experiment. The reference points are the yellow dots inside the yellow circles. Note that the yellow dotted vertical lines, which are directly computed from the calibration of the camera, are in good agreement with vertical object like poles, or vertical patterns on the reaction wall on the left. The red circles indicate the target used to initiate the evaluation of the transforms T_n. The attachment basis A of the Heidenhain is show in cyan, while the green dotted line is the Heidenhain axis. Positions of sensors 3, 10, 16 and 17 are indicated in yellow
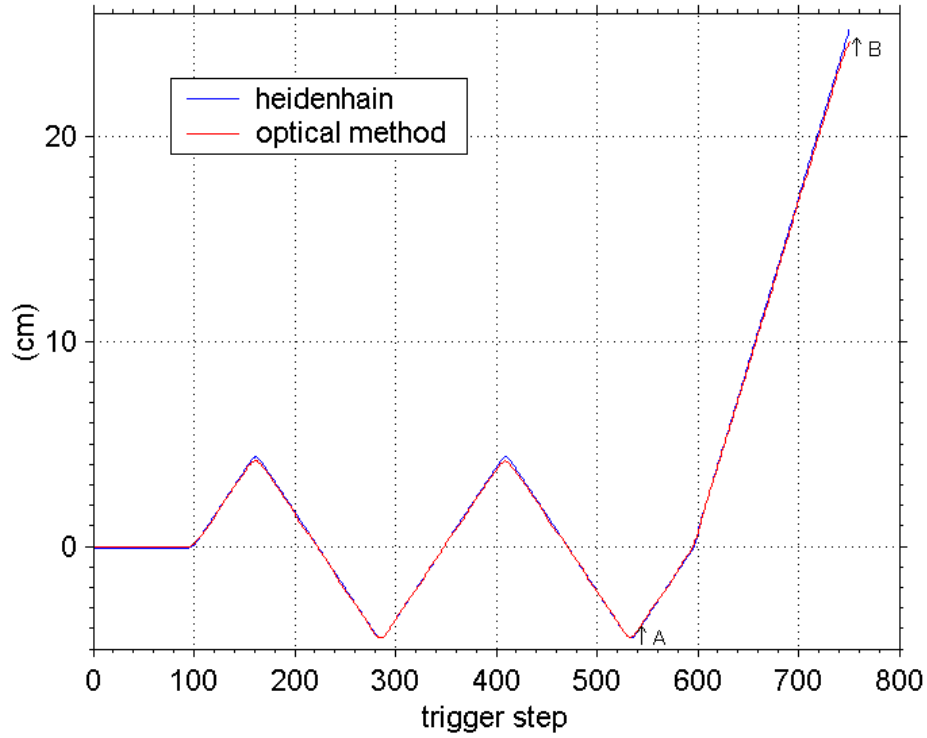
Figure 40: Temporal plot of Heidenhain and optical measurement. See in Figure 43 for meaning of points A and B.
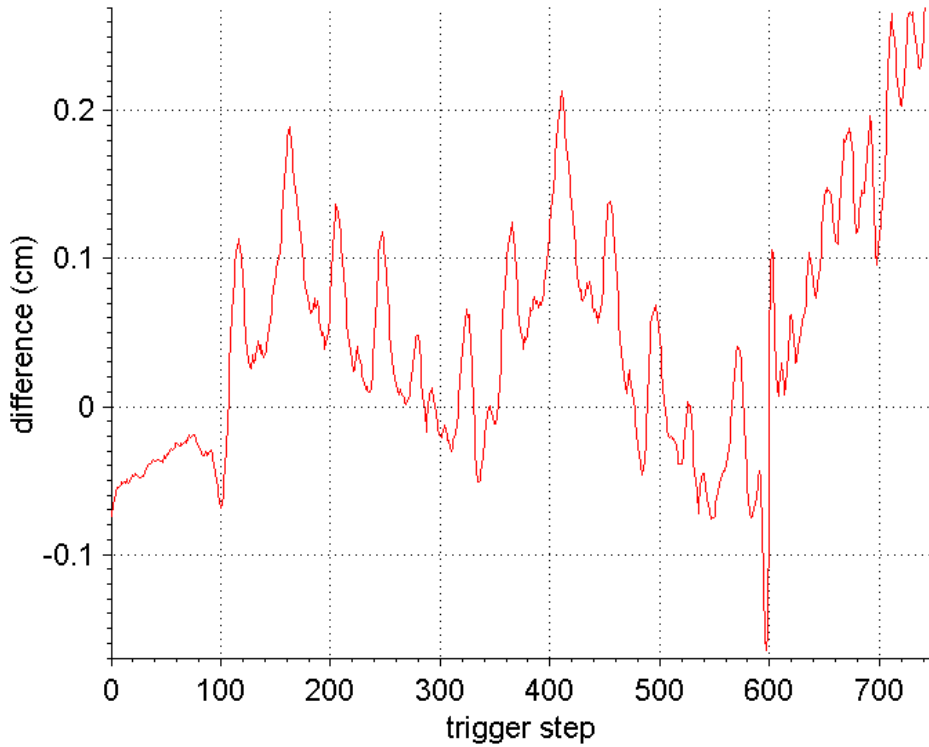
Figure 41: Difference between Heidenhain and optical measurement.
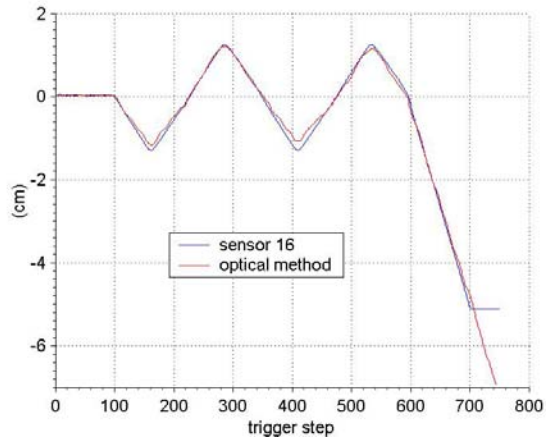
a Lateral displacement of basis part of the tube, south side
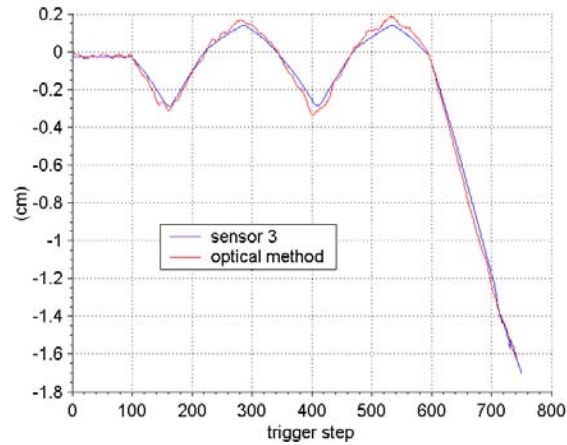
c Elongation of basis part of the tube, south side
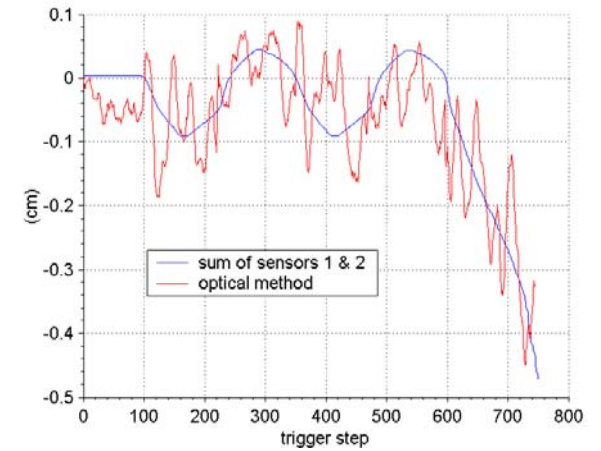
e Distance between the common anchoring point of sensor 2 & 3 and wall, south side
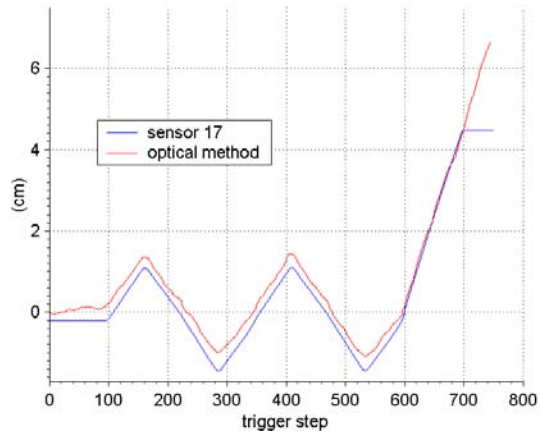
b Lateral displacement of basis part of the tube, north side
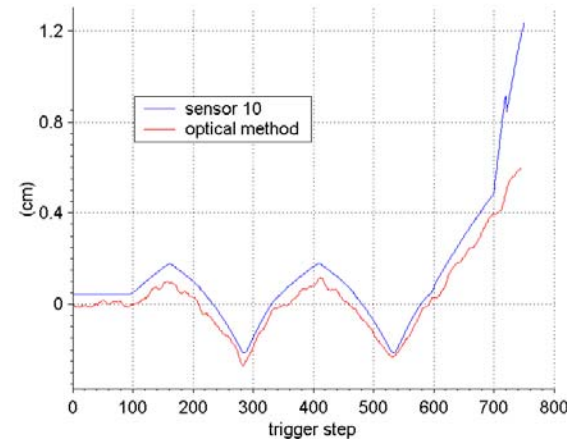
d Elongation of basis part of the tube, north side
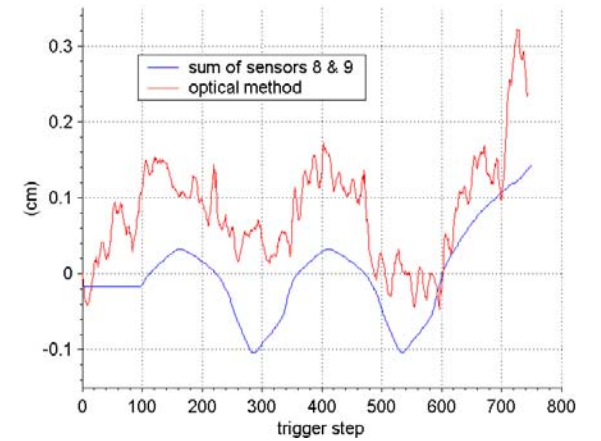
f Distance between the common anchoring point of sensor 9 & 10 and wall, north side

Figure 42: comparison of some extension sensors with the optical method. On a and b, at the end of the experiment, the mechanical sensors are disconnected while the optical method still gives measurements. On e and f, the optical method follows the general trend, although its noise is approximately of 2 mm.
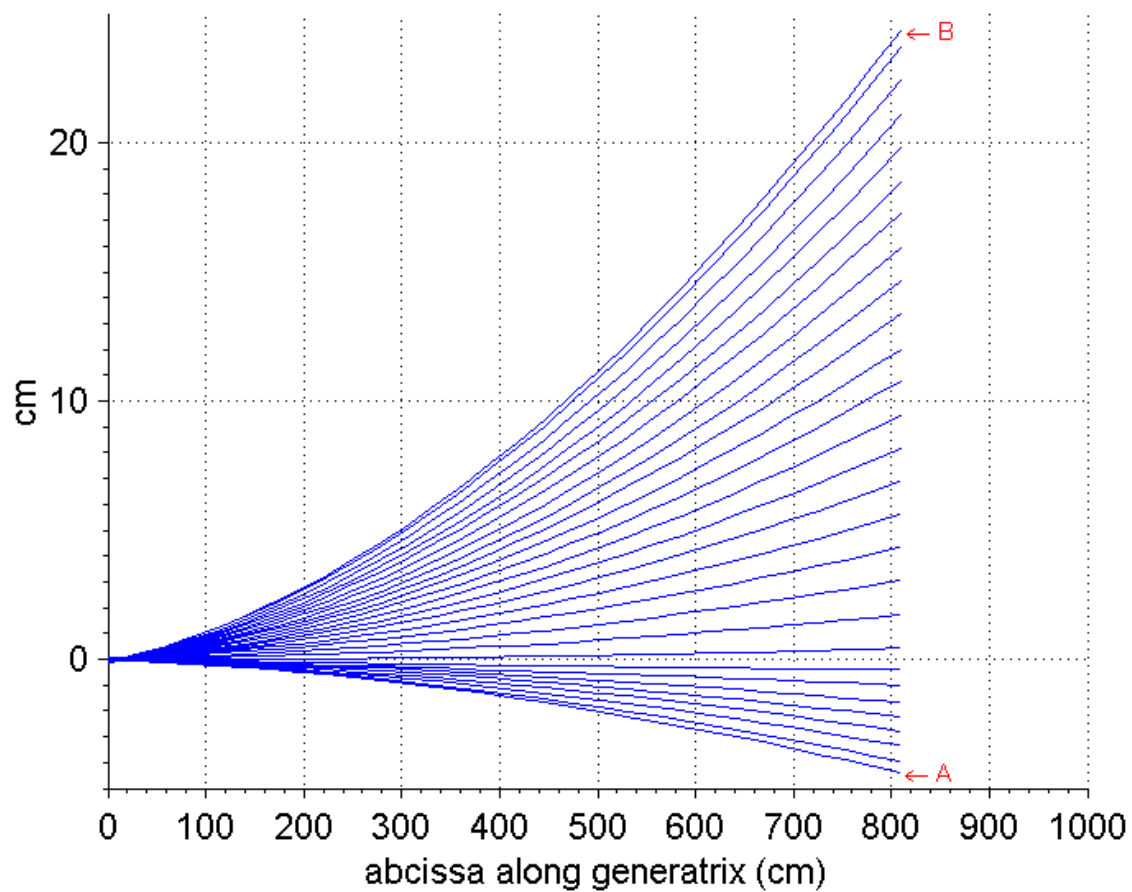
Figure 43: Deformation profiles of the top generatrix of the cylinder, as obtained from optical method. This is on the period AB as indicated in Figure 40.

10 Simplified calculation of the tower shaft stiffness and frequency

The tower shaft stiffness and frequency is computed in the following, using plane section theory and integration of the section stiffness along the height of the tower.

The stiffness of the section is computed based on a fibre model, discretising the concrete and fibreglass materials into a radial distribution. The stiffness and strength properties are given to each material, and the corresponding curvature and elongation are computed as a function of the forces acting on the section.

Cracked and gross properties are computed for each section and the corresponding effective properties are derived. By integrating the section properties over the length of the shaft the global stiffness is derived, which, together with the mass of the tower and of the turbine, permits the calculation of the frequency of the structure.

10.1 Fibre model

The section of the tower is made of a circular ring of concrete of 3.5m diameter with a thickness of 50mm, encircled by two rings of fibreglass of 15mm thickness each. The cross section is disretised into fibres, following a radial distribution with a step of 1 degree. The concrete core fibres are located at a radius of 1.75m, while the inner and outer fibres are located at a radius of 1.718m and 1.783m respectively, consistent with a 3.5m diameter of the tower section.

The geometric centre of each fibre is hence computed, resulting in one fibre for the concrete core and two fibres for the inner and outer rings of fibreglass at each degree fan, for a total of 360 fibres of concrete and 720 fibres of fibreglass, with the following cross sectional areas:

Concrete core fibres:	$A_{cf} = 15.272\text{cm}^2$
Total concrete core:	$A_c = 5498\text{cm}^2$
Fibreglass fibres:	$A_{gf} = 5498\text{cm}^2$
Total for each fibreglass ring:	$A_g = 1680\text{cm}^2$

The material properties of each fibre are described by the modulus of elasticity in the tension and compression branches:

Fibreglass:	$E_g = 29\text{Gpa}$	(tension and compression)
Concrete core:	$E_c = 73\text{Gpa}$	(compression)
	$E_c = 0\text{Gpa}$	(tension / cracked)

Based on plane section theory, the moment M and the axial force N developed by the section are computed as a function of the curvature φ and the elongation δ of the section with respect to its geometric centre. The procedure is explained in the following paragraphs.

For a given set of deformations φ and δ of the section, the deformation ε_i of each fibre i is computed based on the distance y_i of the fibre to the geometric centre of the section. The stresses σ_i of each fibre are then computed as the product of the fibre deformation and the modulus of elasticity E_i as a function of the fibre deformation. The moment and axial force

developed by the section are obtained by summing throughout the section the fibre stresses weighted by the fibre cross sectional areas A_i and lever arms y_i.

$$\varepsilon_i = \varphi \, y_i + \delta$$

$$\sigma_i = \varepsilon_i \, E_i(\varepsilon_i)$$

$$M = \sum_i^n \sigma_i \, A_i \, y_i$$

$$N = \sum_i^n \sigma_i \, A_i$$

The location of the neutral axis with respect to the centre of the section is:

$$N.A. = \frac{\delta}{\varphi}$$

After computing the curvature φ and the elongation δ, it is possible to compute the moment of inertia I and the area A of the section as a function of the concrete modulus E_c (value in compression):

$$I = \frac{M}{E_c \, \varphi}$$

$$A = \frac{N}{E_c \, \delta}$$

The procedure to compute the deformation of the section (φ, δ) as a function of the imposed forces (M, N) is iterative and has been implemented in an excel spreadsheet.

The properties of the composite section (I, A) are computed at six locations along the height of the tower, namely, at 0, 12, 24, 36, 48 and 50 metres from the base. At each section, the bending moment is computed as a function of the shear force V applied at the top of the tower, while the axial force is computed as a function of the weight of the turbine and of the tower. These forces are listed on considering a weight of the turbine equal to 500kN and densities of 2600 and 1850 kg/m^3 for the concrete core and fibreglass; the fibreglass density is further increased by 5% to take into account the larger thickness of connections.

Table 3 Load distribution along tower height.

Height	N	M
(m)	kN	(MN-m)
50	-500	0
48	-540	2 V
36	-794	14 V
24	-1035	26 V
12	-1275	38 V
0	-1515	50 V

The analysis of the section is carried out for five magnitudes of the shear force V: 80, 160, 240, 400 and 800 kN. For each shear force, the position of the neutral axis, the curvature, the elongation, the moment of inertia and area of the cross section, and the maximum and minimum stresses developed by the concrete core and fibreglass fibres are computed and presented in Table 4 through Table 8.

Table 4 Structural properties at 800kN.

V = 800 kN									
Height	**N.A.**	**curvature**	**epsilon**	**I**	**A**	**fiberglass**		**concrete**	
		/10000	/10000			σ min	σ max	σ min	σ max
m	m	m/m	m/m	m^4	m^2	Mpa	Mpa	Mpa	Mpa
50	-200.000	0.00	-0.101	1.043	0.681	0	0	-1	-1
48	-0.356	0.44	0.157	0.514	0.472	-2	3	-4	0
36	-0.757	3.85	2.913	0.398	0.037	-11	28	-28	0
24	-0.783	7.29	5.712	0.390	0.025	-21	54	-51	0
12	-0.793	10.75	8.528	0.387	0.020	-31	80	-75	0
0	-0.798	14.18	11.320	0.386	0.018	-40	106	-99	0

Table 5 Structural properties at 400kN.

V = 400 kN									
Height	**N.A.**	**curvature**	**epsilon**	**I**	**A**	**fiberglass**		**concrete**	
		/10000	/10000			σ min	σ max	σ min	σ max
m	m	m/m	m/m	m^4	m^2	Mpa	Mpa	Mpa	Mpa
50	-200.000	0.00	-0.101	1.043	0.681	0	0	-1	-1
48	0.437	0.15	-0.066	0.754	1.129	-1	1	-2	0
36	-0.662	1.82	1.205	0.424	0.090	-6	13	-14	0
24	-0.719	3.48	2.501	0.408	0.057	-11	25	-26	0
12	-0.740	5.19	3.841	0.402	0.045	-16	38	-38	0
0	-0.750	6.85	5.139	0.399	0.040	-21	50	-50	0

Table 6 Structural properties at 240kN.

V = 240 kN									
Height	**N.A.**	**curvature**	**epsilon**	**I**	**A**	**fiberglass**		**concrete**	
		/10000	/10000			σ min	σ max	σ min	σ max
m	m	m/m	m/m	m^4	m^2	Mpa	Mpa	Mpa	Mpa
50	-200.000	0.00	-0.101	1.043	0.681	0	0	-1	-1
48	1.811	0.06	-0.109	1.043	0.681	-1	0	-2	0
36	-0.520	1.00	0.520	0.465	0.209	-4	7	-9	0
24	-0.626	1.97	1.233	0.434	0.115	-7	14	-16	0
12	-0.662	2.93	1.941	0.424	0.090	-10	21	-23	0
0	-0.683	3.94	2.690	0.418	0.077	-13	28	-31	0

Table 7 Structural properties at 160kN.

V = 160 kN									
Height	**N.A.**	**curvature**	**epsilon**	**I**	**A**	**fiberglass**		**concrete**	
		/10000	/10000			σ min	σ max	σ min	σ max
m	m	m/m	m/m	m^4	m^2	Mpa	Mpa	Mpa	Mpa
50	-200.000	0.00	-0.101	1.043	0.681	0	0	-1	-1
48	2.716	0.04	-0.109	1.043	0.681	-1	0	-1	0
36	-0.286	0.56	0.160	0.535	0.679	-2	3	-6	0
24	-0.502	1.23	0.617	0.470	0.230	-5	8	-11	0
12	-0.558	1.83	1.021	0.454	0.171	-6	12	-16	0
0	-0.589	2.45	1.443	0.445	0.144	-8	17	-21	0

Table 8 Structural properties at 80kN.

V = 80 kN									
Height	**N.A.**	**curvature**	**epsilon**	**I**	**A**	**fiberglass**		**concrete**	
		/10000	/10000			σ min	σ max	σ min	σ max
m	m	m/m	m/m	m^4	m^2	Mpa	Mpa	Mpa	Mpa
50	-200.000	0.00	-0.101	1.043	0.681	0	0	-1	-1
48	5.433	0.02	-0.109	1.043	0.681	0	0	-1	-1
36	0.548	0.20	-0.110	0.787	0.992	-1	1	-3	0
24	-0.011	0.47	0.005	0.618	26.632	-2	2	-6	0
12	-0.142	0.70	0.100	0.578	1.754	-3	4	-8	0
0	-0.251	1.00	0.251	0.545	0.827	-4	6	-11	0

It is important to note that the moment of inertia *I* computed in the above tables corresponds to the cracked moment of inertia. The gross moment of inertia can be computed independently of the acting forces as:

$$I_g = \frac{\left(D_{g\,inner}{}^2 + D_{g\,outer}{}^2\right)}{16}\left[2A_g\,\frac{E_g}{E_c} + A_c\right]$$

The value of E_c corresponds to that of concrete in compression, while $D_{g\,inner}$ and $D_{g\,outer}$ are equal to 3.436m and 3.566m respectively. From the above formula a value of 1.043 m^4 is obtained.

The variation of the effective and the cracked moment of inertia with respect to the height and the applied horizontal force is shown on Figure 44 and Figure 45. It is also possible to plot the variation of the effective and cracked moments of inertia as a function of the bending moments and the axial force acting on the section. These charts can be used as interaction diagrams for design and are shown on Figure 46 and Figure 47.
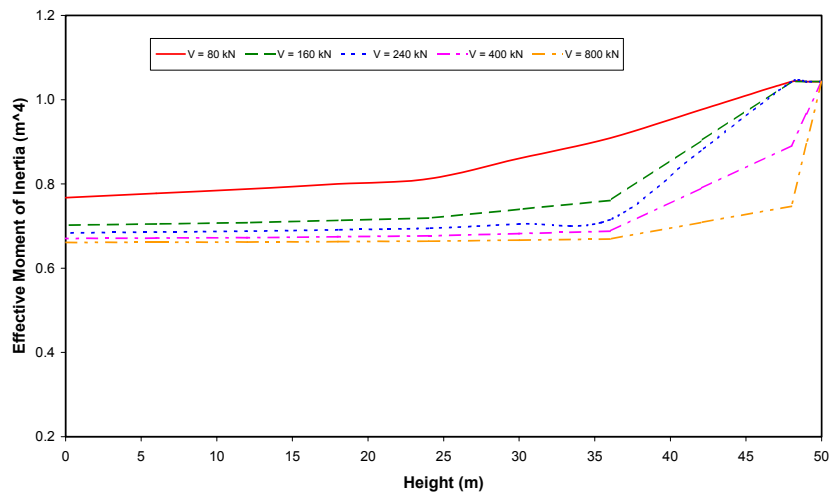
Figure 44 Variation of effective moment of inertia.
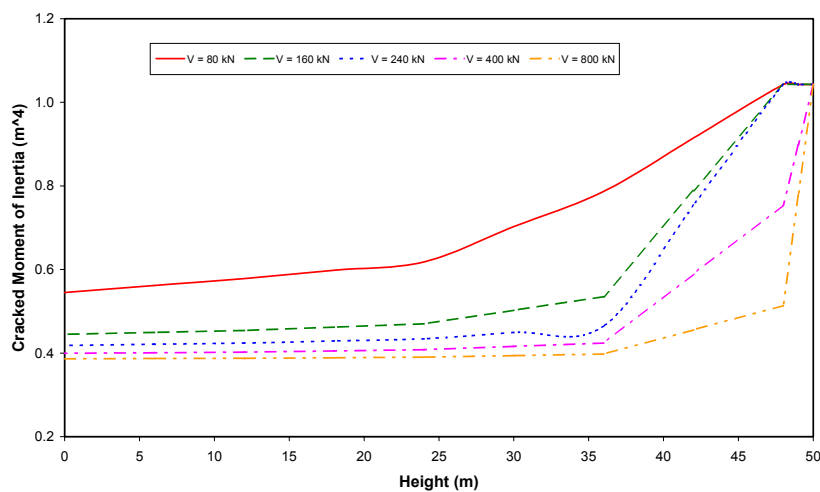
Figure 45 Variation of cracked moment of inertia.
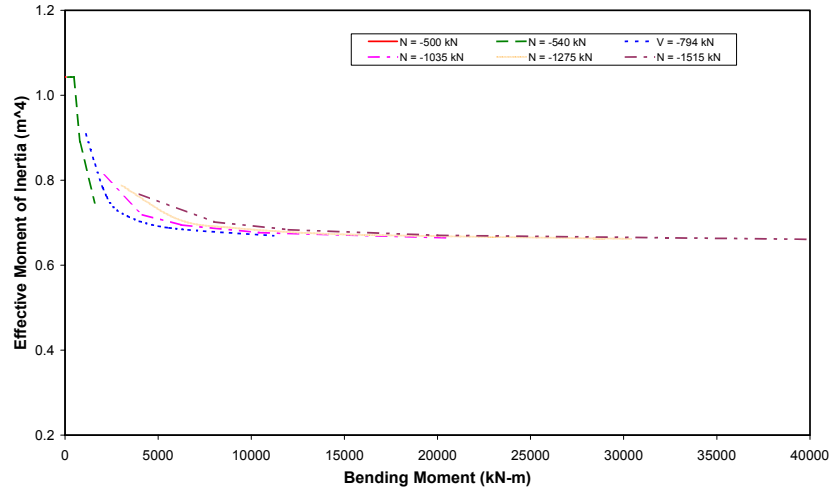
Figure 46 Effective moment of inertia interaction diagram.
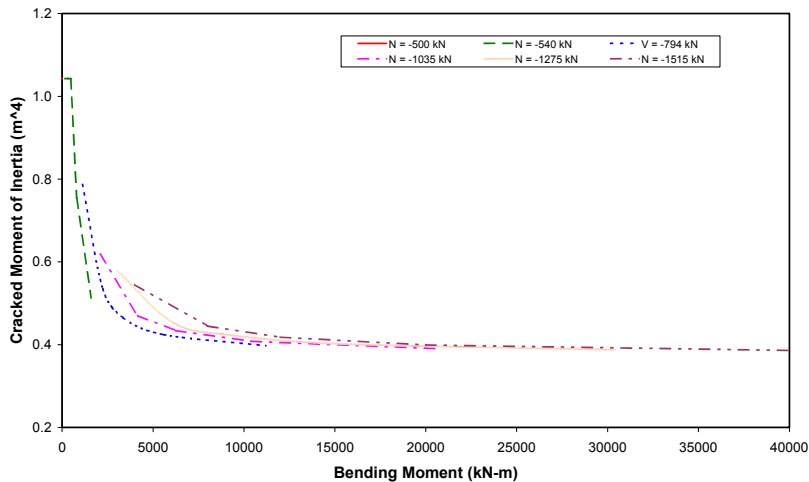
Figure 47 Cracked moment of inertia interaction diagram.

10.2 Tower stiffness and frequency calculation

The stiffness and frequency of the tower are computed by integrating the section properties throughout the height of the tower as a function of the applied forces. For this, a finite element model (FEM) is used, by dividing the tower into segments. Each segment is modelled with beam elements considering flexural deformations only.

The mechanical properties assigned to each beam element consist of a moment of inertia and an elastic modulus. The elastic modulus corresponds to that of concrete in compression E_c, while the moment of inertia may be gross (I_g), cracked (I_{cr}) or an intermediate value called the effective moment of inertia (I_{eff}).

The effective moment of inertia is computed from the sum in series of the linear variation of the moment of inertia between two cracks. The expression is as follows:

$$I_{eff} = \frac{N^*}{\sum\limits_{n}^{N} I_{cr} + \dfrac{i}{N^*}\left(I_g - I_{cr}\right)}$$

Integer N^* denotes the number of points considered in the calculation between the crack and half the length between the two cracks; a number of $N^*=20$ is considered in the calculations.

The number of segments considered in the FEM is equal to five, with the nodes in correspondence with the heights used for the calculation of the cracked moments of inertia of the section. For the segment, the average values between nodes are used. On Table 9, the cracked and effective moments of inertia are given as a function of the height and the applied shear.

Table 9 Stiffness variation as a function of load and height.

Nodal Height	Element Height	V = 80 kN Icr	V = 80 kN Ieff	V = 160 kN Icr	V = 160 kN Ieff	V = 240 kN Icr	V = 240 kN Ieff	V = 400 kN Icr	V = 400 kN Ieff	V = 800 kN Icr	V = 800 kN Ieff
m	m	m^4									
50		1.043	1.043	1.043	1.043	1.043	1.043	1.043	1.043	1.043	1.043
	49	1.043	1.043	1.043	1.043	1.043	1.043	0.898	0.967	0.778	0.895
48		1.043	1.043	1.043	1.043	1.043	1.043	0.754	0.891	0.514	0.747
	42	0.915	0.976	0.789	0.902	0.754	0.879	0.589	0.789	0.456	0.708
36		0.787	0.909	0.535	0.761	0.465	0.715	0.424	0.688	0.398	0.669
	30	0.703	0.860	0.503	0.740	0.450	0.705	0.416	0.682	0.394	0.667
24		0.618	0.812	0.470	0.719	0.434	0.695	0.408	0.677	0.390	0.664
	18	0.598	0.800	0.462	0.713	0.429	0.691	0.405	0.675	0.389	0.663
12		0.578	0.788	0.454	0.708	0.424	0.688	0.402	0.672	0.387	0.662
	6	0.562	0.778	0.450	0.705	0.421	0.686	0.401	0.671	0.387	0.662
0		0.545	0.767	0.445	0.702	0.418	0.684	0.399	0.670	0.386	0.661

The frequency of the tower is computed based on the assembled stiffness of the beam elements and on the assigned masses, one at the top and equal to 500kN/g, and a distributed mass equivalent to 2070 kg/m (31% fibreglass and 69% concrete) for the tower shaft. On Table 10, the first mode frequencies and the associated horizontal stiffness of the tower are given as a function of the applied shear force, considering the cracked and the effective moment of inertia distributed along the full height of the section. The upper bound of the first mode frequency is computed using the gross moment of inertia, obtaining a frequency of 0.777 Hz and a stiffness of 1810 kN/m.

Table 10 Effective 1st mode frequency as a function of load.

	V = 80 kN	V = 160 kN	V = 240 kN	V = 400 kN	V = 800 kN
	Frequency (Hz)				
w/ Icr	0.584	0.518	0.500	0.486	0.476
w/ Ieff	0.679	0.643	0.634	0.626	0.621
	Stiffness (kN/m)				
w/ Icr	1024	806	749	709	680
w/ Ieff	1382	1242	1205	1176	1156

The variation of frequency and stiffness as a function of the horizontal shear is shown on Figure 48 and Figure 49 for the cracked, effective and gross moments of inertia.
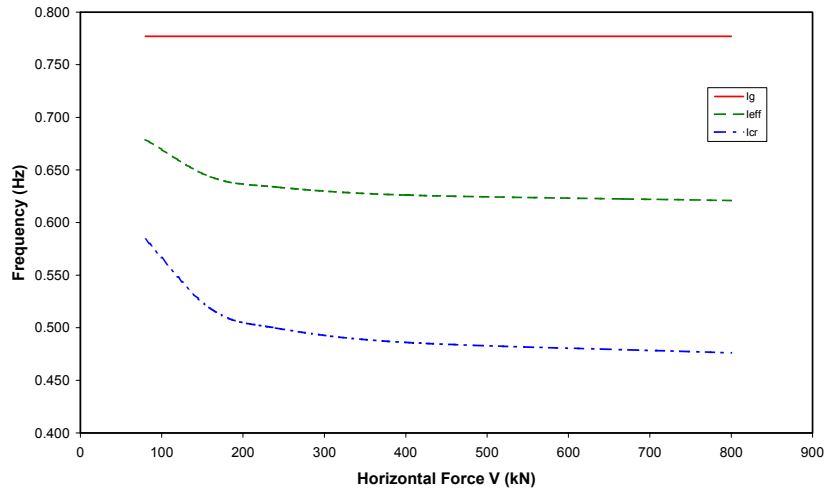
Figure 48 Frequency vs horizontal force.
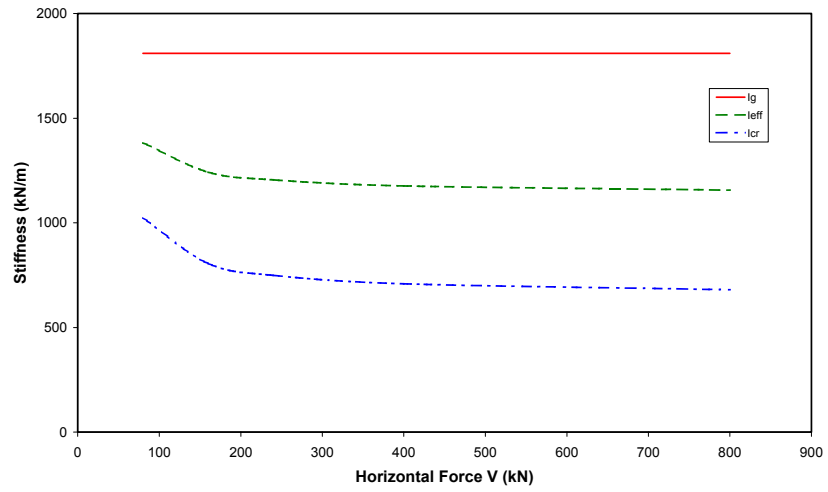
Figure 49 Horizontal stiffness vs horizontal force.

11 Finite Element Model

Two different Finite Element Analysis are described in the following section using the Visual Cast3 program, each FE model reproduces a tested specimen (monolithic and hybrid) the results are and then compared to the experimental data. These models are not intended as definitive but only as a first calculation aiming to know if simple common theories in Civil Engineering can be applied, after specific changes, to composite structures where material homogeneity does not exist. Finally guidelines of the design for the tower at full scale are provided in order to predict its behaviour during an extreme wind gust.

11.1 Model for the Monolithic Tower

The Mesh geometry for the monolithic tower is composed of a 8-metre cylinder of 1.1 diameter (Figure 10) with a rigid plate at the top used for application of forces (see Figure 32). The thickness is constant along the tower and is equal to 16.1 mm, except for the end and the intermediate joints where the thickness is 25 mm. The material is elastic and orthotropic: material properties are deduced from laminate theory through a stratification of $[UD\pm5°, FW\pm85°]_s$ and a volume fraction of 40%. Laminate values are reported as follows:

$$Q_{[UD\pm5°,FW\pm85°]_s} = \begin{bmatrix} 17.0 & 1.7 & 0 \\ 1.7 & 19.0 & 0 \\ 0 & 0 & 5.1 \end{bmatrix} GPa.$$

$$E_x = 16.9 GPa., \ E_y = 18.9 GPa., \ \nu_{xy} = 0.0915, \ \nu_{yx} = 0.1023, \ G_{xy} = 2.55 GPa.$$

where x is longitudinal axis and y is transversal axis. The density for glass fibre is taken as $1850 Kg/m^3$.
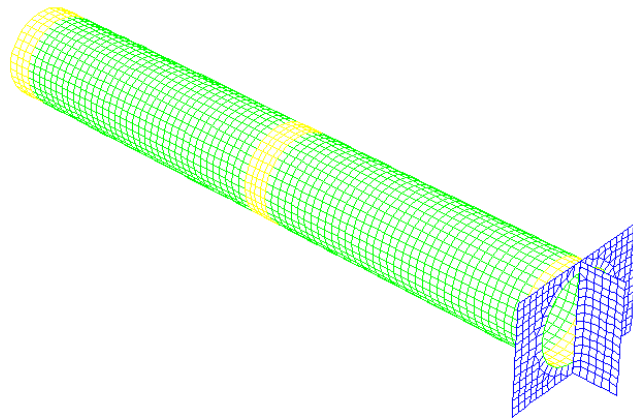
Figure 50 Monolithic tower FE mesh.

The elements used are 4-node shell elements with three degrees of freedom per node; the pitch of elements is 0.1 m. The mesh element is shown in Figure 50. The performed analysis is linear. The boundary conditions are represented by the lack of rotation displacement at the

base nodes as in the case of a cantilever. The measured piston forces are the loads used as input for the analysis; in addition, during the test the specimen in the laboratory was in the horizontal position so the dead load and the effective loads caused by the tower and nacelle mass have been applied to the history of loading by the lateral pistons as described above in section 6.3. The three piston load features are extracted from the FE for five specified position on the tower of the tm28 test (final test Figure 85).
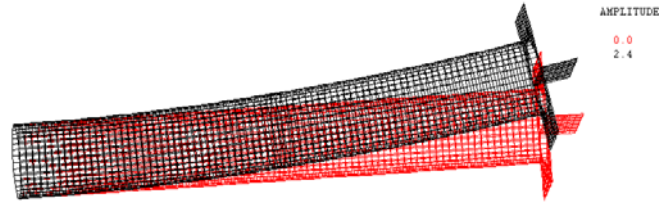
Figure 51 Deformation of the monolithic tower.

The combination of loads just before the failure in the experimental case is reproduced by the FE analysis shown in Figure 51 with displacement scale factor of 2.4. For the same combination of loads the longitudinal strain is shown in Figure 52, the peak values is *5.5mε* which is in agreement with the experimental data.
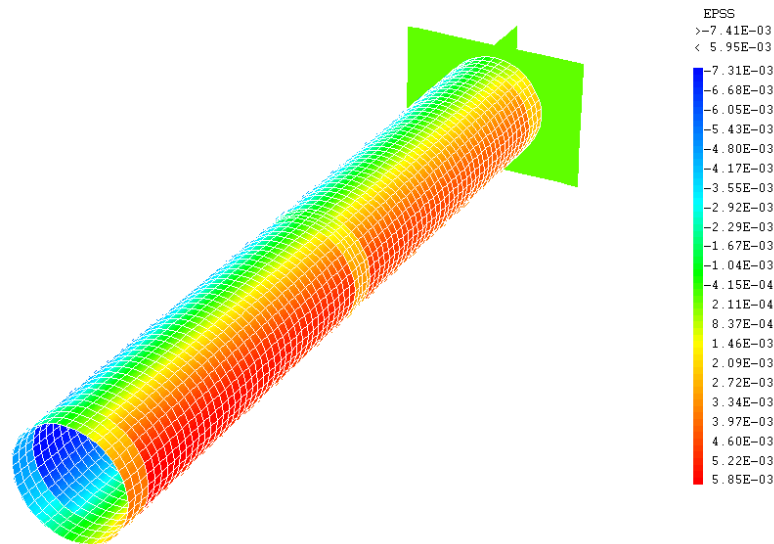
Figure 52 Longitudinal strains in the Monolithic Tower.

In Figure 53 the story of the top displacement (at 8 meters) for the experimental and analytical data are compared. In addition a subsequent analysis is considered based on simple equations of the beam theory to which the top displacement is given by:

$$\delta_{TOP} = \frac{V \cdot l_V^3}{3 \cdot EI} + \frac{M \cdot l_M^2}{2 \cdot EI} \quad \text{where } V = P_1 \quad M = P_2 \cdot 1 - P_3 \cdot 1 \text{ and } l_V = 8.56m. \ \ l_M = 8m.$$

For the calculation of the stiffness it is assumed that $E=E_x$ and $I=\pi R^3 t$.

In both methods for the final part of the tests the analytical data are different from the experimental. This is may be due to not considering the effects of second order due to the high axial force of 92 ton.
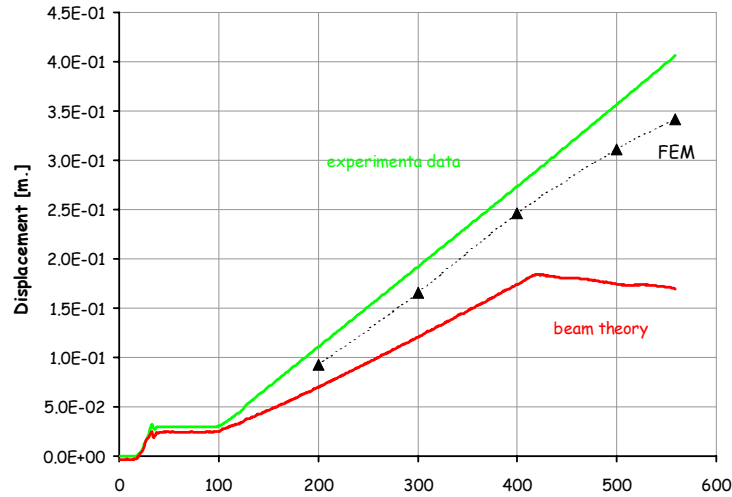
Figure 53 Displacement story at 8 meters versus data point acquisition. (Mono)

Using the equation $\chi = M/EI$ from beam theory the section curvature can be compared to the experimental curvature (see chapter 6.4).
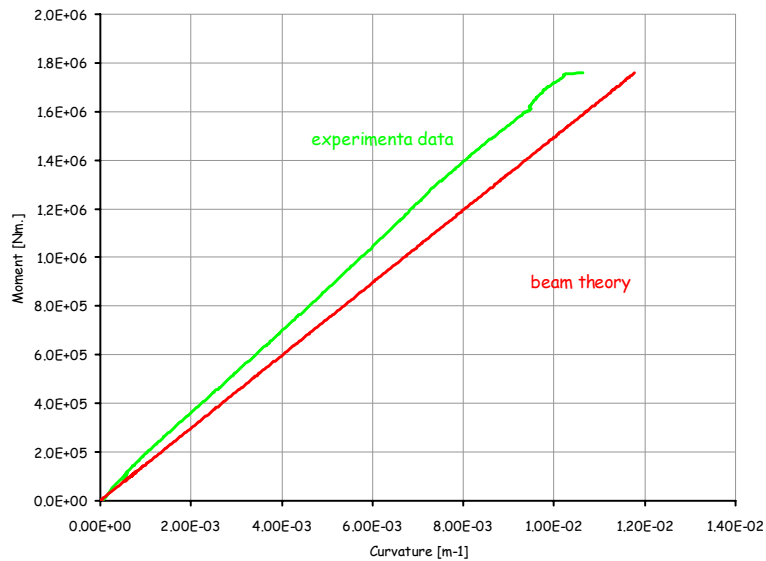
Figure 54 Moment versus curvature. (Mono)

The FEM model accuracy is very good, but even a simple beam theory can evaluate the displacement and curvature to reasonable accuracy, even when non-homogenous elements such as the presence of joints, a non isotropic material (as well as the small ratio between length and diameter) may be outside the usual range of classical beam theory.

11.2 Model for Hybrid Tower

To determinate the hybrid tower behaviour two models are used: a non-linear FEM and a piece-wise linear beam theory. As for the FEM model, the geometry is still an 8-metre cylinder of 1.1 diameter. The circular crown section (see Figure 12) is composed of two 5-mm glass fibre skins and a 18 mm concrete core. This section remains constant along the tower because intermediate base and top joints, are not considered. For the FRP an elastic orthotropic material is used, its properties are obtained from laminate theory with a stratification of *[UD±4°, 2FW±86°]ₛ* and a volume fraction of 40%. The numerical values are shown below.

$$Q_{[UD\pm4°,2FW\pm86°]_s} = \begin{bmatrix} 12.9 & 1.8 & 0 \\ 1.8 & 23.1 & 0 \\ 0 & 0 & 5.2 \end{bmatrix} GPa.$$

$$E_x = 12.7 GPa., \; E_y = 23 GPa., \; \nu_{xy} = 0.078, \; \nu_{yx} = 0.14, \; G_{xy} = 2.6 GPa.$$

For the concrete, given its high compressive capacity ($f_c=210MPa$), an elastic material linear in compression with a young modulus ($E=71GPa$) is used. In tension the non-linear Ottosen[1] model was used.
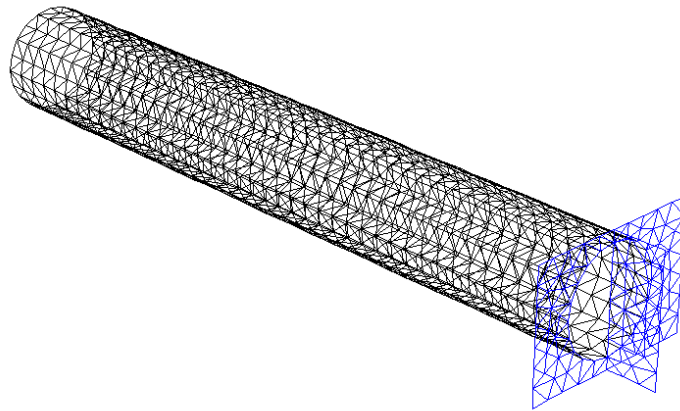
Figure 55 Hybrid tower mesh FE.

In Figure 55 the mesh is shown for which 3-node triangular shell elements and thin shell Kirchhoff's discrete hypothesis are used. This element is sufficiently numerically stable to model the concrete core using Ottosen's model, the element pitch is of 0.2 m. The model is composed of five levels of this mesh. They represent: the inside and outside glass fibre skin, a

[1] Smeared crack analysis using generalized fictitious crack model. Ola Dahlblom and Niels Saabye Ottosen. Journal of Engineering Mechanics, Vol 116, January 1990.

three-layer concrete core. The elements are radially connected, but during the experimental phase, slipping between concrete and the FRP laminate occurred, so that the transfer of tangential tensions was very limited. More accurate analytical results will not be obtained unless en element modelling the interface is developed.

The boundary conditions are represented by the lack of rotation displacement at the base nodes as in the case of a cantilever. The loading protocol is that used in test ts07 (Figure 121).
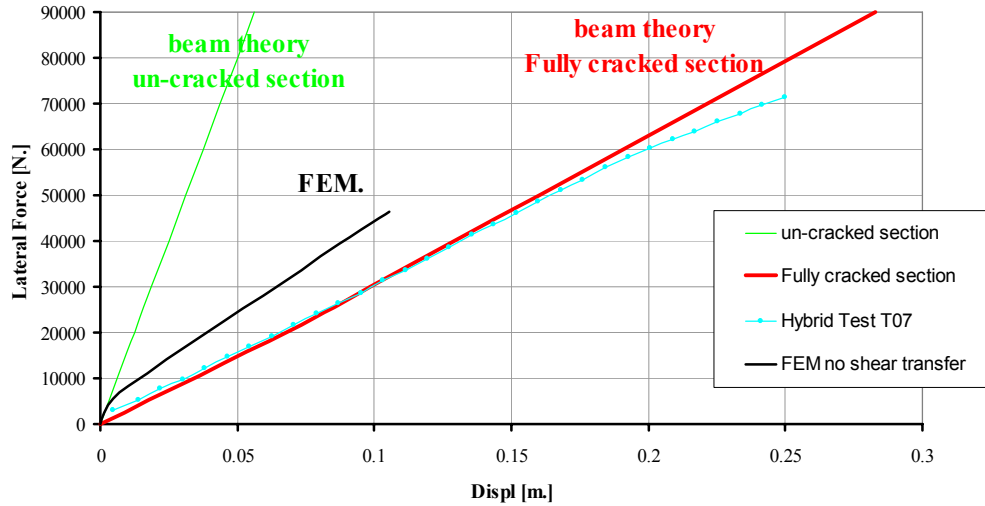
Figure 56 Displacement at 8 meter, Hybrid Tower.

Also in this case a simplified beam theory model is used to compare calculations. The tower is divided into 20 elements; for each combination of loads the lateral displacement is calculated at a height of 8 metres, referring to two different hypotheses. The first considers all the available area and includes concrete in tension which is referred to as I_{gross} stiffness, the second considers the cracked section composed of glass fibre and cracked concrete referred to as I_{crack}. The loads considered are: lateral force from 10kN up to 90kN which is assumed to be applied at a height of 16 metres, an axial force of 50kN and the assumed dead weight for the 16 metre tower. The whole formulation is reported in Figure 57.

Experimental and analytical data are compared in Figure 56. A first consideration is that the two lines obtained from beam theory should mark the upper and lower bounds of a reinforced concrete tower, indeed the line obtained with the FEM is between them. The experimental line follows the fully cracked line, as the tension cannot be transferred from fibre to concrete; for higher values of lateral force, the specimen shows a lower stiffness compared to the fully cracked tower; as in this case, a base rotation near the joint is possible adding a further displacement component at the top (see photo in appendix 16). In addition beam theory gives values nearer to experimental data.

```
> Ef := 12 10^9
> h := 8.0

> tf := .5e-2; tc := .16e-1; nc := (73.0 10^9)/Ef, R := (1.1 + 2 tf + tc)/2.0

> funz := Iyn(thn)/Syn(thn) + R cos(thn) - e

>

> iter := 20; iterf := 9

delta1=un-cracked          delta2=full-cracked

> for j from 2 to iterf do
      δ1(j) := 0;
      δ2(j) := 0;
      for i to iter do
          hxi := h i/iter;
          Force(j) := 90000 j/iterf;
          Mf := Force(j) (hxi + 8);
          N := -50000 - 1930 (hxi + 8);
          e := evalf(Mf/N);
          Syn := thn -> 2 evalf( ∫_0^π (R cos(th) - R cos(thn)) R 2 tf dth + ∫_0^π nc (R cos(th) - R cos(thn)) R tc dth );
          Iyn := thn -> 2 evalf( ∫_0^π (R cos(th) - R cos(thn))^2 R 2 tf dth + ∫_0^π nc (R cos(th) - R cos(thn))^2 R tc dth );
          sols := fsolve(funz = 0, thn, 0 .. π);
          Iygyn := Iyn(sols) + R cos(sols) Syn(sols);
          curvi1 := Mf/(Ef Iygyn);
          δ1(j) := δ1(j) + curvi1 hxi h/iter;
          Syn := thn -> 2 evalf( ∫_0^π (R cos(th) - R cos(thn)) R 2 tf dth + ∫_0^thn nc (R cos(th) - R cos(thn)) R tc dth );
          Iyn := thn -> 2 evalf( ∫_0^π (R cos(th) - R cos(thn))^2 R 2 tf dth + ∫_0^thn nc (R cos(th) - R cos(thn))^2 R tc dth );
          sols := fsolve(funz = 0, thn, 0 .. π);
          Iygyn := Iyn(sols) + R cos(sols) Syn(sols);
          curvi2 := Mf/(Ef Iygyn);
          δ2(j) := δ2(j) + curvi2 hxi h/iter
      end do
  end do
```

Figure 57 Integral calculus for beam theory based on Maple Script.

11.3 Full scale Tower

The pre-production drawings of the full-scale tower are shown in Figure 63 and Figure 64. The contractors for the tower and foundation components will generate the final production drawings once a final location and budget has been agreed. The tower is composed of four parts, each of a 3.5 inside diameter and of a 12-metre length for a total height of 44 metres from the ground. The first two parts have a hybrid section with a skin thickness varying along the height. At the base both the inside and the outside skin have a thickness of 30 mm, diminishing in a linear way up to an elevation of 20 metres where the thickness is 15 mm. The concrete core thickness is constant, at 50 mm, for the first two sections. The top part of the tower is built with two monolithic section glass fibre modules with a linearly varying thickness ranging from 40 mm to 20 mm.

The base of the tower (detail A) will be embedded into a reinforced concrete foundation for a length of 4 metres. In order to increase the adherence between the tower base and the concrete, the exterior FRP skin will taper from 30 to 140 mm, in addition to this two rings or radial bores will be fitted with steel rebar shear connectors in order assure the anchorage at the base. The joining details at the various heights of the tower are shown in Figure 64. In all cases the ends of the tower modules are finished in solid monolithic quasi-isotropic lay-up in order to build the joints around them using the fibre-wrapping joining method used for the 1/3 scale monolithic prototype. For the joint between the two hybrid sections nearest the base of the tower the proposed joint type is shown in detail B1, whereby the ends of the two hybrid sections are finished with a monolithic 400 mm length section that are then joined by a single exterior scarf joint, however, if a double scarf joint can be arranged by the production (detail B2) then the latter would be the preferred option.

The joint between the last hybrid section and the first monolithic module is shown in detail C, it consists of an exterior scarf joint between the quasi-isotropic monolithic ending of the hybrid element and the end of the first fully monolithic module. In detail D the joint between the two monolithic elements is essentially the same type of joint tested in the 1/3 scale monolithic specimen. Finally at the top of the tower detail E shows a taper that will be added to the end of the last module in order to arrange for the attachment of nacelle bearing ring (detailing here will be specified by the wind turbine contractor or will be adapted in order to conduct the full-scale destructive test).

Detailing for openings at the base of the tower has not been considered given the absence of input on this aspect from the wind turbine contractor partner. If openings are required at the base of the tower, the opening will be locally strengthened with carbon fibre lay-up. These details will be designed and calculated using FE analysis once, and if, specific requirements are made and dimensions provided.

The concrete properties are:

Static modulus of elasticity:	$E = 71\ GPa.$
Poisson's ratio:	$v = 0.25$
Compressive strength:	$f_c = 210\ MPa.$
Tension strength:	$f_t = 5\ MPa.$
Fracture energy:	$G_f = 12\ KN/m$
Density:	$\rho = 2420\ Kg/m^3$

72

The FRP material is elastic and orthotropic. Material properties are taken from the laminate theory with a stratification of *[2UD±5°, FW±85°]ₛ* and a volume fraction of 60% and a density of glass fibre is 1850 Kg/m³. The numerical values are reported below.

$$Q_{[2UD\pm5^\circ,FW\pm85^\circ]_s} = \begin{bmatrix} 32.9 & 4.13 & 4.07 & 0 & 0 & 0 \\ 4.13 & 23.1 & 4.21 & 0 & 0 & 0 \\ 4.07 & 4.21 & 9.25 & 0 & 0 & 0 \\ 0 & 0 & 0 & 5.89 & 0 & 0 \\ 0 & 0 & 0 & 0 & 6.62 & 0 \\ 0 & 0 & 0 & 0 & 0 & 8.16 \end{bmatrix} GPa.$$

$E_x = 31 GPa.$, $E_y = 21 GPa.$, $E_z = 8 GPa.$

$v_{xy} = 0.11$, $v_{yx} = 0.07$, $v_{xz} = 0.4$, $v_{zx} = 0.1$, $v_{yz} = 0.42$, $v_{zy} = 0.16$

$G_{yz} = 2.9 GPa.$, $G_{zx} = 3.3 GPa.$, $G_{xy} = 4.1 GPa.$,

We have also considered the 40% volume fraction in this case the properties are:

$E_x = 21 GPa.$, $E_y = 14.5 GPa.$, $E_z = 5.5 GPa.$

$v_{xy} = 0.11$, $v_{yx} = 0.08$, $v_{xz} = 0.4$, $v_{zx} = 0.1$, $v_{yz} = 0.42$, $v_{zy} = 0.16$

$G_{yz} = 1.9 GPa.$, $G_{zx} = 2.1 GPa.$, $G_{xy} = 2.5 GPa.$,

The mesh is built in a similar way to the previous models; apart from the geometry, the only difference is the variation of skin thickness. Joints along the tower are not considered in the model. The element pitch is 0.5 m.
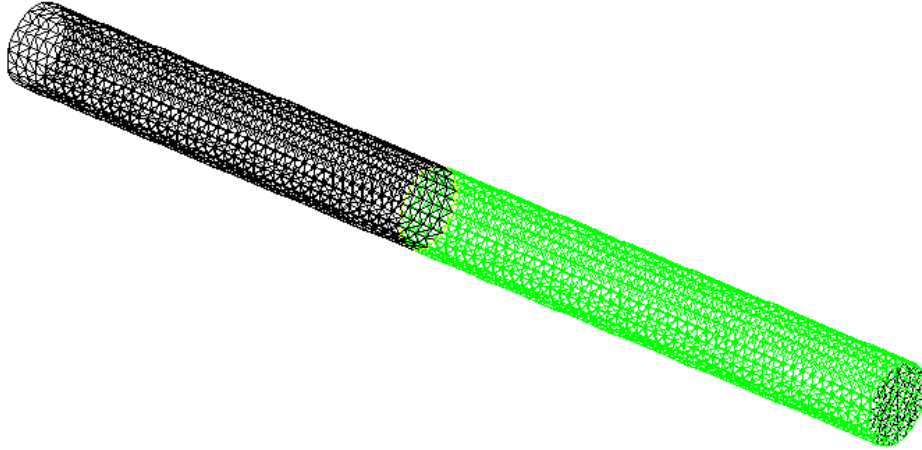
Figure 58 Full-scale tower FE mesh.

The boundary conditions are represented by the lack of rotation displacement at the base nodes as in the case of a cantilever.

The loading history is performed in three steps:

- The axial load is applied.
- The lateral load is increased while maintaining the axial load constant.
- After 80% of the nominal peak lateral load is achieved, the local step is reduced in order to increase the convergence speed of the algorithm.
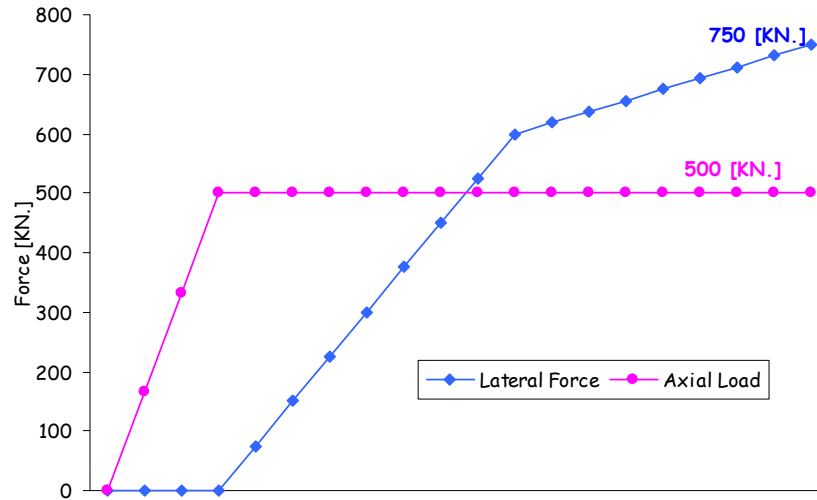
Figure 59 Loading protocol.

In Figure 60, FEM and beam theory analytical results are compared. The FEM line starts with a slope equal to an un-cracked section as calculated using both the linear FEM and beam theory, after then its stiffness decreases with increasing load and concrete cracking.
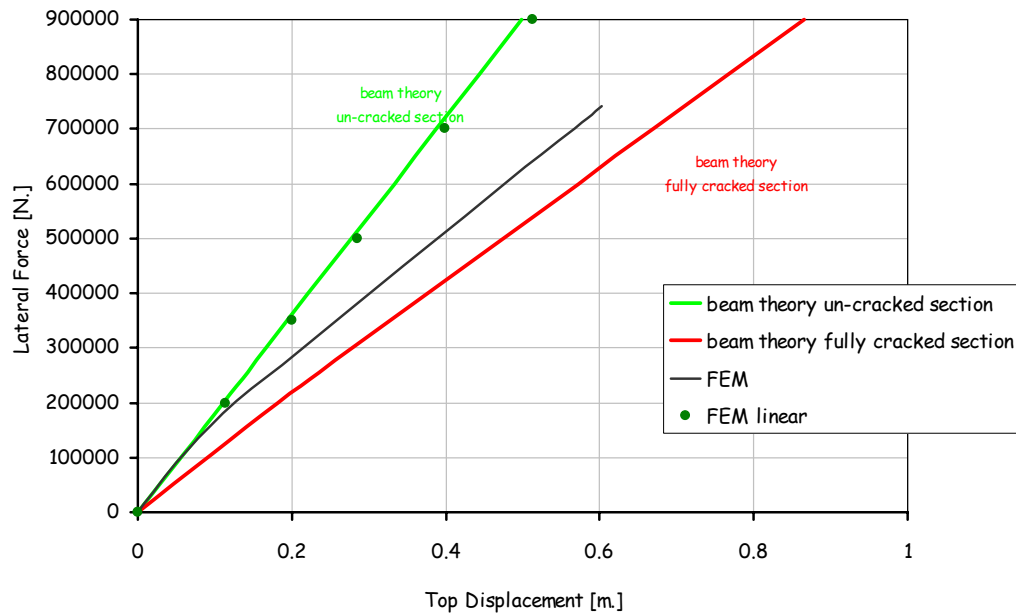
Figure 60 Lateral force versus displacement (Full scale Tower).

74

Considering the difficulties in manufacturing the two specimens, a second calculation is proposed to show how a volume fraction reduction results in a considerable stiffness reduction. In this case a variation of 20% (net) on the *Vf* of fibre produces a 40% reduction of stiffness.
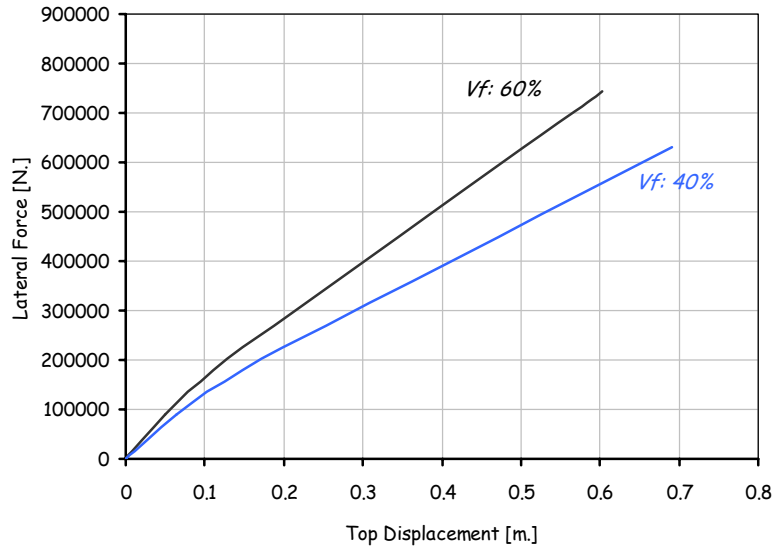
Figure 61 Variation of Stiffness as a result of reduction of fibre volume fraction.

Using the fully cracked beam theory (in the worst case) with a lateral load of 900kN, the behaviour of longitudinal tensions as a function of the tower elevation is shown in Figure 62. In the first two parts the skin thickness variation allows a constant tensile stress for the first 20 metres the transition of the hybrid to the monolithic section at mid height is shown. As expected, the increase in compressive stress in the FRP fibre is a result of the fact that all the compressive load in the top section is taken by the FRP, whereas the compressive stress in the concrete vanishes. In addition, at the point of change from the hybrid to the monolithic section there is no major discontinuity, on the basis of these a results it can be said that as a first approximation to the full-scale tower, the dimensions given are sufficiently optimised. Also, based on an assumed nacelle mass at 50t the first mode of the tower wood be not less then *0.73Hz*.
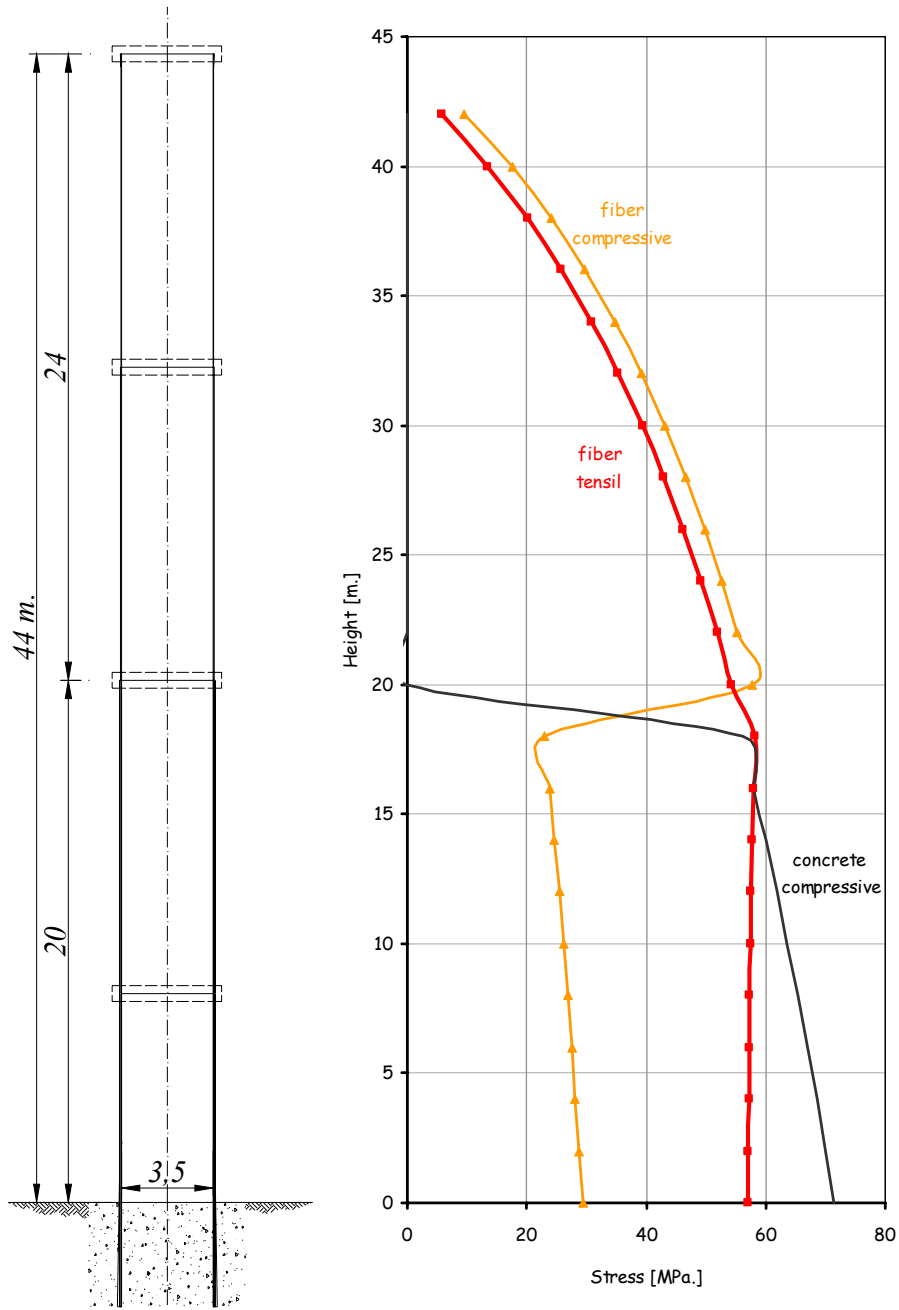
Figure 62 Stresses along the full-scale tower with lateral load of 900KN.
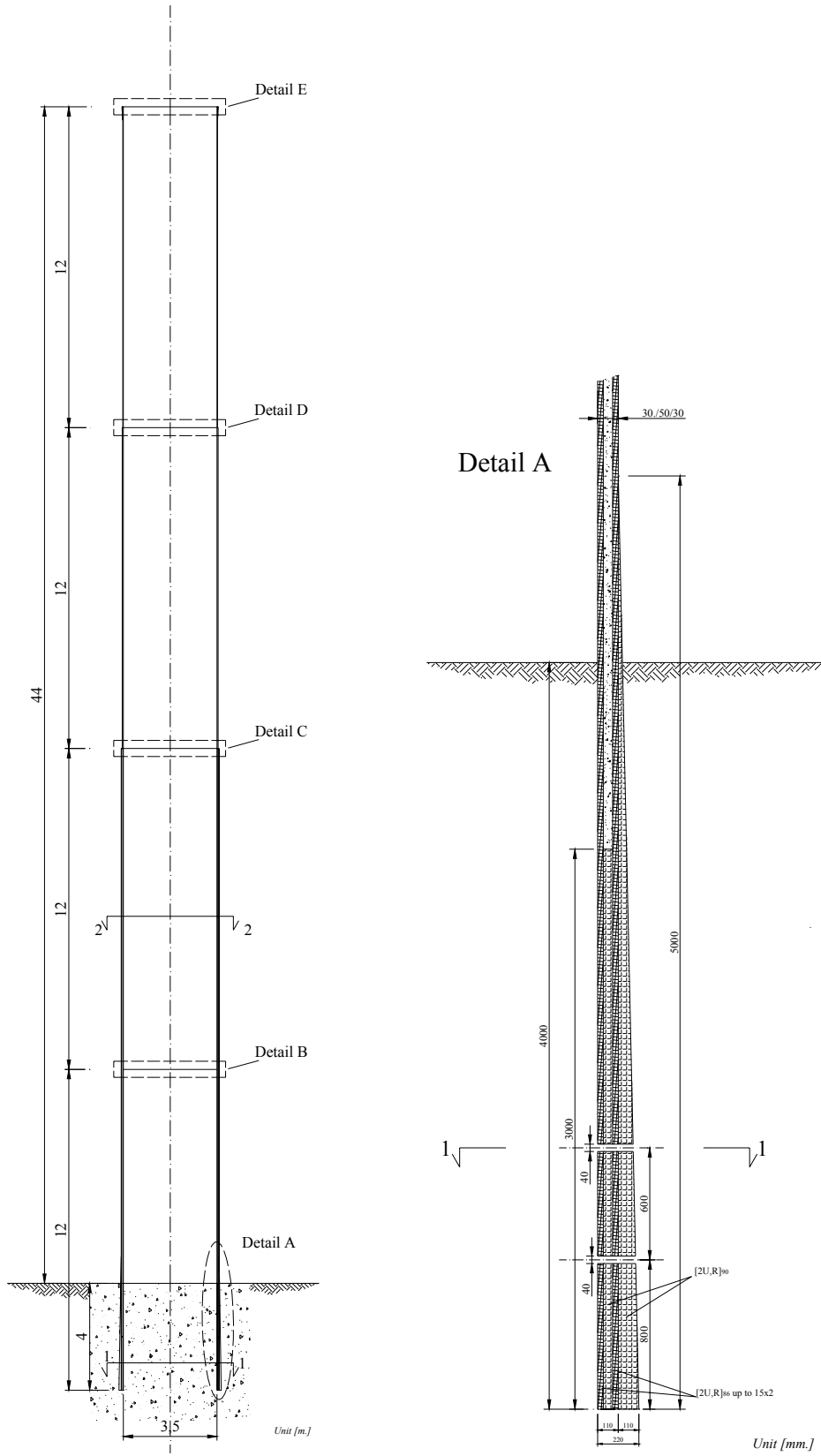
Figure 63 Full-scale tower and detail A.
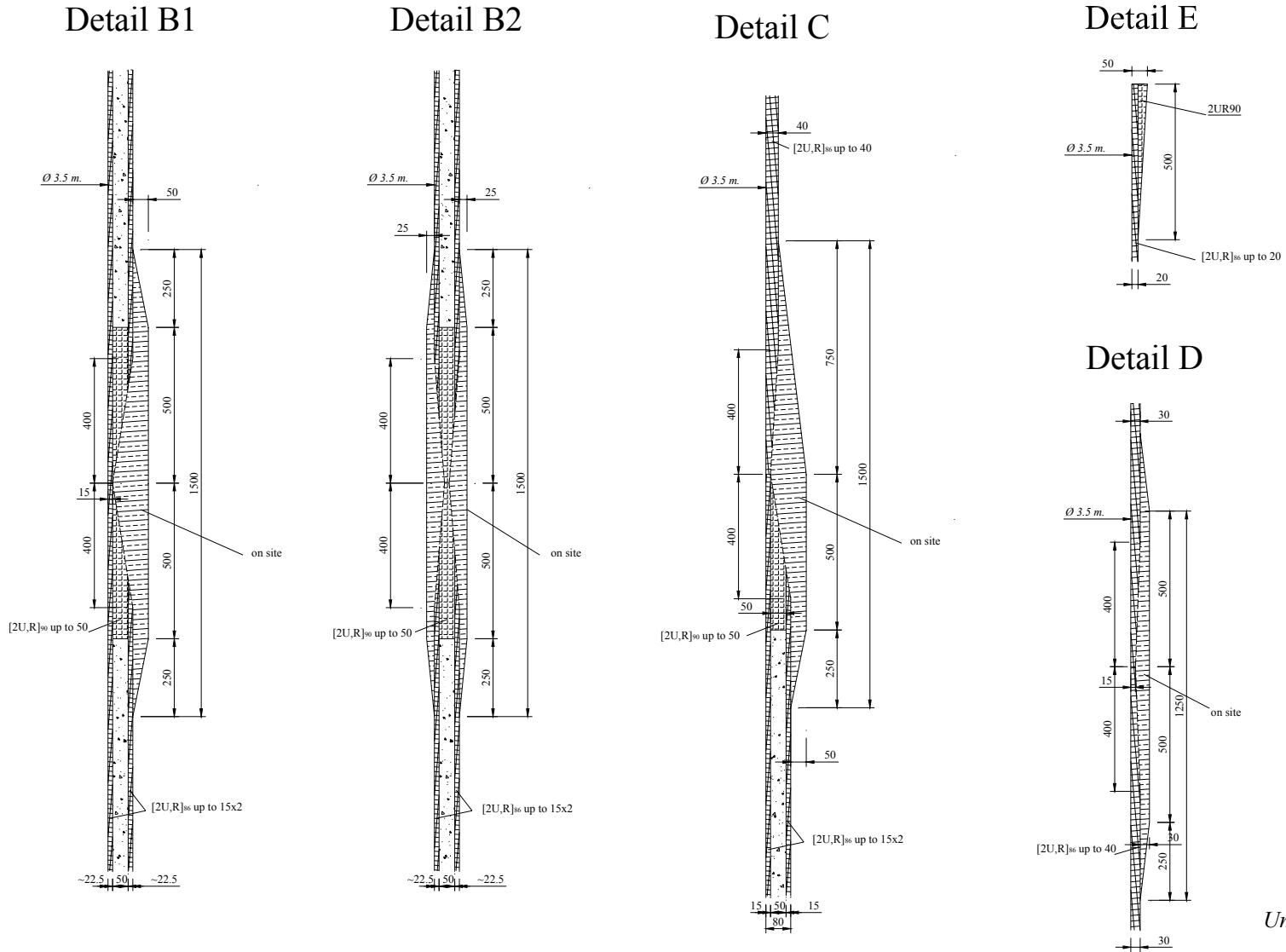
Figure 64 Joint details of the full-scale tower.

Unit [mm.]

12 Environmental tests

12.1 Experimentals

The ASTM G53-96, Standard Practice for Operating Light and Water Exposure Apparatus (Fluorescent UV-Condensation Type) for Exposure of Nonmetalic Materials was considered as guideline for the construction of the environmental chamber and consequent organization of the tests. This standard prescribes the following procedure in order to have an accelarated, simulated environmental impact on polymers and composite materials:

PHASE A: SPECIMEN PRECONDITIONING

Specimens are stored at about 50 % relative humidity conditions, at 23°C without UV for 7 days.

PHASE B: SPECIMEN AGEING

Specimens are subjected at alternating cycles of UV-B (302 nm) and Condensation according to the following scheme: 4h UV-B at 60°C without condensation followed by 4 h condensation (98% RH) at 50°C. This cycle repeats for about 1008 hours or 42 days (6 weeks).

The above simulated environmental ageing practice can be schematically represented as Figure 65 below shows.
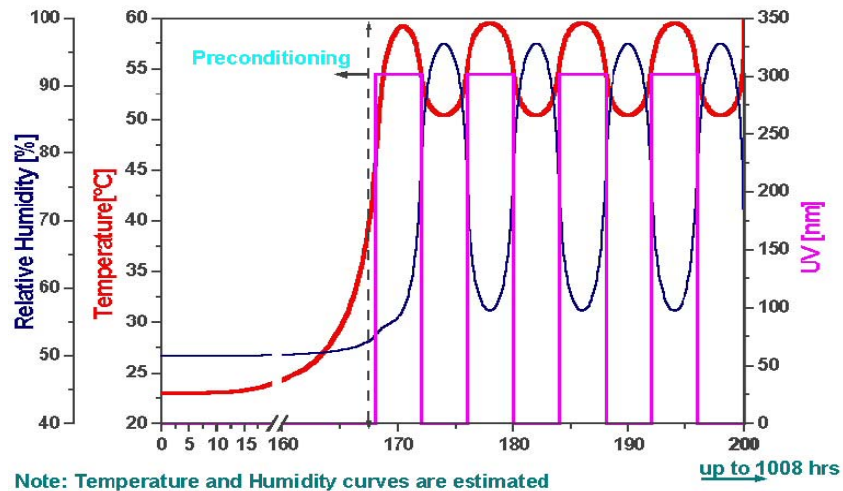
Figure 65 Presentation of the Environmental Ageing Cycles for 42 days plus preconditioning.

The above representation however is imaginary and does not represent the real Environmental Chamber Response. This is due to the differentiating behaviour of the Chamber in heating and cooling and the changes induced in the chamber atmosphere humidity by the humidifier installed. The real behaviour of the EAC constructed is depicted in Figure 66 below.

Figure 66, shows a typical 24-hour cycle of operation of the environmental ageing chamber. It is easy to observe how temperature rises at the beginning of the UV-on cycle to stabilize around 60 °C whereas the chamber is dried by a damper below 20% RH. These conditions are maintained for 4 hours. Afterwards, the chamber is let to cool down to room temperature by

itself while the chamber atmosphere is humidified up to 98%RH and UV radiation is turned off. The effect of the dried atmosphere exposure to high temperature and UV radiation resembles that of a hot dry day, whilst the low temperature exposure to high humidity levels corresponds to humid night conditions.

It has to be stated that the monolithic plaque put inside the ageing chamber was sealed with a special elastic sealant resin around the edges, to prevent moisture absorption in other than the through the thickness directions. In this way, Fickian diffusion of moisture in the material is ensured. The specimens were not subjected to any special preconditioning prior to the initiation of the chamber cycles since the conditions maintained in the storage room, where the monolithic plaques are kept were almost identical those of the preconditioning phase.
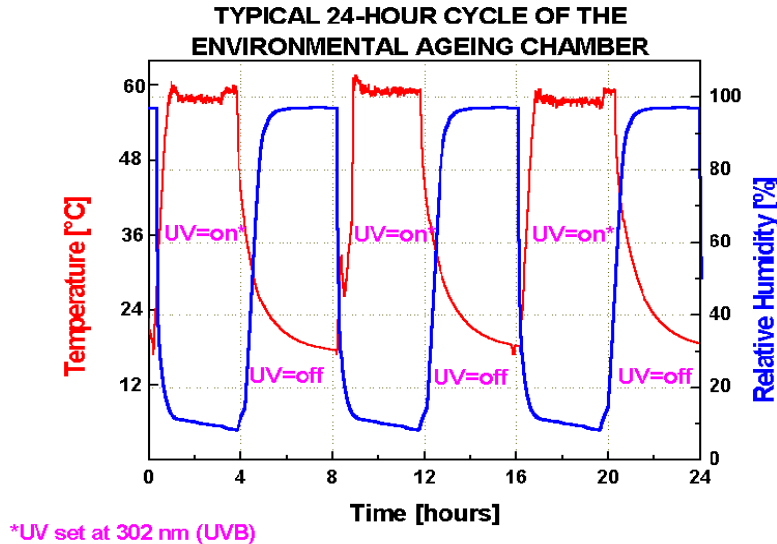
Figure 66 Real Time Recorded Humidity-Temperature Graphs of the Environmental Ageing Chamber.

Uppon completion of the environmental ageing campaign (42 days) for the monolithic skin composite, the skin plaque was removed from the chamber and sealed in a plastic bag to ensure it will keep its humidity during specimen machining for other test purposes. Mainly semi-static tensile testing and dynamic mechanical analysis were performed in order to evaluate the impact of environmental ageing on the overall material mechanical response.

Static tensile tests were performed on a MTS 20KN universal testing machine per ASTM D3039/D3039 M-94a at 2mm/min crosshead speed. Tensile strain was measured by strain gauges attached along the specimen longitudinal axis. Specimen dimensions were 250x25x2 mm^3. A number of 8 specimens was used for the averaging of the pristine material mechanical properties.

A Q800 TA Instruments Dynamic Mechanical Analysis system was used for the assessment of the skin composite dynamic behaviour before and after the environmental ageing. Specimens of 60x12x2 mm^3 were carefully machined from the skin plaques for this purpose. Three point bending test set up under controlled strain loading conditions was used. Maximum bending deflection was set at 10μm and static preloading was set at 0,125 N. Frequency scans were performed for the pristine and aged skin composite within the range of 0 to 10 Hz. Temperature scans were also performed for the same materials at a loading frequency of 5 Hz within a temperature range of –40 to +100 °C.

The surface examinations of the specimens were performed at the AMTT premises in Seibersdorf, Austria, with a Zeiss DSM 950 Scanning Electron Microscope with the following

specifications: accelerating voltage 0,5 - 30 kV; magnification 15x - 200000x; and integrated digital framestorage.

In addition to the environmental ageing of the monolithic skin composite, sample plaques were subjected to salt spraying atmosphere at the specially designed chamber of AMTT premises, according to DIN 50 021 "Salt spray test with different sodium chloride solutions". This campaign was parallel to the Environmental Campaign of the ICEHT. The sample plaques were subjected to constant spraying with natrium chlorine solution at 50°C for a period of 20 days. The testing was meant to simulate the effects of seaside or offshore environments on the tower skin composite.

All testing procedures at the AMTT facilities in Seibersdorf, Austria were supported by the EC-Project: Improving the Human Research Potential and Socioeconomic Knowledge Base, HPRI-CT-1999-00024.

12.2 Results

12.2.1 Mechanical Properties

Tensile mechanical properties of the monolithic skin composite as determined on non-aged plaques are shown in Table 11 below. These data lay within the normal property range for glass mat reinforced polyester composites.

Table 11 Tensile Properties of the pristine monolithic skin composite along its main axis.

Property Condition	Tensile modulus E [GPα]	Tensile Strength σ_B [MPα]	Fracture Strain ε_B [%]
Pristine Composite	11.8±0.36	156.8±15.06	1.82±0.19
Skin Subjected to Salt Spraying	10.8±0.15	145.2±4.05	1.81±0.08

Small changes in the tensile mechanical properties could be detected salt sprayed skin-composites as seen above. A small degradation of the skin composite mechanical properties can be deduced from the semi-static tensile data for the composite subjected to salt-spraying for 20 days. Tests are currently running for the deduction of the static mechanical properties of the Environmentally Aged Skin Composite.

12.2.2 Dynamic Mechanical Analysis-Frequency & Thermal Scans

The dynamic mechanical behaviour of the pristine and the environmentally aged skin plaques is presented in Figure 67 below. Some aged specimens were dried prior to

DMA testing in order to assess the pure influence of ageing without the presence of water in the polymer matrix.

A matrix plastification effect can be easily stated due to water sorption by the polyester matrix. This is well reflected in the tanδ data of the aged material which are almost by 300% increased with respect to the non-aged material. The effect of matrix plastification and possible interface damaging caused by water sorption and/or temperature fluctuations (thermal fatigue) effects can be clearly deduced by the dynamic moduli plots vs frequency for the skin material before and after the 42 period of environmental ageing. Observe that the dynamic storage moduli of the pristine material in flexural loading are almost identical to the tensile E-modulus

of the material as given in Table 11. An abrupt reduction in the material stiffness appears to be the direct effect of the material ageing. Another important conclusion drawn here is the insensitivity to loading frequency the skin material exhibits for the specific frequency range. Still, the dried specimens do not show strong deviation with respect to the storage moduli in comparison to the wet ones.
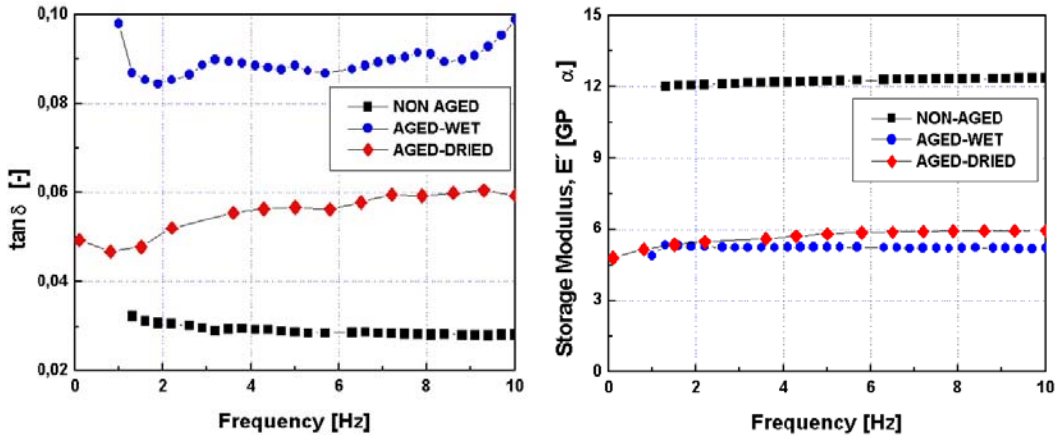
Figure 67 Dynamic Storage Moduli and tanδ vs Frequency plots for the pristine and aged skin composite in wet and dried conditions respectively.

The plastification effect stated for the skin material is also well reflected in the tanδ plots prior and after ageing. tanδ parameter represents the material ability to dissipate energy to the environment, also a measure of the material damping ability. There is a significant increase in the tanδ data after the environmental ageing procedure. This is probably due to the matrix plastification effect and also to the destruction of fiber–matrix interface. Still, the DMA frequency scans on dried aged specimens show the differenciating material behaviour owing to these two effects. Even the dried specimens exhibit high damping ability, a clear sign of the deteriorated fiber-matrix adhesion and friction effects after the ageing process.
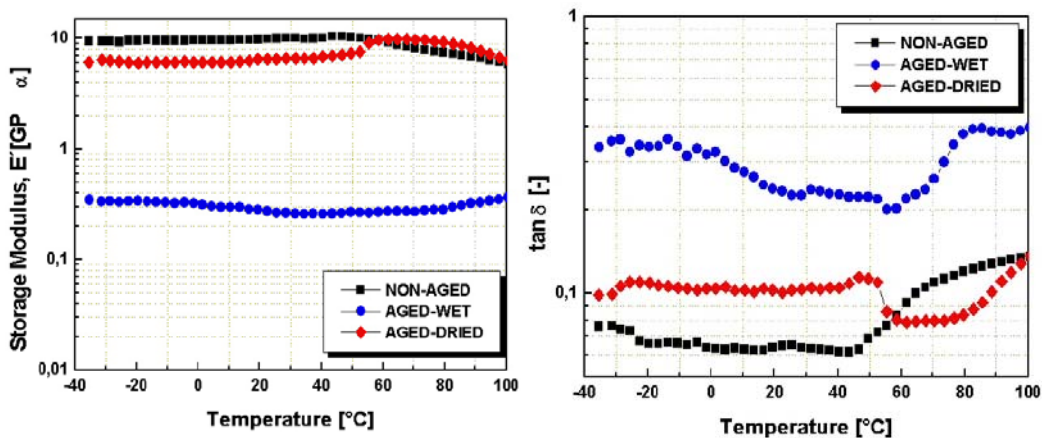
Figure 68 Dynamic Storage Moduli and tanδ vs Temperature plots for the pristine and aged skin composite in wet and dried conditions respectively.

Thermal DMA scans ran for the same materials are presented in Figure 68 above. Clearly, the plastification effects stated due to the presence of water in the matrix are confirmed also in a wide temperature range. A very interesting fact here is the similarity in the storage moduli data for the pristine and dried-aged composites. Still, the situation clears out when the tanδ data are

concerned. An enhancement in the damping ability of the material can be observed after ca. 40°C which verifies the polyester matrix glass transition region. This assumption is reversed for the pre-dried specimens which show a reduction in this region. Possibly, this stiffening effect seen also in the storage moduli data owes to areas of the polymer damaged by hydrolysis.

Still, the reduction in the dynamic storage moduli of the material by an order of magnitude is very impressive and special attention should be drawn here to the designers. Special protection has to be applied to the skin composite against moisture sorption , possibly by applying a gel coating on the skin surface.

A series of DMA testing is under way to determine the dynamic mechanical response of the salt-spray aged skin composite with respect to temperature and frequency.

12.2.3 Surface Topography Scans

Scanning Electron microscopy revealled very interesting features of the surface in the environmentally aged aspecimens. As seen in Figure 69 below, taken from the surfaces of the non-aged and aged skin composites at the same magnification factor, radical changes can be recognized.   The normally rough as-fabricated surface of the specimen (picture on the left), is transformed after the 42 ageing period (picture on the right). Microcracks of the type shown in the right frame, can be observed throughout the surface of the aged specimen, in contrast to the unmarked pristine material. Such microcracking is usually typical for the combined action of UV radiation, temperature fluctuations (fatigue) and swelling due to humidy absorption. In fact a swollen polymer surface can be easily seen in the frame on the right. Such microcracking can become a potential area of crack build-up especially under fatigue loading of the tower structure, as it is known that mechanical vibrations due to aeroelastic loads will be present. Again, it has to be reported here that the composite was environmentally aged under "worse case scenario" conditions of course, not protected by a gel coating which is usually applied to the surface. However, all types of gel coatings tend to develop crazing and microcracking due to environmental factors so, after the gel-coat barrier has been made penetrable, the skin composite will develop a surface as shown below.
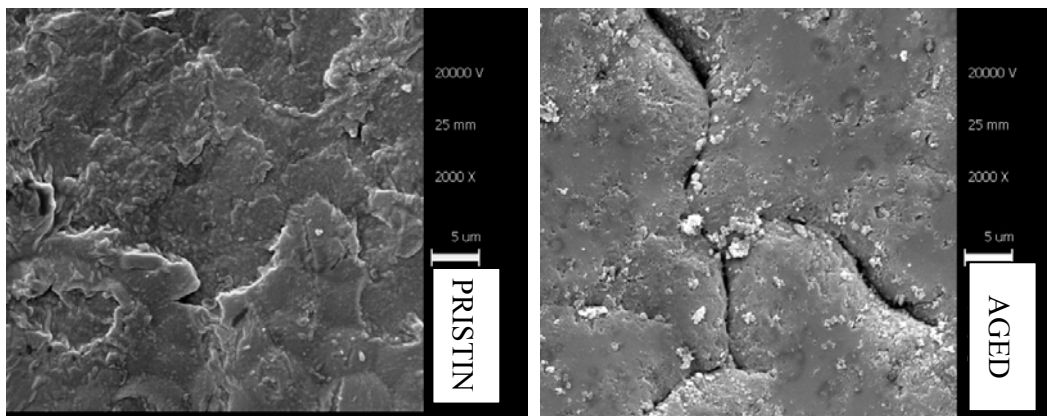
Figure 69 SEM Surface scans of the pristine (frame left) and environmentally aged (frame right) skin composites respectively.

12.3 Conclusions

Major conclusions that can be drawn from the series of testing for the environmentally and salt spraying aged monolithic tower skin composite are:

- ✓ The procedure of ageing the skin under the combined action of UV radiation, Humidity and Temperature results in degradation of the material thermomechanical properties and especially of dynamic stiffness data.
- ✓ Salt Spraying ageing resulted in reduced static stiffness and strength data.
- ✓ Matrix microcracking was detected as a result of environmental ageing

13 Appendix A: Experiments and test results.

13.1 Experimental set-up and instrumentation
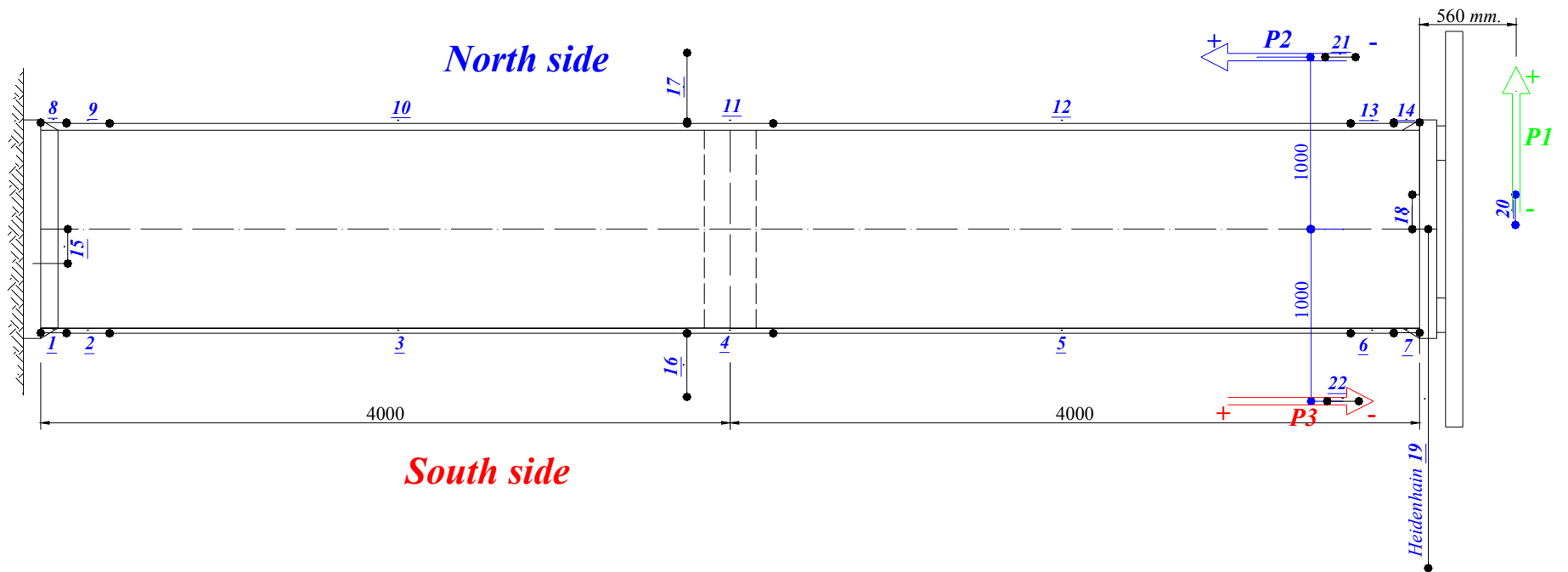
Figure 70 Displacement transducers monolithic tower.

Table 12 Type of transducers on monolithic tower.

Channel number	Type	Range	Gauge-length [mm.]
1	Gefran PZ12	±12.5mm.	150
2	Gefran PZ12	±12.5mm.	250
3	Gefran PZ12	±12.5mm.	3350
4	Gefran PZ12	±12.5mm.	500
5	Gefran PZ12	±12.5mm.	3350
6	Gefran PZ12	±12.5mm.	250
7	Gefran PZ12	±12.5mm.	150
8	Gefran PZ12	±12.5mm.	150
9	Gefran PZ12	±12.5mm.	250
10	Gefran PZ12	±12.5mm.	3350
11	Gefran PZ12	±12.5mm.	500
12	Gefran PZ12	±12.5mm.	3350
13	Gefran PZ12	±12.5mm.	250
14	Gefran PZ12	±12.5mm.	150
15	Gefran PZ12	±12.5mm.	-
16	Gefran PZ12	±50mm.	-
17	Gefran PZ12	±50mm.	-
18	Gefran PZ12	±12.5mm.	-
19	Heidenhain	±500mm.	-
20	Temposonic	±500mm.	-
21	Gefran PZ12	±50mm.	-
22	Gefran PZ12	±50mm.	-

North Outside
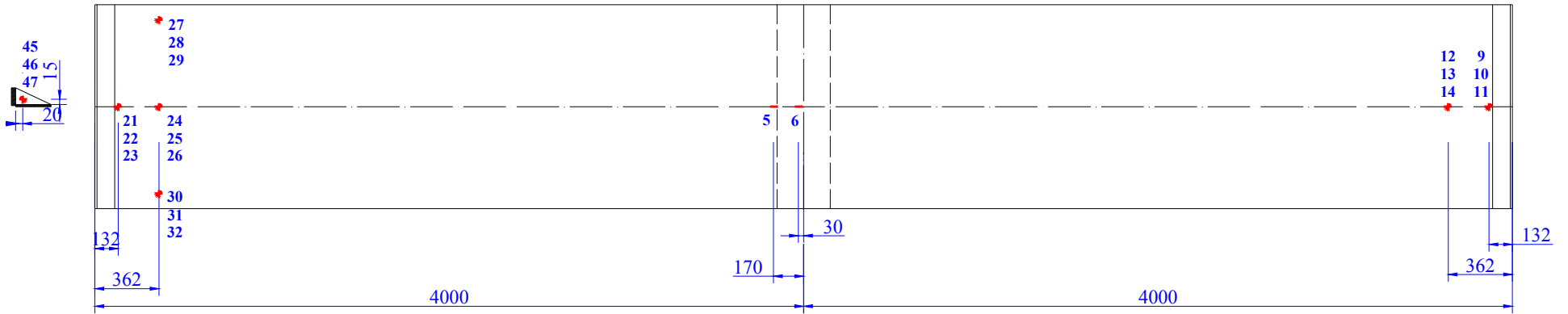
North Inside
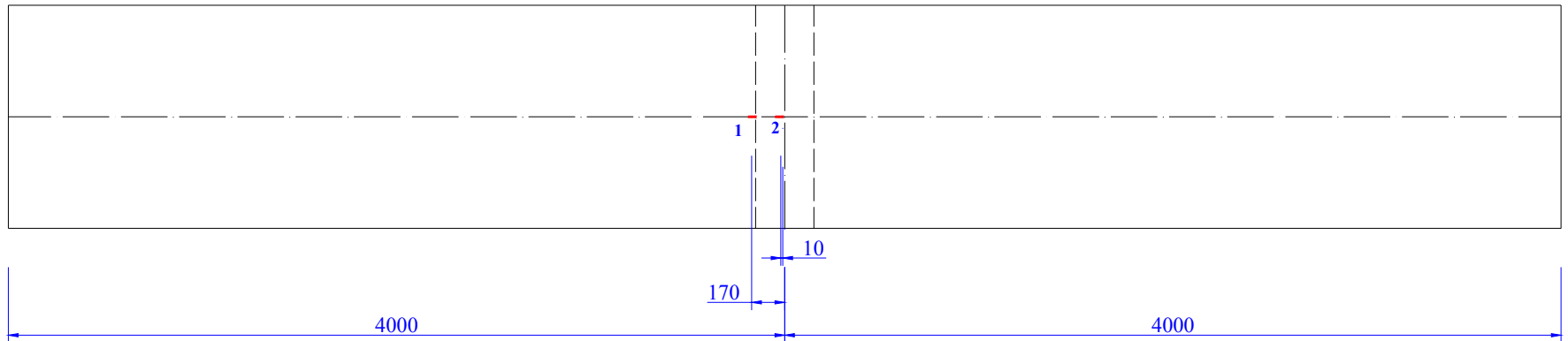
Figure 71 Strain gauges north side, monolithic tower.

South Inside
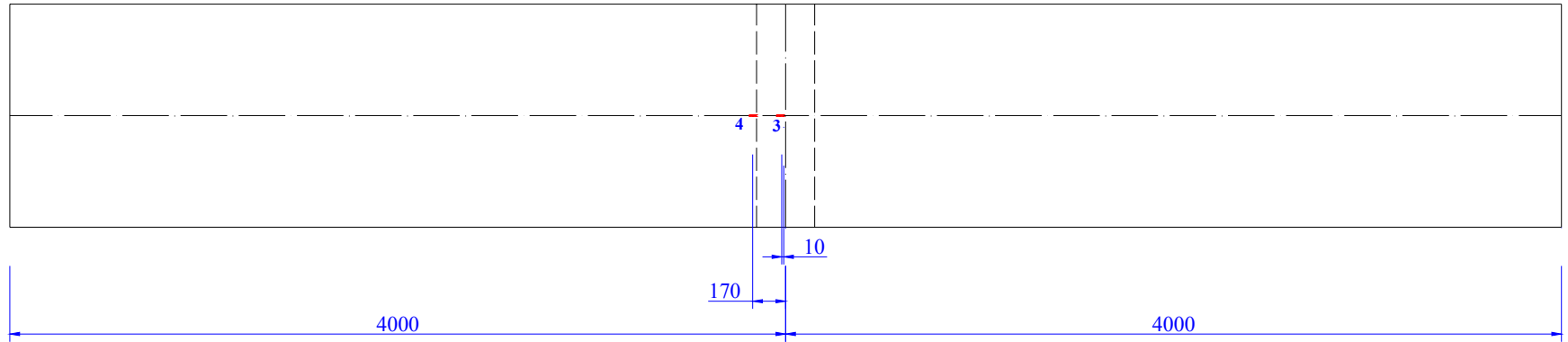
South Outside
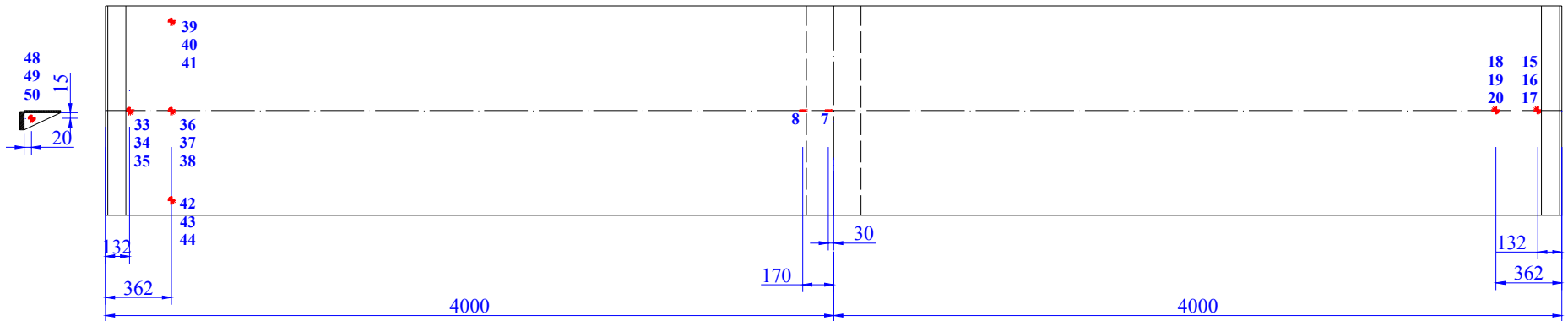
Figure 72 Strain gauges south side, monolithic tower.

Table 13 Data sheet of strain gauges, monolithic tower.

Number	1	2	3	4	5	6	7	8	9	10
Type	M-M/EA06	M-M/EA06	M-M/EA06	M-M/EA06	M-M/EA06	M-M/EA06	M-M/EA06	M-M/EA06	TML/FRA 6	TML/FRA 6
Resistance	350Ω	350Ω	350Ω	350Ω	350Ω	350Ω	350Ω	350Ω	120Ω	120Ω
Gage factor	2.125	2.125	2.125	2.125	2.125	2.125	2.125	2.125	2.12	2.12

Number	11	12	13	14	15	16	17	18	19	20
Type	TML/FRA 6	TML/FRA 6	TML/FRA 6	TML/FRA 6	TML/FRA 6	TML/FRA 6	TML/FRA 6	TML/FRA 6	TML/FRA 6	TML/FRA 6
Resistanse	120Ω	120Ω	120Ω	120Ω	120Ω	120Ω	120Ω	120Ω	120Ω	120Ω
Gage factor	2.12	2.12	2.12	2.12	2.12	2.12	2.12	2.12	2.12	2.12

Number	21	22	23	24	25	26	27	28	29	30
Type	TML/FRA 6	TML/FRA 6	TML/FRA 6	TML/FRA 6	TML/FRA 6	TML/FRA 6	TML/FRA 6	TML/FRA 6	TML/FRA 6	TML/FRA 6
Resistance	120Ω	120Ω	120Ω	120Ω	120Ω	120Ω	120Ω	120Ω	120Ω	120Ω
Gage factor	2.12	2.12	2.12	2.12	2.12	2.12	2.12	2.12	2.12	2.12

Number	31	32	33	34	35	36	37	38	39	40
Type	TML/FRA 6	TML/FRA 6	TML/FRA 6	TML/FRA 6	TML/FRA 6	TML/FRA 6	TML/FRA 6	TML/FRA 6	TML/FRA 6	TML/FRA 6
Resistance	120Ω	120Ω	120Ω	120Ω	120Ω	120Ω	120Ω	120Ω	120Ω	120Ω
Gage factor	2.12	2.12	2.12	2.12	2.12	2.12	2.12	2.12	2.12	2.12

Number	41	42	43	44	45	46	47	48	49	50
Type	TML/FRA 6	TML/FRA 6	TML/FRA 6	TML/FRA 6	TML/FRA 6	TML/FRA 6	TML/FRA 6	TML/FRA 6	TML/FRA 6	TML/FRA 6
Resistance	120Ω	120Ω	120Ω	120Ω	120Ω	120Ω	120Ω	120Ω	120Ω	120Ω
Gage factor	2.12	2.12	2.12	2.12	2.12	2.12	2.12	2.12	2.12	2.12
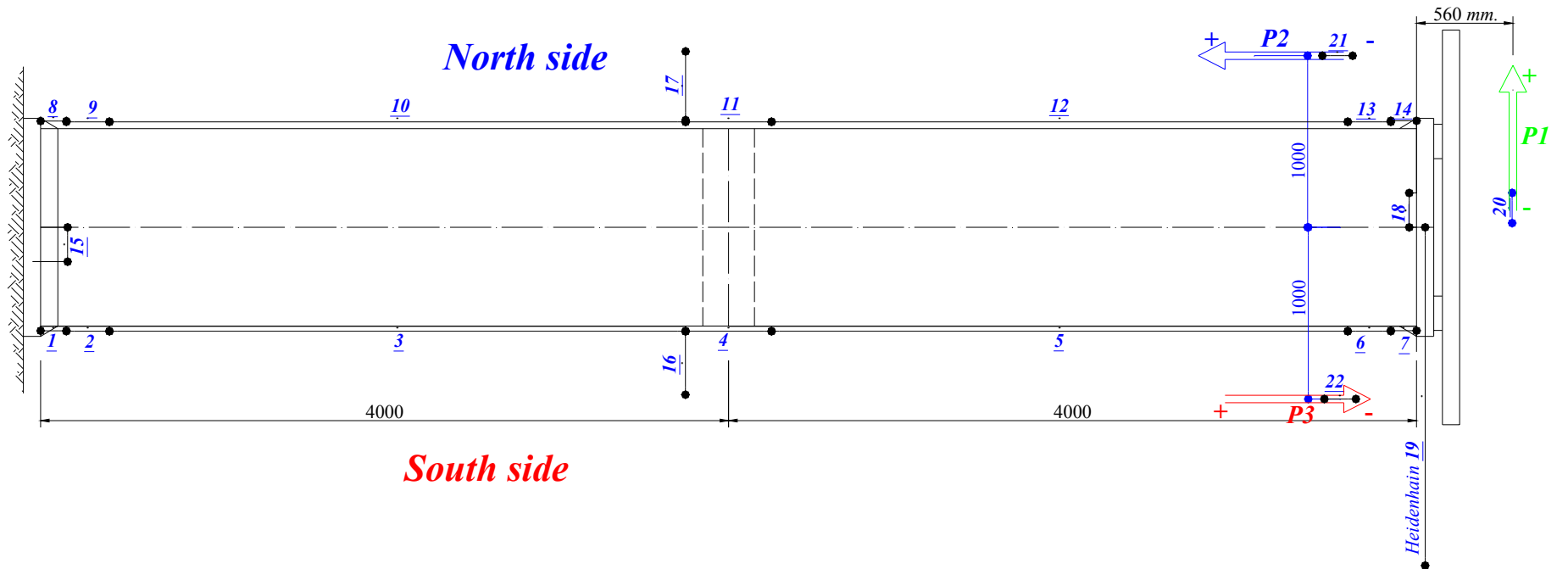
Figure 73 Displacement transducers hybrid tower.

Table 14 Type of transducers on hybrid tower.

Channel number	Type	Range	Gauge-length [mm.]
1	Gefran PZ12	±12.5mm.	150
2	Gefran PZ12	±12.5mm.	250
3	Gefran PZ12	±50mm.	3350
4	Gefran PZ12	±12.5mm.	500
5	Gefran PZ12	±50mm.	3350
6	Gefran PZ12	±12.5mm.	250
7	Gefran PZ12	±12.5mm.	150
8	Gefran PZ12	±12.5mm.	150
9	Gefran PZ12	±12.5mm.	250
10	Gefran PZ12	±50mm.	3350
11	Gefran PZ12	±12.5mm.	500
12	Gefran PZ12	±50mm.	3350
13	Gefran PZ12	±12.5mm.	250
14	Gefran PZ12	±12.5mm.	150
15	Gefran PZ12	±12.5mm.	-
16	Gefran PZ12	±50mm.	-
17	Gefran PZ12	±50mm.	-
18	Gefran PZ12	±12.5mm.	-
19	Heidenhain	±500mm.	-
20	Temposonic	±500mm.	-
21	LVDT RDP-DCT6000C	±150mm.	-
22	LVDT RDP-DCT6000C	±150mm.	-
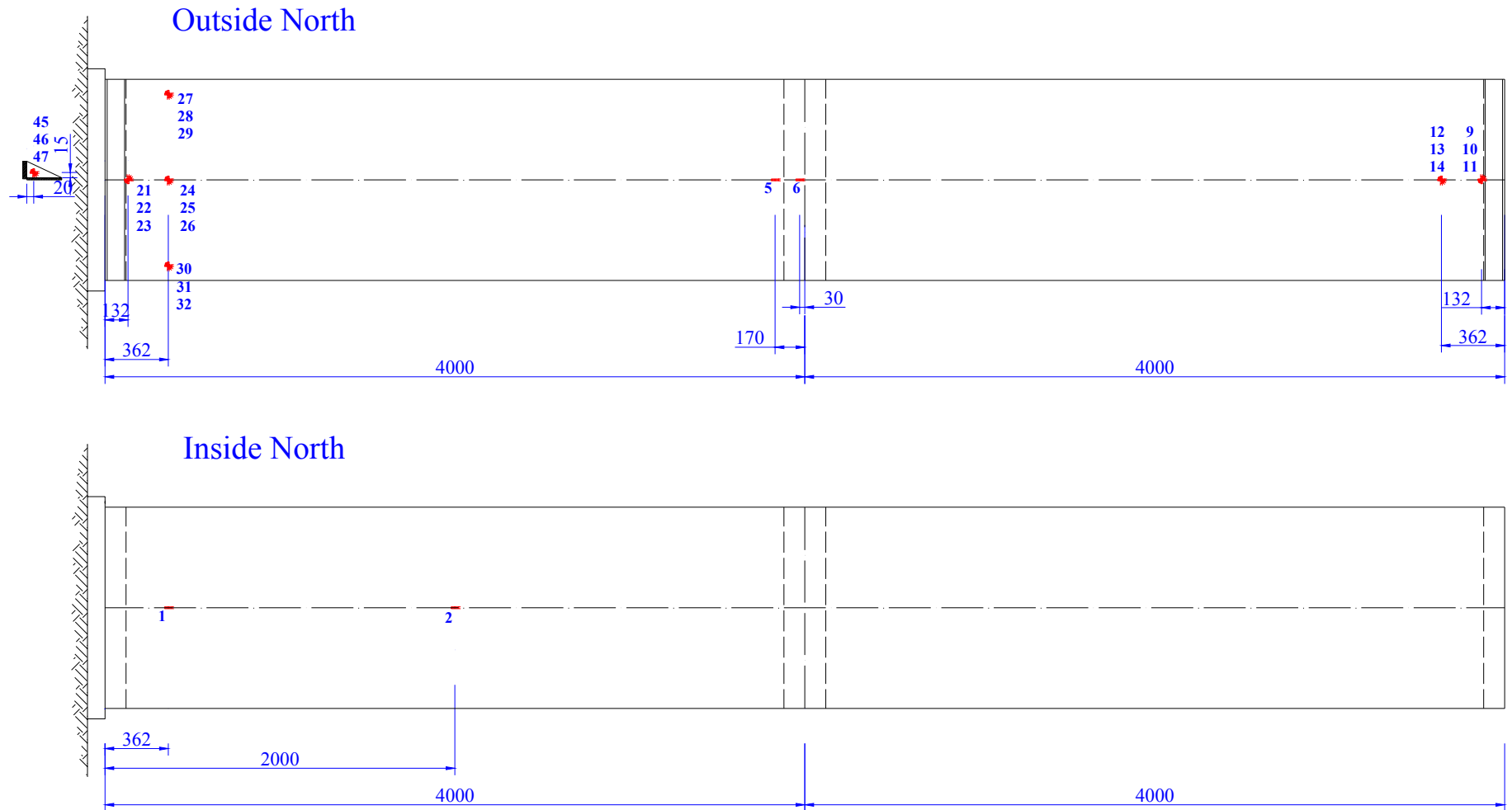
Figure 74 Strain gauges north side, hybrid tower.

Inside South

Outside South
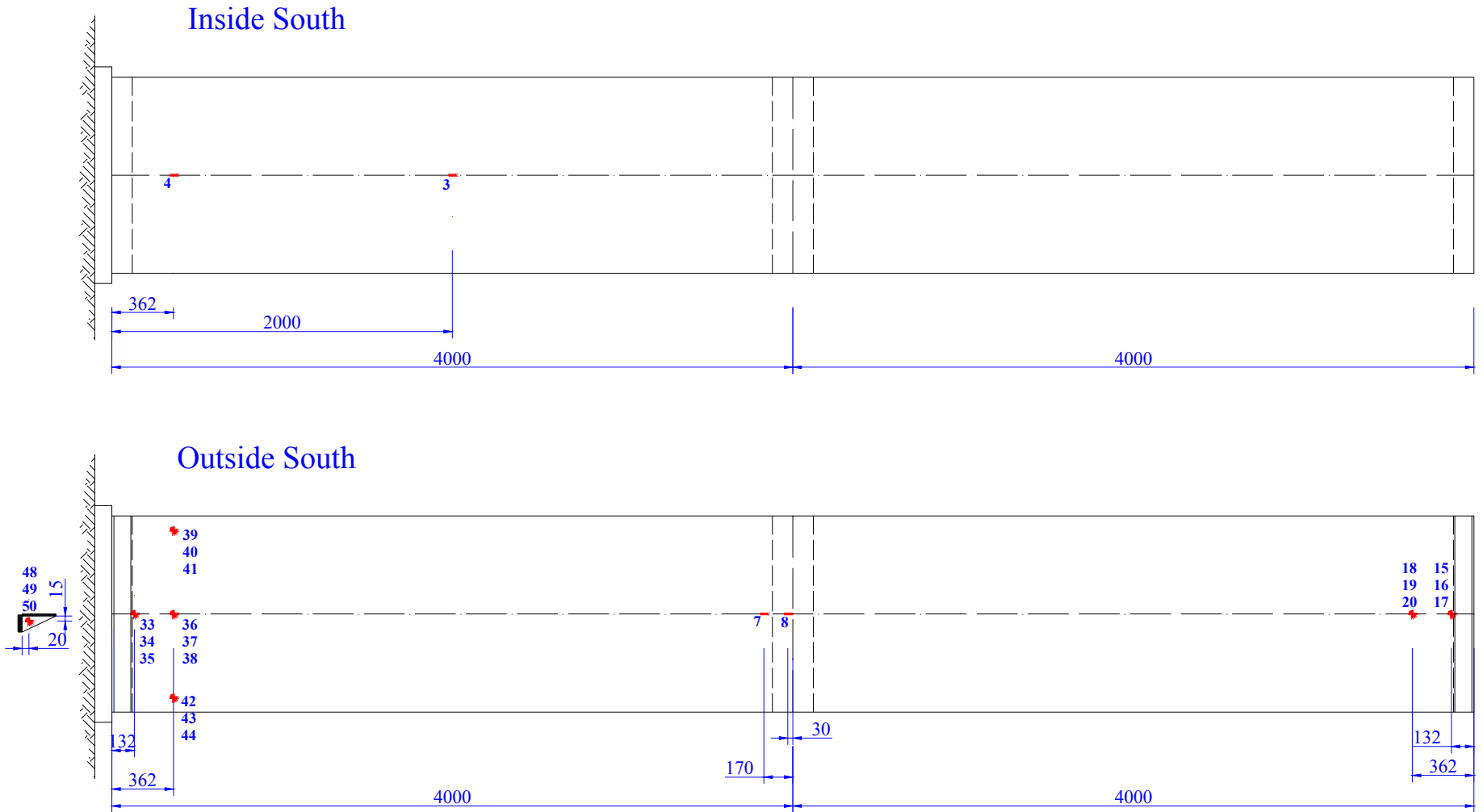
Figure 75 Strain gauges south side, hybrid tower

Table 15 Data sheet of strain gauges, hybrid tower.

Number	1	2	3	4	5	6	7	8	9	10
type	M-M/EA09	M-M/EA09	M-M/EA09	M-M/EA09	M-M/EA09	M-M/EA09	M-M/EA09	M-M/EA09	TML/FRA 6	TML/FRA 6
Resistance	350Ω	350Ω	350Ω	350Ω	350Ω	350Ω	350Ω	350Ω	120Ω	120Ω
Gage factor	2.09	2.09	2.09	2.09	2.09	2.09	2.09	2.09	2.12	2.12

Number	11	12	13	14	15	16	17	18	19	20
type	TML/FRA 6	M-M/EA09	M-M/EA09	M-M/EA09	TML/FRA 6	TML/FRA 6	TML/FRA 6	M-M/EA09	M-M/EA09	M-M/EA09
Resistance	120Ω	350Ω	350Ω	350Ω	120Ω	120Ω	120Ω	350Ω	350Ω	350Ω
Gage factor	2.12	2.09	2.09	2.09	2.12	2.12	2.12	2.09	2.09	2.09

Number	21	22	23	24	25	26	27	28	29	30
type	TML/FRA 6	TML/FRA 6	TML/FRA 6	M-M/EA09	M-M/EA09	M-M/EA09	M-M/EA09	M-M/EA09	M-M/EA09	M-M/EA09
Resistance	120Ω	120Ω	120Ω	350Ω	350Ω	350Ω	350Ω	350Ω	350Ω	350Ω
Gage factor	2.12	2.12	2.12	2.09	2.09	2.09	2.09	2.09	2.09	2.09

Number	31	32	33	34	35	36	37	38	39	40
type	M-M/EA09	M-M/EA09	TML/FRA 6	TML/FRA 6	TML/FRA 6	M-M/EA09	M-M/EA09	M-M/EA09	M-M/EA09	M-M/EA09
Resistance	350Ω	350Ω	120Ω	120Ω	120Ω	350Ω	350Ω	350Ω	350Ω	350Ω
Gage factor	2.09	2.09	2.12	2.12	2.12	2.09	2.09	2.09	2.09	2.09

Number	41	42	43	44	45	46	47	48	49	50
type	M-M/EA09	M-M/EA09	M-M/EA09	M-M/EA09	TML/FRA 6	TML/FRA 6	TML/FRA 6	TML/FRA 6	TML/FRA 6	TML/FRA 6
Resistance	350Ω	350Ω	350Ω	350Ω	120Ω	120Ω	120Ω	120Ω	120Ω	120Ω
Gage factor	2.09	2.09	2.09	2.09	2.12	2.12	2.12	2.12	2.12	2.12

13.2 Experimental Data
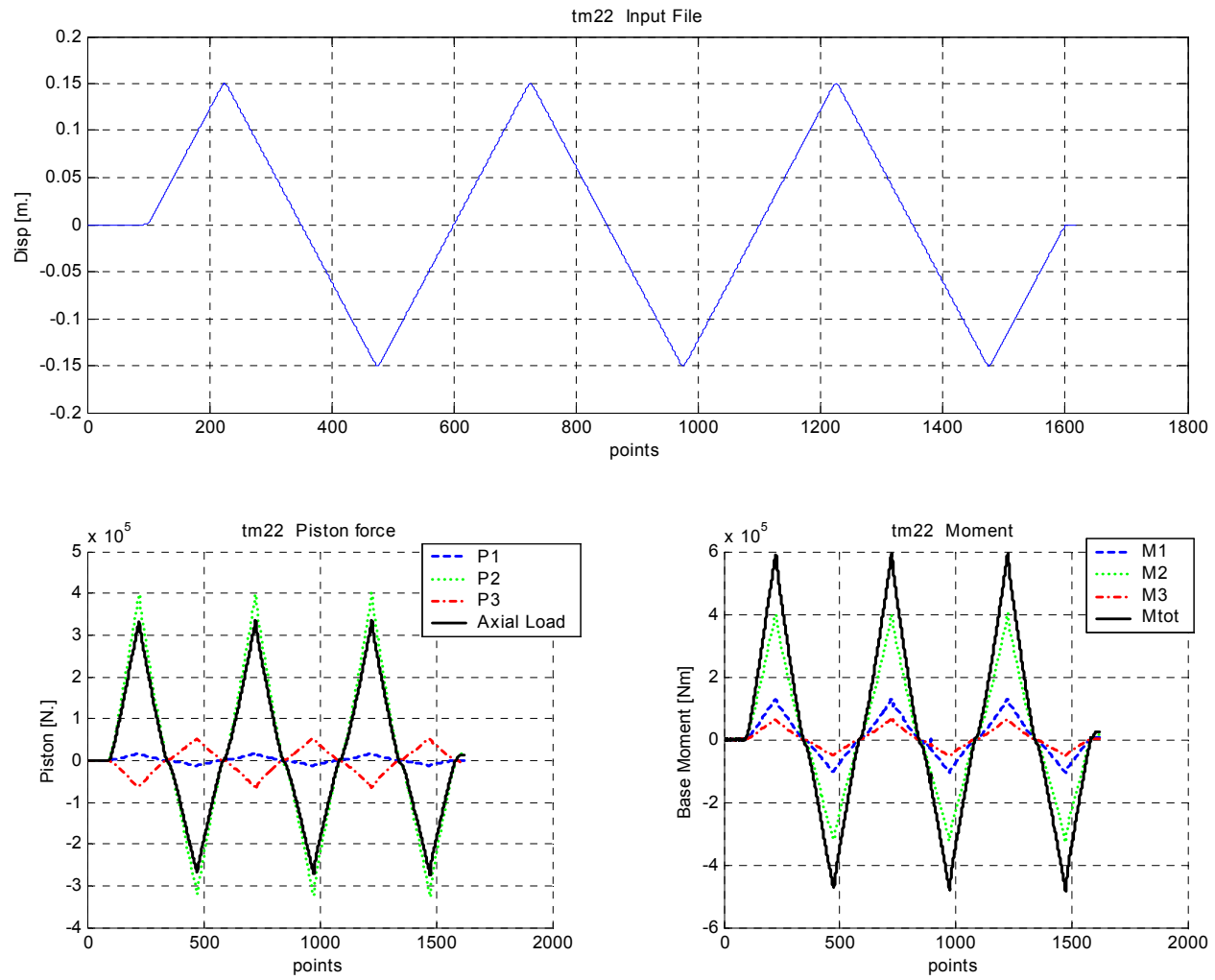
Figure 76 tm22: Input file, Piston forces and Moments.
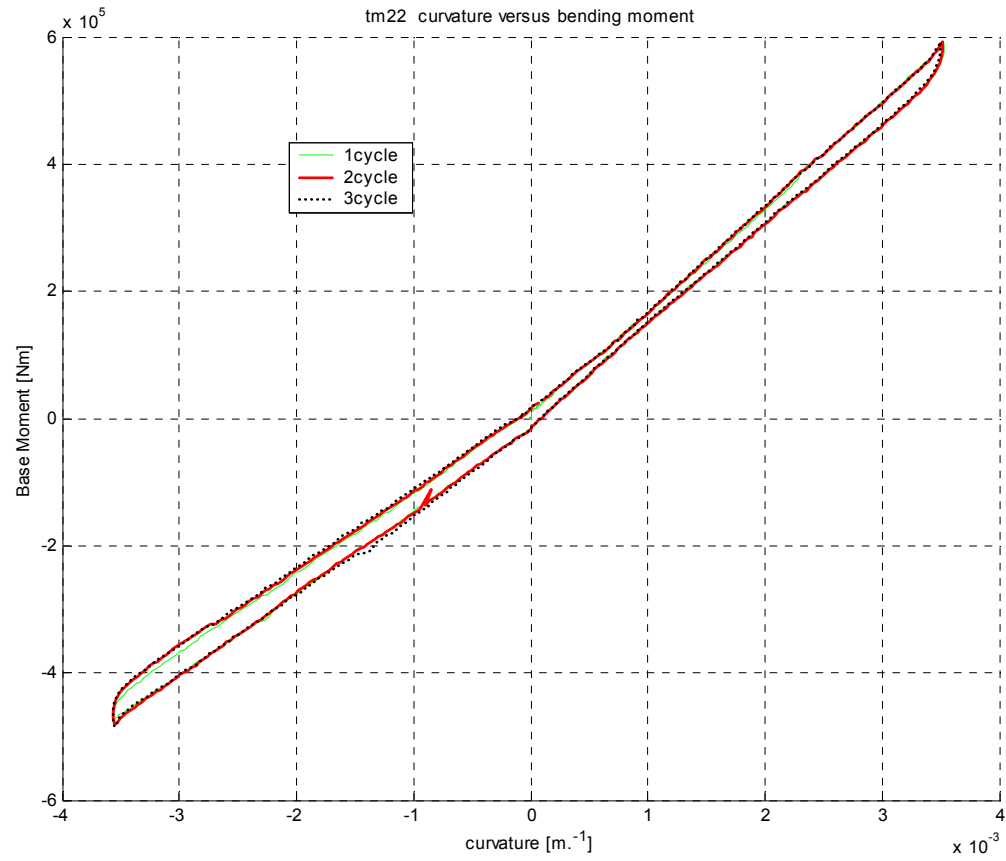
Figure 77 tm22: Hysteresis cycles.
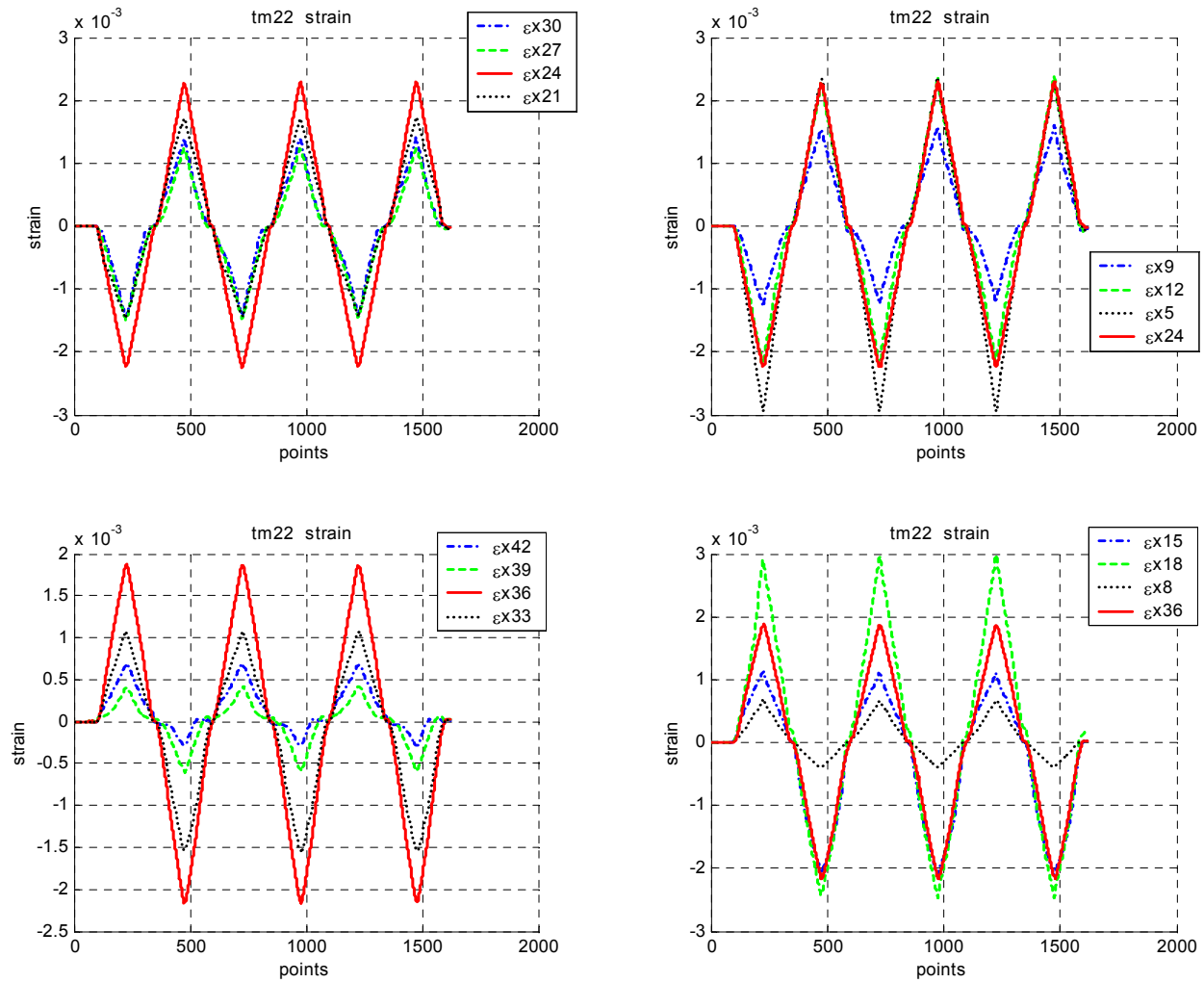
Figure 78 tm22: Longitudinal strains.

99
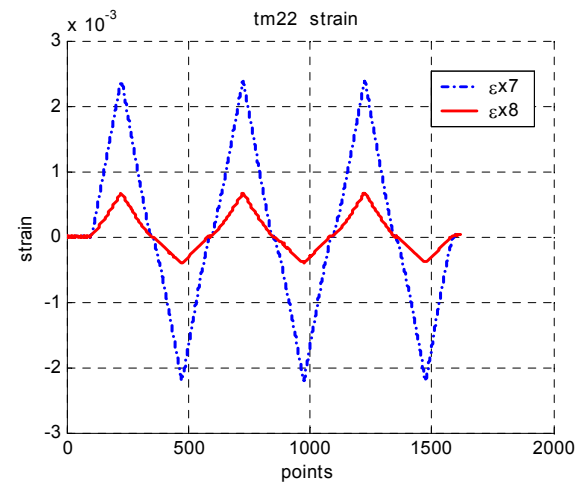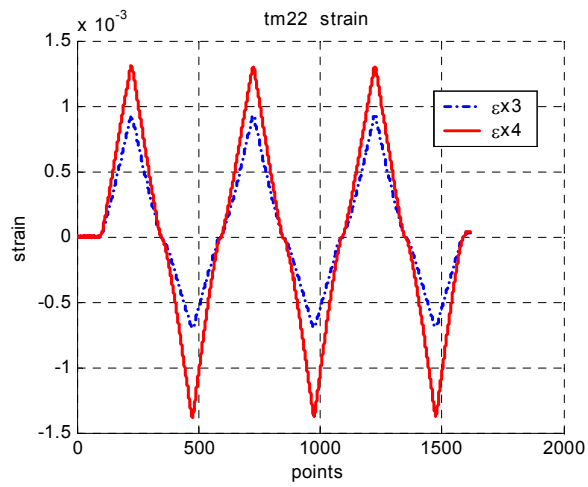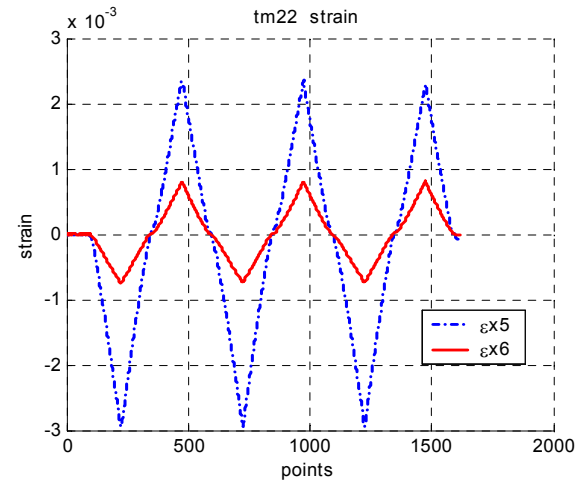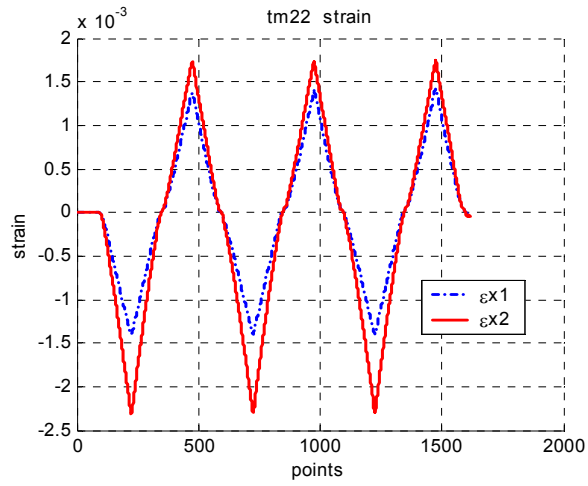
Figure 79 tm22: Internal (left) and intermediate joint (right) strain gauges.
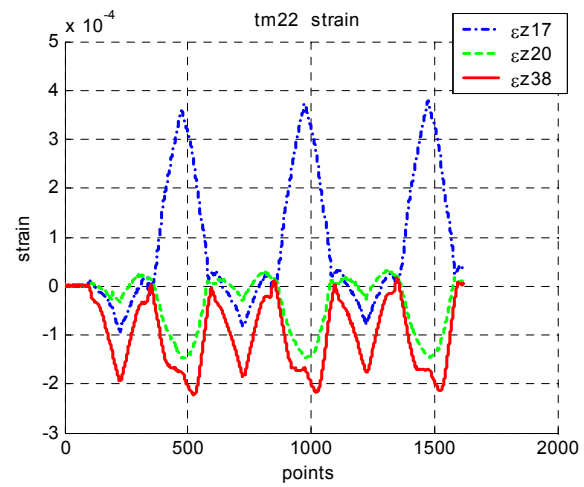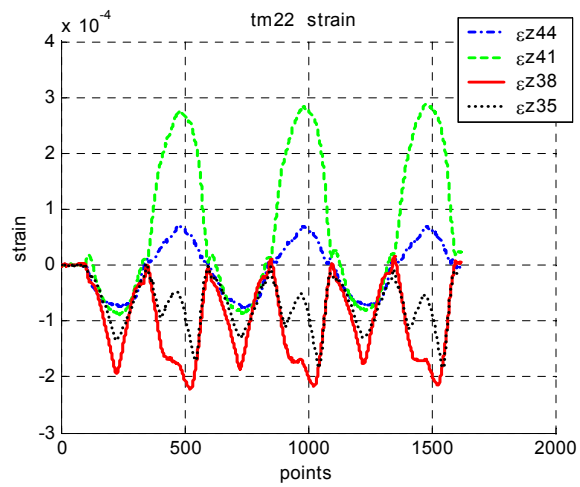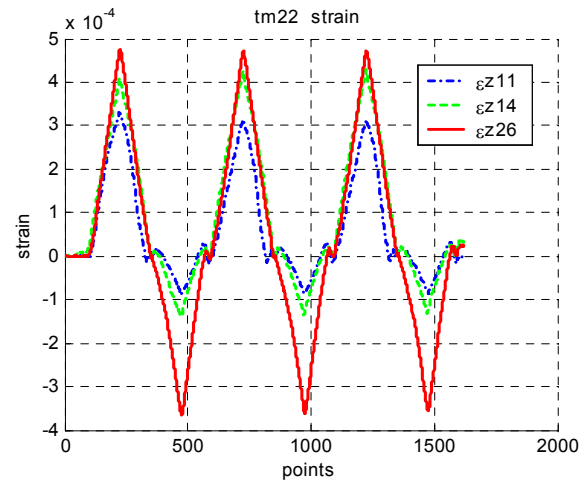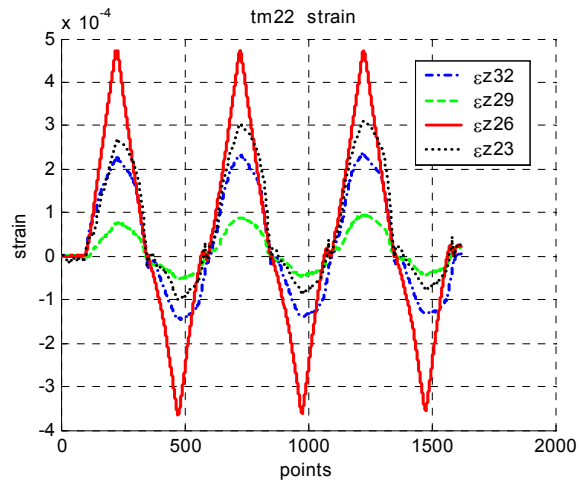
Figure 80 tm22: Hoop strains.
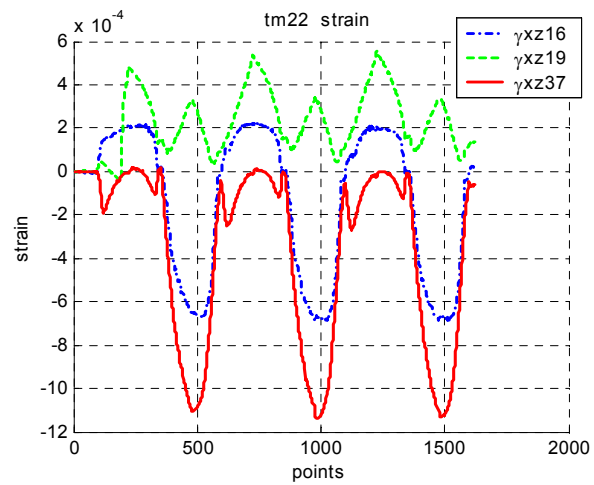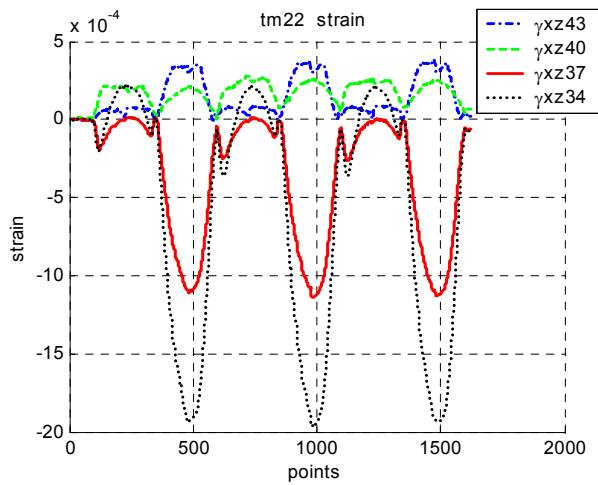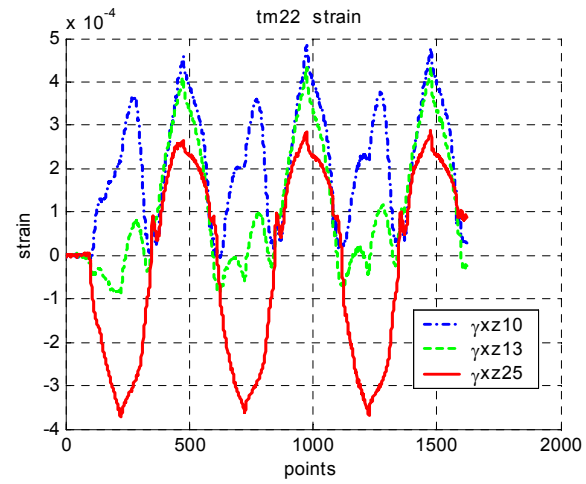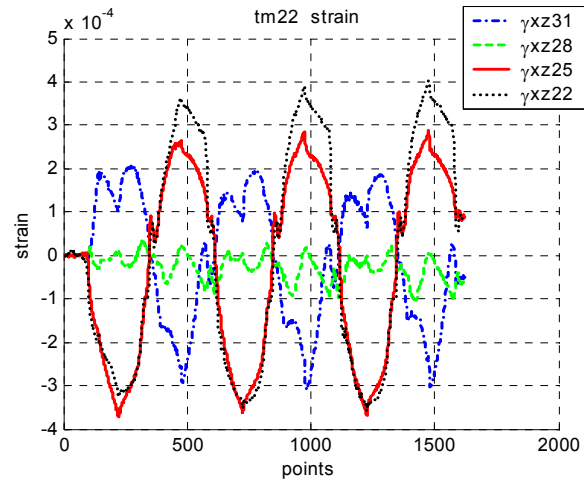
Figure 81 tm22: Shear strains.
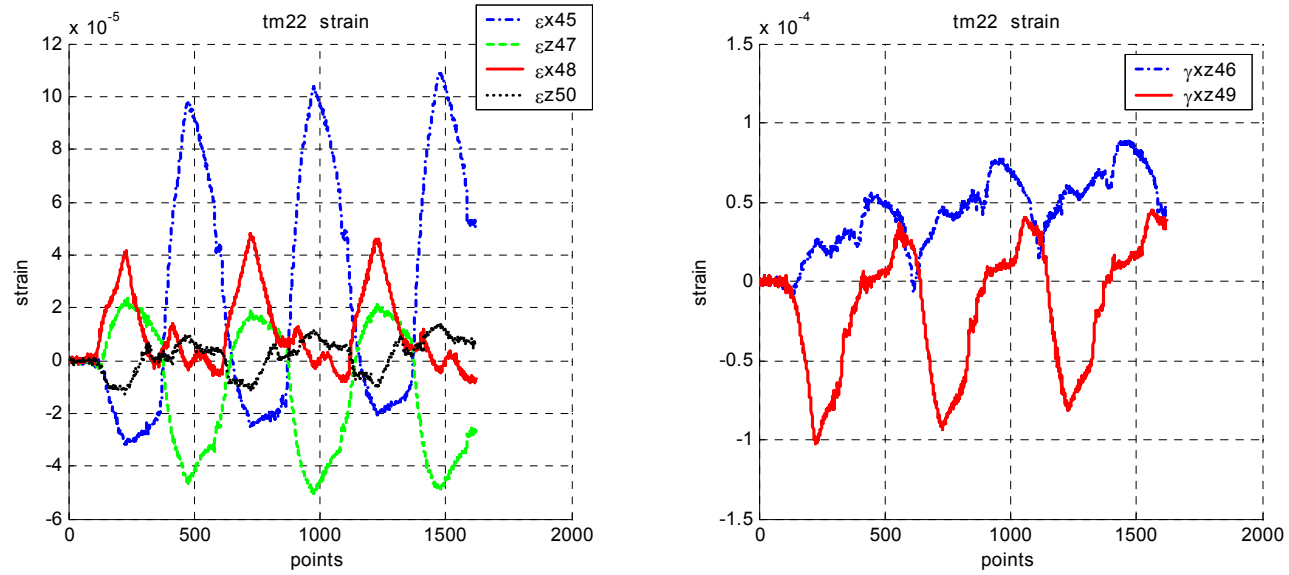
Figure 82 tm22: Strain on flange of base steel joint.
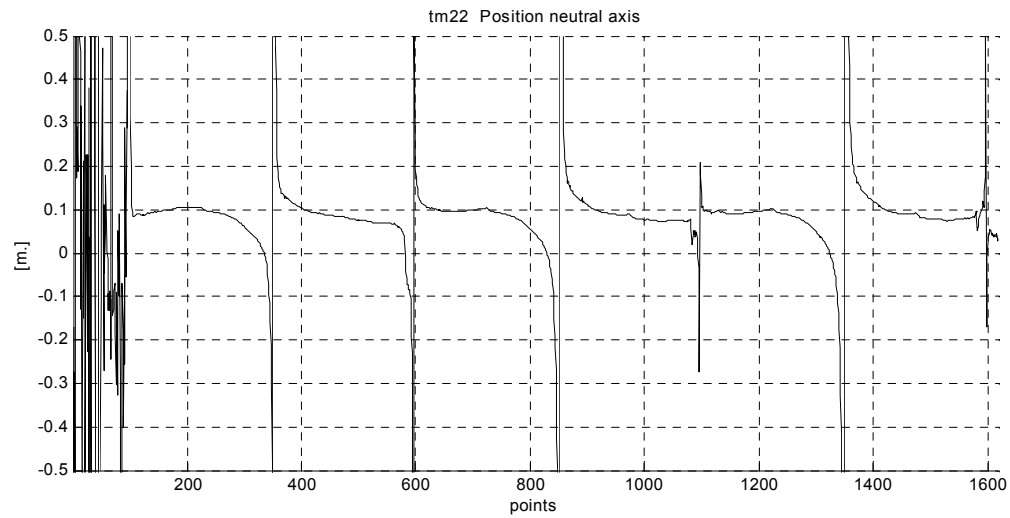
Figure 83 tm22: Position of neutral axis.

103
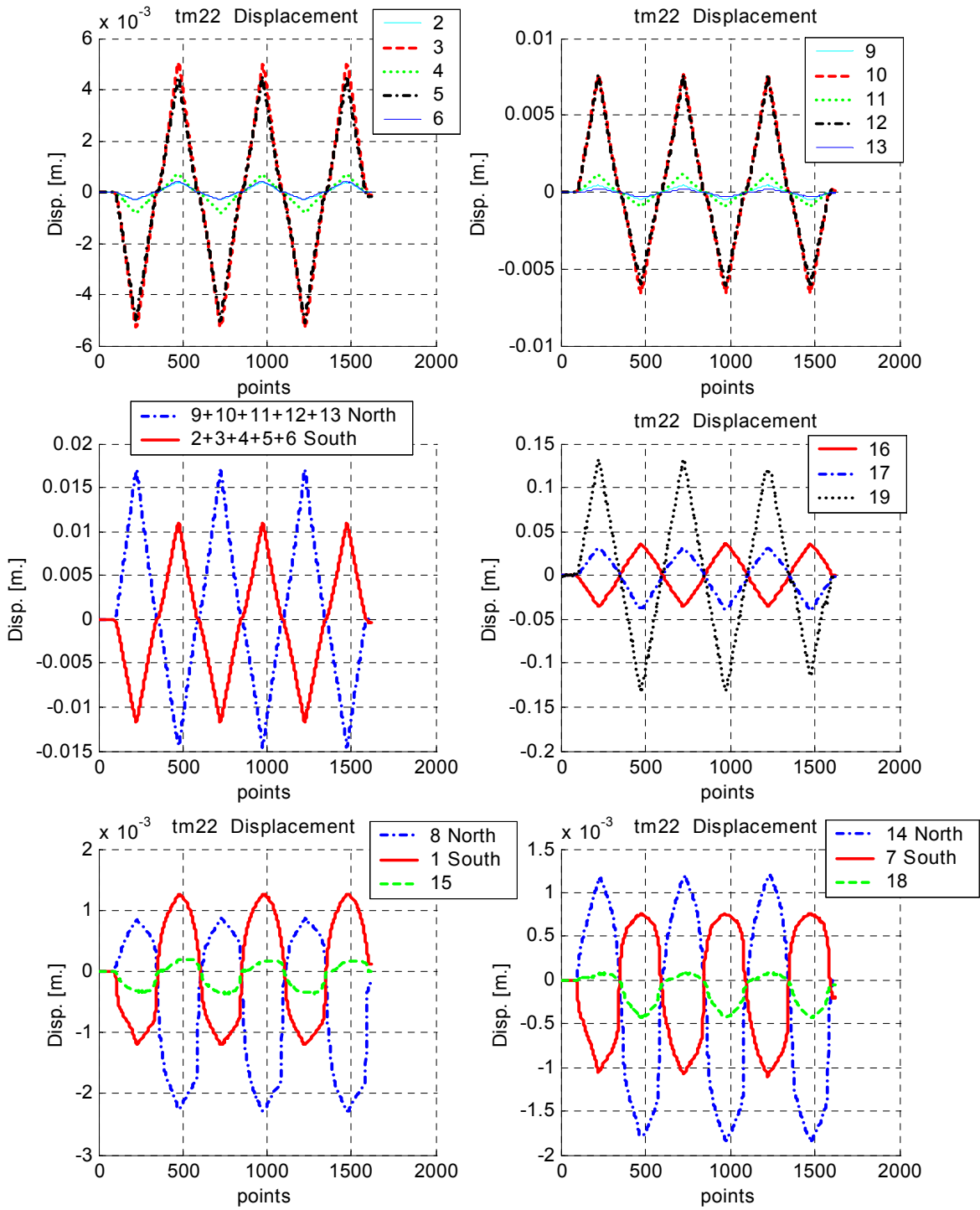
Figure 84 tm22: Displacement transducers.
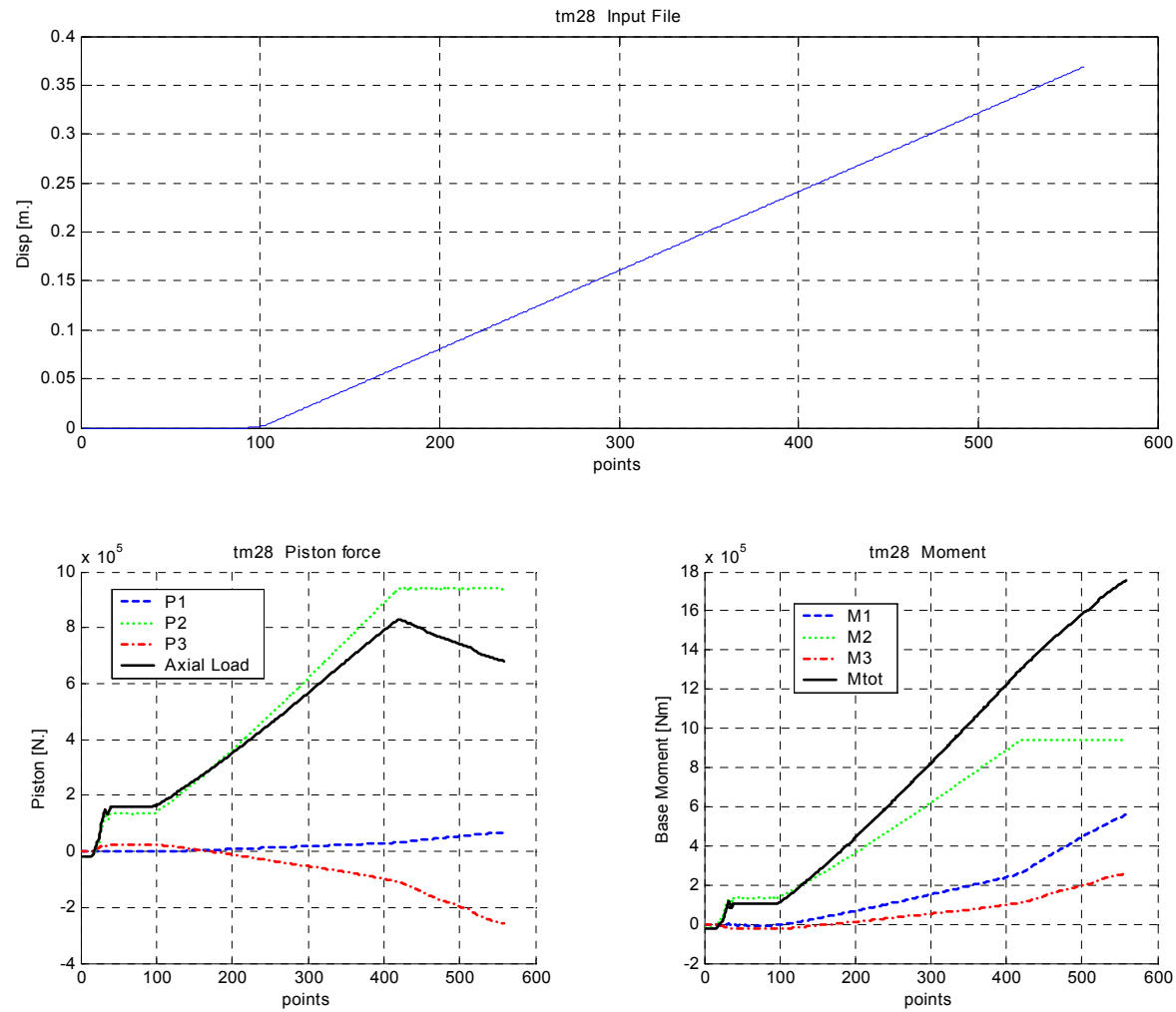
Figure 85 tm28: Input file, Piston forces and Moments.
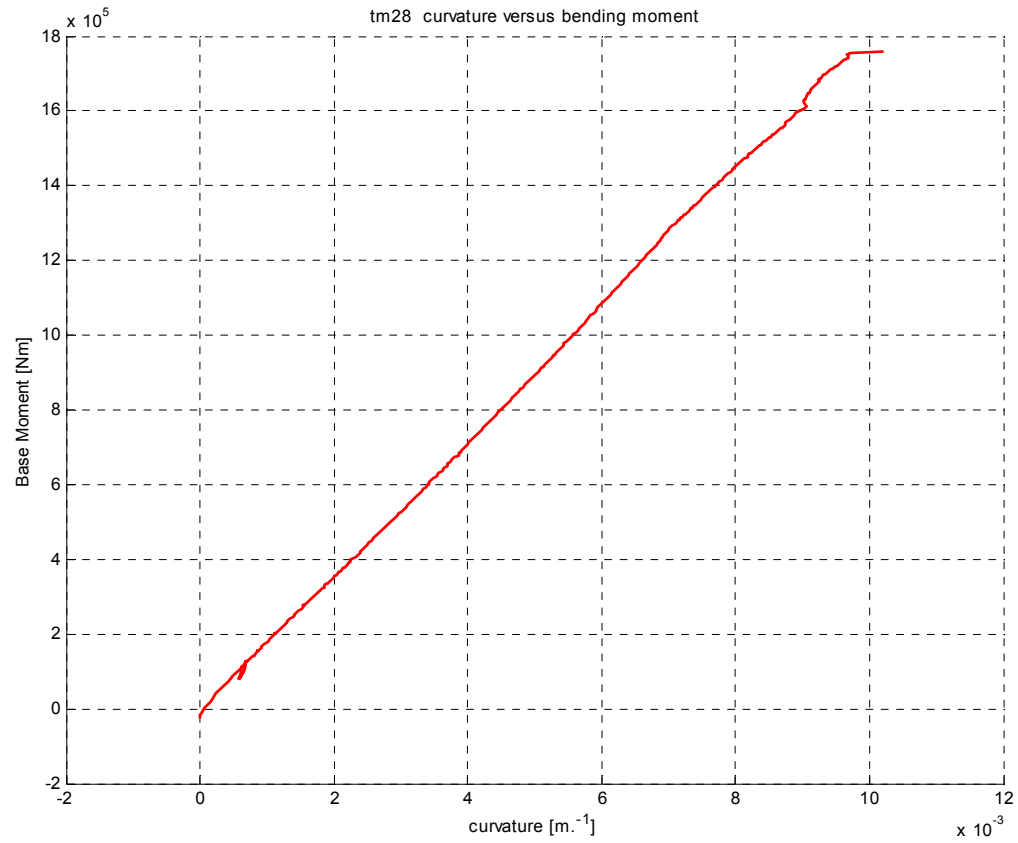
Figure 86 tm28: Hysteresis cycles.
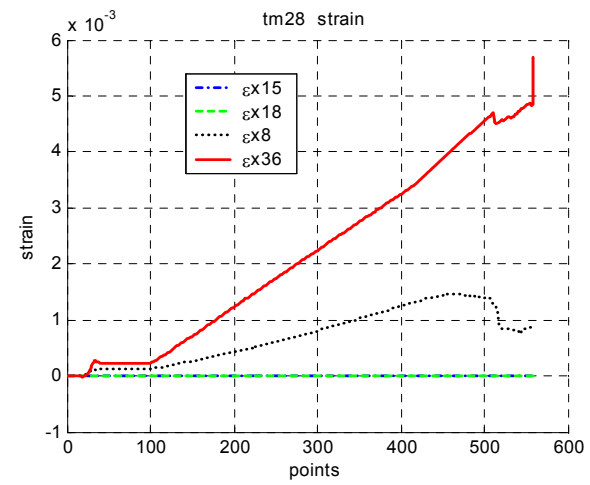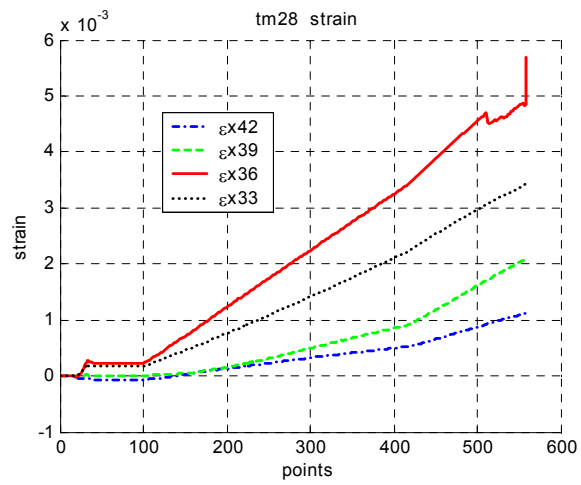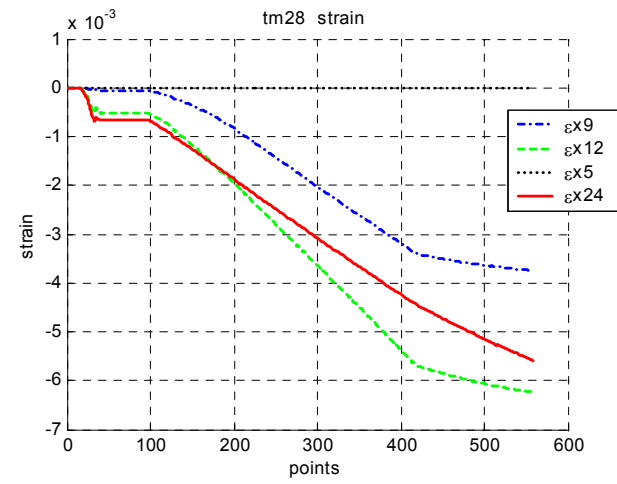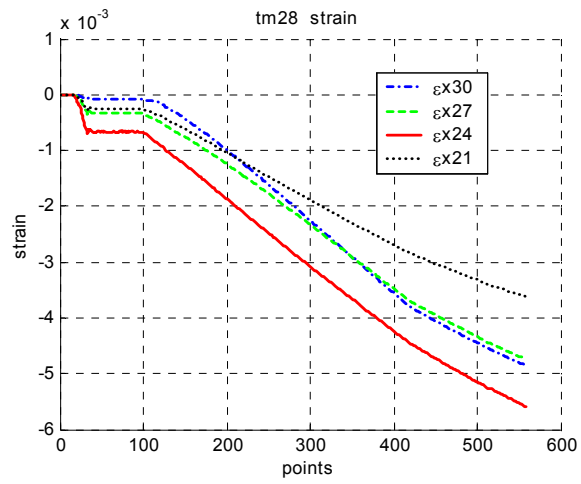
Figure 87 tm28: Longitudinal strains.
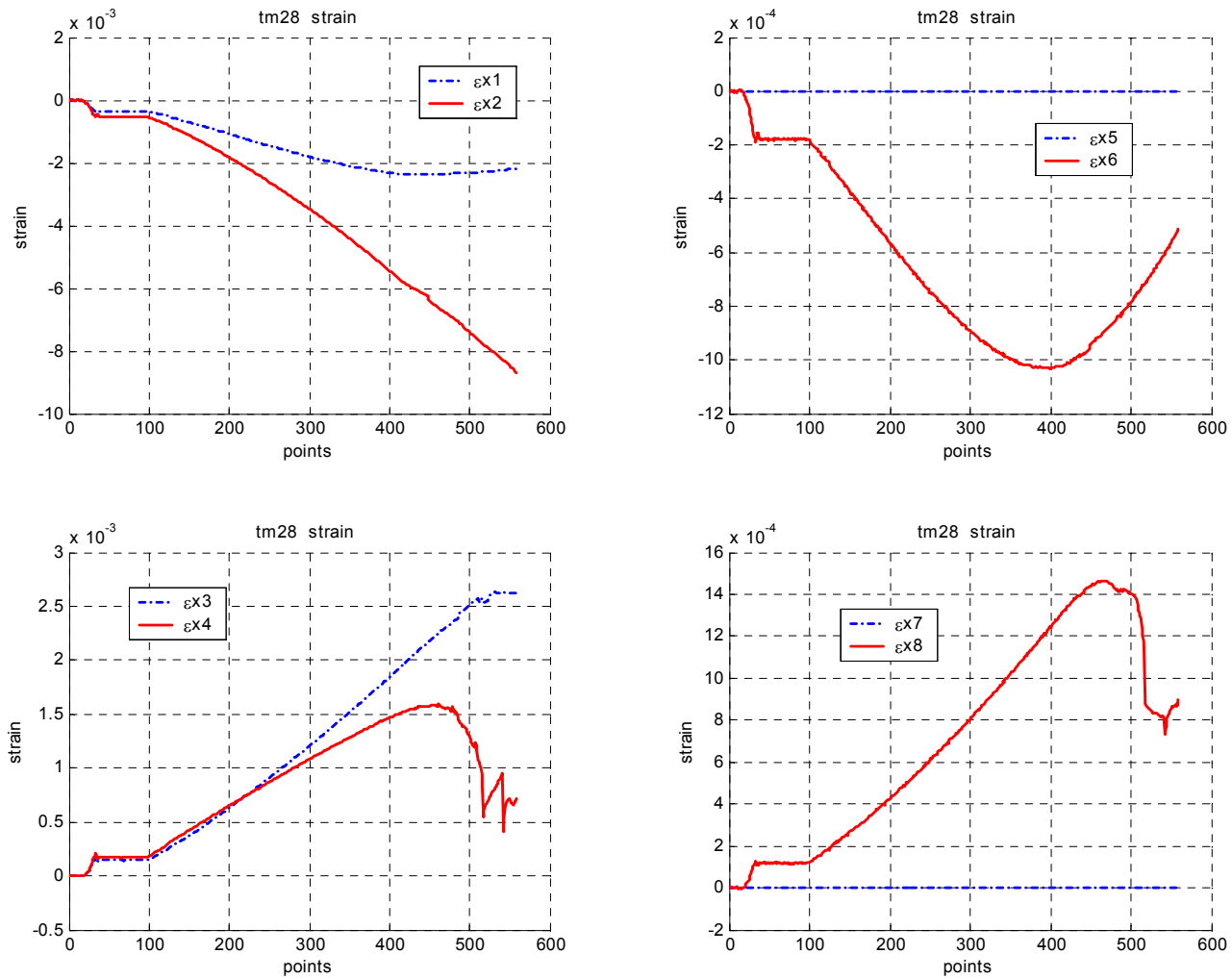
Figure 88 tm28: Internal (left) and intermediate joint (right) strain gauges.
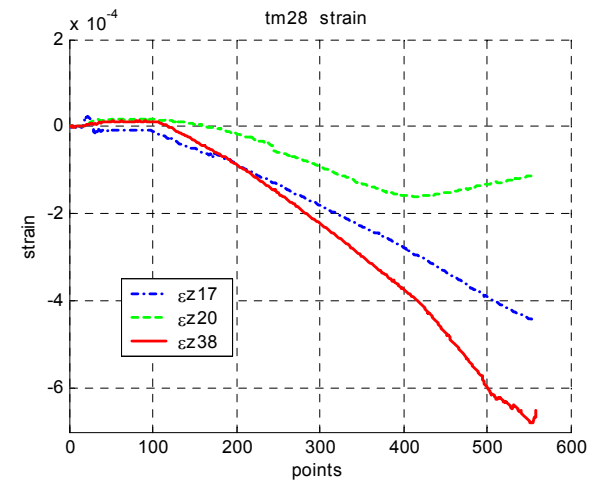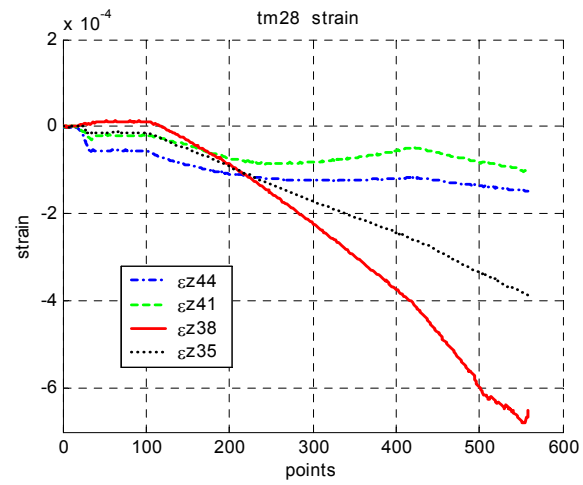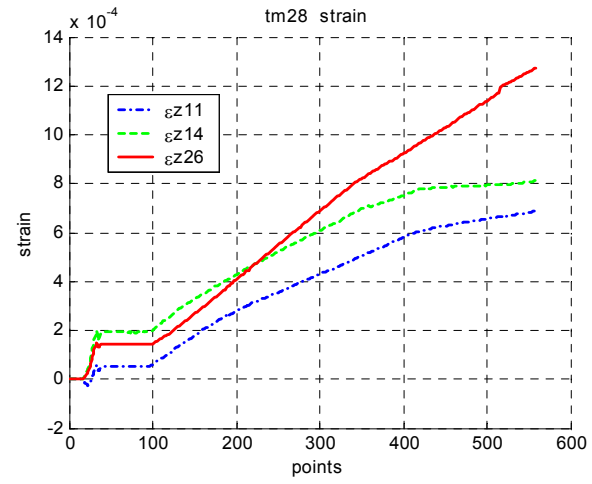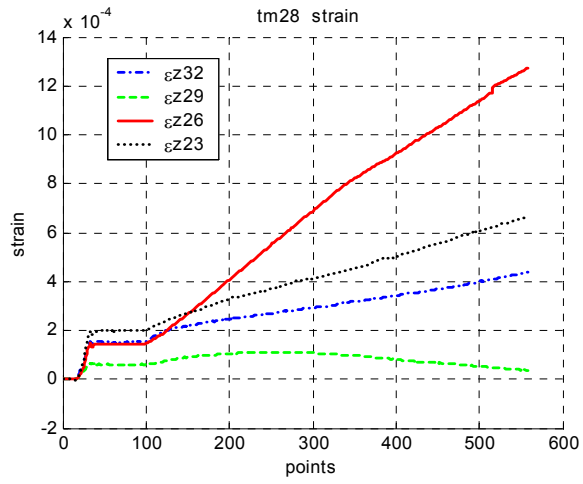
Figure 89 tm28: Hoop strains.
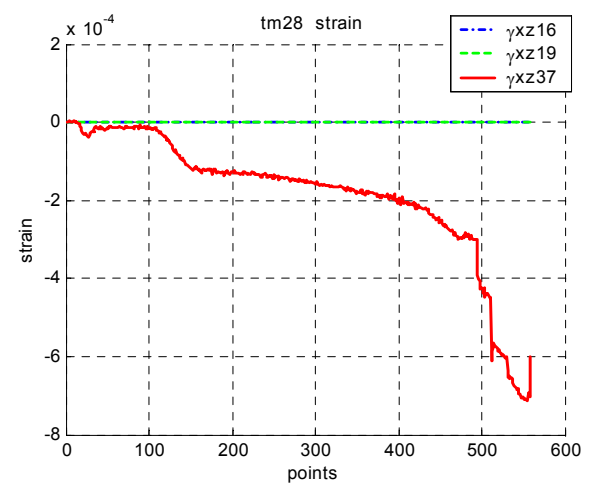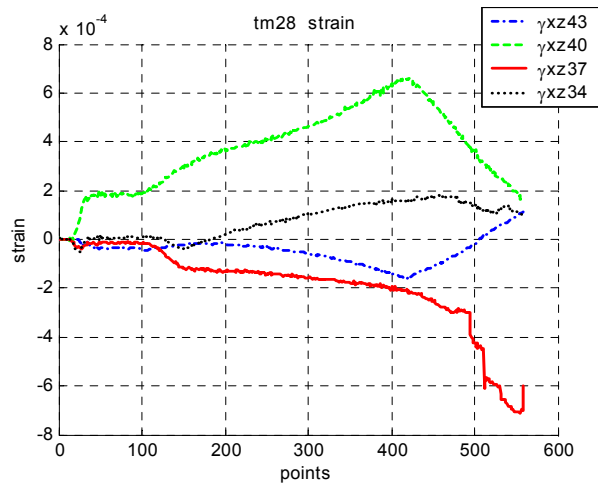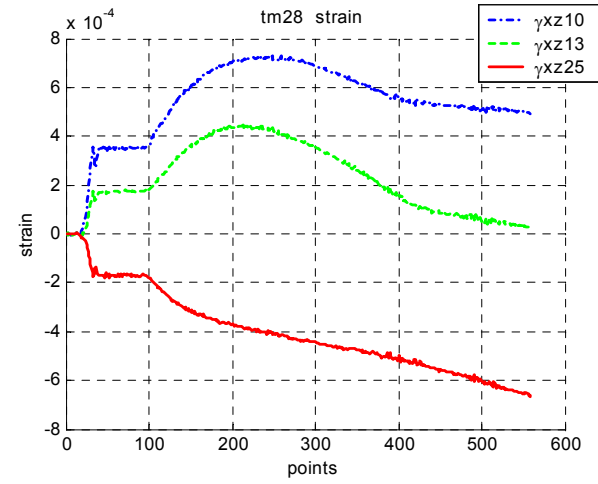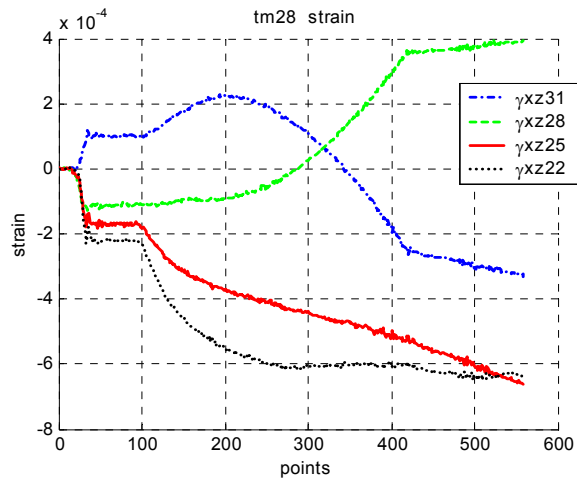
Figure 90 tm28: Shear strains.

110
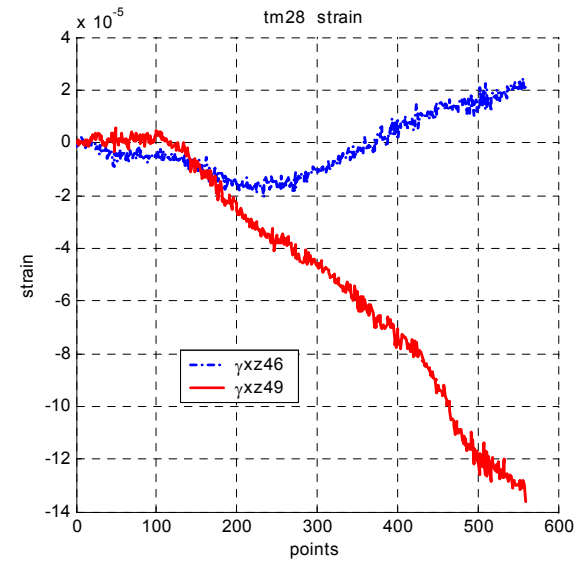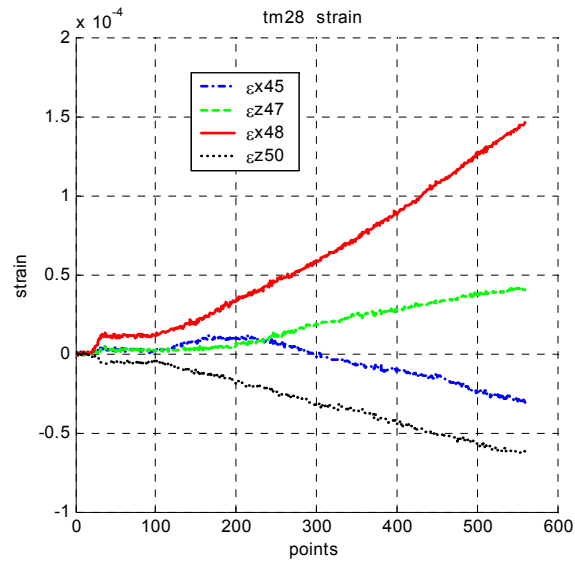
Figure 91 tm28: Strain on flange of base steel joint.
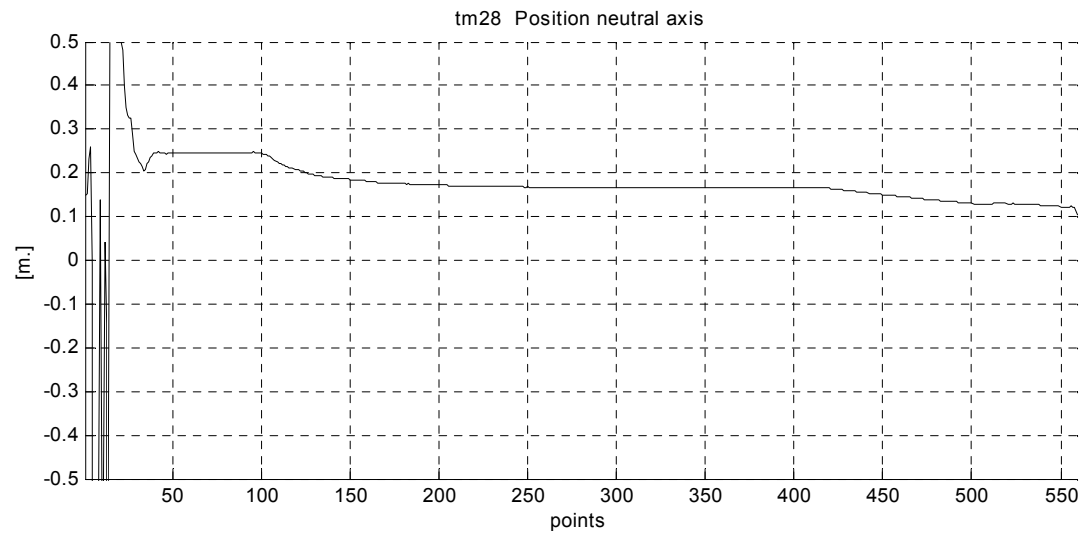
Figure 92 tm28: Position of neutral axis.
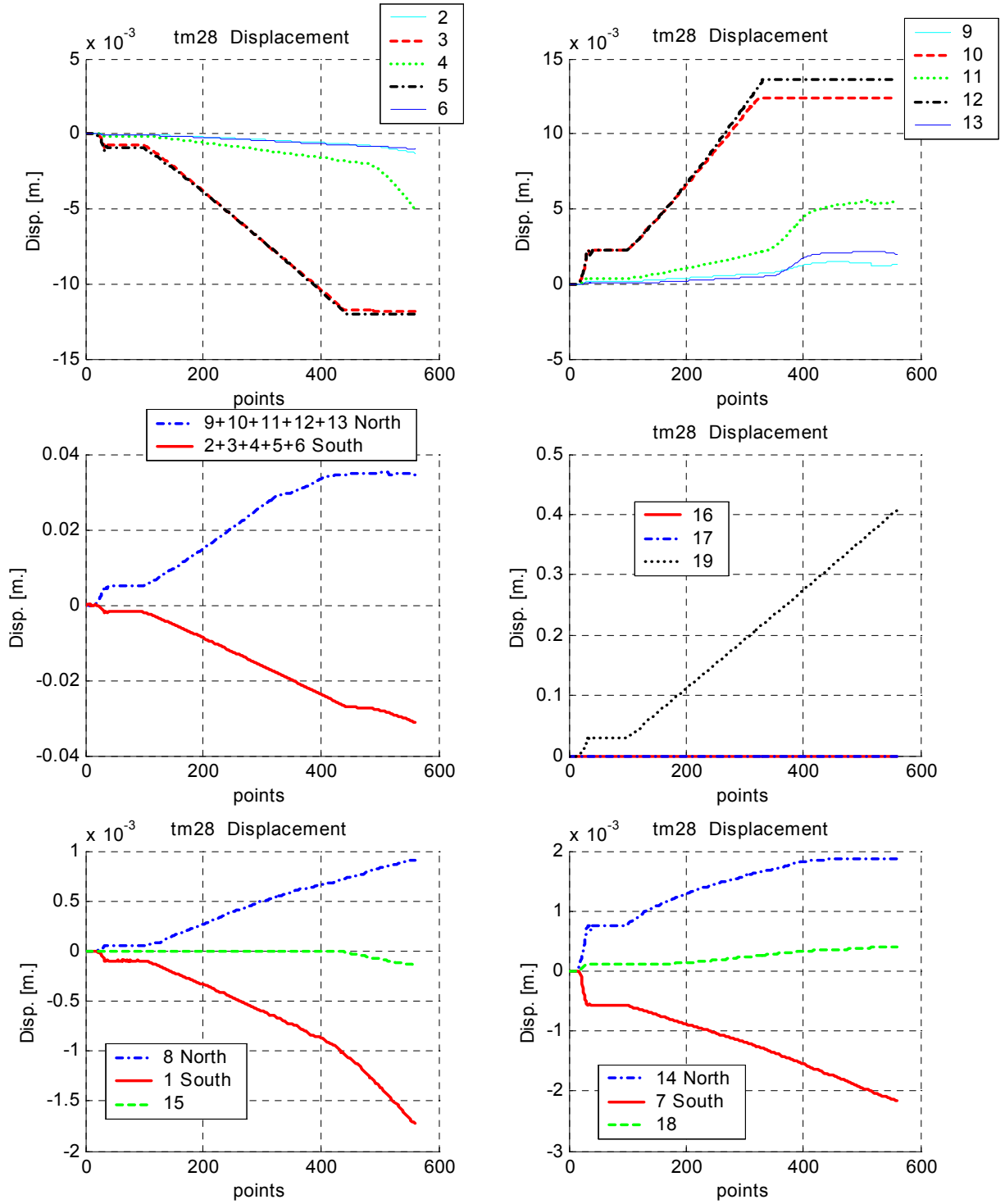
Figure 93 tm28: Displacement transducers.
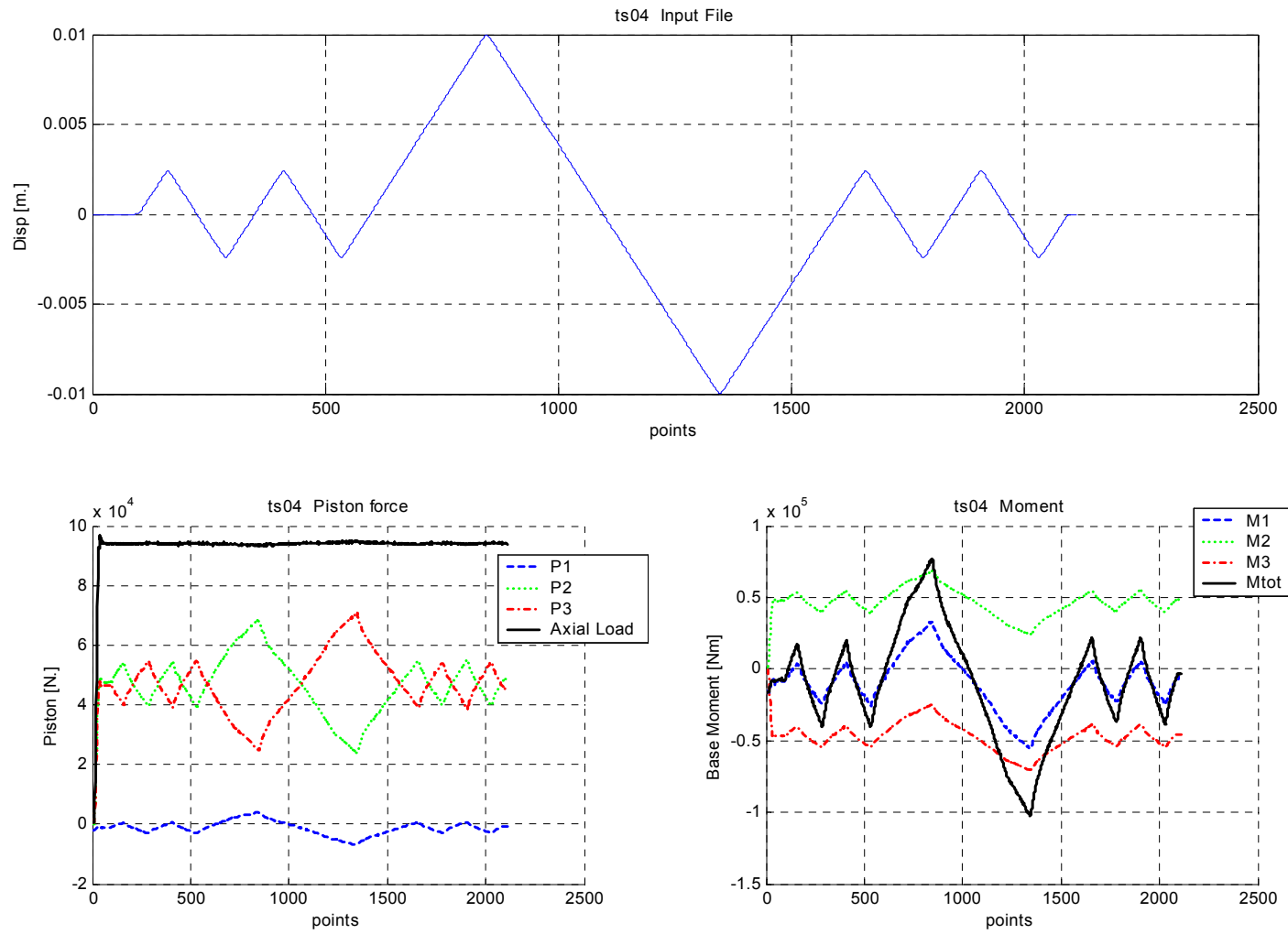
Figure 94 ts04: Input file, Piston forces and Moments.
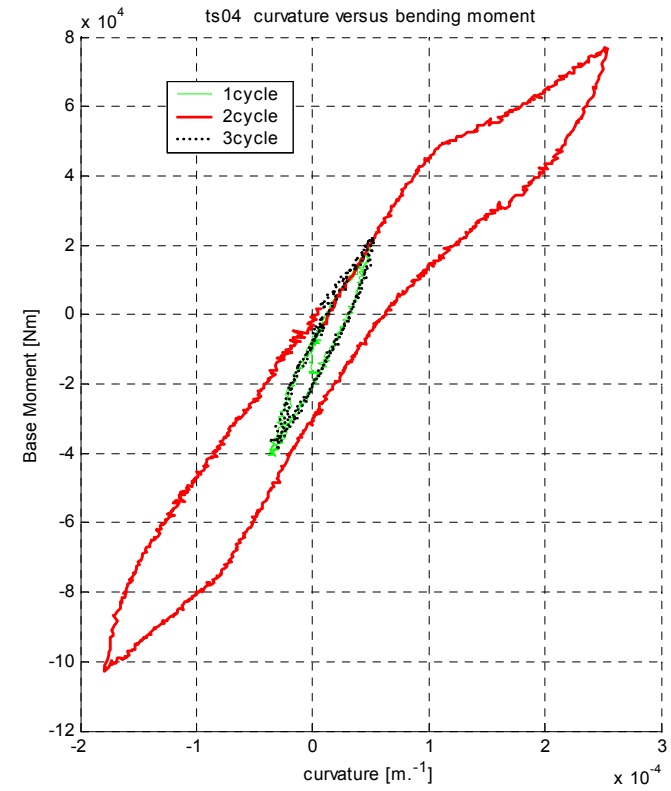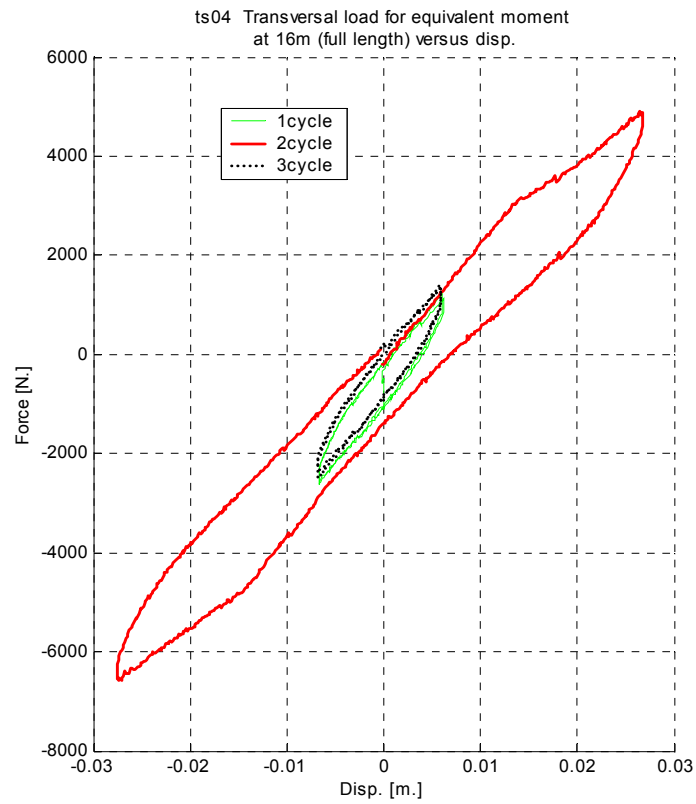
Figure 95 ts04: Hysteresis cycles.
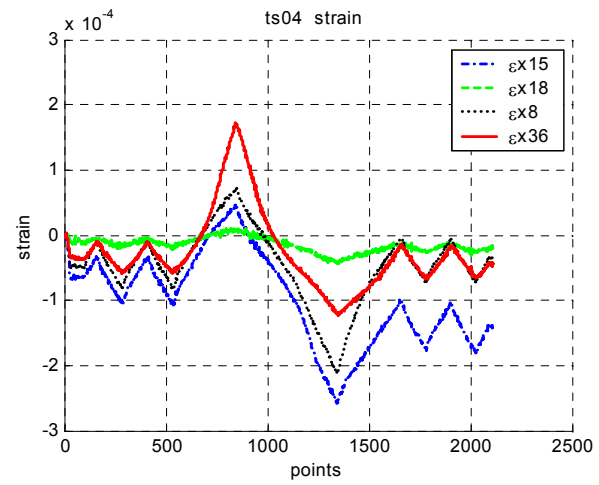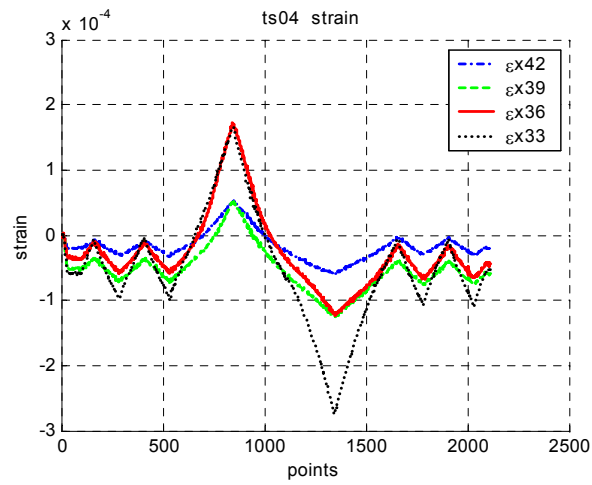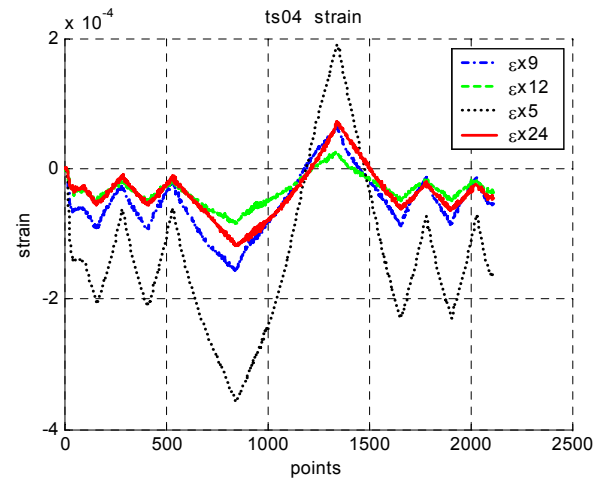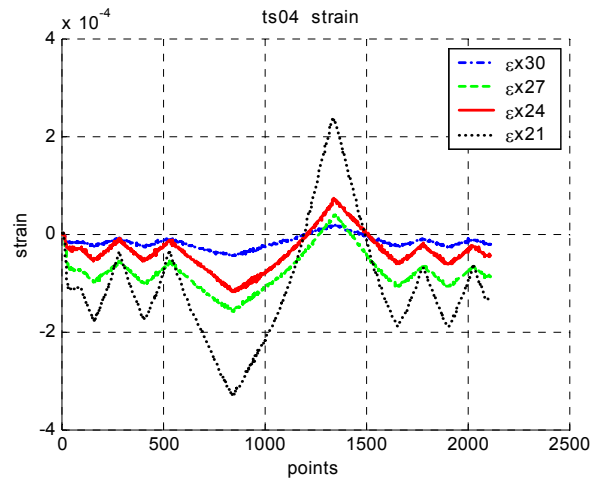
Figure 96 ts04: Longitudinal strains.
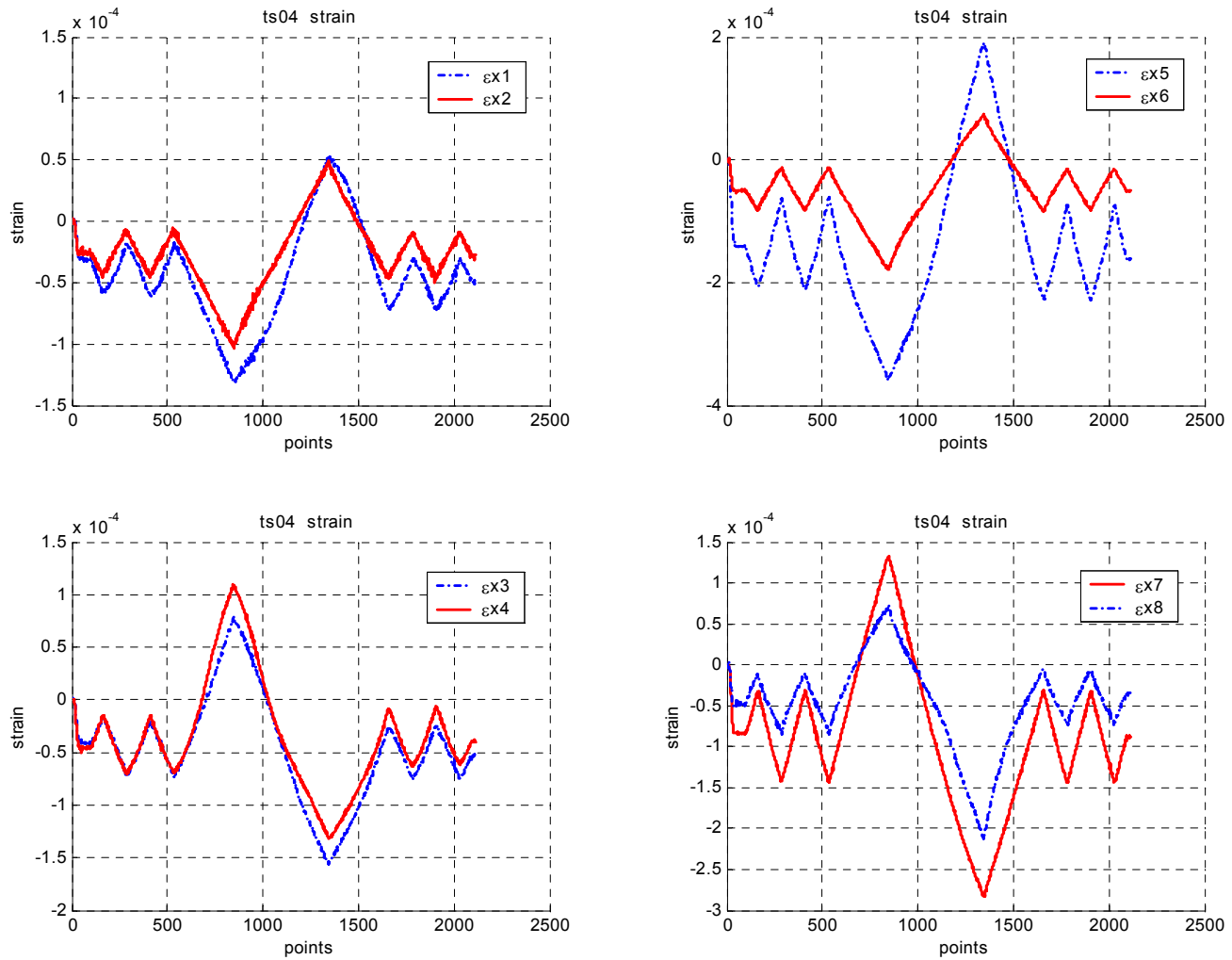
Figure 97 ts04: Internal (left) and intermediate joint (right) strain gauges.
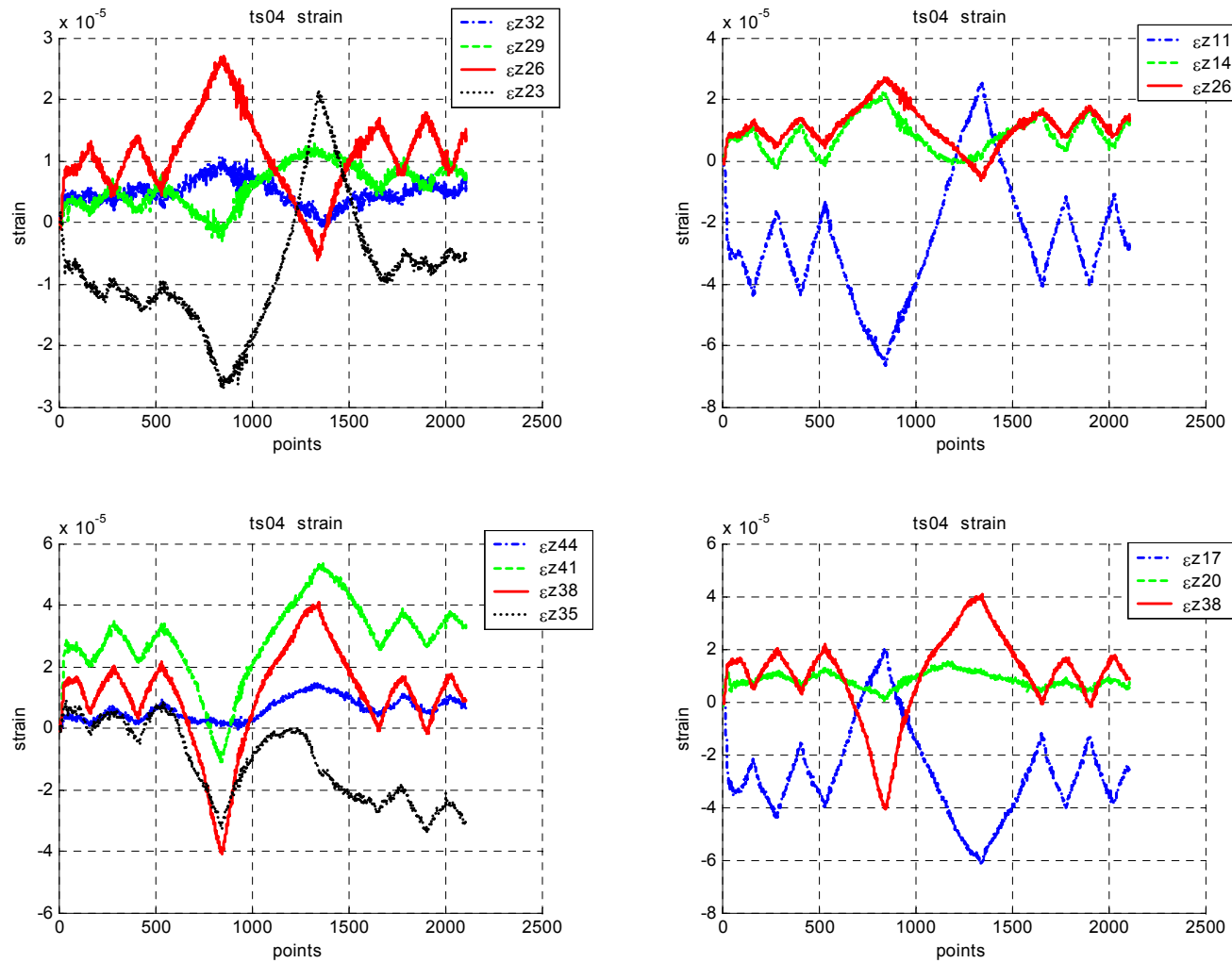
Figure 98 ts04: Hoop strains.

117
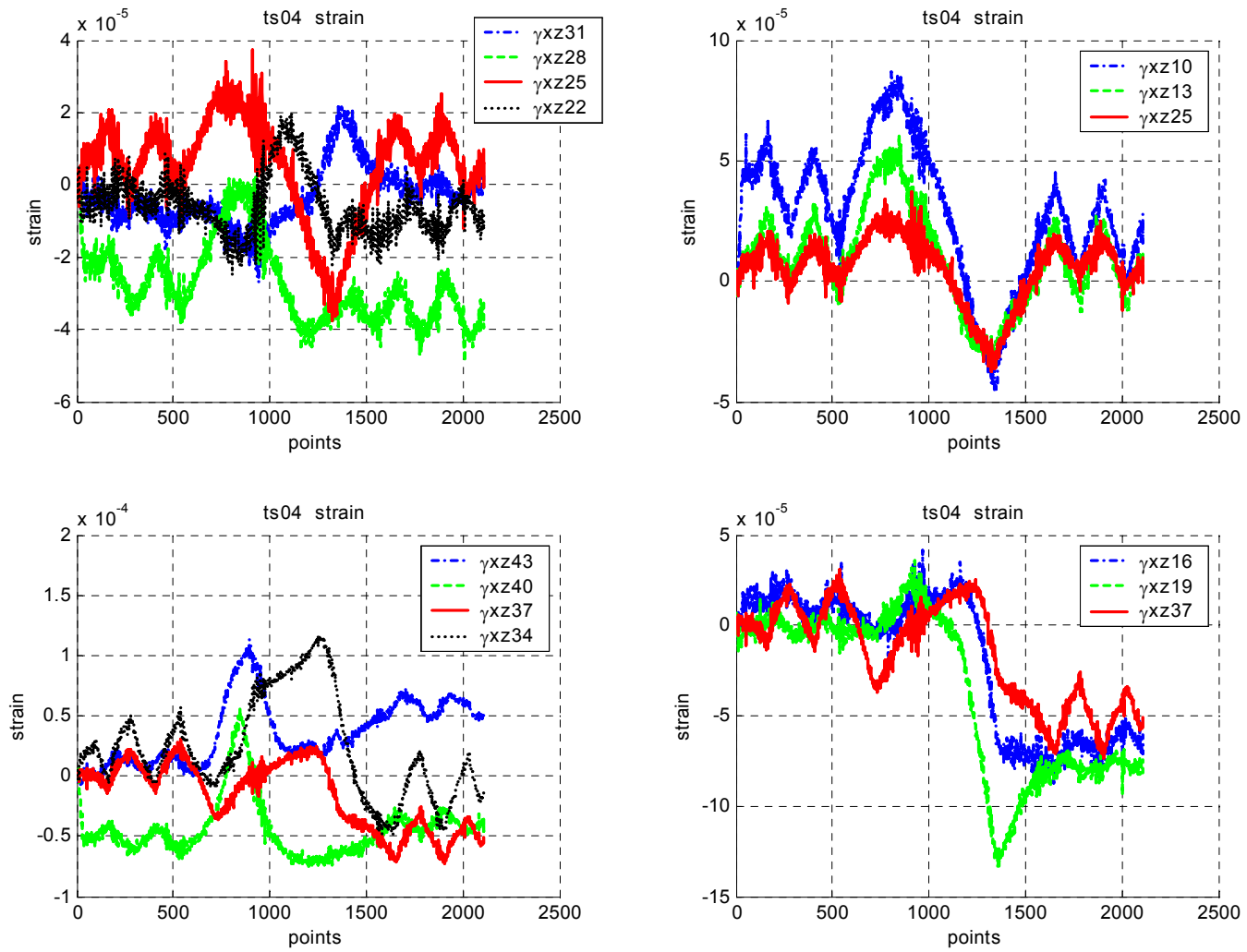
Figure 99 ts04: Shear strains.
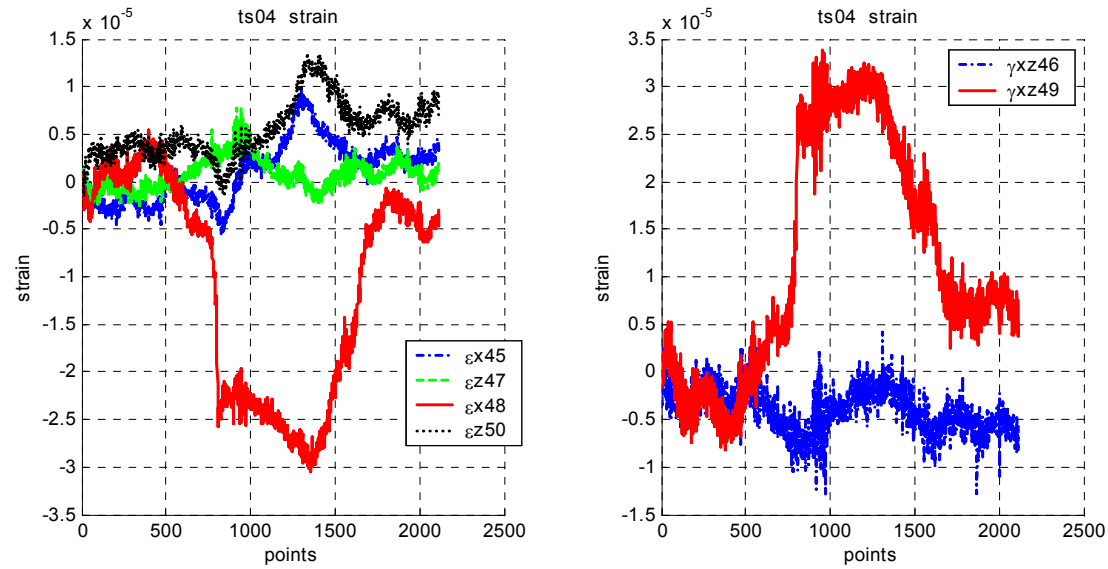
Figure 100 ts04: Strain on flange of base steel joint.
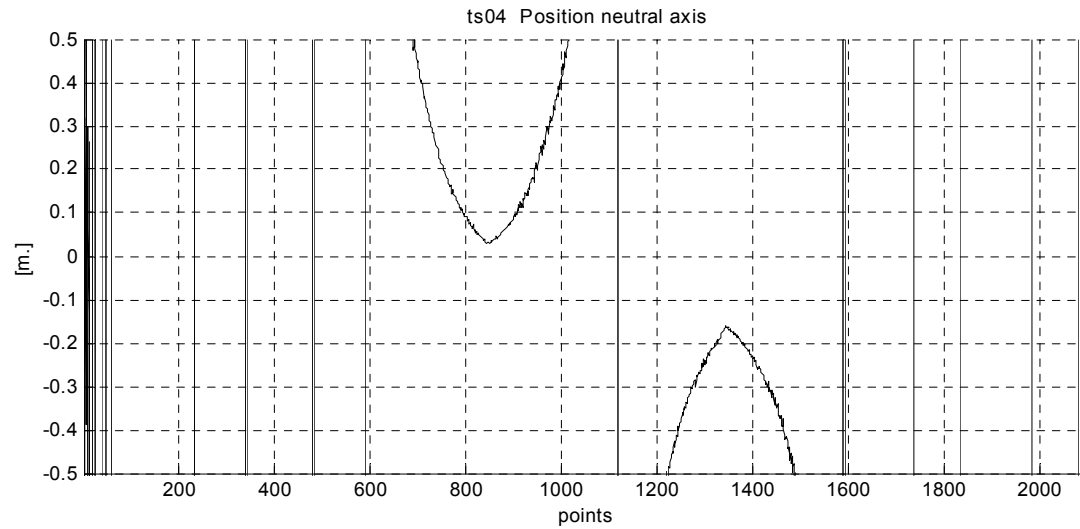
Figure 101 ts04: Position of neutral axis.

119
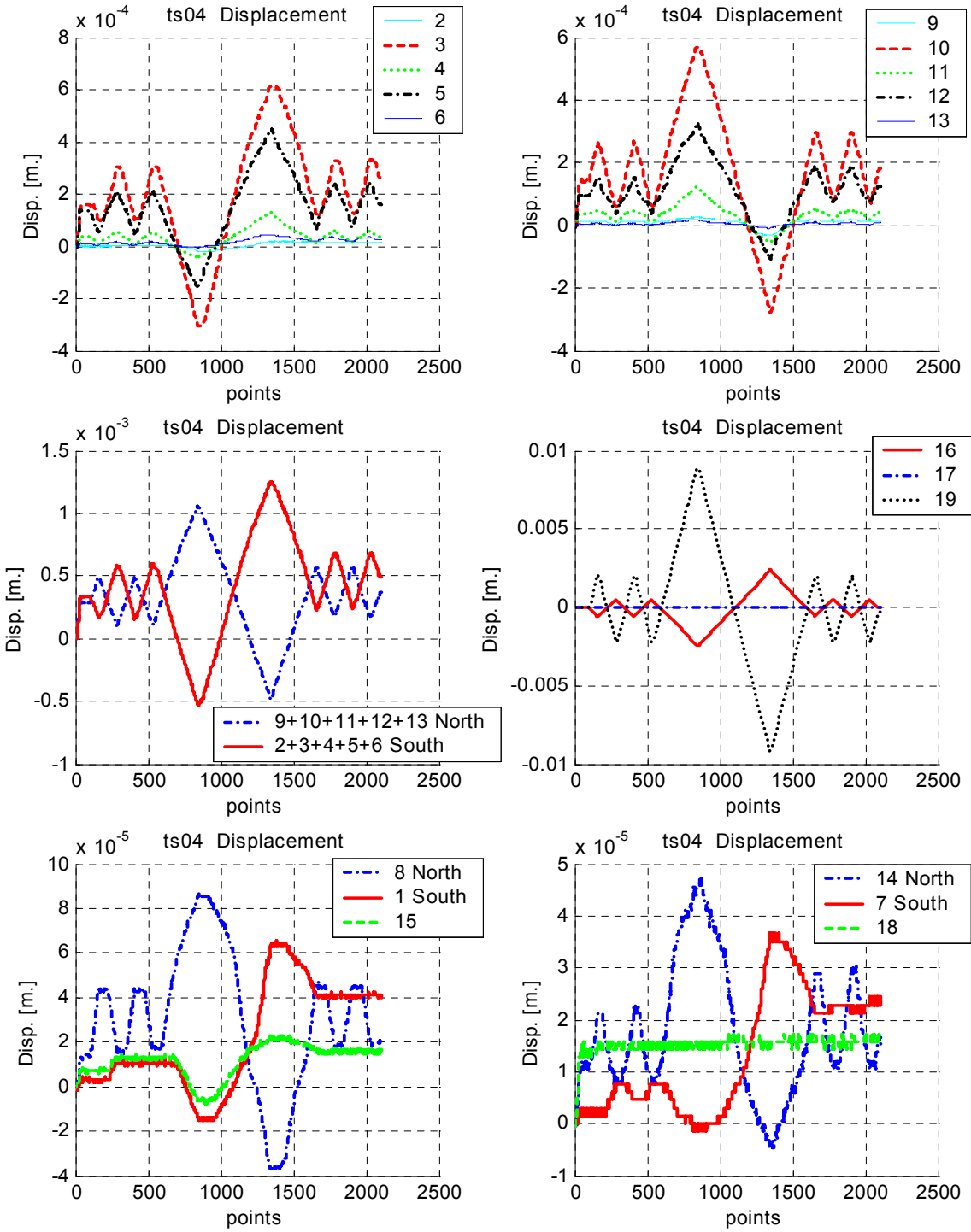
Figure 102 ts04: Displacement transducers.
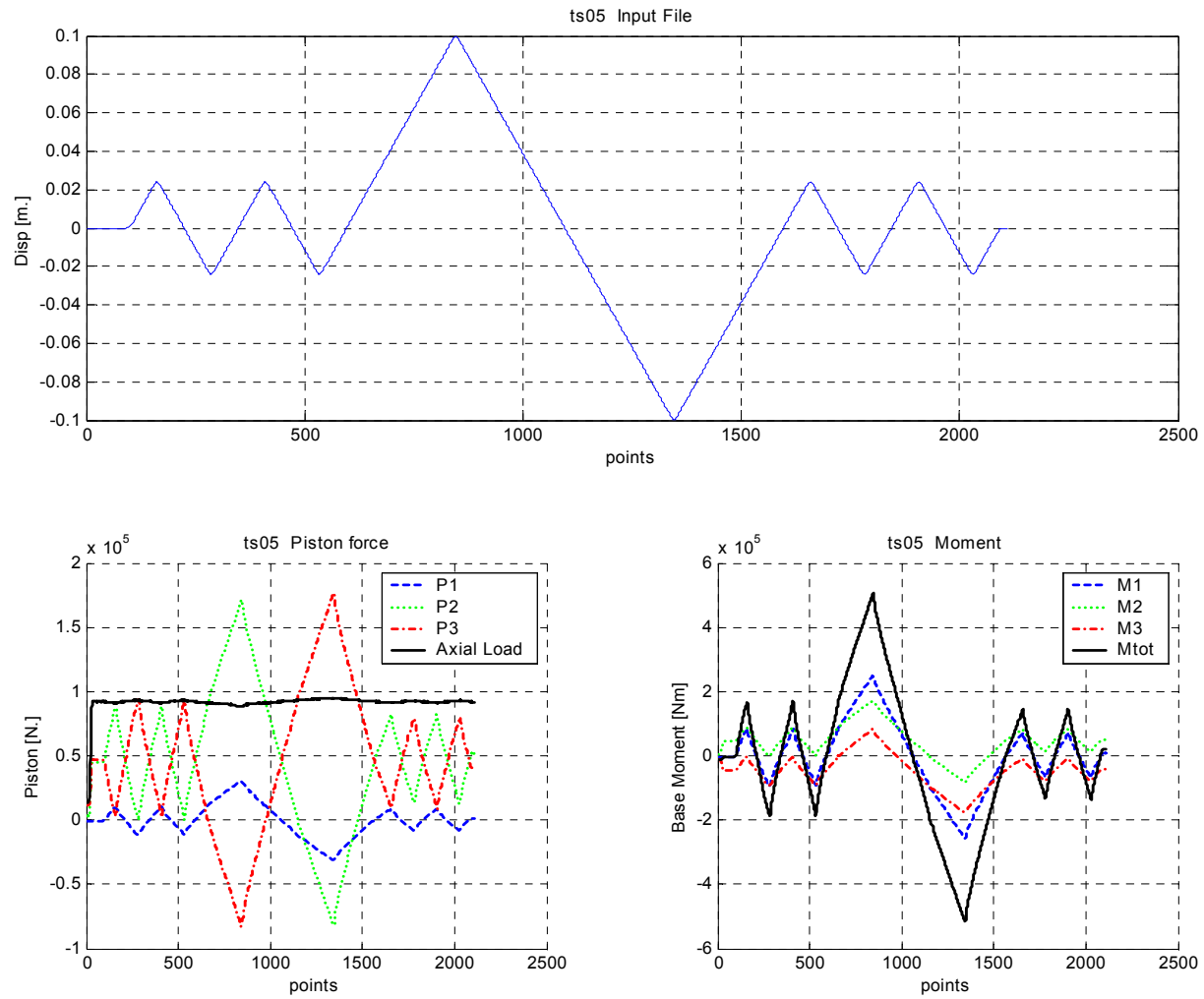
Figure 103 ts05: Input file, Piston forces and Moments.
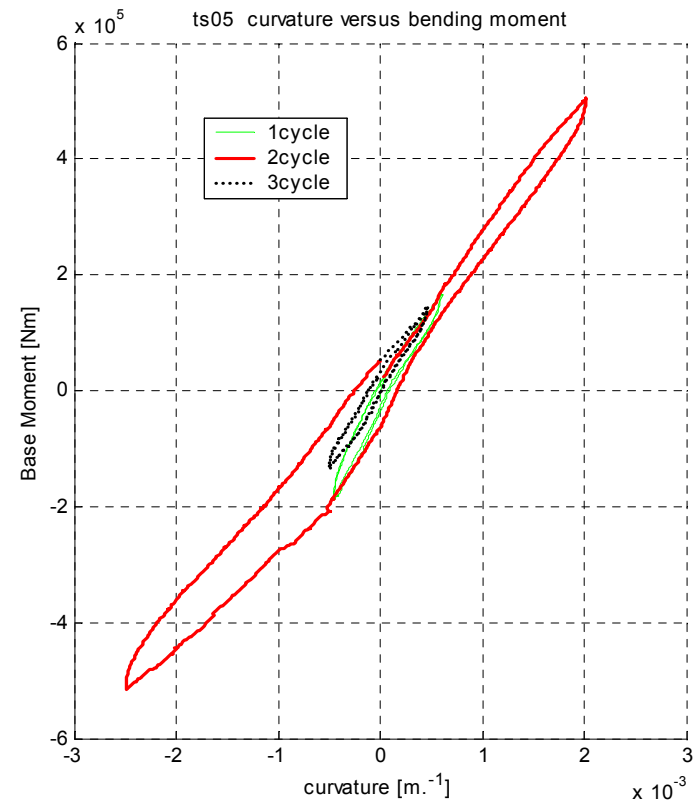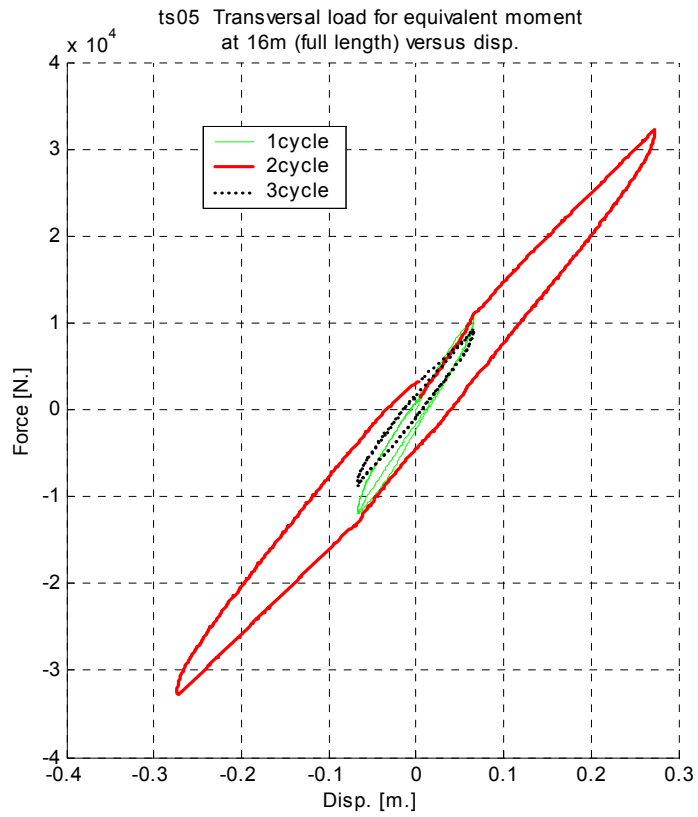
Figure 104 ts05: Hysteresis cycles.
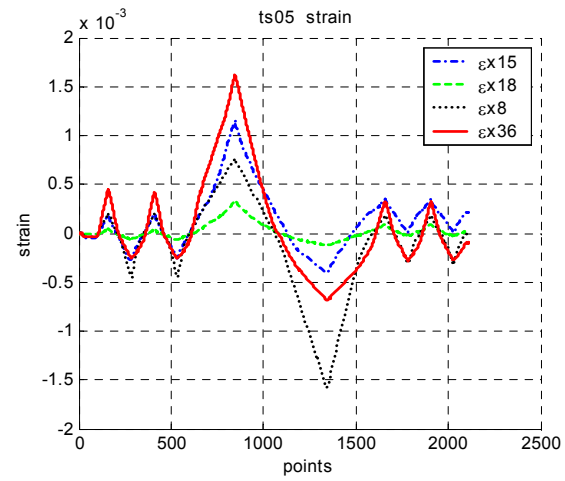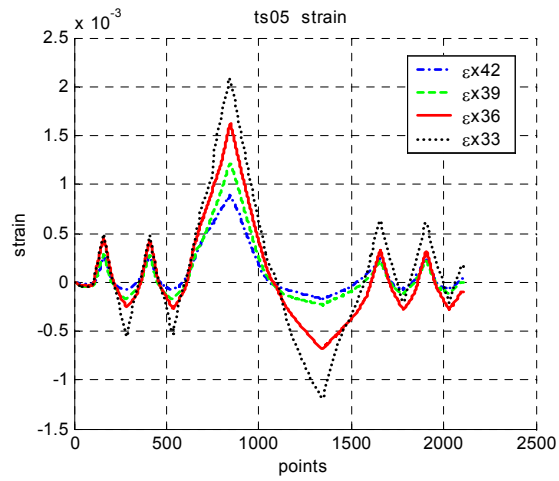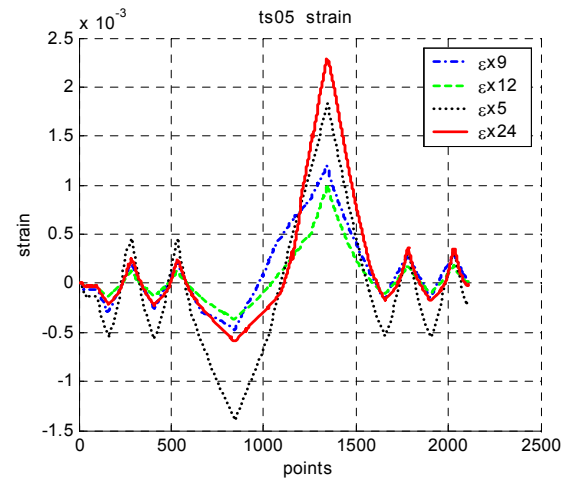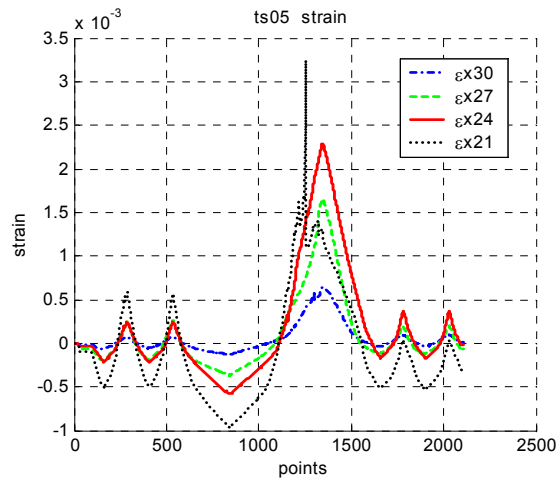
Figure 105 ts05: Longitudinal strains.
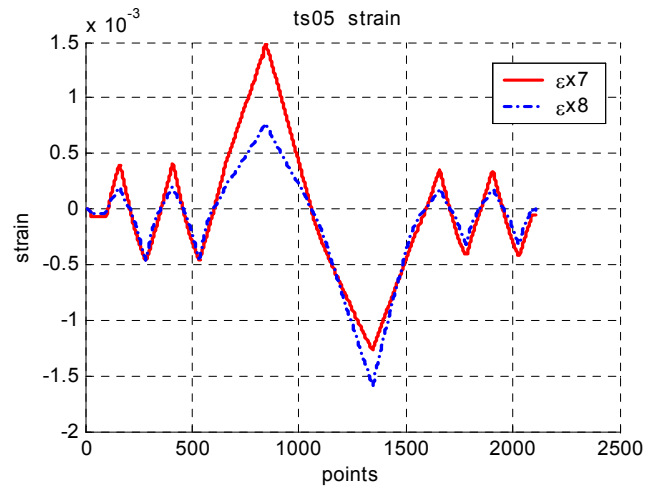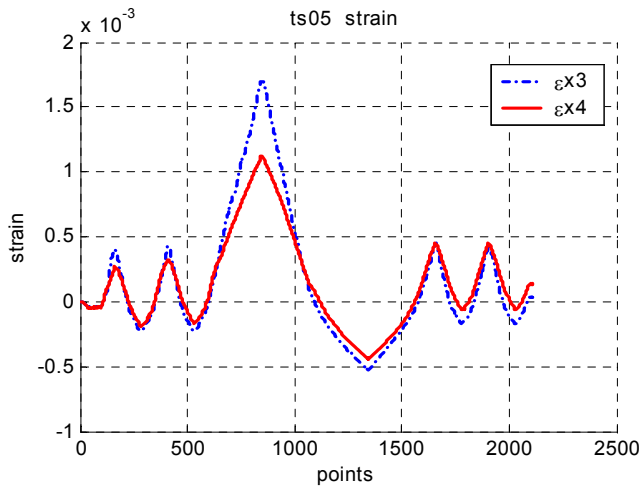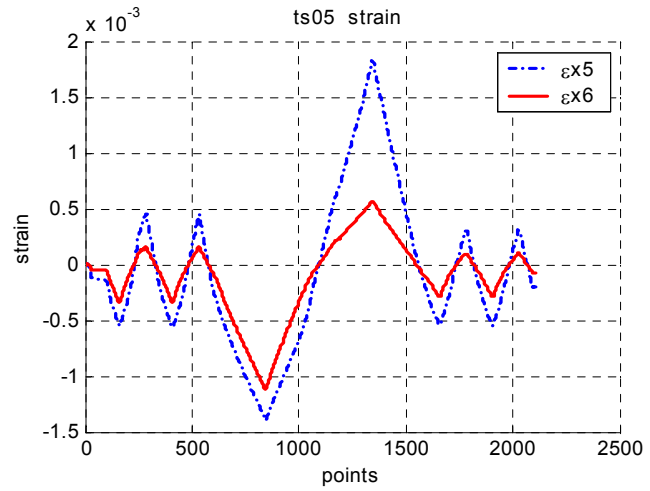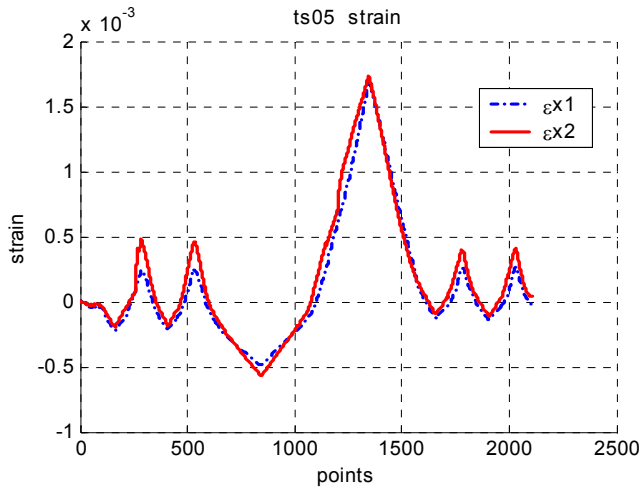
Figure 106 ts05: Internal (left) and intermediate joint (right) strain gauges.
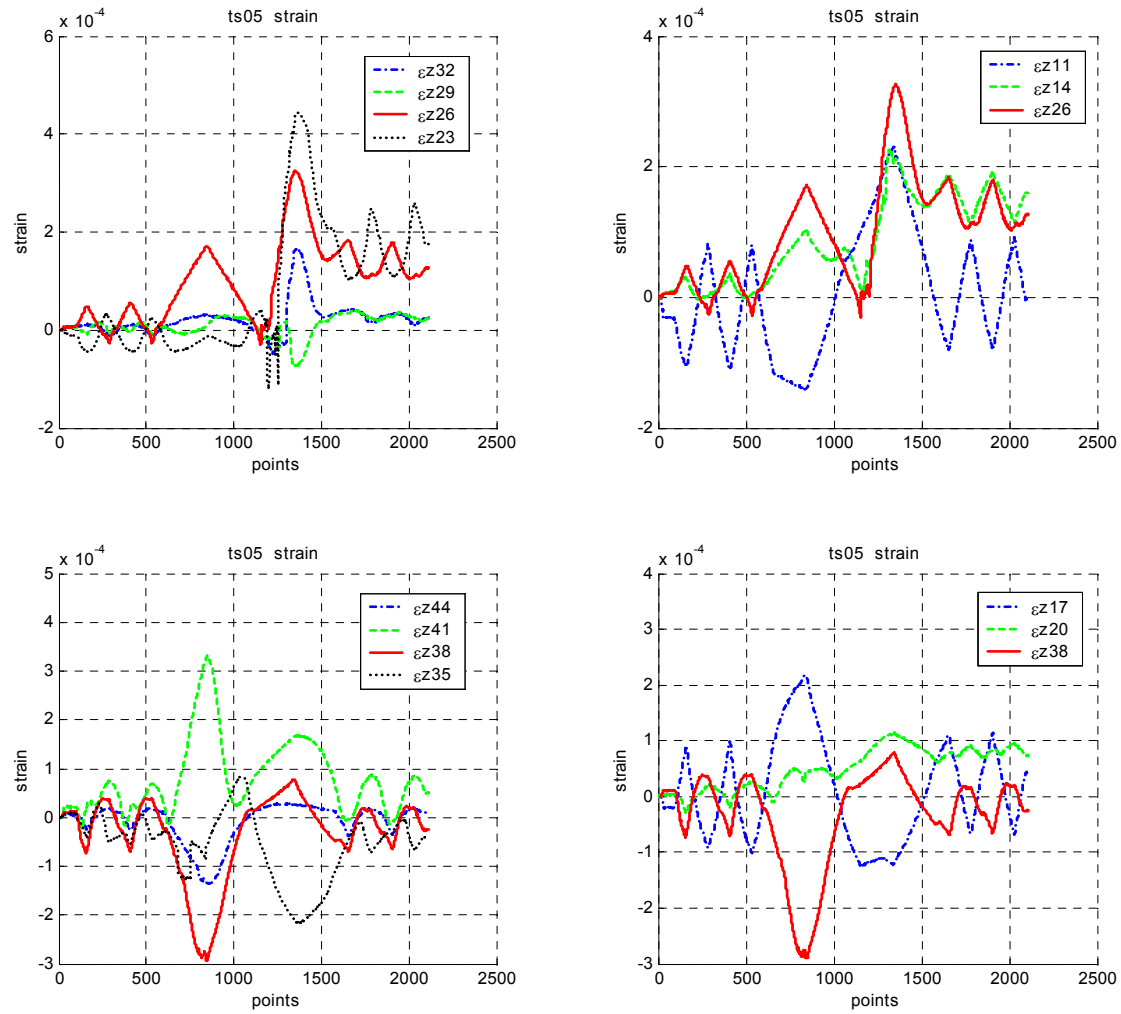
Figure 107 ts05: Hoop strains.
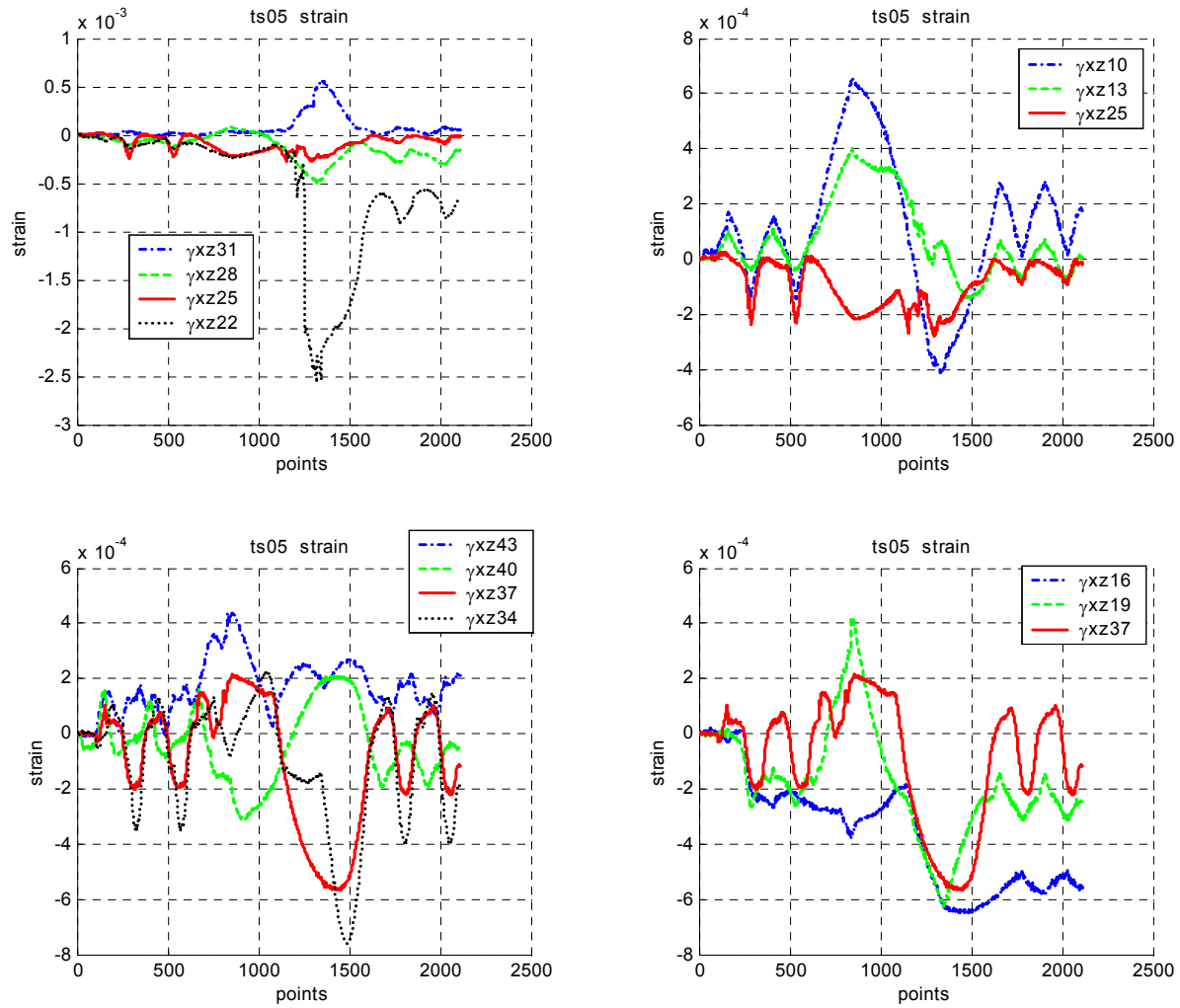
Figure 108 ts05: Shear strains.
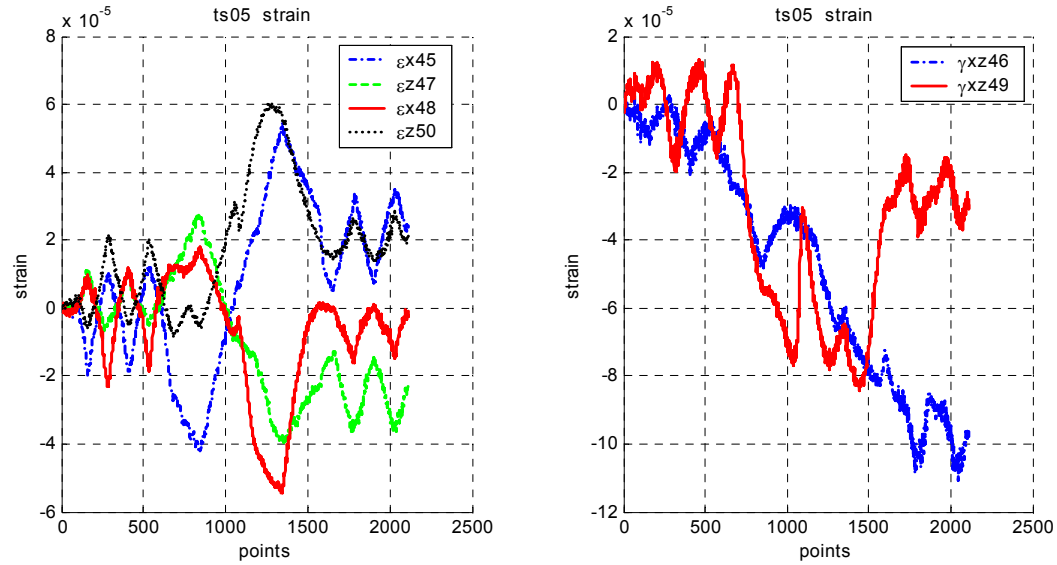
Figure 109 ts05: Strain on flange of base steel joint.
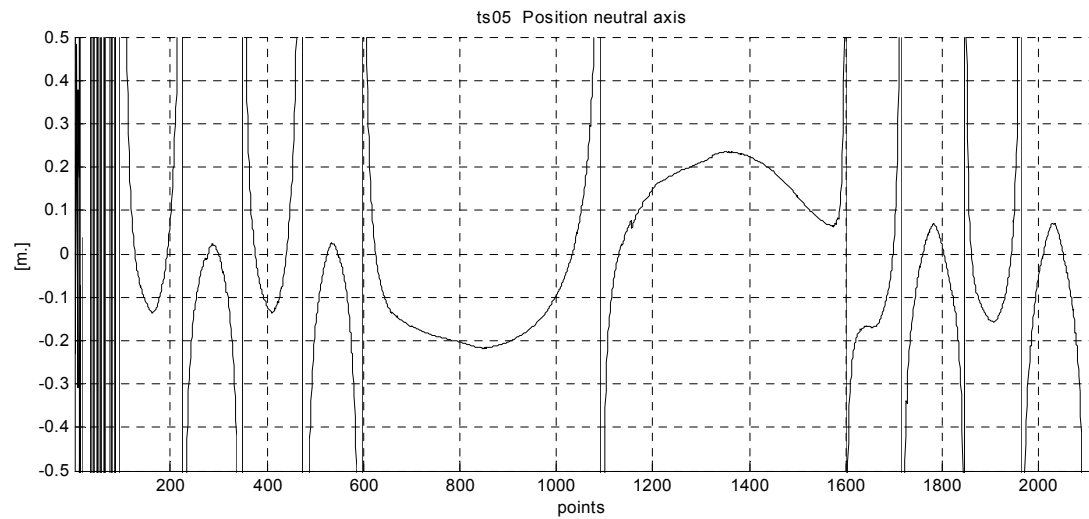
Figure 110 ts05: Position of neutral axis.

127
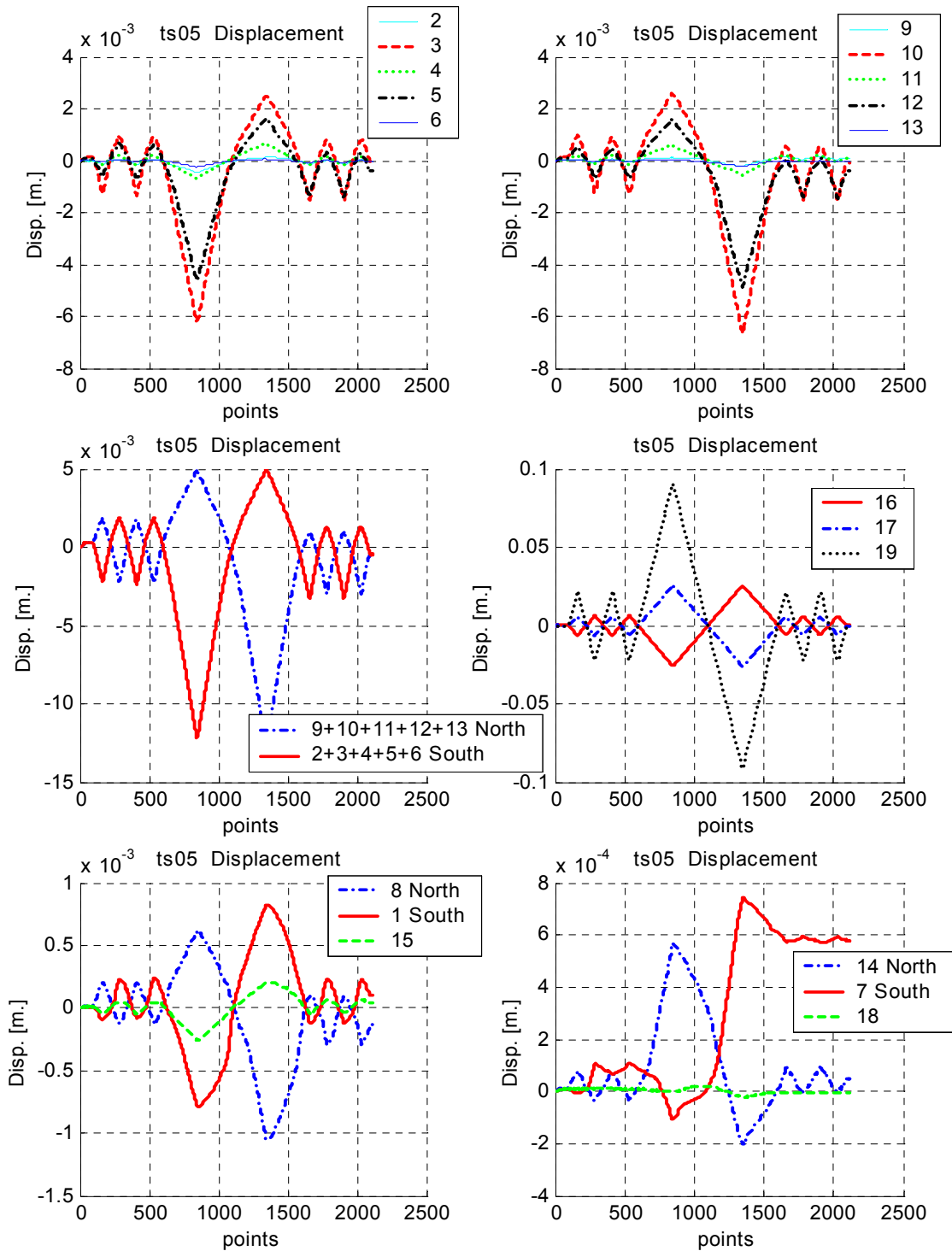
Figure 111 ts05: Displacement transducers.
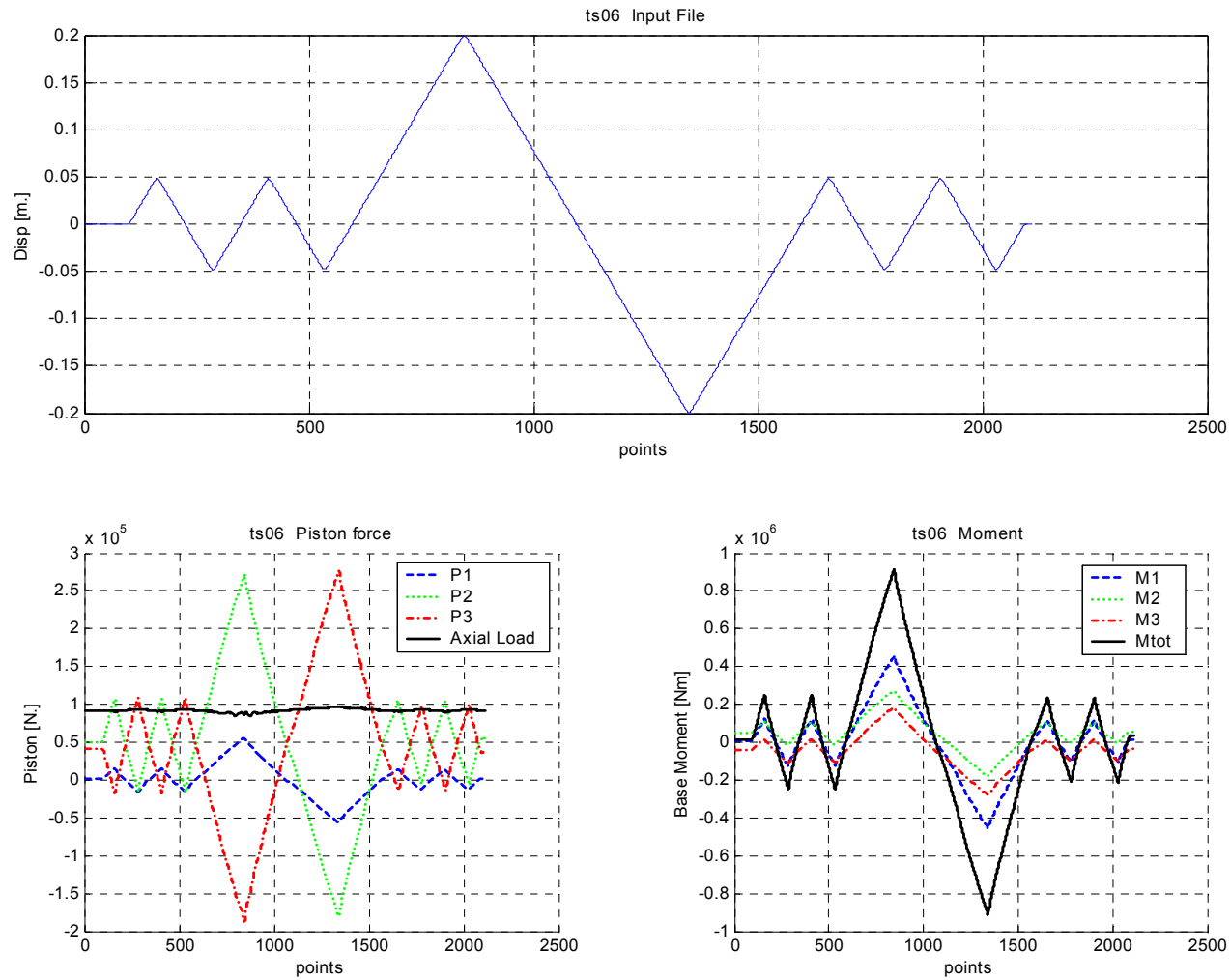
Figure 112 ts06: Input file, Piston forces and Moments.
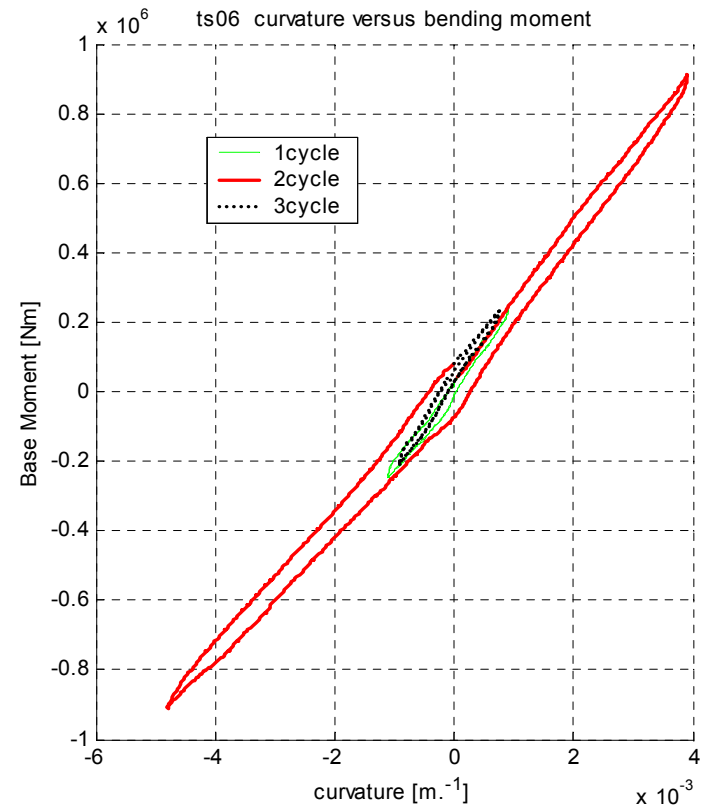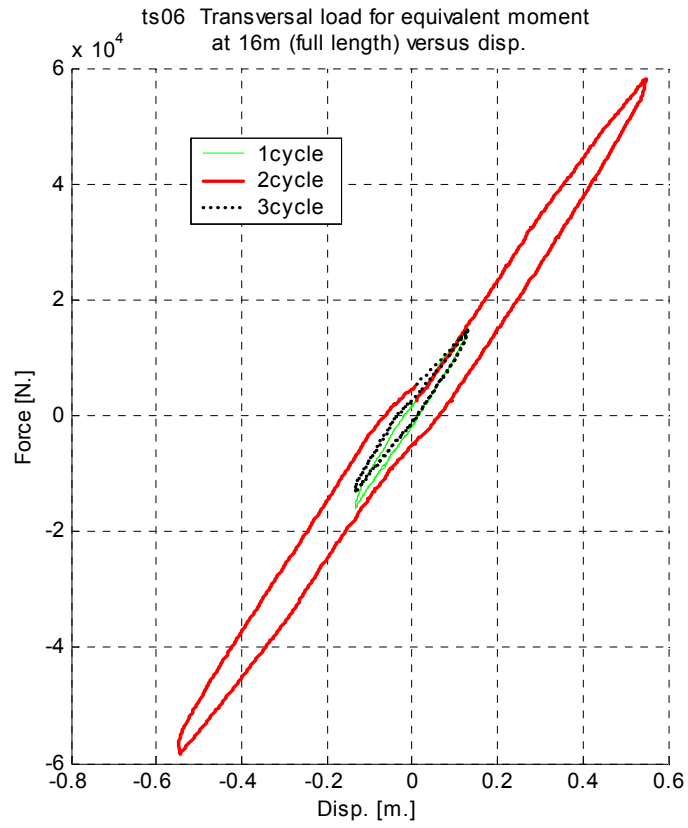
Figure 113 ts06: Hysteresis cycles.
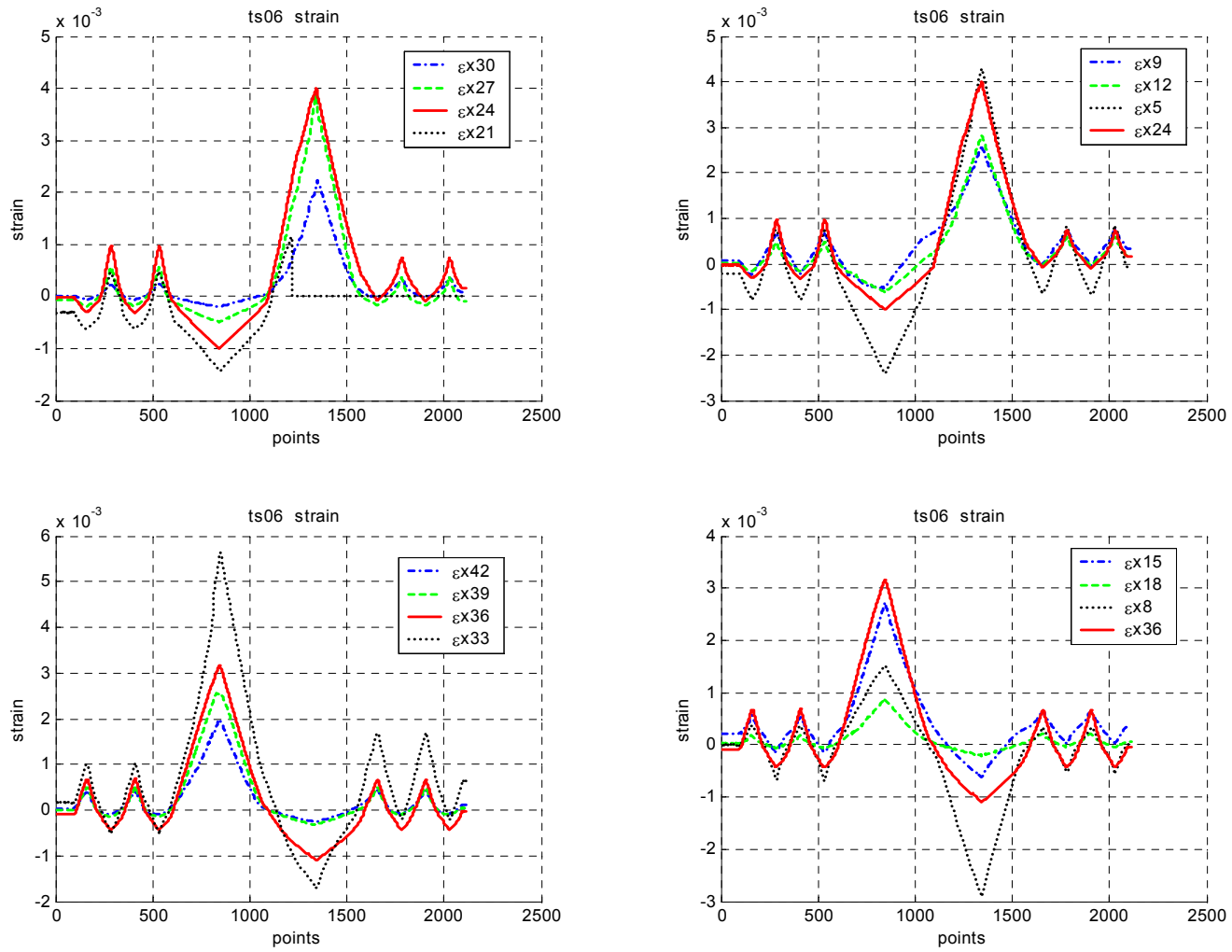
Figure 114 ts06: Longitudinal strains.
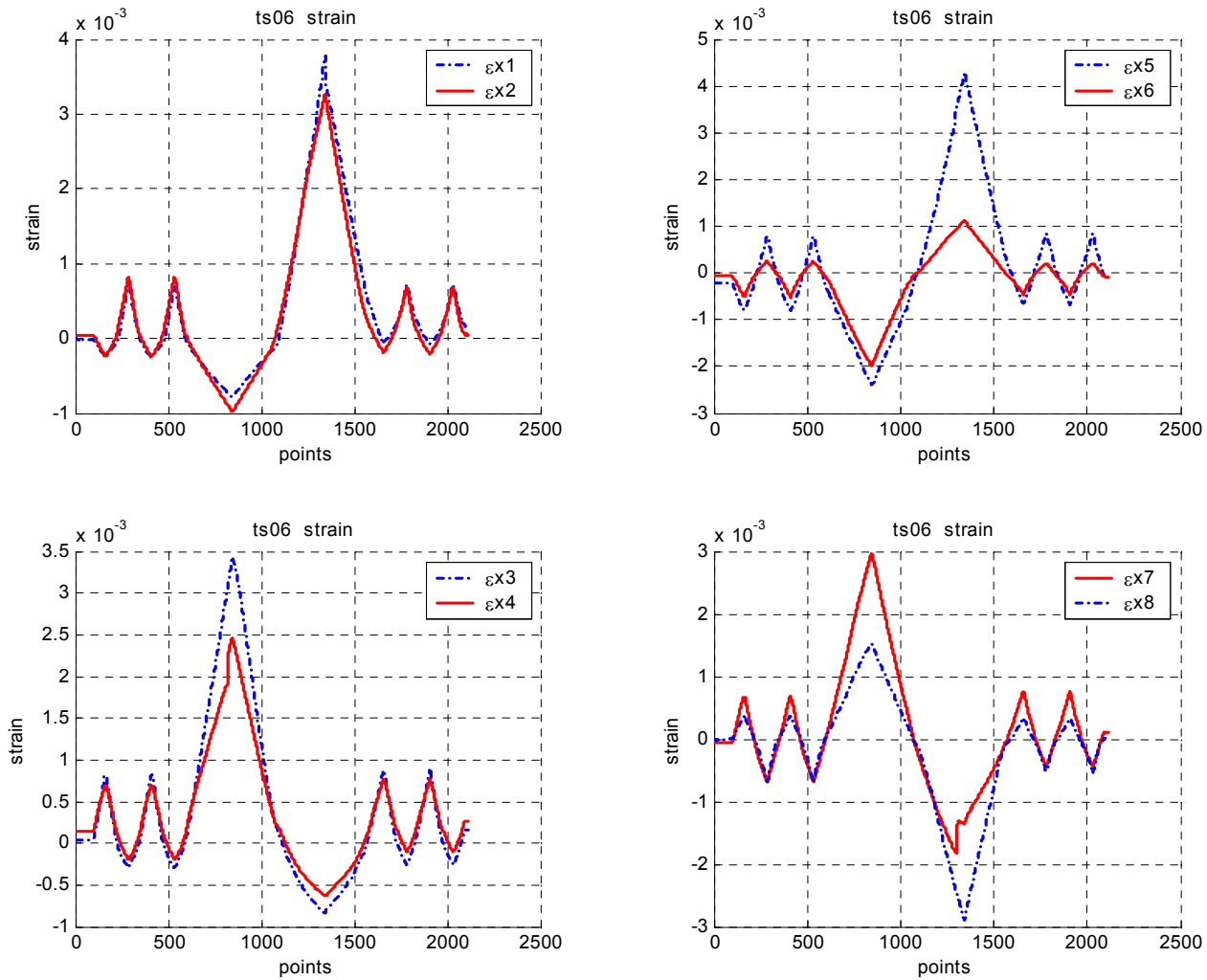
Figure 115 ts06: Internal (left) and intermediate joint (right) strain gauges.
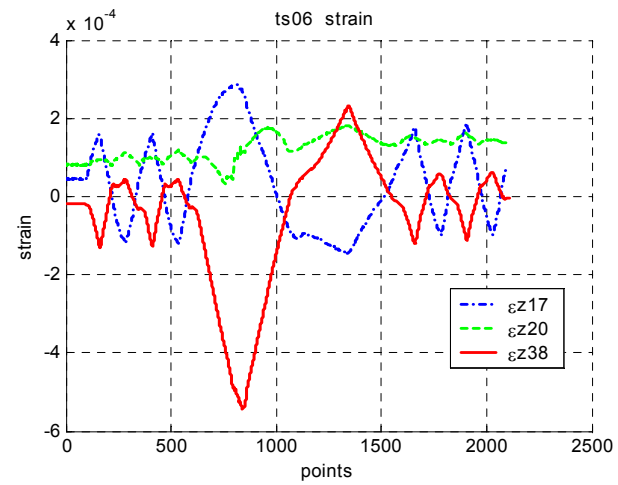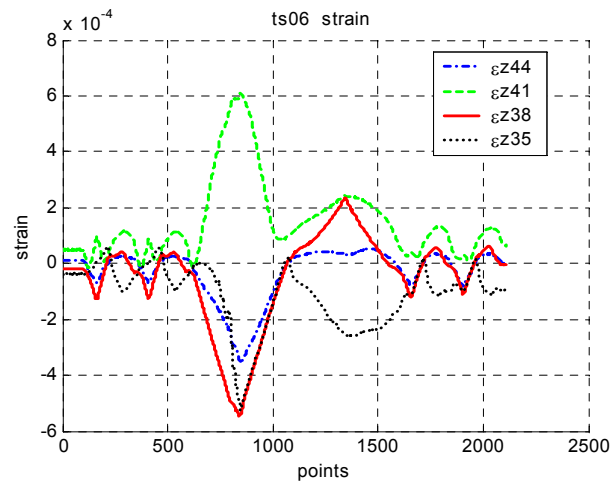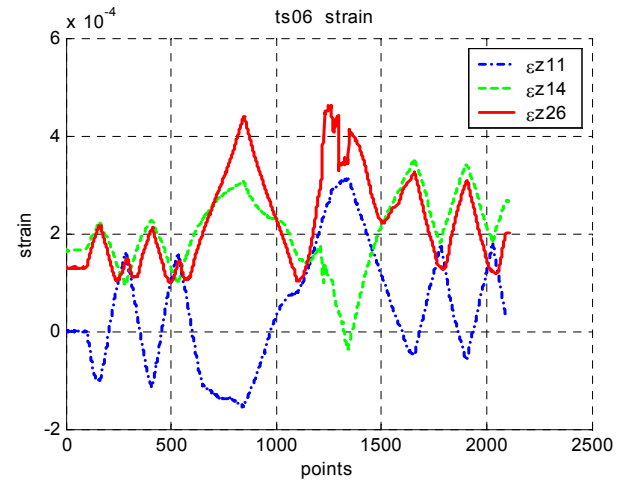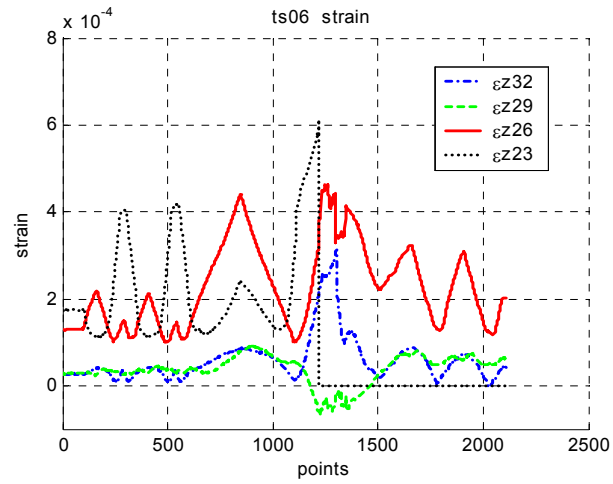
Figure 116 ts06: Hoop strains.
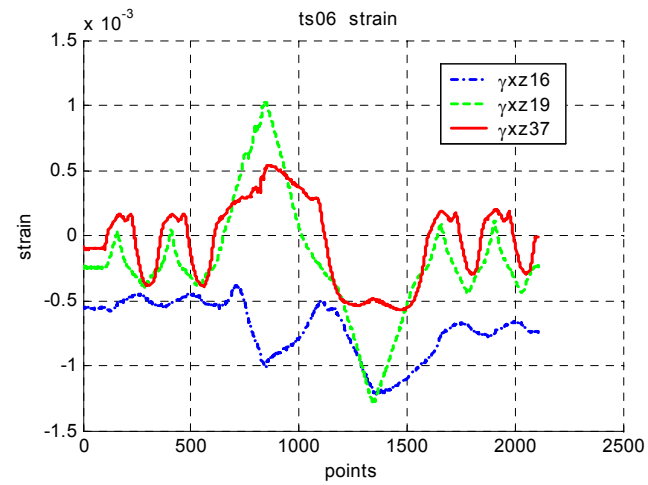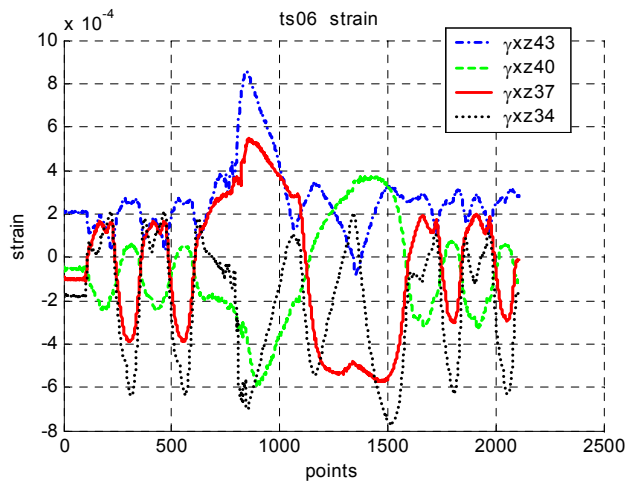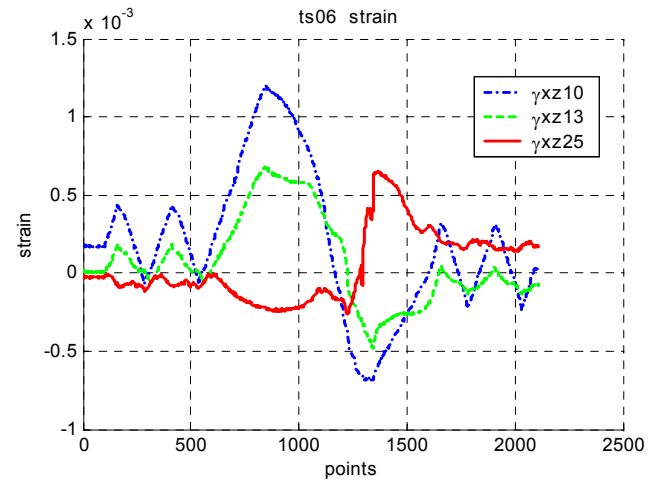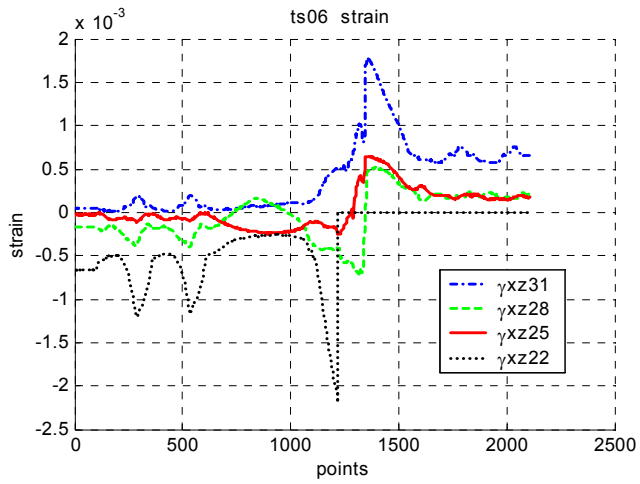
Figure 117 ts06: Shear strains.
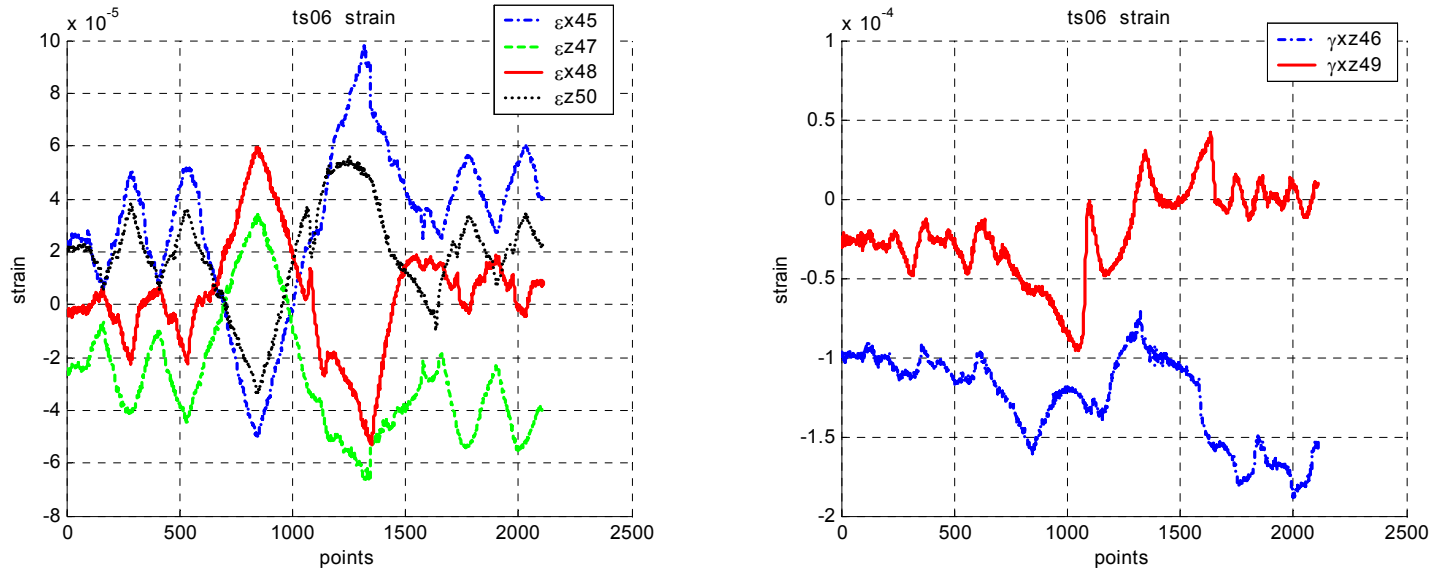
Figure 118 ts06: Strain on flange of base steel joint.
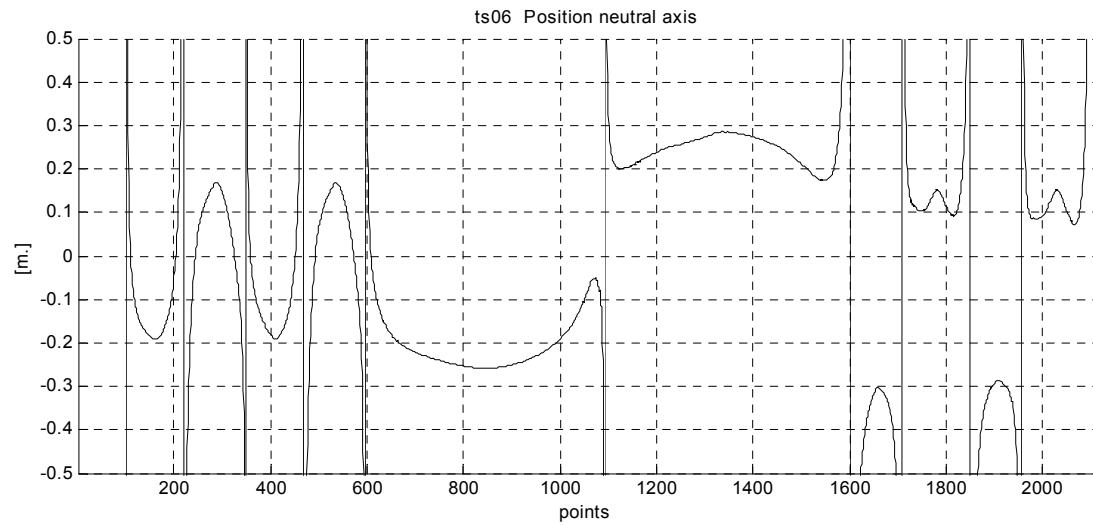
Figure 119 ts06: Position of neutral axis.
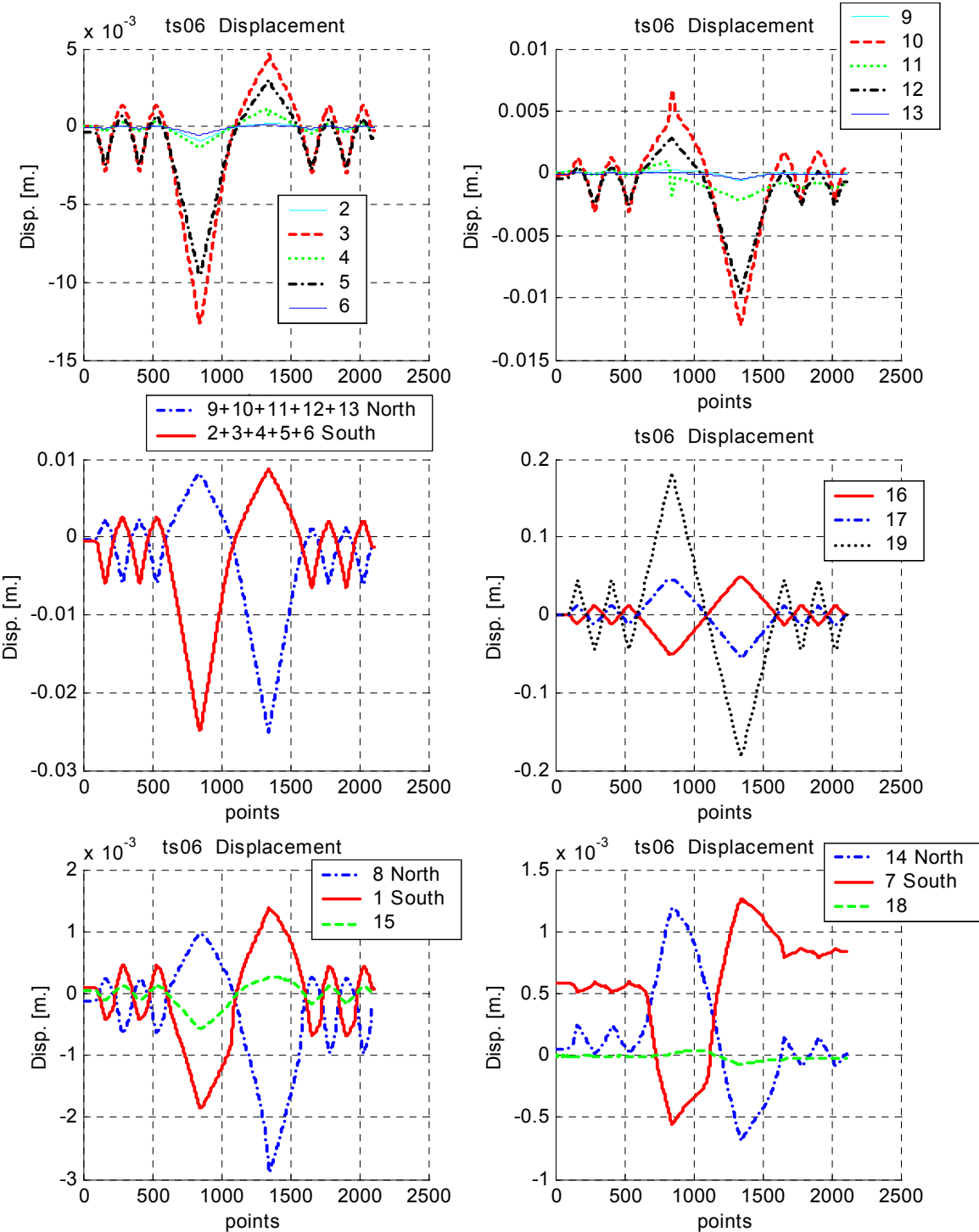
Figure 120 ts06: Displacement transducers.
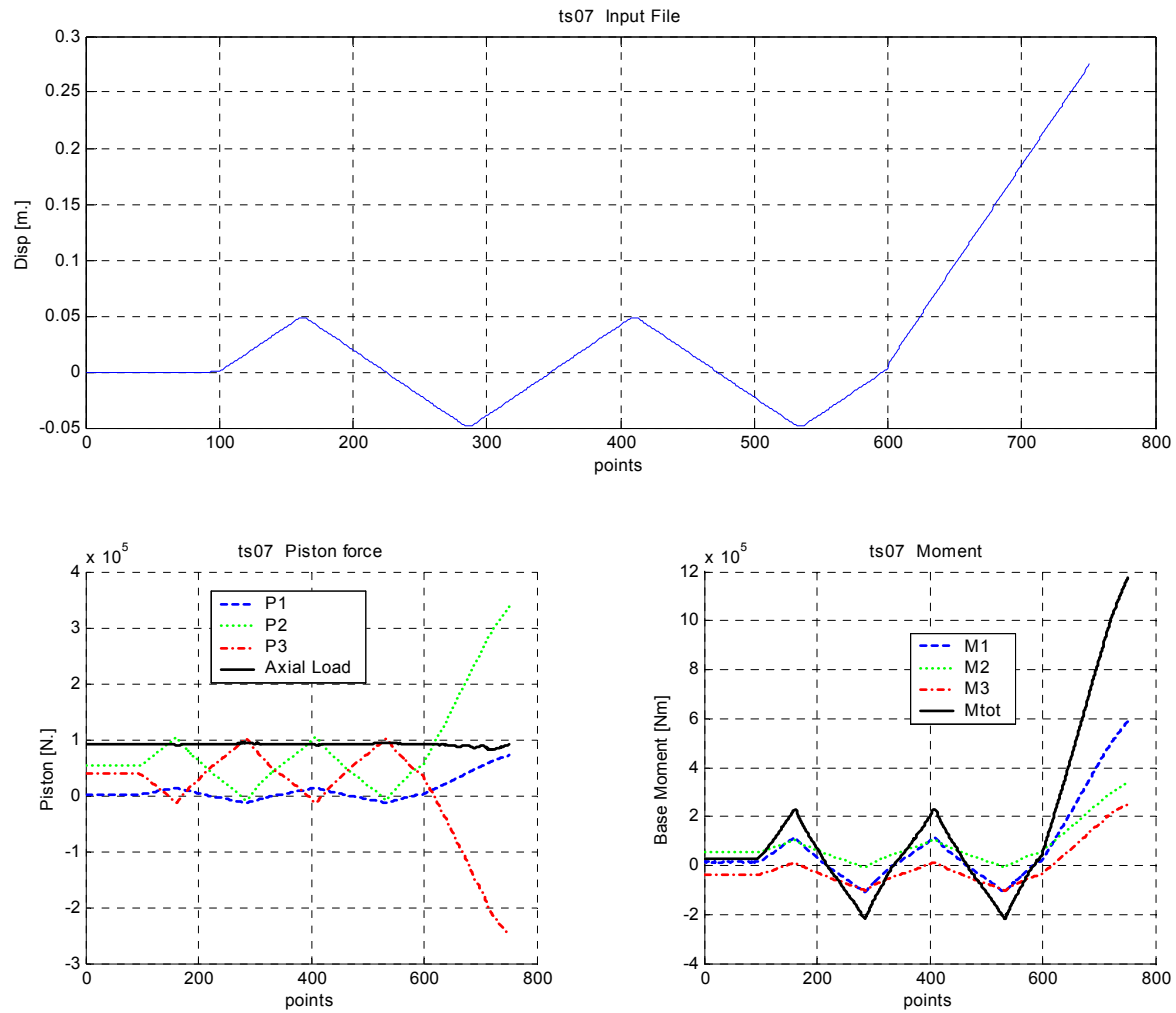
Figure 121 ts07: Input file, Piston forces and Moments.
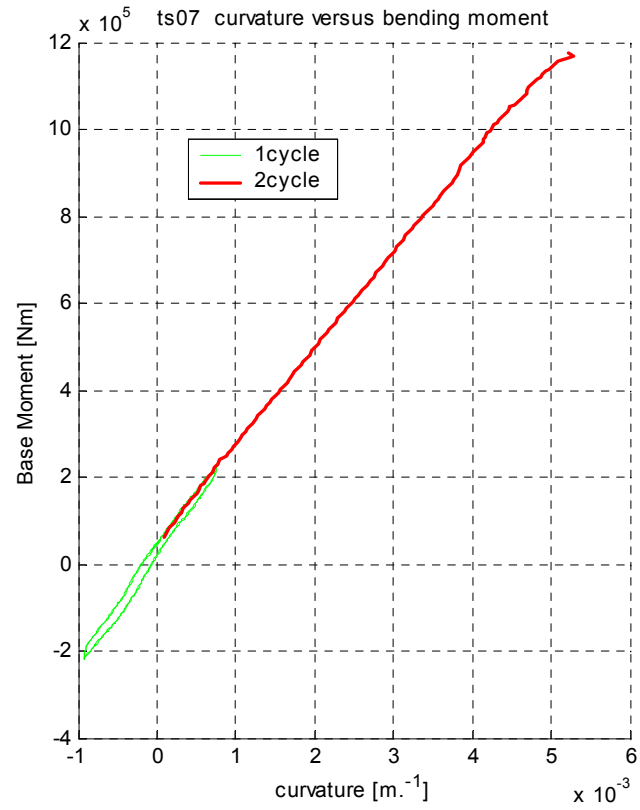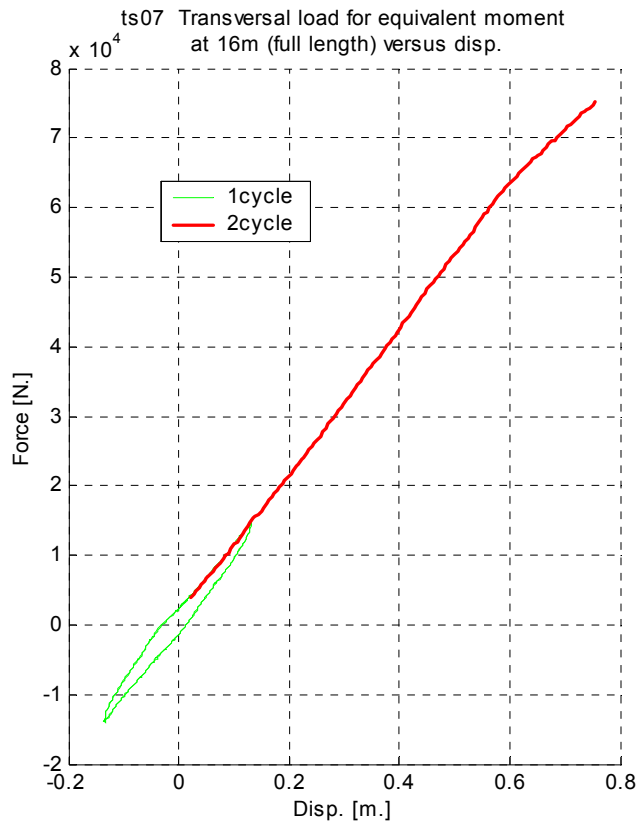
Figure 122 ts07: Hysteresis cycles.
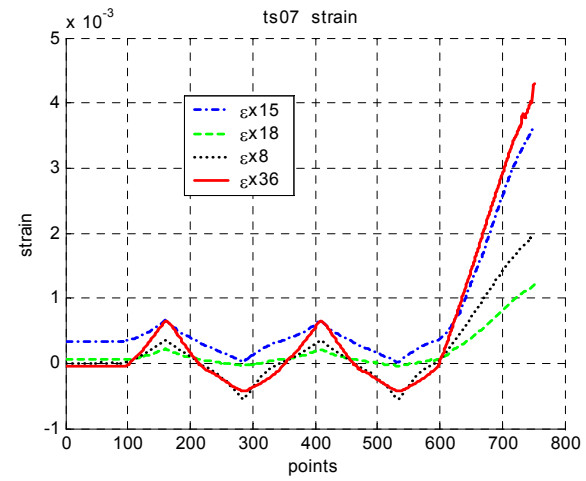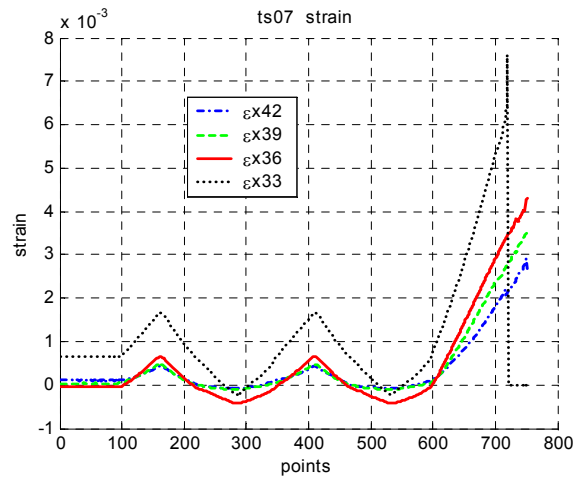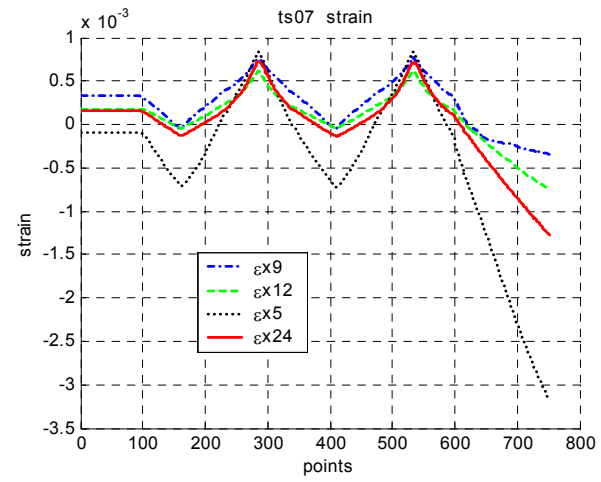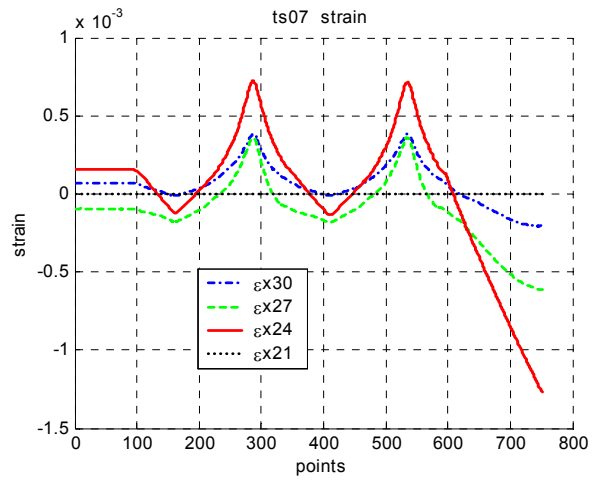
Figure 123 ts07: Longitudinal strains.
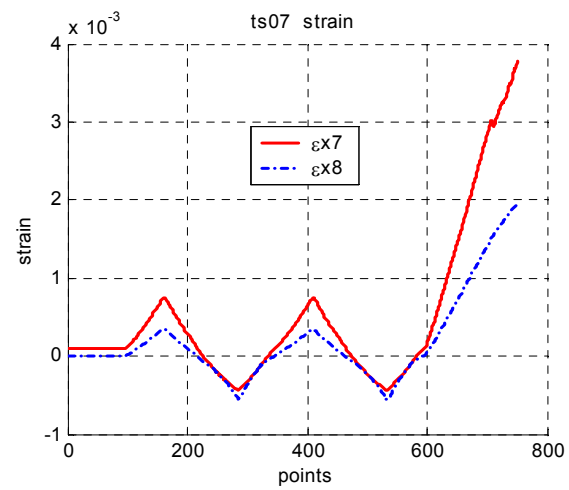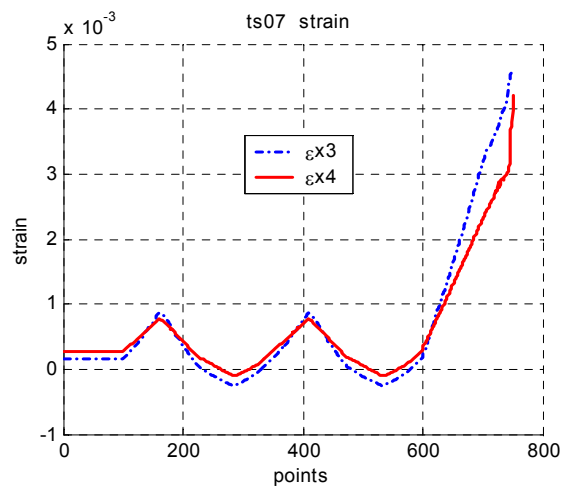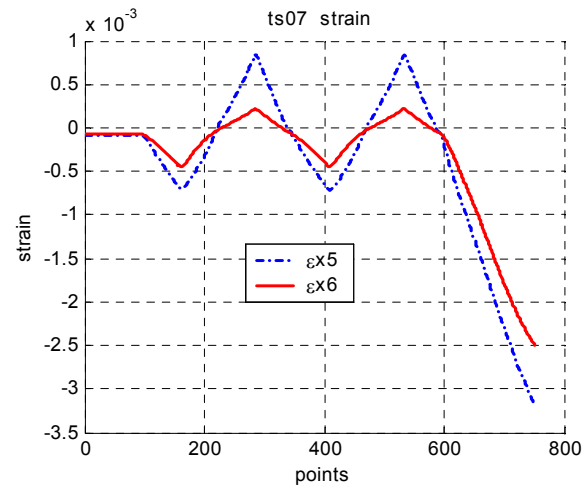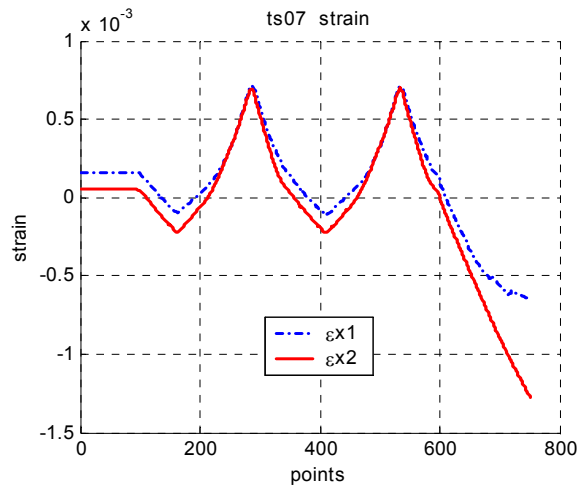
Figure 124 ts07: Internal (left) and intermediate joint (right) strain gauges..
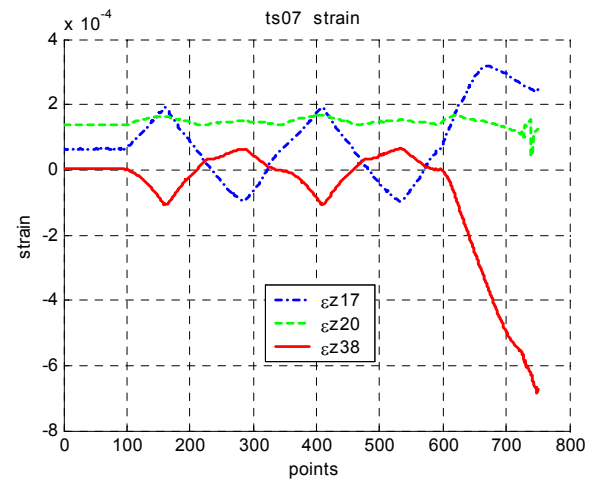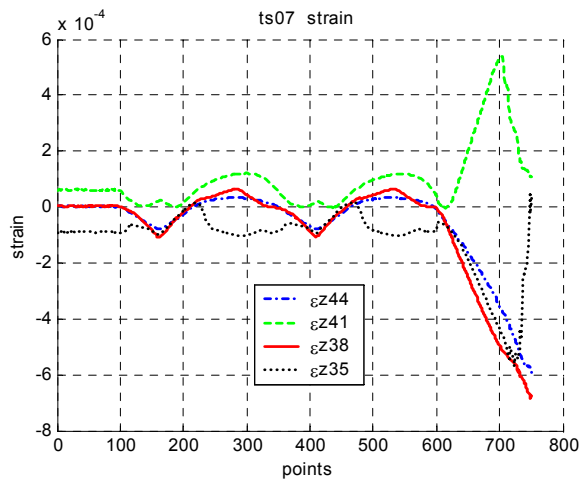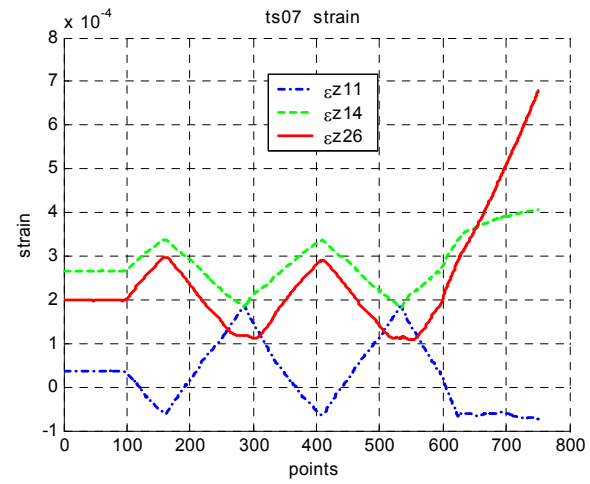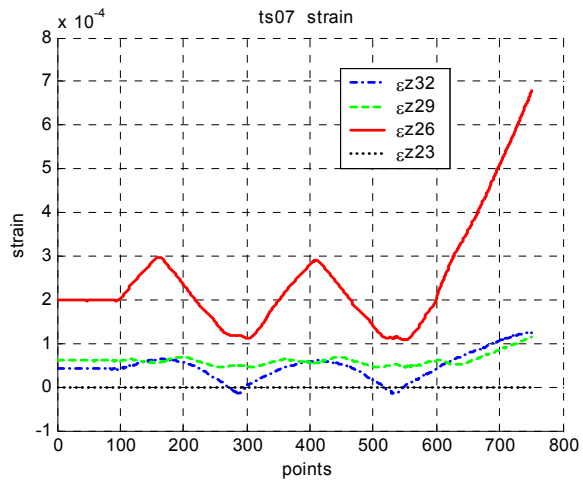
Figure 125 ts07: Hoop strains.
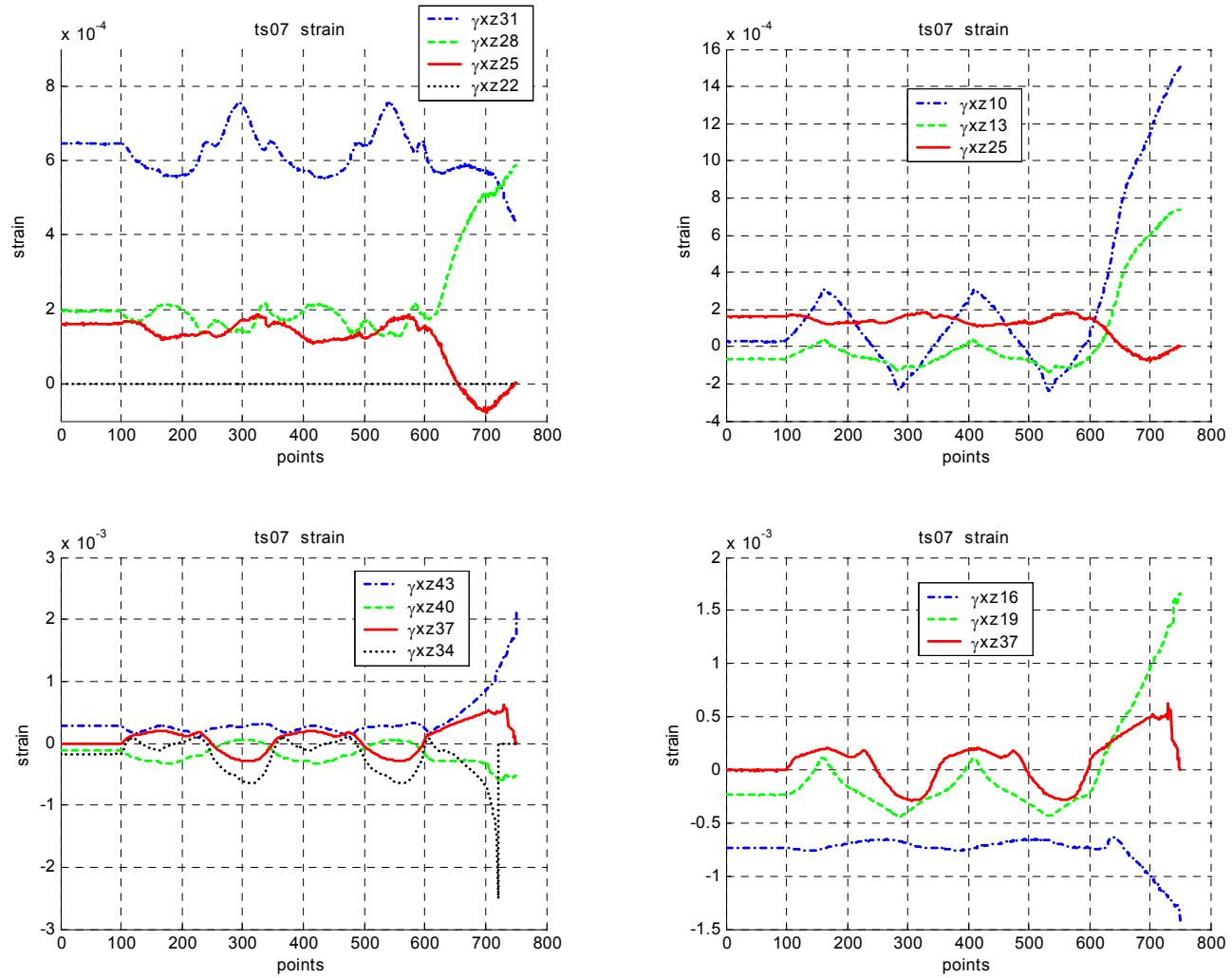
Figure 126 ts07: Shear strains.
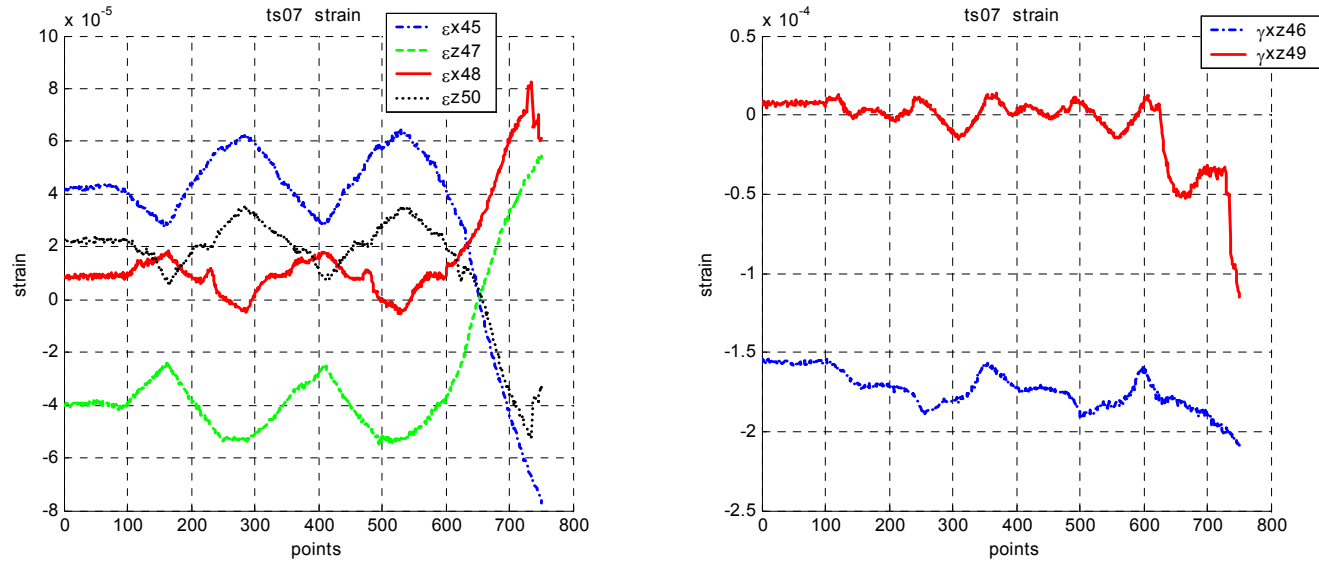
Figure 127 ts07: Strain on flange of base steel joint.
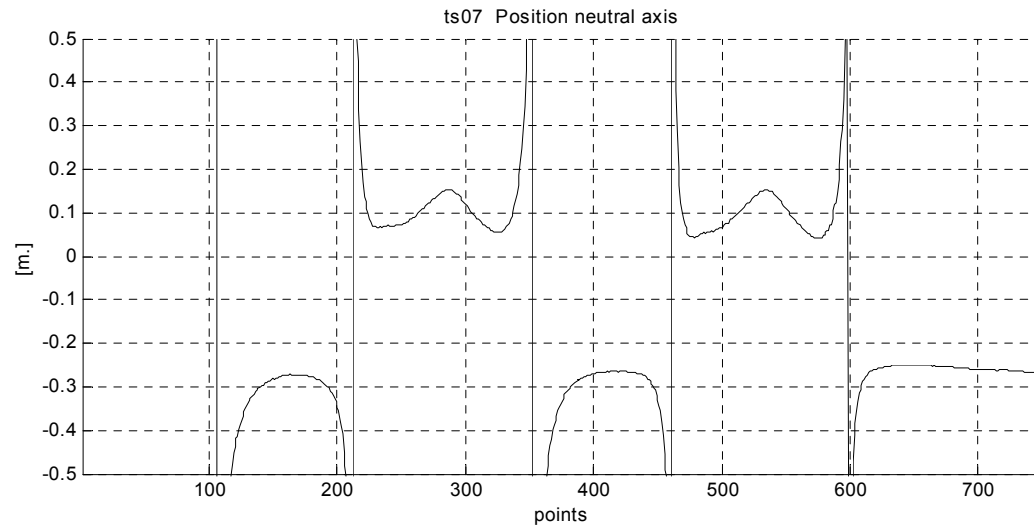
Figure 128 ts07: Position of neutral axis.

143
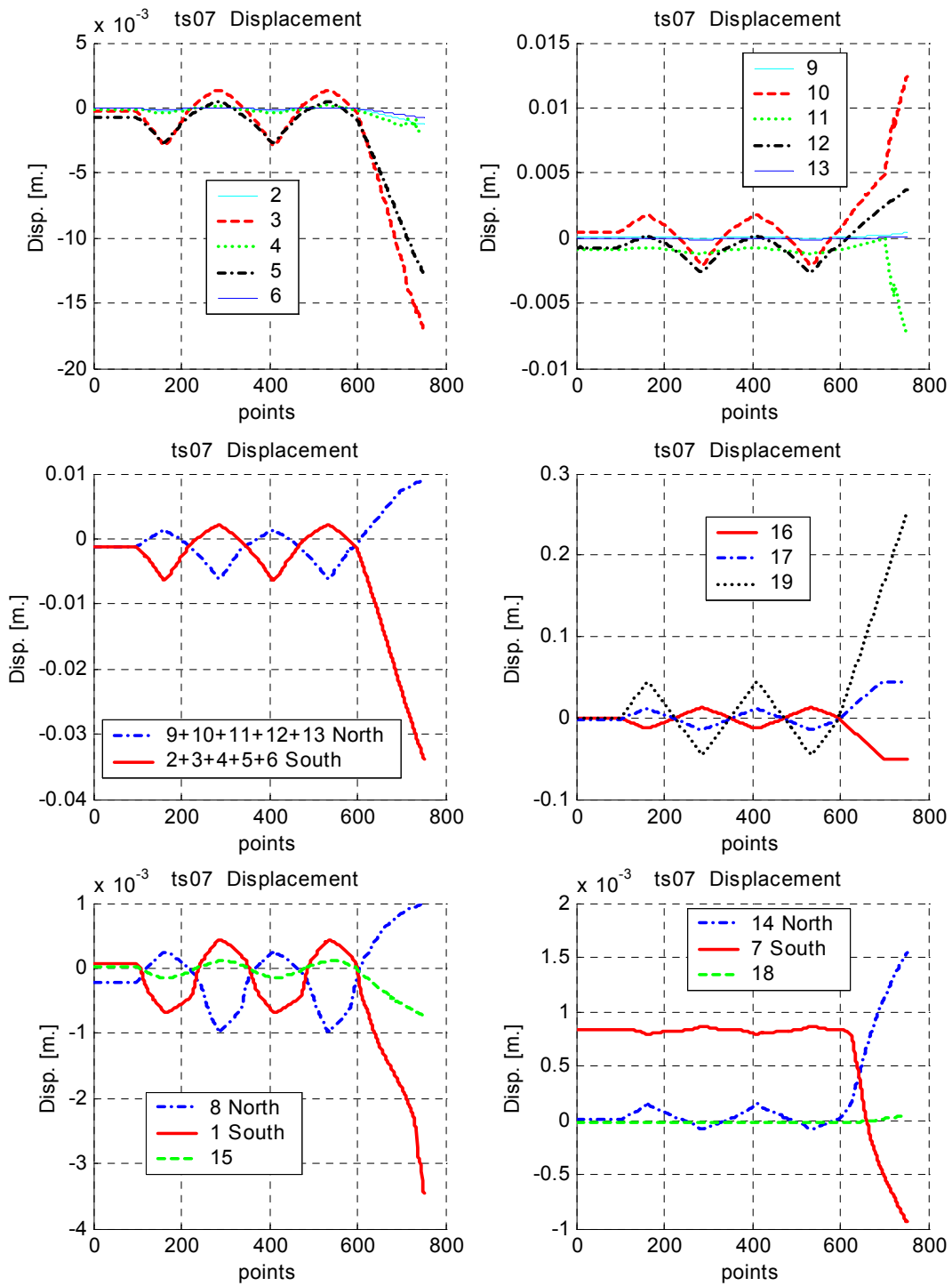
Figure 129 ts07: Displacement transducers.

14 Appendix B: Design Joint type B1

The joint type B1 at the base of the tower, in Figure 20, is designed as follows.

Ultimate lateral force in the full scale is *V=900kN* (initial ultimate force given at start of project)

Scale factor is *FS=⊘3.5/ ⊘1.1=3.18*

With our scale, the maximum lateral load is $V=900/3.18^2=90kN$.

Performing a combined compressive and bending stress analysis of a circular base section with a 1.1 meter diameter, and assuming that in tension only the bolts are load bearing whereas, in compression the load is taken by the horizontal 50 + 50 mm plate (Figure 131) it was calculated that the required bolt diameter is 12 mm, equally spaced of 50mm pitch.

The calculation gave a stress on bolts equal at 225MPa (from a Maple file, integral calculus) see Figure 130.

```
Tower JointB1 bolt:M12 class:8.9 fdN=560MPa
> restart;

> h := 16.0; Ares := evalf( (.12e-1² π)/4 ); i := .495e-1

> tc := .100; ts := (2 Ares)/i; R := (1.1 + .3e-1)/2.0

> Mf := 90000 h; N := 90000 + 1000 h; e := evalf( Mf/N )

> Syn := thn → 2 evalf( ∫₀^thn (R cos(th) - R cos(thn)) R tc dth + ∫_thn^π (R cos(th) - R cos(thn)) R ts dth )

> Iyn := thn → 2 evalf( ∫₀^thn (R cos(th) - R cos(thn))² R tc dth + ∫_thn^π (R cos(th) - R cos(thn))² R ts dth )

> funz := Iyn(thn)/Syn(thn) + R cos(thn) - e

> sols := fsolve(funz = 0, thn, 0 .. π); evalf( (sols 180)/π )
                                                    41.54023871
```

stress on bolt in Mpa
```
> sigma_bolt := (Mf(R + R cos(sols)))/(Iyn(sols) 10⁶)
                                        sigma_bolt := 225.0280623
```

shear ultimate slip
```
> V := (.3 2 Mf R tc ∫₀^sols R cos(th) - R cos(sols) dth)/Iyn(sols)
                                        V := 525639.9518
```

Vslip=525 KN < 90 KN ok
```
>
```

Figure 130 Bolt-stress calculation.

The area of a bolt M12 is *84* mm²

The designed joint is for a load equal to the bolt breaking point. So:

$$T = A_{res} \cdot f_y = \begin{array}{l} 84 \cdot 560 = 47040 \xleftarrow{\text{Design}} \\ 84 \cdot 225 = 18900 \end{array}$$

joint detail type B1
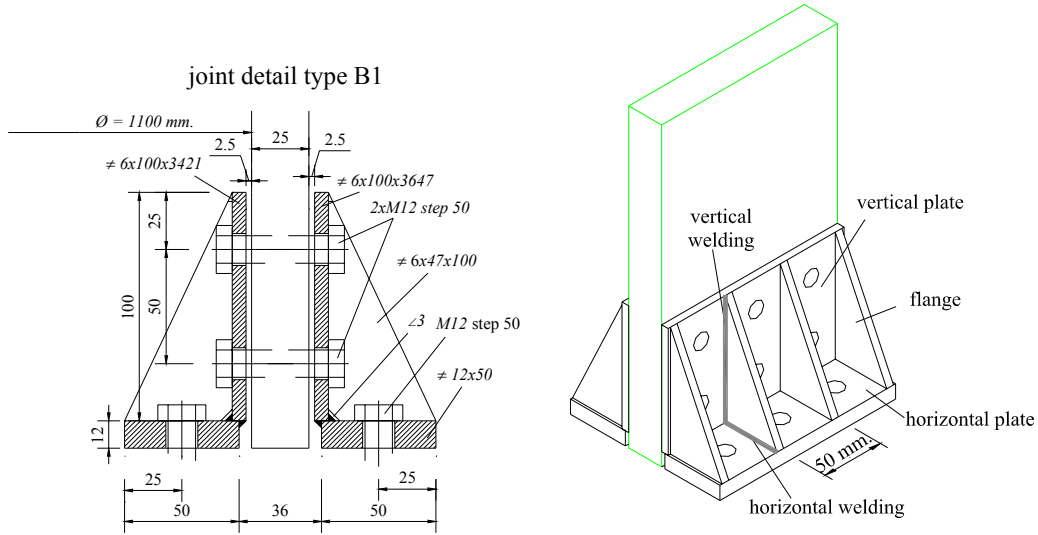
Figure 131 Joint details.

The reference for the Italian code normative is CNR10011; the material properties are:

- Steel Fe 360 *E=206GPa f_d=235MPa.*
- Bolt M12 class 8.8 *f_{dN}=560MPa f_{dV}=396MPa.*

All distances between the holes meet the normative requirements.

Check of shear load for the two horizontal bolts.

$$\tau = \frac{T}{2 \cdot A_{res}} = \frac{47040}{2 \cdot 84} = 280 MPa. \le f_{dV} \qquad \frac{396}{280} = 1.41$$

$$N = \frac{T \cdot 30}{50} = 28224 N. \quad \sigma = \frac{N}{A_{res}} = \frac{28224}{84} = 336 MPa. \le f_{dN}$$

$$\left(\frac{\tau}{f_{dV}}\right)^2 + \left(\frac{\sigma}{f_{dN}}\right)^2 \le 1 \quad \left(\frac{280}{396}\right)^2 + \left(\frac{336}{560}\right)^2 = 0.86 \le 1$$

Check for bearing failure:

$$\sigma_{rif} = \frac{T/2}{d \cdot t} \le \alpha \cdot f_{dV} \qquad \alpha = \min\left\{\frac{a}{d}; 2.5\right\} \qquad \frac{a}{d} = \frac{25}{12} = 2.08$$

$$\sigma_{rif} = \frac{47040/2}{12 \cdot 6} = 326 MPa. \le 2.08 \cdot 235 = 488 MPa. \qquad \frac{488}{326} = 1.5$$

where *t* is the thickness of plate, *a* is the edge distance and *d* is the nominal diameter of the bolt.

The tension between the vertical and horizontal plates is supposed to pass through the flanges.

Check stresses in the vertical plates.

$$\tau = \frac{T}{(100 - 2 \cdot \phi) \cdot t} = \frac{47040}{(100 - 2 \cdot 14) \cdot 6} = 108 MPa. \leq \frac{f_d}{\sqrt{3}} = 135 MPa. \qquad \frac{135}{108} = 1.25$$

where ϕ is the hole diameter and t is the thickness of plate.

Check vertical welds.

$$\sigma_\perp = \frac{M}{\frac{2a \cdot 100^2}{6}} = \frac{47040 \cdot 25}{\frac{2 \cdot 2.83 \cdot 100^2}{6}} = 124.6 MPa. \qquad \tau_\parallel = \frac{T}{2a \cdot 100} = \frac{47040}{2 \cdot 2.83 \cdot 100} = 83.1 MPa.$$

$$\sqrt{\tau_\parallel^2 + \sigma_\perp^2} = 150 MPa \leq 0.85 \cdot f_d = 0.85 \cdot 235 = 200 MPa. \qquad \frac{200}{150} = 1.33$$

Check horizontal welds.

$$\sigma_\perp = \frac{T}{2 \cdot a \cdot 50} = \frac{47040}{2 \cdot 2.83 \cdot 50} = 166.2 MPa. \leq 0.85 \cdot f_d = 0.85 \cdot 235 = 200 MPa. \qquad \frac{200}{166.2} = 1.2$$

where a is the effective throat section.

Considering the difficulty in foreseeing the behavior of both the plates and the flange, a computer model using FEM with CST elements was developed for the 2D analysis of the flange; a modeling with plate elements was chosen for the 3D analysis. In both cases the result was a maximum VonMises stress on steel of 200MPa, lower than the limit of 235MPa (Figure 132).
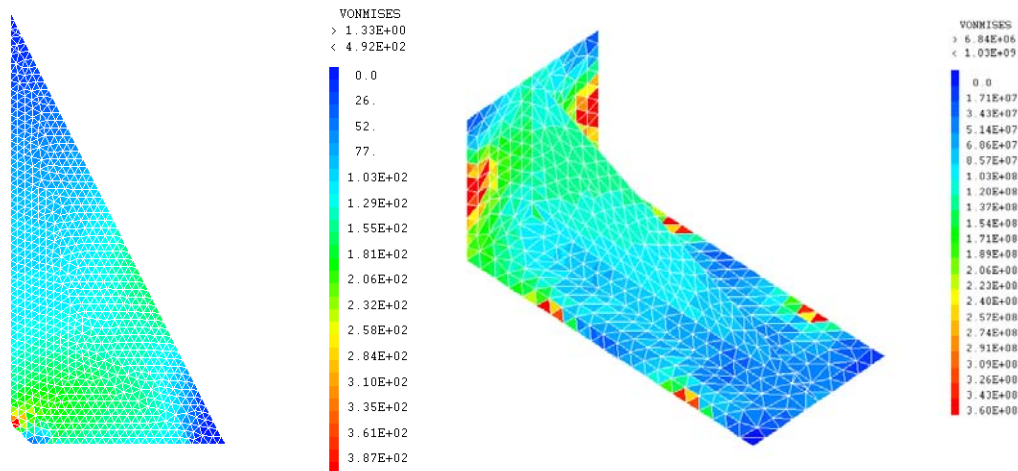
Figure 132 Model in FEM, 2D flange model (left) and 3D model (right).

15 Appendix C: Photo gallery.

15.1 Monolithic Tower
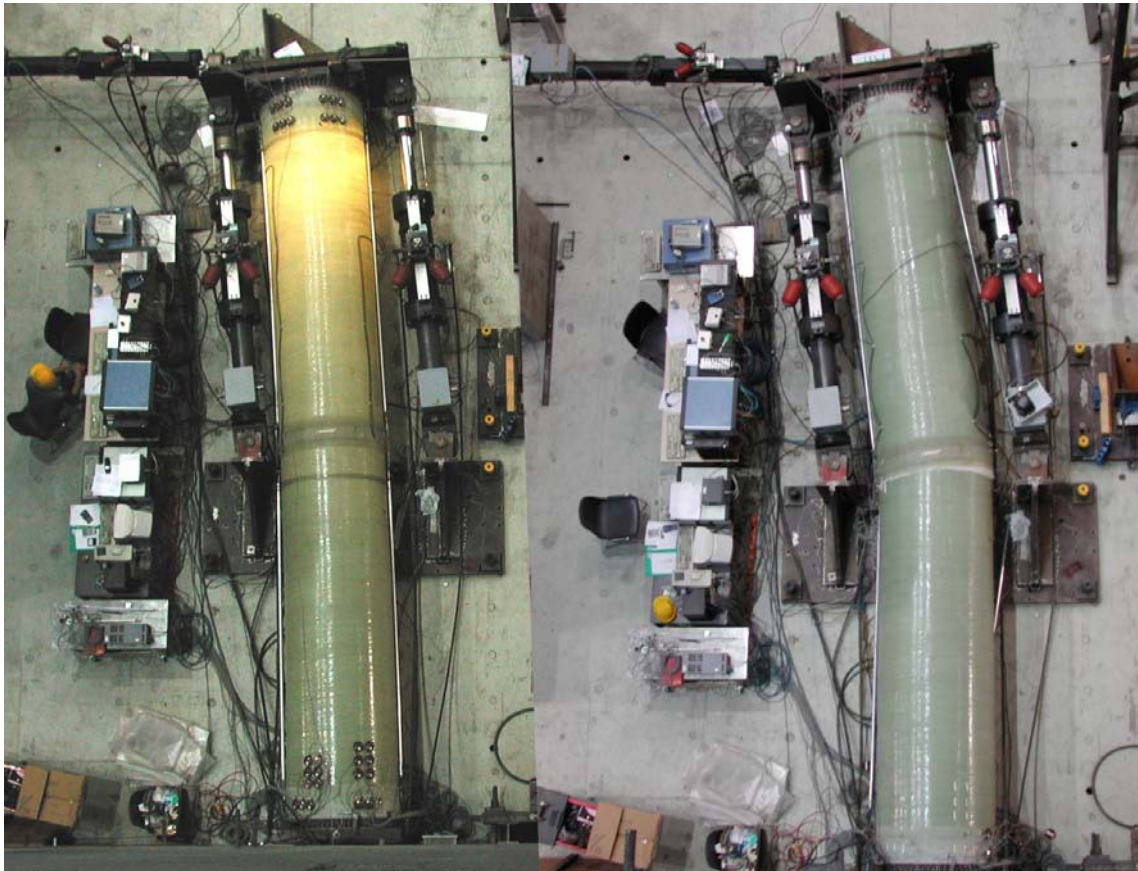
Figure 133 The 1/3 scale monolithic tower during testing (left) and at failure (right).
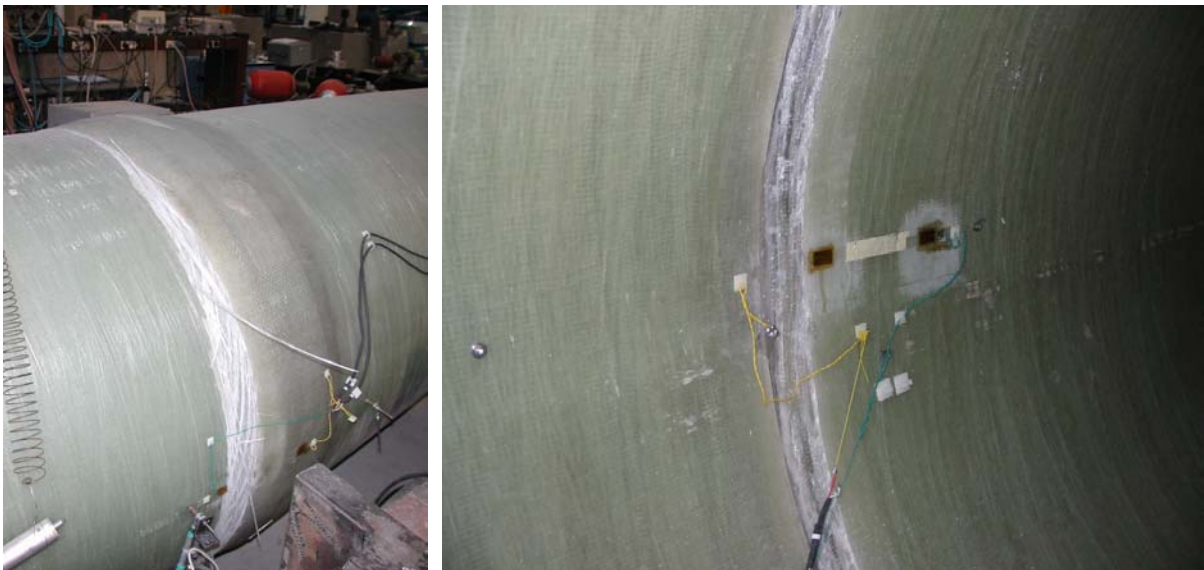
Figure 134 Detail of intermediate joint failure from outside (left) and inside (right) tube.
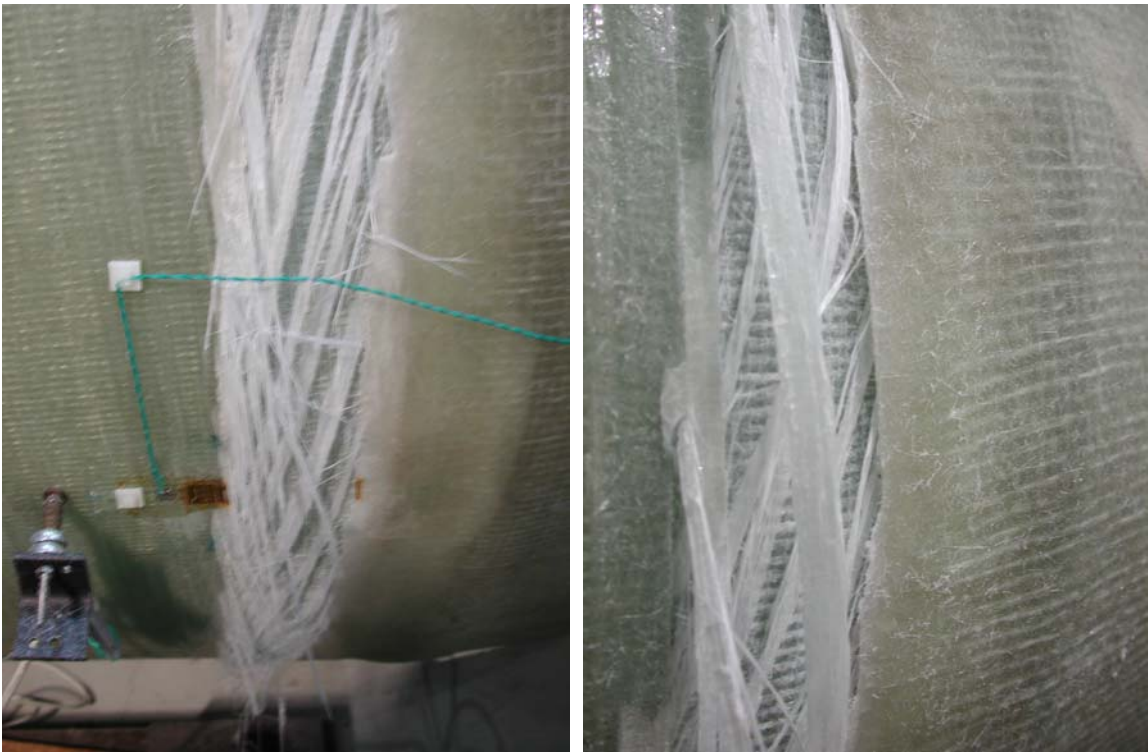
Figure 135 Detail of intermediate joint failure taken from outise on tensile face.
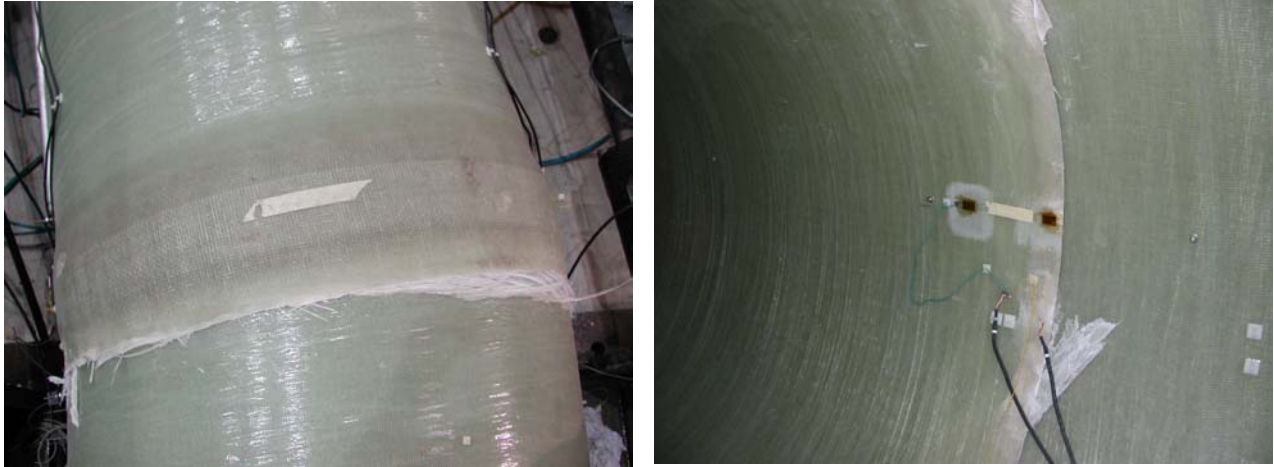
Figure 136 Intermediate joint failure on compressive face.

Figure 137 Detail of bolt area showing signs of local deformation around bolt holes.

15.2 Hybrid Tower
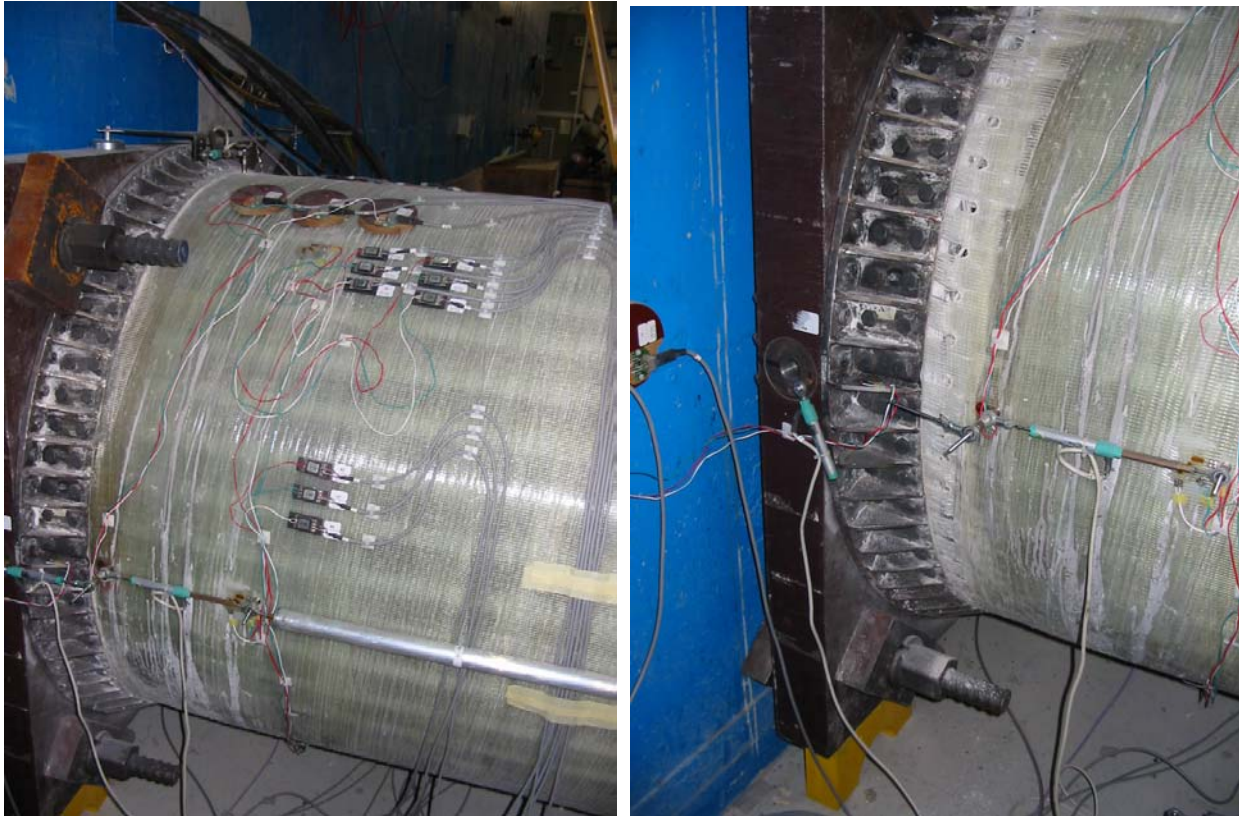
Figure 138 Detail of steel flange and tower base.

Figure 139Detail of laminate pull-out area around steel flange
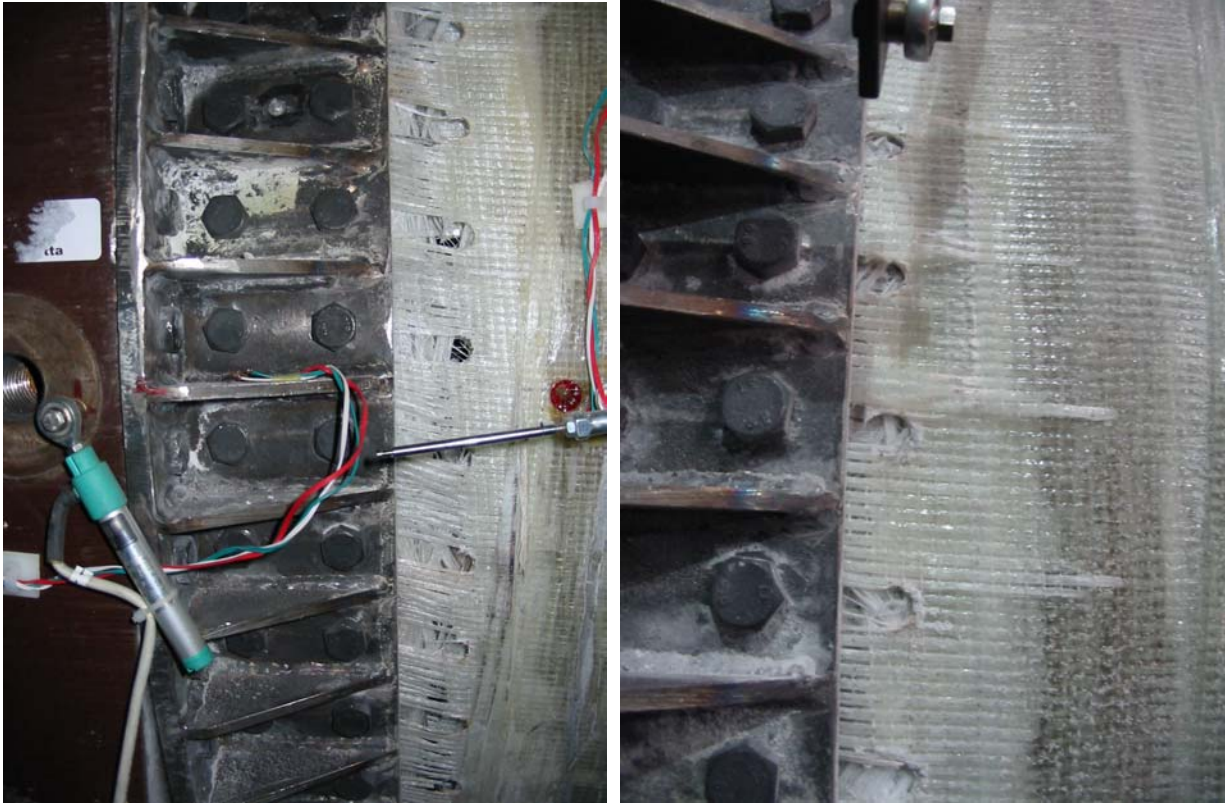
Figure 140 Detail of delamination and pull-out originating from bolt holes.

Figure 141Detail of laminate pull-out in hybrid tower and bearing loads around bolt holes

Figure 142 Detail from inside tower base at tensile pull-out area.
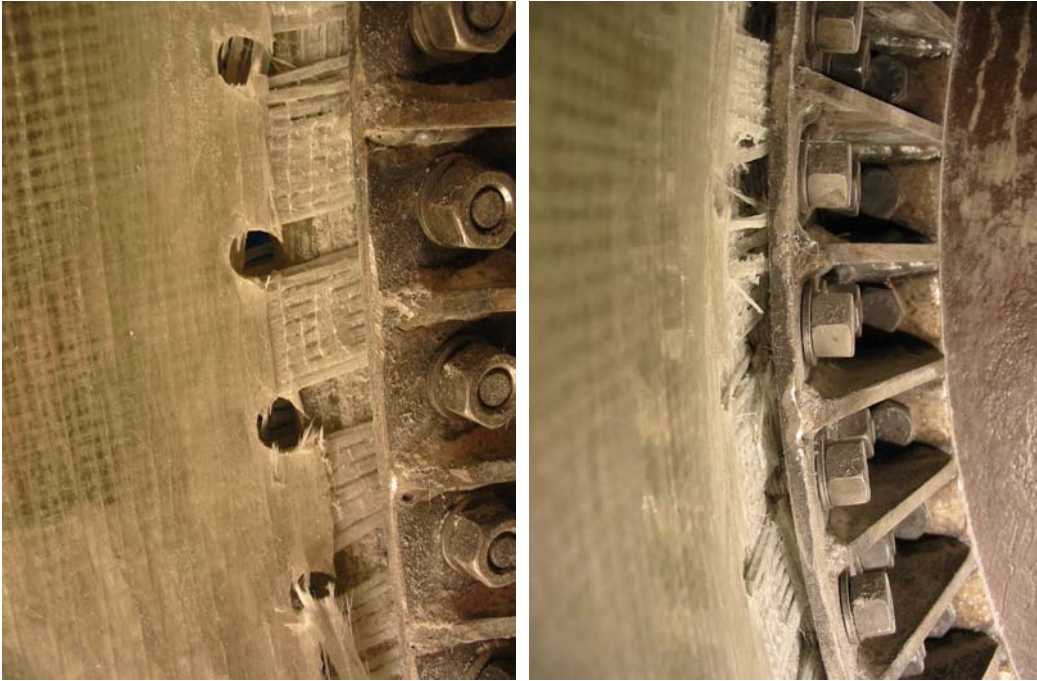
Figure 143 Detail from pull-out inside the tube at base.

154

Figure 144 Final extraction of tower base from steel anchorage ring.

16 Appendix D: List of Figures and Tables

List of Tables

17 Appendix E: Bibliography

17.1 General background

For a general guide to the basic theory of composite materials we have used the titles given below. They serve as a background to most of the work presented in this report but especially to the concepts discussed in Sections 2 4 7 8 and 11.

B. D. Agarwal and L. J. Broutman, *Analysis and performance of fiber composites*, John Wiley & Sons, 1990.

I. M. Daniel and O. Ishai, *Engineering Mechanics of Composite Materials,* Oxford University press, 1994.

D. Hull and T. W. Clyne, *An Introduction to Composite Materials*, Cambridge University Press, 1996.

17.2 Concrete FRP interaction (repair and confinement):

The references given here address those aspects related to the interaction between FRP and concrete. The *fib* bulletin provides a guide for use of FRP for concrete strengthening and repair, the aim is not to apply such a methodology to new structures as is done in this report, however, many design issues of repair are common to aspects addressed in this project. Several papers have been included concerning the aspects related to confinement of concrete such as by Nanni et al, Mirmiram et al, Harmon et al and , P. Johansen. Other generic cases of uses of FRP with concrete are given in Rodriguez et al, Norris et al as well as an extensive report by the US Navy on the applications of FRP for repair of marine structures. Finally Gutierrez et al provide an example of an FRP beam formwork system that is closely related to the work presented in this report.

Federation Internationale du béton *(fib)*, Bulletin 14 *Externally bonded FRP reinforcement for RC structures*, Task Group 9.3 FRP (Fibre Reinforced Polymer) reinforcement for concrete structures, 2001.

E. Gutiérrez, G. Di Salvo, J.M. Mieres, L. Mogensen, E. Shahidi, W. Schnabel and G. Verzeletti, *Experimental results from laboratory test on an 8 metre beam manufactured from hybrid composite formwork*", Advanced Composites Letters Vol. **7,** No. **6**, pp. 155-160, 1998.

T. Harmon, H. Wang*, Behaviour of composite confined concrete under cyclic loading*, Proc. 41st Intl. SAMPE Symposium, pp. 975-989, 1996.

P. Johansen, *Application of fibre reinforced composite to improve the structural efficiency of existing structure*, Master thesis, Faculty of Mechanical Engineering, Department of Applied Mechanics NTNU Norwegian University of Science and Technology, 2000.

A. Mirmiram, M. Shahawy, *Behaviour of concrete columns confined by fiber composites,* ASCE, Vol **123**, No **5**, pp 583-590, 1997.

A. Nanni, M. Bradford, *FRP jacketed concrete under uniaxial compression,* Construction and building materials*, Vol.**9**, No **2**, pp. 115-124. 1995.

A. Nanni, M. Norris, *FRP jacketed concrete under flexure and combined flexure compression*, Construction and building materials*, Vol.**9**, No **5**, pp. 273-281. 1995.

Naval Facilities Engineering Service Center, *Navy advanced composite technology in waterfront infrastructure*, Special Publication SP-2046- SHR, US Navy Port Hueneme, California, 1998.

T. Norris, H. Saadatmanesh and M.R. Ehsani, *Shear and flexural strength of R/C beams with carbon fiber sheets,* J. Struct. Engrg. ASCE, Vol. **123**, No **7**, pp. 903-911, 1997.

J. Rodríguez, J. M. Mieres and E. Gutiérrez, *Shear Repair of Massive Viaducts: Actual reinforcement in a High-Speed Railway viaduct,* Proc. Intl. Conf. Fracture of Composites, Institute of Materials UK , UMIST, March 2001.

17.3 FRP trends in civil engineering:

The following references are a useful guide to the trends, past and present that are currently being addressed by resrachers in the field of FRPs in civil engineering. The paper by Meier provides an indication of how this field was perceived some fifteen years ago, whereas the papers by Karbhari et al and the key note papers in the Proceedings of the recent conference of composites in civil engineering (edited by Teng) provide an extensive overview of the current topics being currently studied.

V. Karbhari, F. Seible, *Fibre reinforced composites- Advanced Materials for the Renewal of Civil Infrastructure*, Applied Composite Materials **7**: 95 124, 2000.

U. Meier, *Designing and producing materials by combination*, Materials and Structures/Matériaux et Constructions, **21**, pp. 85-89, 1988.

J.G. Teng (editor), *FRP Composites in civil Engineering,* Proc. Of Intl. Conf. on FRP Composites in Civil Engineering, Vols. **1** and **2**, 2001.

17.4 Pultrusions:

Pultrusions are discussed as an alternative solution to the tower considered as a frame structure as discussed in Section 2. The papers given below are useful starting points to gain an insight into the main structural issues concerning this production technique. However pultrusion gratings could be used as core stiffeners in order to solve some of the problems encountered in the manufacture and performance of the hybrid formwork system as discussed in Sections 3 and 8. Two pultrusion producers' sites are given where it is possible to find useful information concerning available pultrusion sizes both for beams, connectors and gratings, as well as guides for design and connections.

J. Mottram, G.J. Turvey, *State- of- the-art review on design, testing analysis and application of polymeric composite connections,* Polymeric Comp. Struct. Working Group 7. COST C1, Project on civil engineering connections, DG XII, Publications Office Luxembourg, European Commission, 1998.

J. Mottram, Y. Zheng, *Further tests on beam-to-column connections for pultruded frames: web-cleated*, J. Struct. Engrg. ASCE, Vol **3**, No **1**, pp. 3-11, 1999.

Strongwell Pultrusions (USA) : http://www.strongwell.com/
Fiberline Pultrusions (DK) : http://www.fiberline.com/gb/home/index.asp

17.5 Failure, crushing and interlaminar stresses in thick laminates:

These papers address aspects specific to composites, especially for stability of thick laminates such as in the paper by Hull that is a major factor in the design of the joints for the tower. Classic papers by Pipes and Pagano on the nature of interlaminar stresses and the paper by Polyakov et al on the nature of free edge stresses are worth a look as they play a fundamental role in the inititiation of failure at joints and discontinuities as discussed in Sections 4 and 7.

D. Adams, G. Finley, *Analysis of thickness-tapered unidirectional composite compression specimens,* J. Composite Materials, Vol. **31**, No. 22, pp. 2283-2305, 1997.

D. Hull*, A unified approach to progressive crushing of fibre-reinforced composite tubes, Composites Science and Technology*, **40**, pp. 377-421, 1991.

G. Michel, A. Limam, J.F. Jullien, *Buckling of cylindrical shells under static and dynamic shear loading,* Engineering Structures, **22**, pp. 535-543, 2000.

R. Pipes and N. J. Pagano, *Interlaminar Stresses in Composite Laminates Under Uniform Axial Extension*, J. Composite Materials, Vol. **4**, 1970.

V.A. Polyakov, I.G. Zhigun, V.V. Khitrov, *Evaluation of stresses in the edge effect zone in tension of composite laminates,* Mechanics of Composite Materials, Vol**. 23**, No.5, pp544-552, 1988.

17.6 Sandwich Composites:

The failure of sandwich panels due to delamination of the sandwich skins and basic general guidelines for basic falire modes are discussed in Avery and Sankar and Noury et al. Joining of sandwich structures to metallic and Koch and Starliner which although applicable to soft cores provides useful background material for the analysis of the potential problem areas in the design of the hybrid tower. Extensive theory of sandwich panels is given in the textbooks by Zenkert and Vionson (the latter is especially useful for the dyanamic analysis of orthotropic plates an shells).

J. Avery III, B. V. Sankar, *Compressive failure of sandwich beams with debonded face-sheets,* J. Composite Materials, Vol. **34**, No. **12**, pp. 1176-1199, 2000.

S. Koch, A. Starlinger, *Joining of sandwich composites to metallic structures: a comparison between riveting and elastic bonding*, Proc. 5th Intl. Conf. on Sandwich Construction, Zurich, Switzerland, pp. 373-386, 2000.

P. Noury, A.T. Echtermeyer, B. Hayman, *Sandwich failure for design guideline*, Proc. 5th Intl. Conf. on Sandwich Construction, Zurich, Switzerland, pp. 401-411, 2000.

J. R. Vinson, The behaviour of sándwich structures of isotropic and composite materials*, Technomic Publishing Co. Lancaster, 1999.*

D. Zenkert, The handbook of sandwich construction, *EMAS publishing, 1997.*